MECHANICAL PERFORMANCES OF COMPOSITE-STRENGTHENED CONCRETE STRUCTURES WITH EMBEDDED FBG SENSORS

by

Alan, Kin-tak Lau

A thesis submitted in fulfilment of the requirements for the degree of Doctor of Philosophy at The Hong Kong Polytechnic University

Department of Mechanical Engineering

Acknowledgement

I wish to express my great appreciation to my supervisor Dr. Li-min Zhou and Co-supervisor Professor Chung-ho Woo, for their guidance, encouragement and support throughout the course of study. This project could not be eventuated without their invaluable supervision, direction and continued encouragement. My thanks go to Dr. Wei Jin and Mr. Kok-cheung Chan from the Department of Electrical Engineering, The Hong Kong Polytechnic University for providing equipment and optical fibre to conduct experimental tests.

Special thanks go to the staff from the Industrial Centre, The Hong Kong Polytechnic University for their help, and support of facilities and materials to make concrete specimens for testing. Sincere thanks also go to the staff in Project Laboratory of the Department of Mechanical Engineering, The Hong Kong Polytechnic University for their help of manufacturing concrete moulds and setting up the experimental rigs.

Finical supports from the Hong Kong Polytechnic University Research Grant (GV-528) and Sir Edward Youde Memorial Fellowship are much appreciated.

Finally, I would like to thank my wife, Edith Wai-kam Chan for her continued love, understanding, support and never ending encouragement over the years.

Declaration

I declare that this thesis contains no material, which has previously been presented for the award of any other degree or diploma in any other University or Institute. To the best of my knowledge, the material is original except where due reference is made in the text of the thesis.

Alan, Kin-tak Lau

Abstract

Investigations on the use of fibre reinforced plastic (FRP) composites to strengthen and reinforce civil concrete structures have been found increasingly in recent years. Lightweight and high-strength FRP plate or sheet is laid up on the concrete surface to maintain structural integrity and increase load carrying capacity of deteriorated or aged concrete structures. Meanwhile, the optimisation on the design of using the materials in FRP concrete strengthening with high strength efficiency, low manufacturing and labour costs, long serviceability life and minimum traffic interruption becomes an important issue in the civil and construction engineering applications. In addition, the development on the structural health monitoring system for a structure, which is strengthened by the FRP materials is also significant for inspecting the subsequent damages.

Current study aims to investigate the mechanical behaviours of concrete structures, which are strengthened by the FRP materials on the concrete surface subjected to international standard test. The scope of the study also includes the development of smart structure health monitoring system for these strengthened structures by embedding fibre-optic Bragg grating (FBG) sensors inside the concrete and at the interface between the concrete surface and externally bonded composite materials.

An extensive review is given to discuss the present practice on the utilisation of the FRP materials in the civil concrete applications. Materials, configurations of the structures, quality control and manufacturing methods for the FRP strengthened concrete structure were also reviewed. Another focus was placed on the adaptability of using the embedded optical fibre sensor as strain- and temperature-measuring devices in engineering applications. The survivability and mechanical performance of the FRP and optical fibre sensor in harsh environments were also addressed.

Following the comprehensive review, several results from preliminary experimental studies are given. These studies include fundamental mechanical property tests for the concrete, composite and interfacial bonding behaviour of composite plate with an embedment of opti-

cal fibre. The results from the lap joint shear test for the composite-concrete bonded joint shows that an epoxy resin can provide a strong bonding characteristic to the concrete materials.

Mechanical behaviour of composite-wrapped concrete structure was investigated. The laboratory-sized concrete cylinders were wrapped around its circumference by glass fibre composite laminates. The composite-wrapped concrete cylinder was then subjected to the uniaxial compression load. Several effects on the composite-wrapped system were also investigated through experimental work and numerical analysis. In the experiment, it was found that the load carrying capacity of the wrapped cylinder increases with increasing the number of laminate layers. Splitting failure occurred at both ends of wrapping laminate and continuously propagated toward the mid-height of the cylinder. Numerical analysis using the finite element method (FEM) interpreted the strengthening efficiency and failure mechanisms of the composite-wrapped concrete structure with different wrapping dimensions, material properties and thicknesses. The maximum load carrying capacity of the composite wrapped cylinder increases with increasing the wrapping size, thickness and modulus of the wrapping material while the maximum hoop stress in the wrapping material increases at both ends of the wrapping laminate. However, the negative hoop stress in the wrapping material occurs when using high modulus and thick wrapping laminate. Optimised design can be achieved by using the FEM analysis.

Composite-bonded rectangular concrete beams (with/without crack formation at mid-beam) subjected to the three-point bending were investigated through experimental observation, analytical and numerical approaches. Glass fibre composite plates with different bonding lengths and thicknesses were adhered on tension or shear surfaces of the beam in order to investigate the mechanical behaviour of the whole composite-strengthening system. Flexural-cracks in the concrete and debond at the interface between the concrete and composite were observed during the test for long plate-bonded structures. For short plate bonded structures, crack was initiated at plate end region in the concrete. The strengthened beam was then failed catastrophically. No debond at the interface between the concrete and composite was found for the thick and short bonding length system. The overall performance of the composite-strengthened beam was better than that of the plain beam in term of flexural

strength properties. Wet lay up technique gave higher ultimate flexural strength than the pre-cured plate-bonded method for the composite strengthened beam. For a notched concrete beam with an injection of epoxy resin, the modulus and ultimate strength were slightly increased compared with the plain beam.

Linear elastic analytical model was derived to investigate adhesive shear and peel-off stresses with different strengthening plate geometries and material properties for the composite-strengthened structure. The results show that the adhesive shear and peel-off stresses increases with increasing the plate modulus and thickness. Theoretical prediction in determining the stress intensity factor (K_I) for the strengthened structure was also conducted. The K_I decreases with increasing the strengthening plate thickness and modulus.

The adaptability of using embedded fibre-optic Bragg grating (FBG) sensor for strain measurement was investigated experimentally. The FBG sensors were embedded at the interface between the concrete and composite in both the composite-wrapped and plate-bonded concrete structures. Externally bonded strain gauges were adhered on the surface of the composite to compare the strain measuring results from the sensors. Four-cylinder theoretical model was established to determine the stress transferring properties and minimum embedding length for the embedded sensor. The theoretical prediction reveals that the axial strain measured at the fibre core region of the sensor is lower than the true strain of the host material if using the embedding sensor with thick adhesive layer and short plate bonding length. Experimental results also show that the surface mounted strain gauge could not detect the true strain of the host material when debond at the interface was happened. However, the embedded sensor could give signal to the operator that the structure was operated in strange condition.

Environmental effect on composite-strengthened structures is one of the most important aspects in the application of the FRP. The mechanical performance of the plate bonded reinforced-concrete (RC) structures after immersing into the saline water, fresh water, acidic (PH 4.01) and alkaline (PH 10) solutions for 6 months were studied. Experimental results show that the overall flexural strengths of the composite-strengthened RC beam is increased compared with the plain RC beams at the same chemical environments. The strength of the

RC beam is susceptible to acidic solution, a 24.8% drop in flexural strength was measured for the beam submerged into PH 4.0 solution for six months.

Finally, conclusions and recommendations for the further study in the design of composite-wrapped and plate-bonded structures, strain measuring system and installation process are presented.

Nomenclature

λ	Light reflective wavelength, nm.
α	Modulus ratio of the concrete and wrapping sheet.
α_f	Fibre longitudinal coefficient of thermal expansion.
α_m	Matrix longitudinal coefficient of thermal expansion.
ε_θ, ε_r, ε_z	Strain in the hoop, radial and fibre directions, respectively.
σ_θ, σ_r, σ_z	Stress in the hoop, radial and fibre directions, respectively.
ε_1	Axial strain along the lengthwise direction of the fibre.
τ_{12}	Interlaminar shear strength, Pa.
ε_2, ε_3	Principle strains in the cross-section plane of the optical fibre core.
γ_a	Adhesive shear strain.
τ_a	Adhesive shear stress, Pa.
σ_a	Peel-off stress of the adhesive material, Pa.
δ_a, δ_p	Relative displacements of adhesive layer and protective coating, m.
τ_{ap}	Shear stress in protective coating, Pa.
λ_B	Bragg's wavelength, nm.
σ_c	Axial stress in the fibre (optical fibre) core, Pa.
σ_{co}	Compressive stress in the concrete cylinder at the middle of the cylinder, Pa.
σ_f	Flexural strength, Pa.
σ_h, σ_{ho}	Axial and maximum tensile stresses at the bottom of the beam, respectively, Pa.
β	Moduli ratio of fibre and matrix, E_f/E_m.
θ_i	Light incident angle.
ΔL	Change in length of a structure after loading, m.
ξ_o	Coefficient of both the thermo-optic component and thermal expansivity of the optical fibre.
ε_o, ε_c	Axial strain in the host material (surrounding matrix) and fibre core.
σ_o, σ_p	Applied stress in the concrete beam and composite plate, respectively, Pa.

ω_p, ω_c	Axial deflections of wrapping sheet and concrete cylinder, respectively, m.
v_f	fibre volume fraction of composite.
ε_p, ε_c	Axial strains of the wrapping sheet and concrete cylinder, respectively, m.
v_p, v_c	Deflections of the composite plate and concrete beam, respectively, m.
ΔT_h	Differential temperature of the composite.
ΔT_c	Different temperature of the fibre core.
σ_{po}	Compressive stress in the wrapping material at the middle of the cylinder, Pa.
θ_r	Light reflective angle.
σ_{ult}	Ultimate compressive stress of the concrete, Pa.
η_w	Wrapping coefficient of the composite wrapped concrete cylinder.
a	Crack length, m.
A	Cross section area of the concrete cylinder, m^2.
A_{ij}	Extensional matrix.
η	Area ratio of the concrete and wrapping sheet.
b	Beam width, m.
B_{ij}	Extensional-bending coupled matrix.
d	Beam depth, m.
D_{ij}	Flexural matrix.
E_a	Modulus of the adhesive material, Pa.
E_c	Modulus of the concrete, Pa.
E_{eff}	Effective modulus of the composite laminate, Pa.
	Embedding length of the optical fibre, m.
E_p	Tensile modulus of the composite plate, Pa.
f	Beat frequency, Hz.
f_c	Concrete compressive strength, MPa.
F_p	Closing force in externally bonded composite plate, N.
G_a	Shear modulus of the adhesive material, Pa.
h	Depth of the rectangular concrete beam, m.
I_c, I_p	Moment of inertia of the concrete beam and composite plate, respectively, m^4.

K	Stress intensive factor, $N/m^{1.5}$.
K_ε	Theoretical gauge constant, nm^{-1}.
k_δ^*	Kink load of the plain concrete cylinder, N.
K_I, K_{II}, K_{III}	Mode I, II and III stress intensity factors, $N/m^{1.5}$.
k_o	Kink load pf the composite wrapped concrete cylinder, N.
L	Original length of the structure before loading, m;
L_f	Wrapping length measured in the axial direction of the cylinder, m.
L_g	Total length of the grating region, m.
M_b	Bending moment along the beam, Nm.
M_c, M_p	Bending moment of the concrete beam and composite plate, respectively, Nm.
ε	Mechanical strain.
N	Axial load in laminate, N.
n	Light refractive index.
N_c, N_p	Normal force of the concrete beam and composite plate, respectively, N.
$n_{cladding}$	Light refractive index in cladding material.
n_{core}	Light refractive index in fibre core material
n_{eff}	Effective light refractive index in grating region.
P	Centre load for three point bending test, N.
P_c	Axial load in the concrete cylinder, N.
ν	Poisson's ratio.
P_p	Axial load in the wrapping sheet, N.
P_{peak}	Peak load, N.
R	Modulus of rupture, MPa.
r_c, r_{ap}, r_h	Outer radius of the fibre core and protective coating, inner radius of the surrounding matrix, respectively, m.
r_i	Inner radius of the wrapping sheet or laminate, m.
r_o	Outer radius of the concrete cylinder, m.
	Span of the test specimens, m.
Λ	Spatial pitch in grating region for fibre-optic Bragg grating system.
T	Ambient temperature (°C).

t_a	Thickness of the adhesive layer, m.
t_p	Thickness of the wrapping sheet or laminate, m.
u_p, u_c	Displacements of the concrete beam and composite plate in y direction, respectively, m. ; Displacements of the protective coating and fibre core in fibre longitudinal direction, m.
X_o	Neutral axis of the composite strengthened cracked concrete structure, m.

TABLE OF CONTENTS

CHAPTER 1

INTRODUCTION

1.1 Aims and Objectives

Many researches and developments on the use of fibre-reinforce plastic (FRP) composite materials in concrete rehabilitation and retrofit have been carried out recently. Focus of those researches was placed on the examination of feasibility rather than in-depth understanding of the failure mechanism, stress transferring properties and environmental effects for composite-strengthened concrete structures. Investigation on the structural health monitoring technique of the composite-strengthened structures using embedded sensor was also very limited. Therefore, a comprehensive study in understanding stress transferring problems, failure mechanisms, effects on the structures with different material properties and geometrical factors for both the composite-strengthened concrete structure and sensor embedding systems is essential.

Present study intends to provide comprehensive information for the composite-strengthened concrete structure associated with the embedment of optical fibre strain sensor under different loading configurations. Two types of composite-strengthened concrete structures are under investigation in current study including (1) composite-wrapped concrete cylinder and (2) composite-bonded rectangular concrete beam. The main objectives of the study are summarised as follows:

- Experimental investigation on the mechanical performance of laboratory-sized glass fibre composite-strengthened concrete structures with different composite bonding dimensions and laminate layers.

- Theoretical studies on the stress transferring problems for the composite-strengthened concrete structures with different bonding dimensions, thicknesses and mechanical properties.
- Numerical studies on the composite-strengthened concrete systems using finite element method (FEM) to predict the overall mechanical performance of the structures.
- Investigation on the fracture problems of concrete structure with a crack on tension surface after strengthening by externally bonded composite plate.
- Establishment of a theoretical model to interpret the effects on strain measurement by using embedded optical fibre sensor with different coating, adhesive and matrix materials.
- Durability of the composite-strengthened structure in different harsh environments.

1.2 Research Significance

The demand on rehabilitation and renewal of aged and deteriorated civil concrete structures has been swiftly increased in recent years. Continuing deterioration of the world's infrastructure elements highlights the urgent need of effective rehabilitation technique with low material and maintenance costs, short installation time and minimum traffic interruption. It is now evident that the deterioration of worldwide infrastructure elements has been caused by a variety of factors including time dependent material degradation, widespread fatigue damage, initial use of poor materials, flaws in design and the use of de-icing salts. In addition, the rapid increase of population in many developing countries enhances the requests of upgrading and retrofitting existing concrete structure as well as the increase of the traffic volume, which is beyond the original design limit. Besides, the world's scientists and engineers are required to find out the solution immediately to reinforce the old concrete structures, which are most susceptible to seismic damages. An estimated need for infrastructure construction and rehabilitation in the Asian areas alone is almost US$2 trillion in the early twenty-first century [Lee et al, 1999]. In United State, 80 billion will be paid for the repair of current deficiencies civil infrastructure [Wu, 1999]. In

California alone, over 3.5 billion is required for seismic retrofitting of concrete bridges.

Due to the increases of public and political concerns about the decay of national infrastructure, it is also required for an effective mean to monitor the condition and strain history of the strengthened and repaired concrete structures [Saouma, 1998]. In the past decade, multi-disciplinary field of engineering known as 'Smart Structure' has represented one of the most major research topics in the World. It is formed by the marriage of engineering materials with structurally-integrated fibre-optic sensor and actuation control system. The system is capable of assessing damage and warning of impending weakness in the structural integrity of the structure [Groves-kirkby, 1998].

According to the above concerns, the development of new rehabilitation technology associated with the 'Smart Structure' concept in the existing civil engineering disciplines is significant. The new rehabilitation methods for the deteriorated structures must be established for long term environmental protection, concrete confinement and good interfacial bond integrity. It leads to provide a durable and economic alternative to conventional repair method.

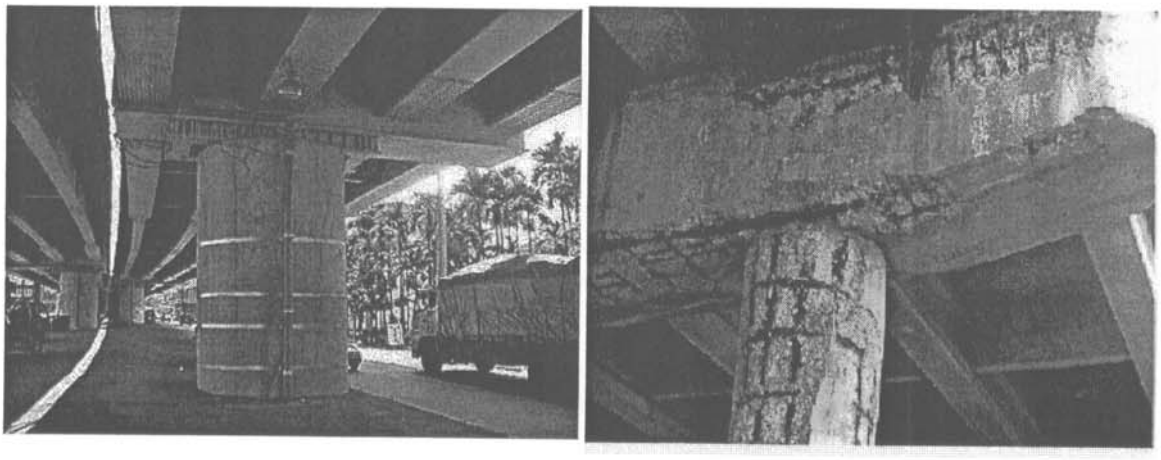

Figure 1.1 Severe cracks appeared at the tops of the concrete column after earthquake in the city of Nantao in 1999 (left). The concrete spalling happened due to the volumetric expansion of corroded steel reinforcement (right).

1.3 Background

Over the past several decades, extensive research and development in the field of materials engineering and science have been carried out with fibre-reinforced plastic (FRP) composites, which have a wide range of practical applications. It has been reported that concrete bridges that remained standing after the 6.6 magnitude earthquake in Los Angeles after jacketing by FRP composite wrap [Seible et al. (1997)].

The conventional rehabilitating techniques using stitching and steel reinforcing patch design can provide a promising strengthening solution in civil concrete applications [Sameer and Ahmad (1997)]. Unfortunately, the weight penalty, labour intensive and subsequent corrosion of the steel material may eventually increase the overall maintenance cost. Accordingly, this requires the development and application of new materials and technologies, which can extend the service life of the constructed facilities with reducing maintenance and improving durability. The new retrofitting technique should be able to restore the strength of or strengthen the deteriorated concrete structures without increasing any traffic disturbance and cost of maintenance. Thus, the use of FRP materials such as glass fibre in polymer matrices is becoming increasingly important to extend the service life of our civil construction facilities in the 21st Century.

The technique of using FRP in upgrading and strengthening the civil concrete structures has been developed only in recent years. In the past, the FRP materials were used primarily in the aerospace and defence industries rather than in civil construction areas. It is due to the prohibitively high cost of raw materials and manufacturing processes. Previous researches showed that the glass fibre composites could be effectively used for concrete beam strengthening which results in the improvement of flexural load carrying capacity. The overall compressive strength of FRP wrap for the confinement of concrete column increases with increasing the number of wrapping size and laminate.

A term of "Smart Structural Monitoring System" technology requires the development of materials with self-optical nerves. Structures constructed from such materials can monitor their own mechanical properties such as strain and thermal states by some measuring means. In civil engineering construction, buildings, bridges, tunnels, highways and railways, the embedded optical fibres can improve concrete evaluation, which provides real-time structural health monitoring and enables immediate condition awareness for service assessment of structural integrity. Also, optical fibre is insensitive to electromagnetic interference and can be configured to sense a variety of physical effects, which include temperature changes, mechanical properties of host materials, electric field strength and magnetic field strength with minimum ambient interference.

In aerospace industries, embedded optical fibres are being used in composite wing for in-flight monitoring purpose. The periodical manual inspection of crack and delamination of composite structures can be greatly reduced and only required when it is needed. In addition, the duration for which the structure is required to withstand damage would be reduced because damage would be detected earlier. The realistic application of embedded optical fibre in the concrete structure is still limited in civil engineering application. Besides, the bonding properties between cladding of the fibre and surrounding matrix and aggregate are not fully understood up-to-date.

CHAPTER 2

LITERATURE REVIEW

2.1 Advanced Composites for Concrete Rehabilitation and Retrofitting

2.1.1 Introduction

Fibre reinforced plastic (FRP) has been recognised as one of the most innovative materials in the applications ranging from the aerospace industry to prevalent sport goods and facilities for more than 30 years. It has been demonstrated that the FRP could be used successfully to replace conventional materials for most primary structural elements in modern aircraft with safe and durability [Niu, 1993]. The most attractive benefits by using the FRP in real-life applications include its high strength to weight ratio, resistance to corrosion, ease of moulding into complex shape without extensively increasing the manufacturing cost, good adhesion properties to most common materials and ability to be pre-fabricated in the factory. Unfortunately, the adoption of the FRP in civil construction is still limited so far. The serious concerns regarding the use of the FRP as reinforcements or substitutes for concrete structures are lack of experimental history, international design code and recognised specifications, and economics related to fabrication [Gilstrap et al. 1997].

Many extensive researches have been paid much attention on the developments of using the FRP in retrofitting and strengthening civil concrete structures in recent years. The implementation of the researches are mainly grouped into five areas, which include: (1) concrete confinement by FRP wrap and grid systems, (2) beam strengthening in flexure by using externally bonded FRP patch, (3) seismic damage resistance of concrete column, (4) investigation on the failure mechanisms and (5) environmental effects of FRP strengthened structures.

2.1.2 Composite Wrapped Concrete Columns

Many experimental and theoretical studies have been conducted by a number of researchers and construction engineers on the use of steel-based isotropic materials for concrete rehabilitation and retrofitting. These materials have been widely accepted in most industrial applications. However, there exist the negative aspects such as the corrosion caused by harsh environments and need of large lifting equipment to hold the steel plate in place during installation process [Mirmiran, 1998], which in turn subsequently increases the time of traffic interruption.

Earlier research regarding the confinement of laboratory-sized Portland cement concrete column by using the FRP laminates was conducted in 1992 [Harmon and Slattrey, 1992]. Plain concrete columns were wrapped by glass fibre composites and subsequently subjected to an uni-axial compressive load in order to investigate the mechanical responses of the column after confining. In recent studies, remarkable results were found that the ultimate compressive stress of the confined column was substantially increased with increasing the number of wrapping laminates [Larralde 1997, Spoelstra et al. 1999]. It was showed that the use of carbon fibre composites to confine the concrete column appeared more reliable than that using glass fibre composites when exposed to harsh environments [Toutanji, 1999].

Karbhari et al. (1997) found that the relation of the compressive stress and strain of the confined concrete column responses bi-linearly in the uni-axial compression test. He also addressed that the use of FRP wrap is an effective means in terms of cost and speed, and overall fabrication process for the purpose of concrete rehabilitation. Mirmiran et al. (1998) concluded that the confinement effectiveness for square column is dependent on the corner radius and jacket hoop strength.

Extensive practice in large columnar concrete structures has been performed in situ by using the automated FRP wrapping system [Karbhari, 1997] which was called "Composites jacketing system". The FRP laminates were laid-up and cured automatically by applying the pressure and heat simultaneously to wrap prepreg materials through the "Robo-Wrapper"

machine (see Fig.2.1). It should be noted herein that the major function of the FRP laminates for the concrete in a state of triaxial compression is to restrain its transverse dilation without involving heavy materials and equipment, which can cause the disturbance of traffic operation.

FRP grid and tube have been developed recently to replace steel reinforcement for reinforced concrete column [Mirmiran et al. 1996, Lee et al. 1999 and Engel, 1999]. Experimental results indicated that the compressive strength and toughness of concrete column with FRP grid were increased compared to those of the fresh column. Lee et al. (1999) pointed out that the use of PVC tube as an insulated layer between the concrete and external FRP filament could prevent fibre damage due to the chemical attack from the concrete and provide the confining action for the whole system. However, the grid and tube method are only suitable for new construction elements since the concrete is required to cure inside the pre-fabricated FRP/PVC tube. For the FRP wrapping technique, FRP can be wrapped on the surface of pre-consolidated concrete structures.

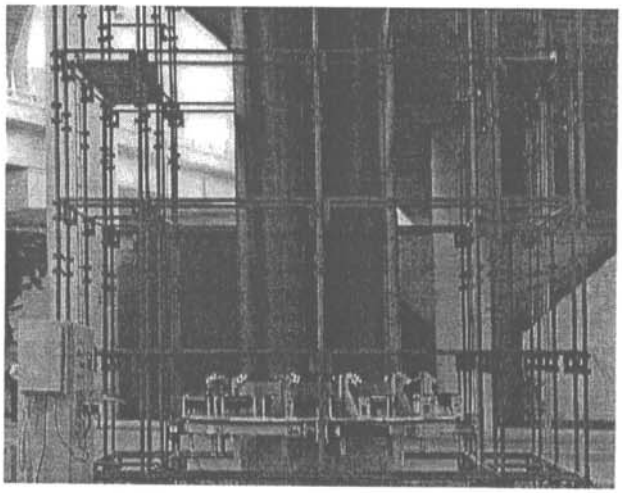

Figure 2.1. The composite jacketing system (ROBO-Wrapper II^{TM})

2.1.3 Composite Strengthened Concrete Beams

Steel plate bonding method for the rectangular concrete beam has been used worldwide for over twenty years to strength concrete members [Garden et al 1998]. The disadvantages of

this method include inconvenient transportation and installation of this heavy material and the subsequent corrosion due to exposure to harsh environment [Toutanji, 1999].

The use of FRP as an external reinforcement for bridge retrofit has been represented as noteworthy improvement in terms of cost-effective, less effort and time than traditional methods [Kaliakin, 1996, Shahawy et al. 1996, Arduini et al. 1997, Garden et al. 1998 and Ritchie et al. 1998]. The FRP materials have a low specific mass, and are easy to handle, particularly when operating in constrained and enclosed situations [Spadea et al. 1998]. Since the FRP have a high tensile strength with relatively low in weight, it allows significant reductions in plate dimensions and installation facilities when used as external plate reinforcement. Due to the corrosion-free property of the FRP materials, they become practice in use for real-life applications [Meier and Deuring, 1991, Meier 1995, and Steiner, 1996].

Ritchie et al. (1998) has observed experimentally that the failure of FRP strengthened beam occurred catastrophically, which was caused by linear-elastic properties of the FRP. It has been shown that the ultimate flexural strength of the FRP plate bonded beams was higher than that of the beam without plate bonding [Chaallal et al. 1998 and Grace et al 1999]. FRP strips can be effectively used for controlling shear cracking, shear strength and stiffness of the beam by bonding the stripes on both sides of the beam in 90° to the shear crack [Taljsten, 1996 and Chaallal et al. 1998].

The debond and peel-off failures of the FRP plate of the strengthened beams would result in sudden drop in load and brittle failure of concrete [Sakai et al. 1996]. In certain aspects, anchoring mechanisms have been used in practice to avoid the peel-off and sliding of the plate at plate end regions [Luke, 1999].

For the purpose of strength restoration of damaged structures, several experimental studies have been performed to investigate the mechanical performance of the cracked-concrete structures after being strengthened by the externally bonded FRP plate. Buyukozturk et al. (1998) found that the flexural strength of FRP bonded cracked-concrete beam was increased

compared to the cracked-beam without strengthening. Surface treatment of the bonding area is essential in order to provide somewhat rough surface to improve the bonding quality.

Possible failure mechanisms of the FRP strengthened beam are grouped into five distinct categories, which include: (a) shear and (b) flexural crackings in concrete without any damages in the FRP plate, (c) rupture of the FRP plate followed by cracking in concrete and (d) peel-off and (e) total debond failures at the bonding interface. A schematic diagram for all possible failure modes of FRP strengthening system is shown in Fig.2.2

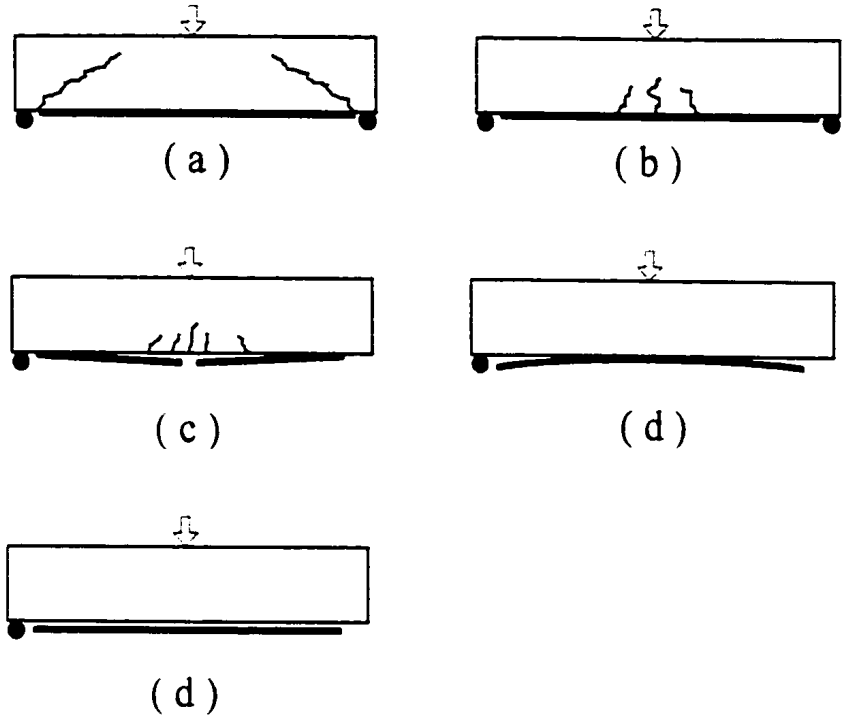

Figure 2.2 Failure mechanisms of FRP strengthened concrete beams. (a) concrete shear. (b) flexural cracking, (c) rupture of an externally bonded plate followed by cracking of concrete (d) plate peeling-off and (e) entire plate debonding.

2.1.4 Seismic Resistance

Recent earthquakes such as the one in Northridge in 1994. Kobe in 1995 and Taiwan in 1999 have repeatedly demonstrated the vulnerabilities of old infrastructure elements to the demands of seismic deformation. For existing reinforced concrete columns with insufficient

transverse reinforcement and/or design for seismic detailing, three different types of failure modes are generally observed under seismic load and deformation inputs. They are (1) column failure by shear, (2) column failure at the flexural plastic hinge region and (3) failure at the lap splice region. These problems under seismic vibration result in the concrete spalling and crushing, and concrete cracking followed by column rupture.

The development of a new seismic retrofit system for the reinforced concrete columns has been demonstrated by jacketing technique with continuous carbon fibre reinforced composites [Mo et al. 1998, Seible et al. 1997]. Carbon fibre composites were wrapped in either the whole RC column or lower column end to form the connection between the footing and column. Experimental study were scaled down to laboratory sized RC specimen. Load was applied repeatedly in lateral direction to simulate the real earthquake conditions. The results indicated that the retrofitted RC column with the surface wrapped composite could improve seismic response characteristics. The ultimate load that the strengthened structures would carry was increased up to 40% and the allowable deformation was more than 180% compared to that of its un-strengthened status. However, the supporting facilities and the time for installing the FRP reinforcement were greatly reduced.

Unreinforced masonry (URM) constructions have been recognised as one of the most poorly performed constructions under the seismic loading and also identified as the main cause of loss of life in recent earthquakes [Ehsami et al. 1999]. Glass fibre composite plate has demonstrated the superior performance in increasing the flexural strength of the walls by adhering vertically on the surface of URM wall under the simulated earthquake loading.

2.1.5 Current Related Researches in Real-life Application

Many researches have been conducted in United Kingdom, Japan and Canada to investigate into the use of carbon fibre composite plate for the real infrastructure retrofits [Luke, 1997, Dellow, 1999, Mayo, 1999 and Connor, 1999]. Strips of carbon fibre composite plate were bonded on the bottom surfaces of existing bridges and wrapped around the circumference of aged columns to improve overall mechanical performance of the structures. A jack-and-anchor arrangement has been used to secure the plate at both ends [Connor, 1999].

Aramid fibre (Kevlar) possesses many advantages over carbon fibre as reinforcement for concrete, which includes (i) low density; (ii) non-catastrophic failure, which can reduce the risk of sudden damage; (iii) better impact resistance (it is suitable for structures liable to collision damage and seismic disturbances) and (iv) electrical insulator (so it can be used close to power lines or communication facilities) [Peter, 1999].

E-glass fibre composites have been used to reinforce the structure, which is designed for accommodating the addition of the helipad on the top of hospital building [Delta 1998]. Total 15 columns were wrapped by a varied number of layers of SHE 51 E-Glass fibre with saturated in an epoxy matrix at the top two floors. A final layer of UV protective coating was applied to ensure long term performance. The project aimed to investigate the mechanical behaviour of the column after being wrapped by FRP laminates. The wrapped structure is shown in Fig 2.3.

Figure 2.3 E-glass/epoxy composite for column strengthening in real-life practice.

The official data issued by the Federal Highway Administration in the use of FRP materials for bridge rehabilitation in 1998 showed that the overall cost for strengthening the bridge by using FRP bonding technique instead of reconstruction was saved up to 91% [Connor, 1999]. The time required for completing the job was only 2 weeks which only caused little impact on traffic interruption. However, the time used to reconstruct the bridge was more

than 15 months. Nevertheless, the strength of the strengthened structures could be restored to its original status (see Table 1).

XXsys Technologies, Inc. California has developed Robo-Wrapped™ auto-wrapping machine for strengthening the existing column where corrosion and cracks are found by using the carbon fibre prepreg. They found that the load carrying capacity of deteriorated and overloaded bridges was increased after being strengthened by carbon fibre reinforced composites. The degree of debonding was also much smaller than that of using steel as reinforcement. Consequently, a far smaller reduction in strength of the structures was expected.

Table 1.1. Comparison for bridge rehabilitation by reconstruction and FRP strengthening methods.

	Total Cost	Duration	Strength Gain	Impact on Traffic
1986 reconstruction	$ 151,000	15 months	100 % of original	Major restrictions
1998 FRP strengthening	$ 12,000	2 weeks	18% increase	Little interruption

2.2 Smart Structures

2.2.1 Introduction

A new development of "Smart materials and structures" was driven by the strong demand for high performance in recent year. A system integrated into structures and being able to monitor the physical and mechanical properties such as temperature and strain during the service condition is appreciated as a "Smart structural health monitoring system". The term of smart material and structure is widely used to describe the unique marriage of material and structural engineering by using fibre optic sensors and actuation control technology [Czarnek et al. 1989]. The smart structure is constructed by the materials which could continuously monitor their internal strain and thermal status, and therefore, capable of assessing

damage and warning of impending weakness in structural integrity. This design results improve safety and economic concerns regarding weight saving and avoidance of over-designing of the structure. In Fig 2.4, structures possibilities created by the confluence of four disciplines are shown.

Recent researches have shown a great interest in using optical fibres as embedded sensors for measuring the temperature variation and strain profile during the manufacturing and loading processes of the advanced composite materials [Uomoto, 1998].

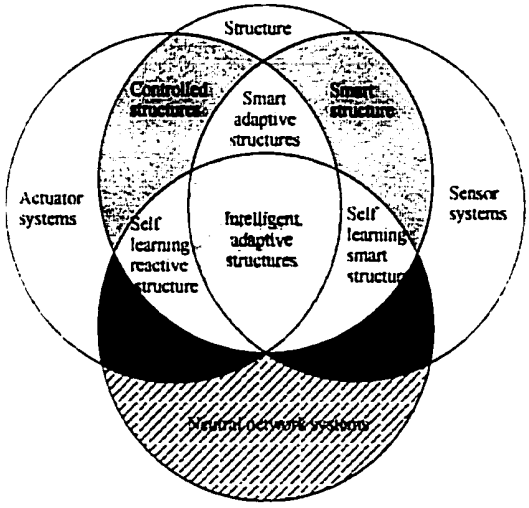

Figure 2.4 Structure possibilities created by the confluence of four disciplines: materials and structures, sensing system, actuator control systems, and adaptive learning neural network [Measures, 1992].

2.2.2 Optical Fibre Sensors

2.2.2.1 Introduction

Optical fibres have been developed for long-distance data transmission in the telecommunication industry. However, in their earliest application, optical fibre was conceived as a medium for transmission of light in medical endoscopy. The use of optical fibres for applications in the telecommunication industry actually started in the mid 1960s, and ever since has

gone through tremendous growth and advancement. The development of optical fibre sensors started in earnest in 1977 even though some related demonstrations proceeded this date [Cole et al. 1977, Butter et al. 1978, Budansky et al. 1979 and Rutherford et al. 1992]. The increased use of advanced composites in aeronautics instigated the need for new damage detection techniques, which can monitor the integrity of structural components during service period. Therefore, the optical fibre sensors have been extensively employed as real-time damage detection tools in advanced aircraft and space vehicles.

External perturbations such as strain, pressure or temperature variations induce changes in the phase, intensity, or wavelength of light waves propagating through the optical fibres. The changes in one or more of the properties of light can then be related to the parameter being measured. Optical fibres are geometrically versatile and can be configured to arbitrary shapes. The smart structure concept takes advantage of the geometric adaptability of optical fibres. In this technology, optical fibre sensors are embedded within the structural material or bonded on the structure surface for the purpose of real-time damage assessment. The most attractive feature of fibre optic sensors is their inherent ability to serve as both the sensing element and the signal transmission medium, allowing the electronic instrumentation to be located remotely from the measurement site. This is especially useful for remote monitoring of the condition of bridges. Moreover, the advantages of using embedded optical fibre sensors in composite materials are dimensional and material compatibilities. The fibres do not degrade during curing, they do not corrode, and bond strongly to the matrix. Incorporation of the fibres during the processing stage also offers the opportunity to monitor the condition of structural elements during fabrication [Hockker, 1979, Afromowitz, 1988, Murphy and Duke, 1988].

The success of optical fibre sensor technology in the condition monitoring of composite materials led to a limited number of research and development activities in the civil engineering discipline. A number of researchers realised that this emerging field of technology could have impact on the condition monitoring of civil structures, so that durability, safety and efficiency of the infrastructure system can be improved. Proper application of optical fibre sensors to concrete structure repair monitoring requires understanding of certain fun-

damental methodologies pertaining to sensor mechanisms as well as sensor multiplexing strategies.

Ups to now, enormous types of optical fibre sensors have been developed. The sensors have been classified in a number of different ways. For instance, they can be categorised based on the monitoring applications. The classification is depicted as

$$\text{Optical fibre sensor applications} \begin{cases} 1.\textit{Localized} \\ 2.\textit{Multiplexed} \\ 3.\textit{Distributed} \end{cases}$$

2.2.2.2 The structure of optical fibre

Optical fibres are one of the world's most influential scientific developments from the latter half of the 20th century. They are dielectric wave-guiding devices used to confine and guide light. In general, the optical fibre consists of silica fibre core, cladding and protective coating. In Fig. 2.5, schematic and micrographic diagrams of the structure of optical fibre are shown.

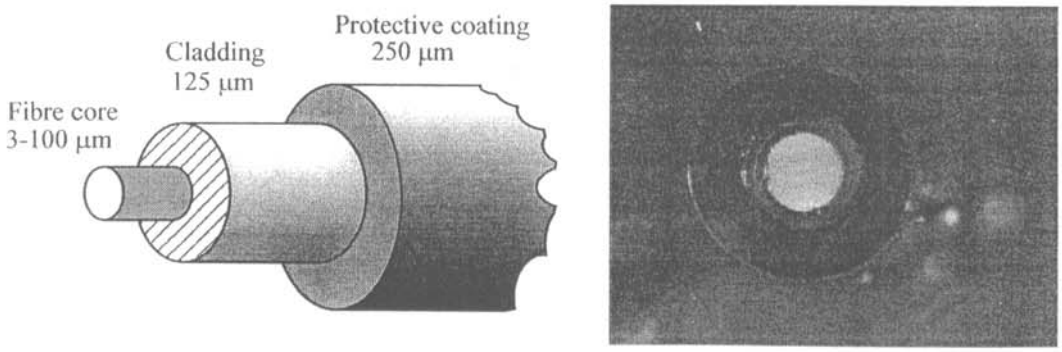

Figure 2.5 A structure of the fibre-optic strain sensor (left) and micrographic view of typical commercial used optical fibre (right).

The core is surrounded by a dielectric material called the cladding. The mechanical properties of the cladding are similar to those of the core but with slightly lower refractive index. It functions to satisfy the Snell's Law for producing total internal reflection and guiding the

light to propagate along the fibre core [Micheal, 1996]. The cladding is generally made from silica glass. A protective coating is used to protect the fibre from damage by providing mechanical strength and reducing the risk of moisture absorption.

2.2.2.3 Fundamental theory of optical fibre

The fundamental principle, which makes the optical fibre possible in all sensing and communication applications is their total internal reflection properties. According to the Snell's Law, the refraction of light from one medium to another is dependent on the incident angle and the differential refractive index between two mediums. In Fig.2.6, it clearly shows that the angle of refraction (θ_{1r}) decreases with decreasing the incident angle (θ_{1i}) . This implies that as the angle is reduced to a certain value, there must be a point at which the light ray is reflected ($\theta_i = \theta_r$). This condition can only be true when the refractive index of the source medium (1) is greater than that of the target medium (2).

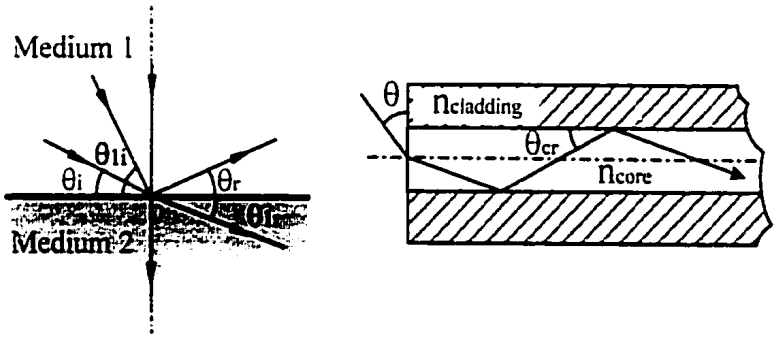

Figure 2.6 Illustration of refraction at an interface from one medium to another.

According to the Snell's Law, it obtains

$$n_{\text{medium 1}} \cos(\theta_{1i}) = n_{\text{medium 2}} \cos(\theta_{1r}) \qquad (2.1)$$

where n represents the reflective index of material. The critical angle, θ_{cr} which results to a total reflection of the ray to travel along the fibre core can be evaluated by assuming $\theta_{1r} = 0$.

$$\theta_{cr} = \cos^{-1} (n_{cladding} / n_{core}) \quad (2.2)$$

A typical value of $n_{cladding} / n_{core}$ for the strain sensing optical fibre is 0.99 [Personick, 1985] and the critical angle θ_{cr} is then 8.11°. Thus rays travelling at an angle less than θ_{cr} relative to the reference acis will be totally internally reflected, and guided by the fibre core. Higher-angle rays will enter the cladding and be lost due to high levels of scattering and absorption.

2.2.2.4 Fibre geometry

A fibre consists of a core region and a cladding region. The core section is typically made of silica glass, and has a diameter of 3μm to 100μm. In general, a small core fibre is only a few times larger than the light wavelength. Due to its physical size, only one ray can propagate through the fibre. The wavelength of light for typical optical fibre systems is between 0.8 and 1.6 μm.

For multi-mode fibre, the core diameter, which is tens or even a hundred times as large as light wavelength (called multi-mode fibre). A silica glass cladding has a slightly lower optical density (reflective index, $n_{cladding}$), which is typical below a fraction of 1%. The diameter of cladding is typically 125μm. Light tends to be guided in the core of the fibre as indicated in Fig. 2.6. The cladding of the fibre is surrounded by a protective coating. The function of the coating is to protect the fibre from damages due to the mechanical strength, aggressive environments and scratching [Powers, 1997].

2.2.2.5 Attenuation

Attenuation refers to the loss of light energy as a pulse of light down a fibre as illustrated in Fig. 2.7. The purity of the fibre can be reflected in both its attenuation properties and its refractive index. The original breakthrough in reducing fibre attenuation was achieved by purifying the glass used to make the fibres. There are other intrinsic and extrinsic factors which contribute to the attenuation, such as absorption by OH- ions, absorption of infra-red

radiation leading to molecular vibrations, leakage from the core and leaky modes. Leakage modes are slightly below the cut-off, but can be propagated for a short distance along the fibre. They can be initially avoided at the light source by restricting the angle at which light enters the fibre.

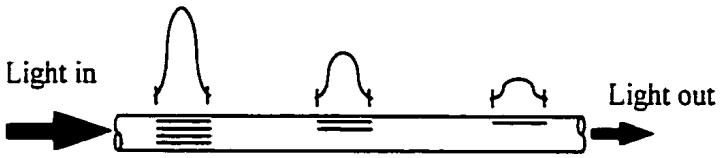

Figure 2.7 Illustration of attenuation

The level of attenuation must be minimised so that the distance the signal can travel along a fibre without amplification can be increased. In 1979, Miya et al. investigated the less loss of an excellent single-mode optical fibre fabricated to operate in a range between 1 and 1.6 μm. He found that the losses at 1.3 and 1.55 μm are below 0.5 and 0.2 dB/km, respectively (see Fig. 2.8).

2.2.3 Fibre-optic Bragg Grating (FBG) Sensor

2.2.3.1 Introduction

In the past few years, one key optical fibre strain sensor has been developed rapidly ahead of the other designs due to its inherent ease of use. The sensor has been dubbed a fibre-optic Bragg grating (FBG) sensor. The FBG sensors have been developed continuously and rapidly since they were first demonstrated for strain and temperature measurements about 11 years ago [Morey et al. 1989]. It possesses several distinguished advantages including (i) invulnerability to electro-magnetic interference, (ii) potential capabilities of surviving in harsh environments [Townsend and Taylor 1996], (iii) much less intrinsic size (typically 125μm in diameter – ideal for being embedded into composites without introducing any significant perturbations to the characteristics of the structure), (iv) great resistance to corrosion when used in open environment, (v) capacity of multiplexing to more than one sensor

along a single optical fibre and (vi) high service temperature (typically ~300°C) and long durable lifetime (>25 years) [Morey et al. 1996]. Kalamkarov (2000) found that the FBG sensor embedded in the carbon fibre reinforced composite plastic (CFRP) rod is unaffected by fatigue load and creep effects.

In recent years, the FBG sensor has been identified as an important component for construction of "fibre-optic Smart structure". It is ready to be embedded into (or attached onto) the structure for achieving a number of technical objectives, such as health monitoring, impact detection, corrosion measurement, composite cure and shape-forming monitoring [Dewynter et al. 1998, Lo and Xiao, 1998, Groves-Kirkby, 1998 and Rao, 1999].

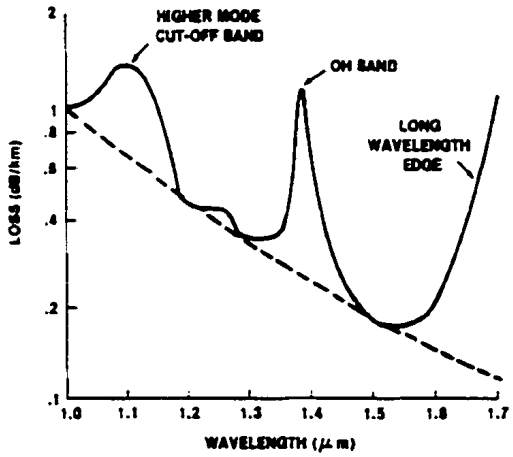

Figure 2.8 Rayleigh Scattering Limit at long wavelengths, and loss vs wavelength of an excellent optical fibre.

2.2.3.2 Basic principle

FBG technology was discovered by Hill et al. in 1978 [Masskant et al. 1997]. It was found that the reflective gratings could be photorefractively formed in the core of the germanium doped silicate fibre. The FBG system is comprised of broadband source (light emission device), coupler, optical spectrum analyser (OSA) and optical fibre with pre-written grating sensor. For the structural strain monitoring, load is directly transferred from the host material at particular position to the fibre-core section by shear. This causes the change of the length of the grating region and the resultant refractive index of the core section accord-

ingly. The mechanical properties of the structure are simply determined by measuring the reflected wavelength change from the system. The FBG system is illustrated in Fig. 2.9.

Grating is written by exposing the fibre to a pair of strong Ultra-violet (UV) interference signal. This creates the grating in the core of the optical fibre, which acts essentially as a wavelength-selective mirror. The method to write the grating in the optical fibre for strain and temperature measurements is called Phase Mask technique. The phase mask technique is less sensitive to environmental disturbances and produce gratings with highly repeatable characteristics [Kashyap et al. 1993]. Limited tuning of the Bragg wavelength has been demonstrated by pre-straining the fibre prior to exposure [Zhang et al. 1994], and by magnifying the phase mask periodicity. The phase mask based interferometer configuration is shown in Fig. 2.10.

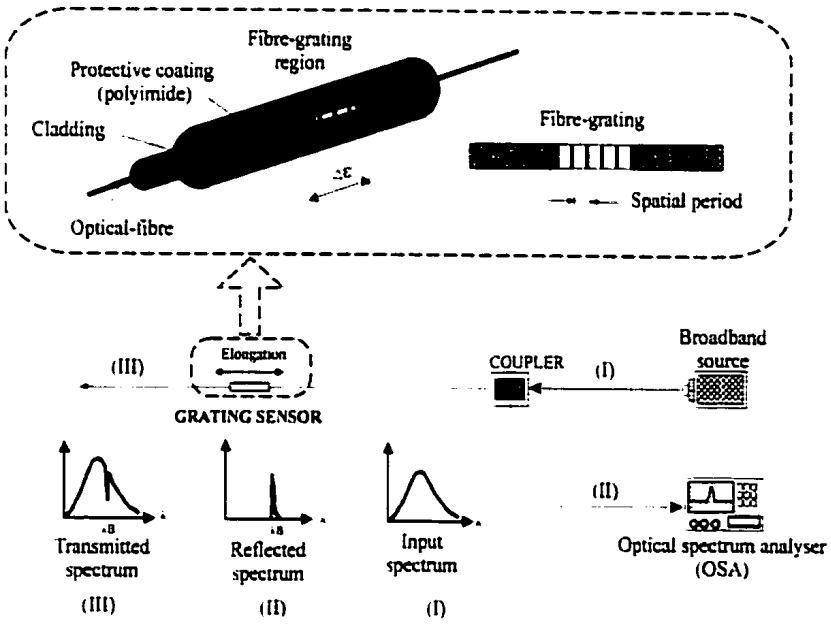

Figure 2.9 The fibre-optic Bragg grating strain measuring system.

When the light is illuminated from the broadband source via the coupler, part of light is reflected back to the coupler and the reflected-wavelength is detected by the OSA as indicated in Fig. 2.9. The strain variation in the grating region is simply determined by the reflective wavelength shift ($\Delta\lambda_B$) from the sensor. The fibre-core is surrounded by the two external materials: (1) cladding and (2) protective coating. Since the actual diameter of the transmit-

ted-core region (only 7μm) is very small, the protective coating is definitely needed to protect the fibre and prevent the power loss in application. The outside diameters of the cladding and protective coating for the commercial strain sensing optical fibre are 125μm and 250μm, respectively.

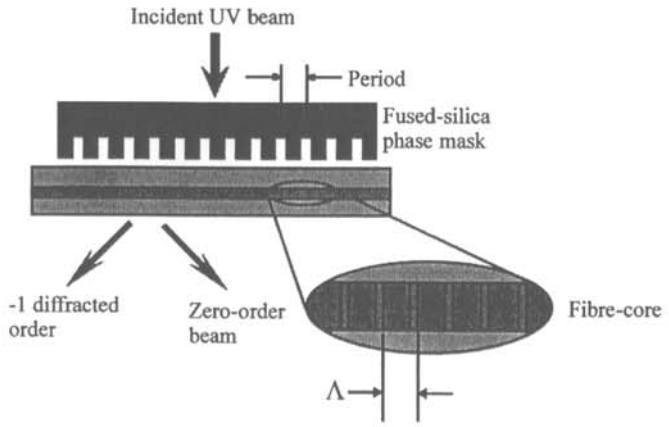

Figure 2.10 Fibre gratings written by Phase mask technique.

According to the Bragg's law, the reflective wavelength can be defined as

$$\lambda_B = 2n_{eff}\Lambda \tag{2.3}$$

where n_{eff} is the core refractive index and Λ is the spatial period of the index modulation. Any changes of the strain in the grating region result in the changing of spatial period and core refractive index. The measurement of the mechanical strain ($\varepsilon = \Delta L/L$) is determined by the variation of the Bragg wavelength (λ_B) shift. It has been approved that the sensors give a linear strain relationship to the reflected wavelength shift from the sensor within the elastic deformation limit of the fibre [Maaskant et al. 1997].

Therefore, the change of the Bragg wavelength can be expressed as:

$$\frac{\Delta\lambda}{\lambda_B} = \left(1 - \frac{n^2}{2}\rho_{12}\right)\varepsilon_1 - \frac{n^2}{2}\left(\rho_{11}\varepsilon_2 + \rho_{12}\varepsilon_3\right) + \xi_o \Delta T \tag{2.4}$$

where ε_1 is the axial strain along the lengthwise direction of the fibre. ε_2 and ε_3 are the principle strains in the cross-section plane of the fibre core. ξ_o is the coefficient of both the thermo-optic component and the thermal expansivity of the optical fibre, and has the nominal value of 6×10^{-6}/°C. ρ_{11} and ρ_{12} are the photoelastic coefficients. In general, the strain transfer to the fibre in transverse directions is very small and can be neglected in practical applications [UDD 1995]. Therefore, the full equation for the FBG sensor by considering the effects from temperature and strain changes can be simplified in a form as

$$\Delta\lambda_B = K_\varepsilon\varepsilon_1 + \lambda_B\xi_o\Delta T \tag{2.5}$$

where K_ε is called "Theoretical gauge constant" [Saouma et al. 1998], which can be determined experimentally. The second term in Eq.(2.5) represents the wavelength shift due to the temperature change in the system, which is normally used in inspecting the manufacturing process of composite materials [Rutherford and Westerman, 1992]. For the silica fibre, the wavelength-strain sensitivity of 1.55 μm FBGs has been measured as 1.15 pm $\mu\varepsilon^{-1}$ [Morey et al. 1989]. By neglecting the thermal effects of the fibre, the measurement of the mechanical strain ($\varepsilon=\Delta L/L$) at the grating region yields (see Fig. 2.11)

$$\varepsilon = K_\varepsilon^{-1}\left(\lambda_f - \lambda_0\right) \tag{2.6}$$

where subscripts *f* and *o* represent final and initial condition of the fibre, respectively.

2.2.3.3 Multiplexing technique

One of the major advantages of using FBG sensor in real life applications is its ability of measuring strains in different locations along structure only by one single optical fibre [UDD, 1995]. This technique is normally called "Multiplexing" or "Quasi-distributed" measurement. Frequency modulated continuous wave (FMCW) technique presents its excellent ability to measure the strain variation along a single optical fibre with more than one grating sensor [Chan et al. 2000]. The FMCW offers a number of advantages compared

with the current multiplexing techniques such as wavelength division (WDM) and optical time-domain reflectometry (OTDR). Typically, the maximum number of sensors that can be multiplexed by using WDM technique is about 10 to 12. Besides, the OTDR technique requires injecting a short pulse of optical power to the optical network and waiting for separating pulse from each sensor. It therefore requires a relatively high power in the pulse system to maintain the same average optical power at the receiving end. By using FMCW technique, it enables to produce up to 20 grating sensors along the single optical fibre if the reflectivities of the grating are correctly chosen. However, the power required is comparatively less than that by using OTDR for the same number of used sensors. Fig.2.12 illustrates the multiplexed FBG sensor arraying system by using FMCW demodulating technique.

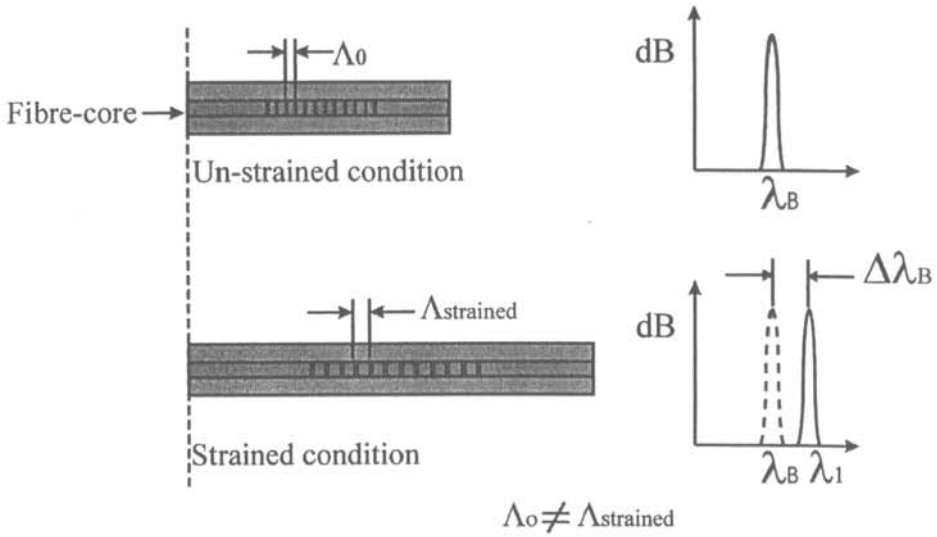

Figure 2.11 Response of the wavelength change due to straining at grating region.

The light signal launched from the broadband source is modulated as a triangular chirped frequency carrier to the FBG sensors. The delayed frequency signal from each individual FBG sensor is returned to the tunable optical filter (TOF) and the photodetector. The detector output is electrically mixed with a reference chirp signal from the voltage-controlled oscillator (VCO), which produces a beat frequency associated with each sensor element. The magnitudes of the beat signals are proportional to the convolution of the individual grating reflection and the transmission spectrums of the tunable filter.

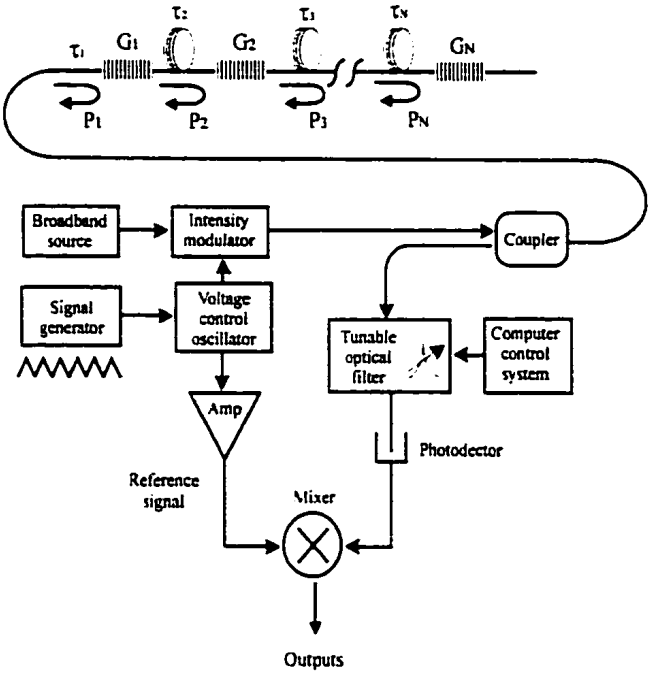

Figure 2.12 Multiplexed FBG sensors system using FMCW demodulating technique.

The beat signals can be viewed by using an electrical spectrum analyser (ESA). The amplitude (voltage) measured by the ESA can be converted to the corresponding strain (ε) of the grating. The principle of operation of the FMCW technique is illustrated in Fig. 2.13

The beat frequency for sensor can be expressed as:

$$f_J = \Delta f \frac{\Delta T_J}{T} \tag{2.7}$$

where f_j, Δf, ΔT_j and T denote the beat frequency, the chirp frequency excursion, the optical delay from the source to detector for the sensor #(j) and the chirp period, respectively.

Two major factors can limit the spatial separation between two neighbouring FBG sensors. The first factor is that the separation should be long enough to avoid the coherence noise occurs. The second one is that the separation between gratings must be large enough to separate the beat signals with their frequency difference between sensors and larger than the resolution of the spectral analysis techniques

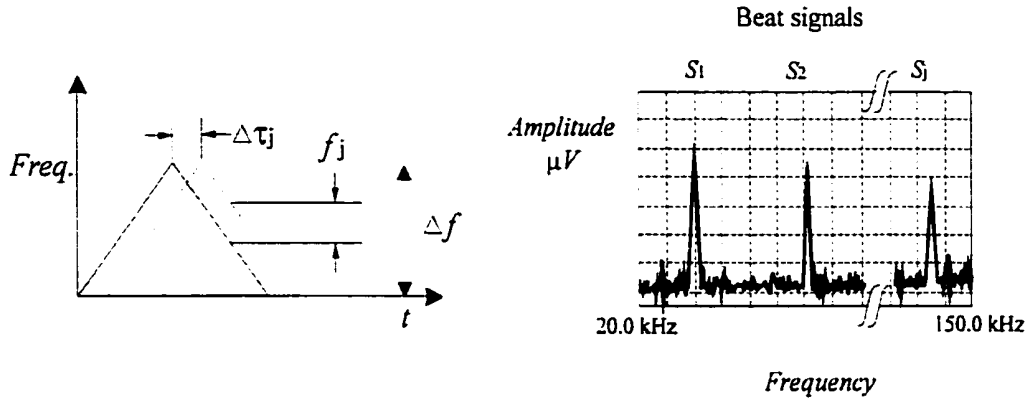

Figure 2.13 Principle of operation of the FMCW technique for a single sensor path (left) and multiplexed intensity sensors array signalling from the spectrum analyser (right).

2.2.3.4 FBG sensors for composite structures

Advanced composite materials (ACM) are now routinely being used for manufacturing engineering structures such as aircraft and automotive structures for more than 30 years. Their advantages over most conventional materials are high fatigue resistance, light in weight and capabilities of forming complex shape without involving enormous amount of cost for mould fabrication [Foote, 1994]. Hence, the use of the composite material with the embedment of the FBG sensor can lead to reductions in weight, inspection intervals and maintenance cost of the structures and consequently improvement in overall performance. Du et al. (1998) used the embedded FBG sensors, which are located between the composite laminates as internal strain measuring devices. He found that the embedded FBG sensors could provide a strain distribution along the structure without influencing the mechanical properties of host material. Dewynter-Marty (1998) embedded the FBG sensors into glass fibre/epoxy laminate to monitor thermal and residual strain properties during curing process in autoclave. The temperature measured gave a good agreement with that measured by autoclave temperature probe. The FBG sensor could sustain compressive strain up to 2200μ strain without failure.

Lo et al. (1998) developed a single-pitch FBG sensor for corrosion detection by coating copper onto the pre-loaded optical fibre. The principle of corrosion sensors is that environment corrosion would change the coating thickness and eventually cause the changes of residual strain inside the fibre grating region. A parameter, which represents the corrosion rate can be measured in according to the reflected wavelength change from the grating. The schematic diagram of the corrosion detected FBG sensor is illustrated in Fig 2.14.

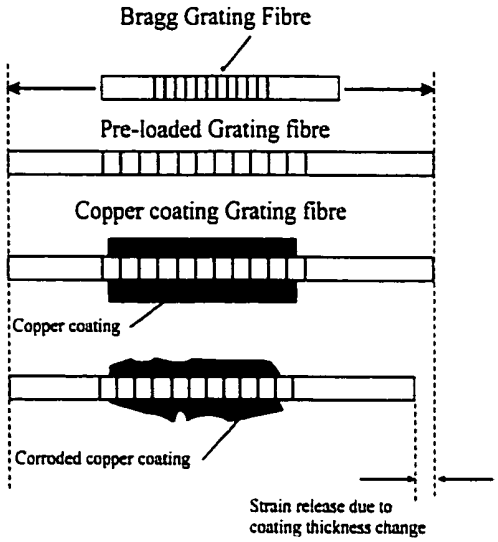

Figure 2.14 Corrosion detection FBG sensor

2.2.3.5 FBG sensors for civil applications

The FBG sensor has been used in civil construction industry only in recent years. The first use of FBG sensors as structural health monitoring device in bridge structure was demonstrated in 1994 [Measures et al. 1994]. Array of FBG sensors was adhered on the surface of carbon fibre composite tendon to measure strain and deformation of the structure. In Fig. 2.15. a schematic diagram of FBG sensor locations for strain monitoring along a bridge is shown. They found that the measuring range of this interrogation system is within 5 mε and 1 με. An accuracy of ~20με was demonstrated. Saouma et al. (1998) has used the embedded FBG sensors to monitor strains of a laboratory sized concrete beam and found that the results gave a good agreement with those measured by externally bonded electric strain gauges.

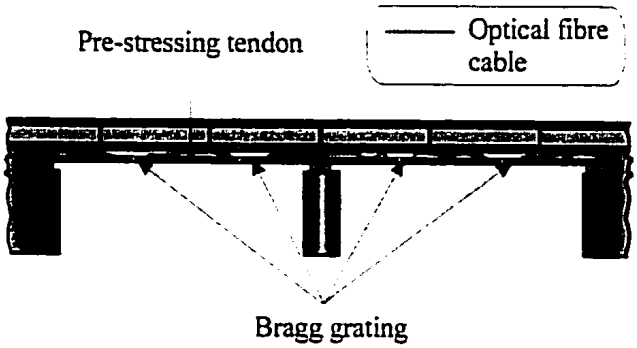

Figure 2.15 A schematic diagram of distributed FBG sensor for bridge strain monitoring.

Navel Research Laboratory in USA [Kersey et al. 1996] performed an experimental study for a bridge, which is in ¼ scale of real structure with the embedment of 60 FBG sensors to measure strain. They found that the FBG sensors could measure the strain in real-time. However, due to the limit of scanning speed of the Fabry-Perot tunable filter used for wavelength-shift measurement, only static strain could be measured. In Canada, multiplexing FBG sensors were embedded during construction along a pre-stressed girders for a bridge, which was made by ACM to monitor strain response in different positions during service [Holton, 1998]. In Fig. 2.16, the installation process of the FBG sensors along the girders is shown.

2.2.4 Problems in Application

Many extensive researches and applications of the FRP materials for concrete rehabilitation and retrofit are reviewed in previous sections. It was clearly shown the tendency of developing a new and effective rehabilitation technique for oldest infrastructure elements by using the FRP materials. However, the acceptance of these materials in civil engineering industry is still very limited due to lack of sufficient design codes, material standards and specifications [Ballinger, 1997].

Moreover, the quality control for the FRP materials used for concrete strengthening is difficult since it is very dependent on several environmental parameters such as humidity and temperature [Luke, 1999]. Long-term durability in harsh environments is also an important

aspect to be concerned for the current strengthening method before further applying to real practise.

Embedded optical fibre sensor has been well agreed as an intrinsic strain and temperature - measuring device to inspect structure condition. However, the installation method and protection device for this tiny sensor require time and effort to be investigated since the optical fibre is easy to break if it is not appropriately handled [Holton, 1998].

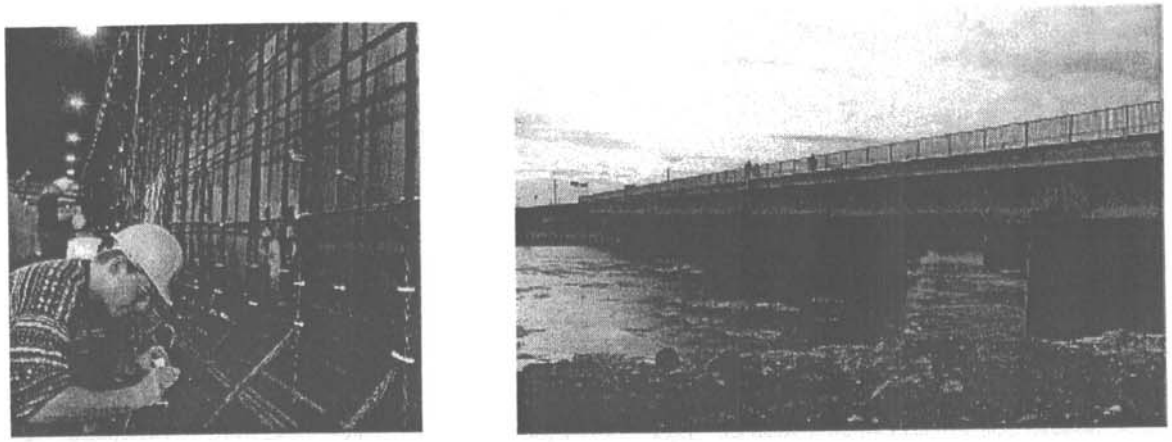

Figure 2.16 The installation of FBG sensors along pre-stressed girders (left). The Taylor bridge is being monitored by the FBG sensors (right).

CHAPTER 3

PRELIMINARY EXPERIMENTAL STUDY

This chapter presents the mechanical performance of concrete and glass fibre composite materials, and optical fibre embedded composite structures through experimental investigations. Several fundamental experiments have been performed to evaluate the quality and determine the mechanical properties of all related materials used in current research.

3.1 Concrete

3.1.1 Sieve Analysis Test (ASTM C 136)

The concrete consists of Portland cement, fine (sand) and coarse aggregates (rock), water and admixtures. The admixtures are not an essential components of the concrete mix. They are defined as chemical substances, which are used to modify the chemical reaction process (called hydration process) between the cement and water. The mechanical properties of the concrete are highly dependent on the ratio of mixture. High water to cement (abbreviated to w/c ratio) ratio results in weakening the strength of the concrete while insufficient w/c ratio may cause the un-satuated chemical reaction inside the core of cement particle. Excess water used in hydration process would cause voids formation inside the concrete after curing. Therefore, the strength and durability of the mix concrete structure are highly influenced by the mixture ratio and purity of all constituents.

In general, the w/c ratio of 0.5 is recommended to use in order to minimise the formation of voids inside the concrete, improve the workability during mixing and achieve the smooth hydration processes [Neville 1997]. The selected mixture ratio of 1:1.5:3 (cement: fine aggregate: coarse aggregate) is used in present study. Sieve analysis test was firstly investi-

gated. This test method is to determine the particle size distribution of fine and coarse aggregates by sieving to ensure constituents quality. The sieve used for present study is shown in Fig. 3.1 and the results are listed in Table 3.1. It is found from the Table 3.1 that the percentages of the particles passing through different size of sieves satisfy the standard requirement.

Figure 3.1 The metal sieves for aggregates sieving.

Table 3.1 Result of the sieve analysis test of fine and coarse aggregates

ASTM Sieve size (mm)	Weight retained (g)	Weight passing (g)	Percentage passing	Standard criteria (percentage)
19.0	77.9	2876.2	97.36	≥80
9.50	1024.6	1851.6	62.68	≥60
4.75	672.7	1178.9	39.91	≥10
2.36	286.5	892.4	30.21	≥15
0.6	436	457.4	15.48	≥5
0.3	156.3	301.1	10.19	≥2
0.15	119.4	181.7	6.15	≥0
remainder	181.7	0	0	
Total	2954.1			
loss in process	3.4			

3.1.2 Uni-axial Compression Test (ASTM C 39)

This test method covers determination of compressive strength of laboratory-sized concrete cylinders. The dimension of test specimens was 100 mm in diameter and 200 mm in height. This test method consists of applying a compressive axial load to the moulded concrete cylinder until its ultimate compressive strength is reached. The concrete was mixed by the ratio of 1:1.5:3 as mentioned in the previous section. Three concrete specimens (manufactured at the same constituent and day) were used for each individual test. Standard cylindrical steel moulds were used to hold pre-cured concrete (fluidity state concrete) in place for 24 hours. The concrete was then de-moulded and put into water tank (100% humidity) with temperature of 25°C for extra 28 days (See Fig.3.2) for completion of the full chemical reaction (called "hydration") between the cement and water inside the concrete. Vibration table was used to consolidate the mixture in order to minimise the voids formation inside the specimen. No admixture was used in the study.

During curing, a hydration of cement generates heat, which causes a rise in the temperature of the concrete. This internal temperature change may cause damage of the concrete after curing due to existence of residual stress, which develops crack on the concrete surface if a high differential temperature (ΔT_δ) between the cool exterior and the hot core of the concrete element occurs [Fitzgibbon 1976]. The temperature inside the concrete and ambient condition was measured by using embedded thermocouples, which were located inside and on the surface of the concrete specimen during curing process. The parameter, ΔT_δ may influence the selection of appropriated strengthening and internal strain sensing tools for further investigations. The schematic diagram and results of temperature measurement are shown in Fig. 3.3. The plot clearly shows that the value of ΔT_δ appears only in the first 28 hours and the difference is within 4°C. It is only true for the type of specimens used in present study. However, for a large concrete structure diffuses more heat during chemical reaction process.

Both compression surfaces of all the cured concrete cylinders were polished within a tolerance of 0.2 mm to ensure both the surfaces were parallel to each other. It was to avoid any

eccentric or concentration loads occurred onto the specimens. Each polished surface was inspected by using Mirco-dial Gauge. The surface polishing machine with special holding fixture was designed and shown in Fig.3.4.

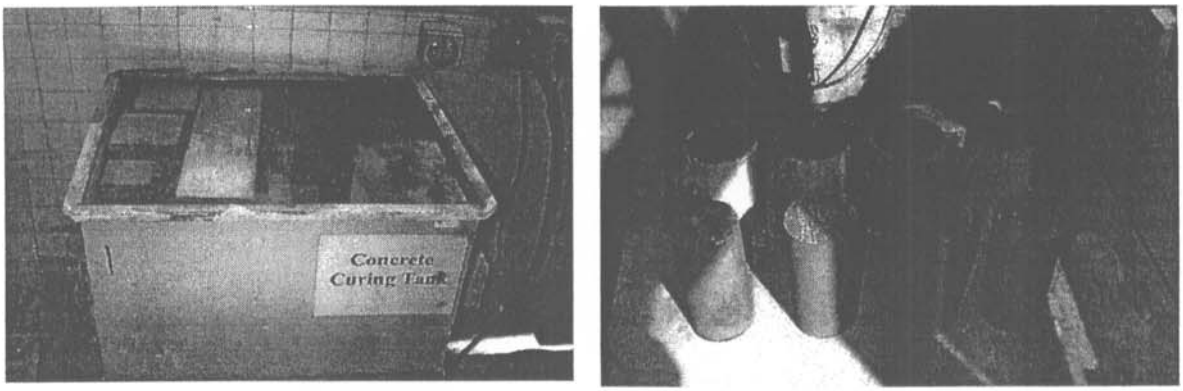

Figure 3.2 A water tank for concrete curing (left). Cylindrical concrete specimens and steel moulds (right).

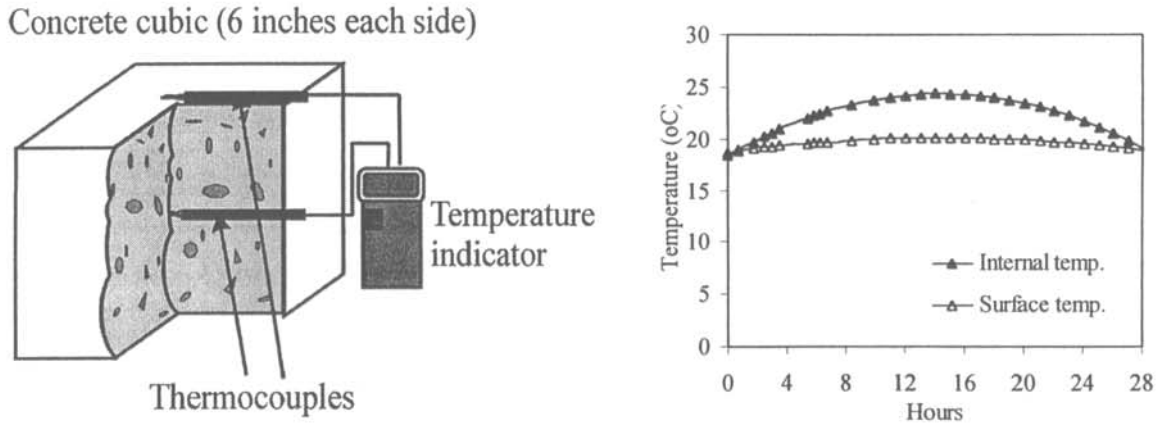

Figure 3.3 A schematic diagram (left) and results (right) of the temperature measurement during curing process.

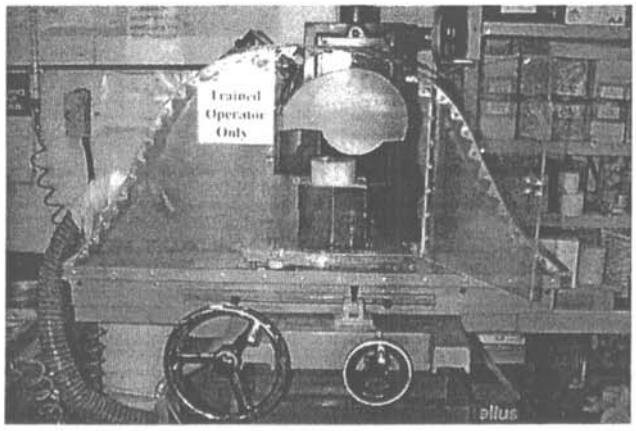

Figure 3.4 Surface polishing machine.

The CONTROLS 50-C4330 compression testing machine was used in the compression tests for the concrete cylinders. A loading rate of 200 kPa/min was set and the peak load was recorded automatically through the connection to the computer. Steel platens were used to transfer the compression load from the testing machine to the concrete surfaces. Protective shield was located in front of the testing zone to avoid violent bursting action of the concrete under high-pressure condition. Externally-bonded strain gauges were adhered on the surface of the concrete specimens in both the column longitudinal and lateral (hoop) directions to measure strains. Ultimate stress and Possion's ratio of the concrete are determined by using the following equations

$$\sigma_{ult} = \frac{P_{peak}}{A} \tag{3.1}$$

$$\nu = -\frac{\varepsilon_{lateral}}{\varepsilon_{Longitudinal}} \tag{3.2}$$

where σ_{ult}, P_{peak}, A, ν, $\varepsilon_{lateral}$ and $\varepsilon_{longitudinal}$ represent the ultimate compressive stress of the concrete, peak load measured during the test, cross section area of the original test specimen, Poisson's ratio, strains in both the lateral and longitudinal directions, respectively. The arrangement of the electric strain gauges of the test specimen is illustrated in Fig. 3.5. The experimental set-up is shown in Fig.3.6.

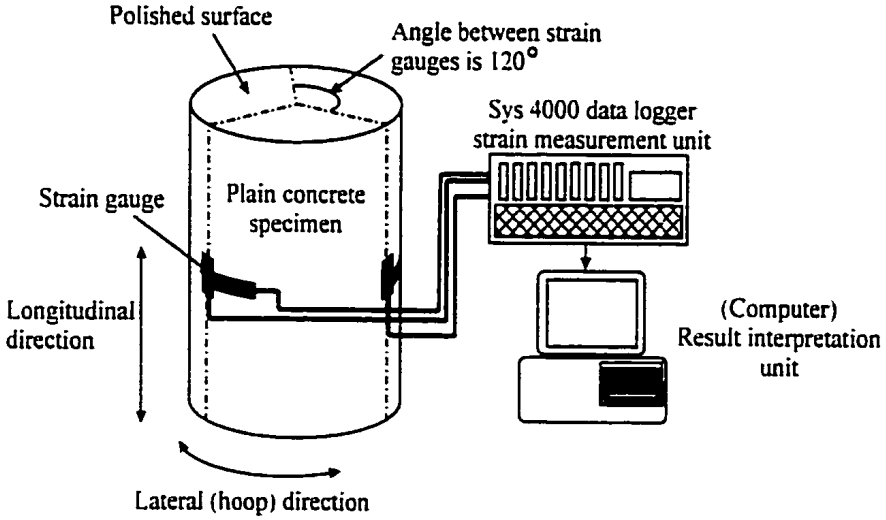

Figure 3.5 The testing specimen set-up for strain measurement by using strain gauges

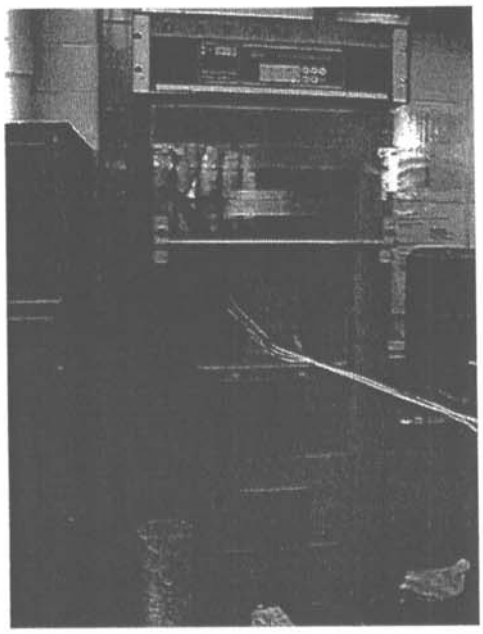

Figure 3.6 The CONTROLS 50-C4330 Compression testing machine.

All the experimental results are shown in Table 3.2 and plotted in Fig. 3.7.

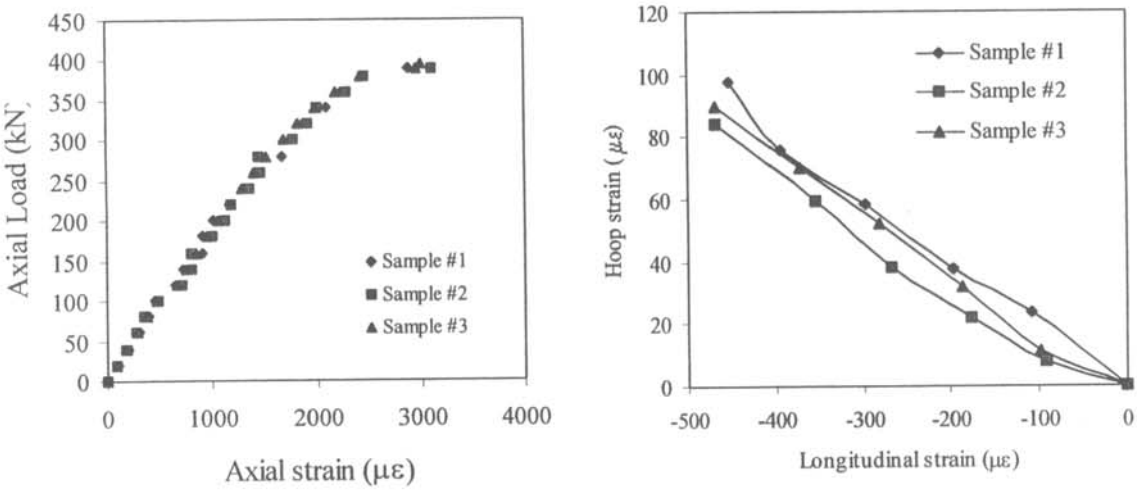

Figure 3.7 Experimental results of the compression load versus average longitudinal strain (left) and the longitudinal strain versus hoop strain (right).

Table 3.2 Experimental results for the plain concrete column subjected to uni-axial compression test.

					Peak load condition		
	P_{peak}	D	A	σ_{ult}	$\varepsilon_{longitudinal}$	$\varepsilon_{lateral}$	ν
Sample	(kN)	(m)	(m^2)	(MPa)	(με)	(με)	
1	390	0.1	0.007854	49.66	-2890	1301	0.2028
2	390	0.0996	0.00779	50.02	-2961	1013	0.1871
3	395	0.1	0.007854	50.29	-3109	1300	0.17
			Mean	49.99	-2986	1204	0.1866
			Standard derivation	0.316	-111.7	165.9	0.0164

According to the experimental results, the modulus of elasticity (E_c), compressive strength (σ_{ult}) and Poisson's ratio (ν_c) of the plain concrete column are determined as 27.8 GPa, 49.99 MPa and 0.187, respectively. The result is quite satisfactory to the American Concrete institute (ACI) code 363R-92 [ACI 1994] for concrete with strengths up to 83 MPa

$$E_c = 3.32 (f_c')^{0.5} + 6.9 \tag{3.3}$$

where f_c' expresses the concrete compressive strength. Several visible cracks appeared at the peak load condition. The splitting-off failure of the specimens at mid-column region also occurred when further applying the compression load to failure. Figure 3.8 clearly shows the failure modes of the plain concrete column after the compression test. Nearly all materials at the middle of the column are fallen off by Possion's expansion.

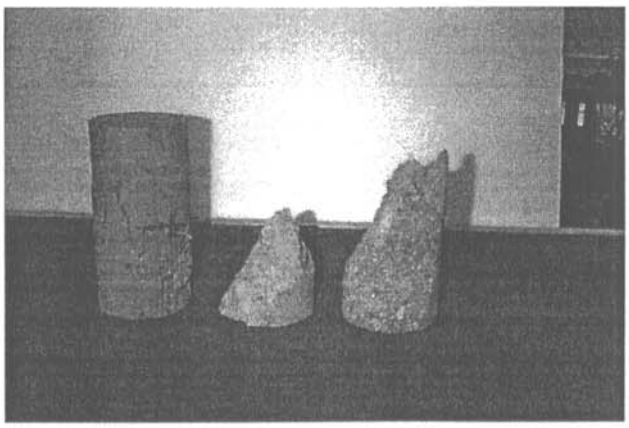

Figure 3.8 Test specimens at the peak (left) and failure (right) loads.

3.1.3 Flexural Strength Test (ASTM C 293)

The flexural strength tests were conducted to examine the flexural behaviour of fresh rectangular concrete beam subjected to three-point bending test. The manufacturing procedures and mixture ratio of the concrete beams was similar to that with the cylindrical concrete cylinders. The dimension of the beam was made according to the ASTM standard C 293 as 6 inches in square and 20 inches in length. Three removable steel moulds were designed and fabricated for frequently moulding process to make the testing beams in later study. Figs. 3.9 and 3.10 illustrate the steel mould used and experimental set-up, respectively for the present study. The theoretical maximum tensile stress reached in the bottom surface of the test beam is known as the modulus of rupture R, which is estimated by

$$R = \frac{3PL}{2bd^2} \tag{3.4}$$

where P, L, b and d denote the maximum applied load indicted by the testing machine, span length, the average width of the specimen and average depth of the specimen, respectively.

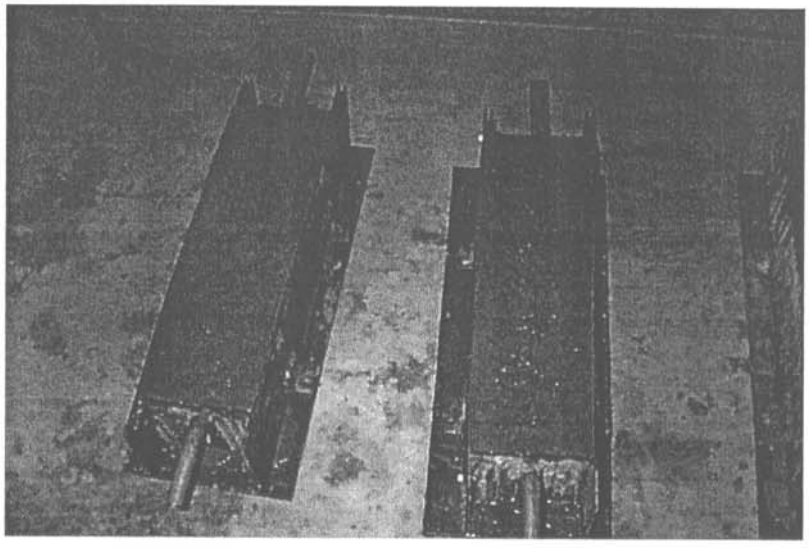

Figure 3.9 Steel moulds for concrete beam fabrication.

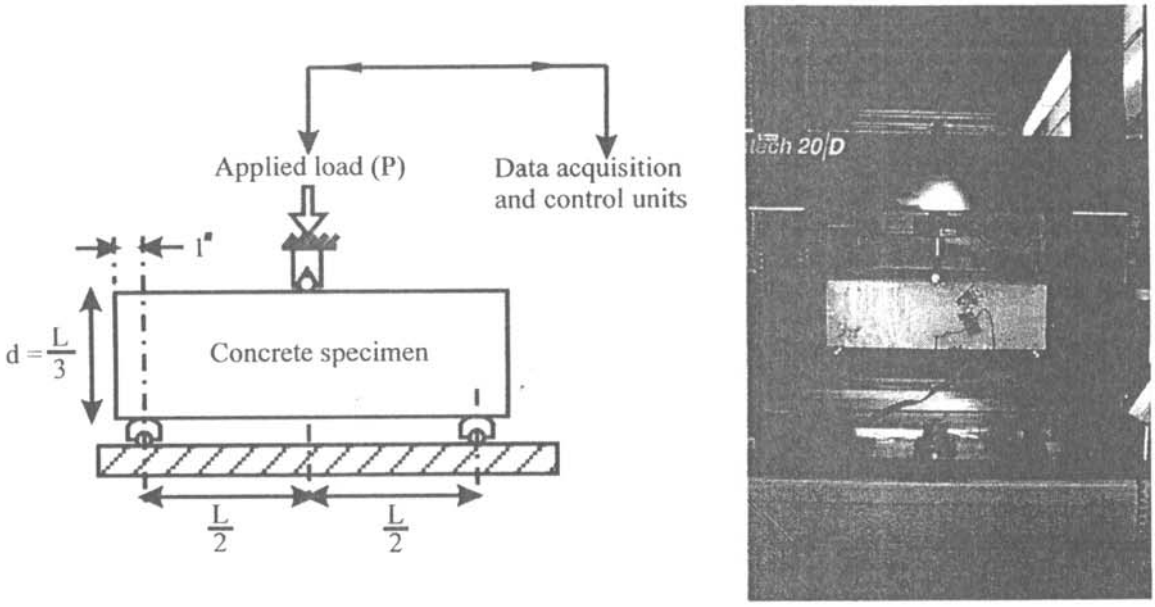

Figure 3.10 A schematic illustration (left) and photographic diagram (right) of the experiment set-up for three-point bending test.

In fact, the modulus of rupture of a small testing specimen does not, in general, coincide with the true tensile strength of the large-scale structure. In average, the rupture modulus is about 25% higher than the true tensile strength of the concrete. Sintech 20/D tensile testing machine was used for three-point bending tests. The loading rate was set at 0.5 mm/min. Strain on the tension (bottom) surface and mid-beam deflection were recorded simultaneously once the load was applied through the computer. According to the results showed in the experiment, it was found that cracks were appeared on the tension surface of the beam and fast propagated toward the direction opposite to the load applied when further applying the load. Failure occurred catastrophically. The experimental results are plotted in Fig. 3.11. It was found that the ultimate flexural load of the tested beams is about 21 kN. However, the deflections measured at peak-load condition are quite different. It may be due to the non-homogeneous properties of the concrete specimens mixed during moulding process and uneven aggregate distribution on the tension surface of the beam. Those factors may influence the interfacial bonding properties between the cement and aggregate of the structure. The variation is within 8%. The moduli of rupture are determined and listed in table 3.3.

The mean and standard derivation of the modulus of rupture (σ_{ru}) of the concrete are 4 Mpa and 0.142, respectively. It is about 8% of its compressive strength. The principle of Eq.

(3.3) is based on the elastic beam theory, in which the stress-strain relation is assumed to be linear and the tensile stress on the bottom therefore should be linear proportional to the distance measured from its neutral axis. In fact, it is not true since the strain gives parabolic relation with the stress when it reaches to one-half of the tensile strength [Raphael 1984]. The tensile strength (f_t) of the concrete is about ¾ of the theoretical modulus of rupture [Neville 1997]. Carpinteri et al. (1997) pointed out that the determination of the tensile strength by using three point bending test may not be appropriated for the small laboratory-sized concrete specimen because of the existence of its non-homogeneous properties and fracture zone in front of the crack. However, the increase of the specimen size may tend to give the true tensile strength of the beam. This effect is generally called size effect of concrete.

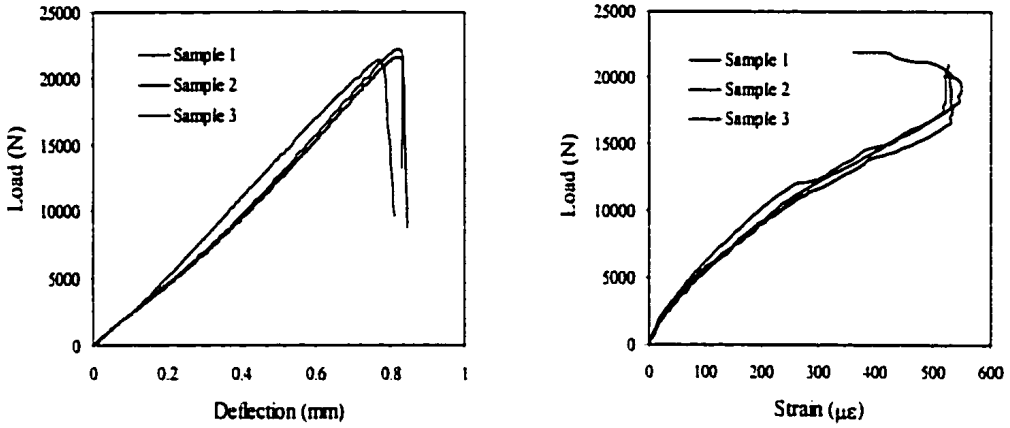

Figure 3.11 Relationships of load-deflection at mid-beam (left) and load-strain on the tension surface (right) recorded during experiment.

Table 3.3 Modulus of rupture for test specimens

	Beam 1	Beam 2	Beam 3
Span, L (m)	0.4572	0.4572	0.4572
Height, d (m)	0.1532	0.1528	0.1542
Width, b (m)	0.1523	0.1536	0.1599
Area, (m^2)	0.0233	0.0235	0.0247
Weight, N	269.8	274.7	269.78
Failure load, (kN)	21.28	21.4	22.03
Deflection at peak load, (mm)	0.832	0.83	0.7812
Max. strain, με	548	533	522
Modulus of rupture (MPa)	4.08	4.07	3.83

3.2 Glass Fibre Composite

3.2.1 Uni-axial Tensile and Compression Test (ASTM D 3039 and D 3410)

In present study, E-glass fibre mat (balanced type) mixed with epoxy base resin forms the composite to confine and strengthen concrete structures. The Araldite MY 750 resin and hardener HY 956 with the mixture ratio of 1:0.25 (resin: hardener) were used. All resin and hardener were mixed under room temperature condition and stirred thoroughly until the mixture formed homogeneously. All mixed resins were placed inside the vacuum pot with the applied vacuum pressure of 740 mmHg for several minutes to remove air, which is trapped inside the resin during stirring process. Hand-lay up method was used to form composite plate. Since the epoxy is highly susceptible to moisture in liquid state, all composite specimens were cured under the temperature (20°C) and humidity (55%) control conditions for 24 hours. A uniform pressure of 4 kPa was applied on the top of the laid-up composite specimens. The cured composite specimens were then placed inside the oven for post-curing for another 8 hours at the temperature of 80°C. A schematic diagram of the test specimen fabrication process is shown in Fig. 3.12.

All cured composite laminates were cut into appropriated dimension and shape, and then undergone the uniaxial tension and compression tests according to the ASTM D 3039 and D 3410 standards. Total five specimens for each individual test were used. During the tests, the ultimate tensile (σ_{tu}) and compressive (σ_{cu}) strengths, modulus of elasticity (E_g) and Poisson's ratio (ν_g) of the E-glass composite for present study were determined.

Fibre volume fraction (v_f) of the test specimens was determined by using resin burn-off method. The resin of composite is evaporated under the temperature of 600°C inside the oven. The remained materials (E-glass mat) are then weighed after the test to determine the amount of resin in the original composite specimen. The value of v_f of the composite specimens is determined by

$$v_f = \frac{w_i - w_f}{w_i} \cdot 100 \tag{3.5}$$

where w_i and w_f denote the weights of the specimens before and after burn-off procedure, respectively. The uniaxial tensile and compressive tests were performed according to the ASTM D 3039 and D 3410 Standards. All testing results are listed in Table 3.4 and plotted in Fig. 3.13.

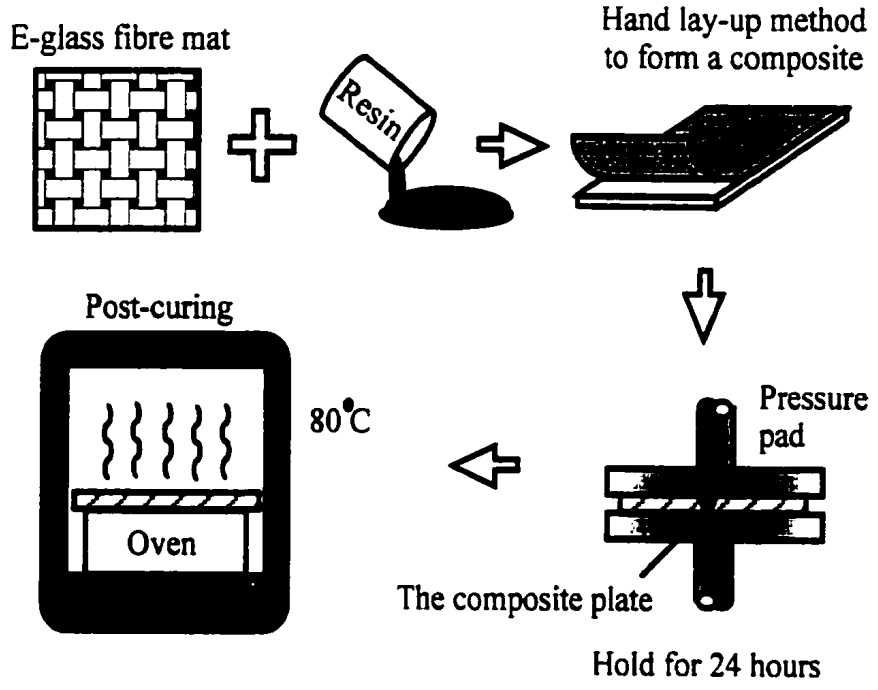

Figure 3.12 E-glass fibre composite fabrication process.

Table 3.4a Experimental results for the glass fibre composite subjected to uniaxial tensile test.

Uniaxial tensile test for E-glass fibre composite				
Sample	Dimension (mm)	v_f (100%)	σ_{tu} (MPa)	E_g (GPa)
1	25.1 x 250 x 2.49	25.7	185	11.9
2	24.9 x 251 x 2.50	25.6	183	12.3
3	25.1 x 250 x 2.49	24.9	178	12.4
4	25.2 x 251 x 2.50	26.0	190	12.9
5	25.1 x 249 x 2.48	25.8	181.5	12.3
Mean value		25.6	183.5	12.39
Standard derivation		0.418	4.44	0.358

Table 3.4b Experimental results for the glass fibre composite subjected to uniaxial compression test.

Uniaxial compression test for E-glass fibre composite				
Sample	Dimension (mm)	v_f (100%)	σ_{cu} (MPa)	Failure
1	25.1 x 155 x 1.47	27.2	62	CB
2	24.9 x 155 x 1.50	26.7	63	CF
3	25.1 x 155 x 1.48	27.0	64	CF
4	25.2 x 155 x 1.51	26.5	65	CB
5	25.1 x 155 x 1.51	26.3	68	CB
	Mean value	27.8	64.4	
	Standard derivation	0.364	2.302	

CB: Composite buckling
CF: Composite failure

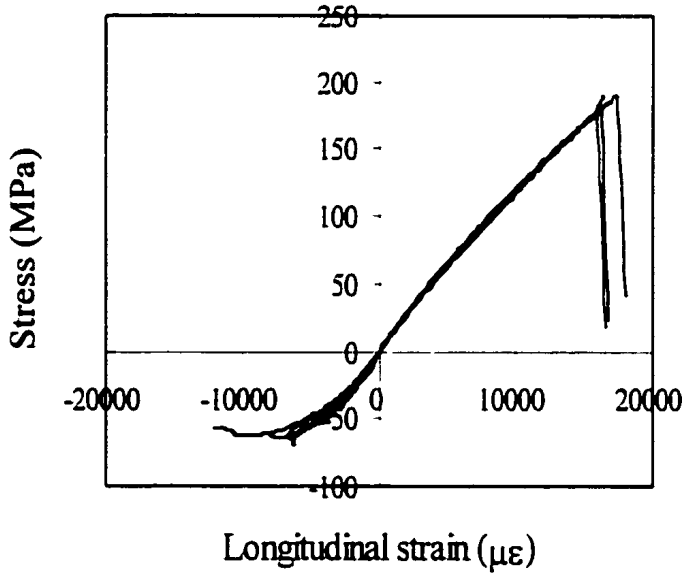

Figure 3.13 A plot of the experimental results of glass fibre composite subjected to axial tensile and compressive tests.

The failure modes of the testing specimens after tensile testing are shown in Fig. 3.14. It must be addressed herein that the ultimate tensile strength of the composite plate increases with increasing the number of laminate layer(s). Fig. 3.15 shows the tensile strength of glass fibre composite plates with different number of laminate layers. It happens due to the excess of resin submerged inside the fibre-matrix system for thin composite laminates.

The volume fraction of resin inside the composite becomes constant when certain number of laminate layers reaches. i.e. the fibre volume fraction of thin composite plate is generally smaller than that of the thick one. A plot of different laminate layers of composite plate subjected to uniaxial tensile stress is shown in Fig.3.16.

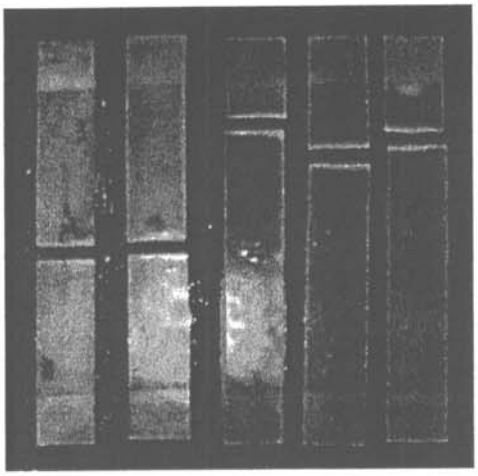

Figure 3.14 Glass fibre composite specimens after tensile test.

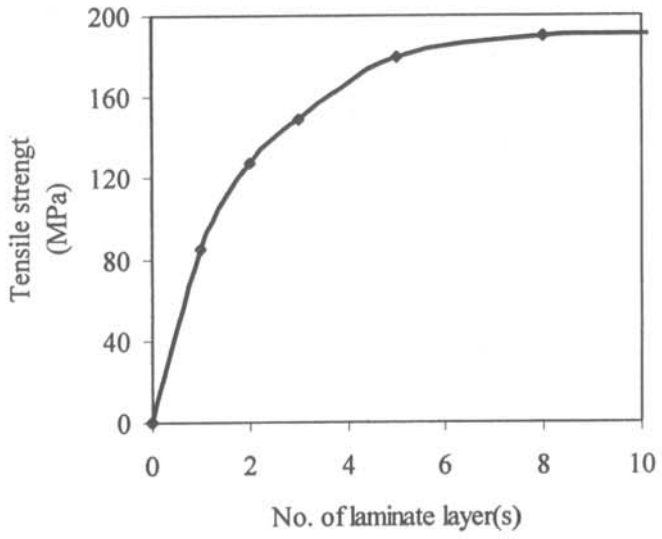

Figure 3.15 A plot of different layers of glass fibre composite subjected to tensile load.

3.2.2 Lap Joint Shear Test (ASTM D 3165)

Glass fibre composites were bonded on the surface of either the composite laminate or concrete structure. Lap-joint shear test was performed for the adhesion joint of the glass fibre composite specimen according to the ASTM D 3165 standard to evaluate interfacial bonding properties. Fabrication procedure of test specimens was similar to that for the composite specimen for the tension and compression tests, which were mentioned in the previous section. The dimension of the testing specimen was followed to the standard requirement. Both bonding surfaces were held after adhering by spring clamp in order to make the sample with a thin adhesive layer. The testing sample for the lap-joint shear test is illustrated in Fig. 3.16. Total five specimens have been used for each type of test. Continuous axial load was applied to the specimen longitudinal direction at a rate of 1 mm/min. The extension at both ends of the specimen and the applied load were recorded automatically during the test.

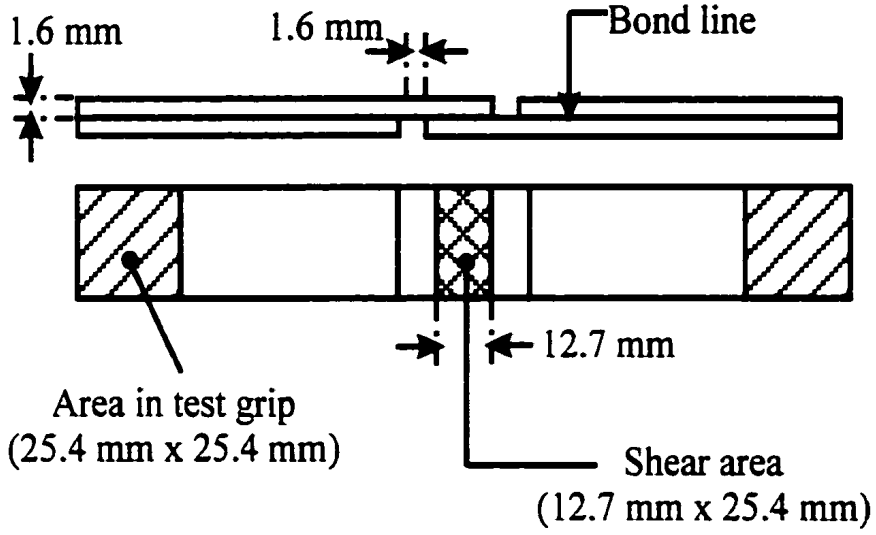

Figure 3.16 Lap-joint shear test specimen

The values of the mean and standard derivation of the adhesive shear stress measured from the experiment were 11.2MPa and 0.486MPa, respectively. All testing samples were failed by shear. The test results are plotted in Fig. 3.17.

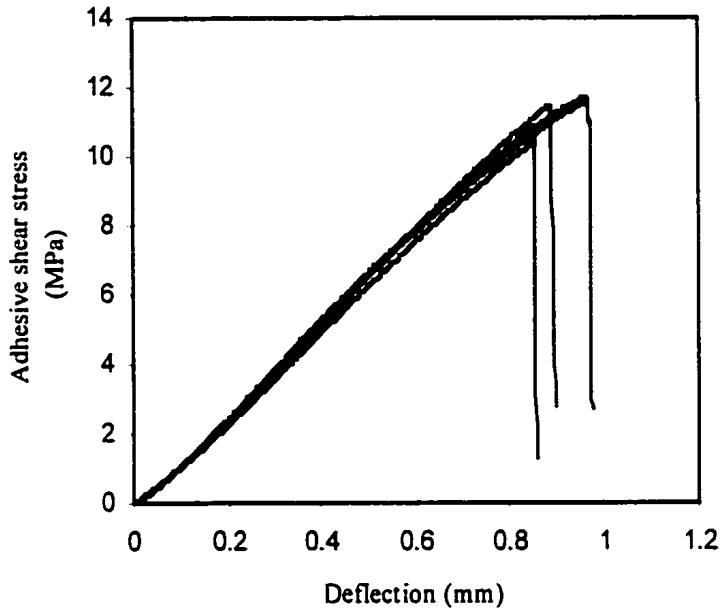

Figure 3.17 Adhesive shear stresses measured from the lap-joint shear test.

3.3 Concrete/glass Fibre Composite Interface

The interfacial properties at bond joint of the glass fibre composite and concrete surface is very important in present study because of their great influences on the stress transferring properties from the concrete structure to the external reinforcement in order to reach the strengthening purpose. Bizindavyi and Neale (1999) proposed analytical methods to evaluate the maximum adhesive shear and externally bonded plate normal stresses by using linear simple shear lag theory. The adhesive shear stress distribution and laminate tensile stress along the bonding length are estimated by

$$\tau(x) = \tau_m \frac{\lambda L_j}{\tanh(\lambda L_j)} \cosh(\lambda x) - \lambda L_j \tau_m \sinh(\lambda x) \tag{3.5}$$

$$f_p(x) = \frac{\tau_m L_j}{t_p \sinh(\lambda L_j)} \left[\sinh \lambda (x - L_j)\right] \tag{3.6}$$

Experimental investigation using lap-joint shear test for both the composite and concrete has also been performed. They found that the maximum shear stress only appears at the plate end regions and rapidly vanishes by increasing the distance from the plate end. The failure mode of the bonded structure mainly catalogues as concrete shearing beneath glue line where the thickness of the glass fibre composite was 1 mm and bonded length of 155 mm was used. The result implies that the failure of the composite/concrete bonded system is dominated by the strength of concrete rather than the adhesion properties or tensile strength of the external bonded reinforcement.

In present study, an experimental study has been performed to investigate the bonding properties of the composite/concrete bonded system by using single lap joint shear test. Glass fibre composite strips have been fabricated with a dimension of 25.4 mm x 2.2 mm x 100 mm. The composite strips were then bonded on the surface of concrete cubic with edges length of 100 mm using epoxy adhesive. Pressure was applied on the bonding surface to ensure that the adhesive was distributed evenly along the glue line. Total ten samples with different bonding lengths (L=25.4 mm and 76.2 mm) were used for the tests. The schematic diagram of the experiment set-up is shown in Fig. 3.18 and the experimental results are listed in Table.3.5.

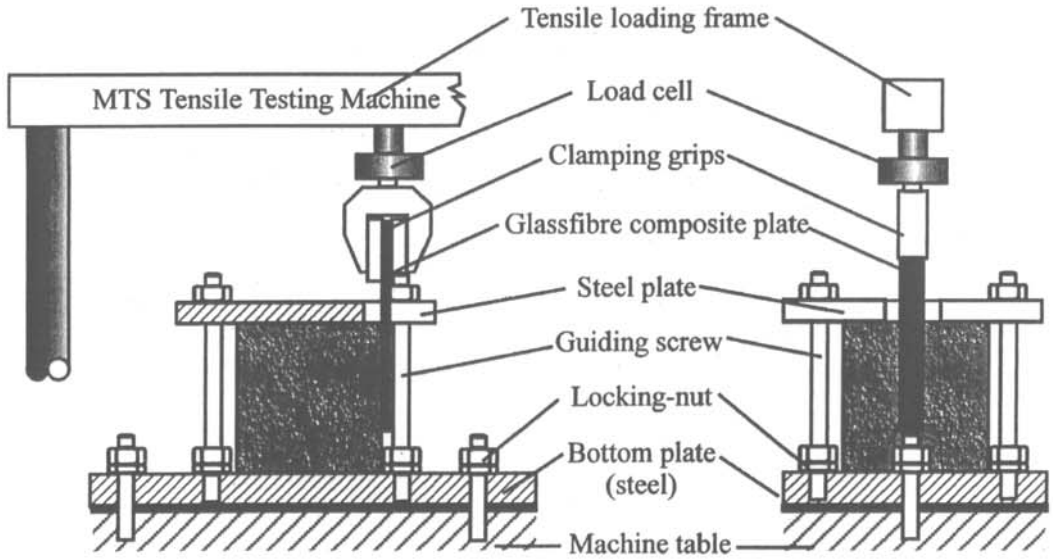

Figure 3.18 Experiment set-up for single lap-joint shear test for composite/concrete bonded specimen.

Table 3.5 Experimental results and modes of failure of the glass fibre composite / concrete bonded system.

Sample No.	Number of layers	Thickness (mm)	Bonded length (mm)	Failure load (kN)	Failure Mode
1	6	2.23	25.4	1.62	CC
2	6	2.21	25.4	1.51	CC
3	6	2.15	25.4	1.55	CC
4	6	2.27	25.4	1.59	CC
5	6	2.22	25.4	1.60	CC
6	6	2.22	76.2	1.92	CC/CS
7	6	2.23	76.2	1.88	CC
8	6	2.19	76.2	2.03	CC
9	6	2.26	76.2	2.12	CC/CS
10	6	2.20	76.2	2.23	CC/CS

CC: Cracks and rupture were found beneath the bonding region.
CS: Several cracks appeared beside the bonding region.

According to the results showed in the Table, it is concluded that epoxy resin provides strong bonding properties to the concrete. During the bonding process, it was found that part of the adhesive has been absorbed by the concrete surface. Therefore, the surface may has higher tensile and shear strengths than the original concrete material. The failure mode of the test specimen with the bonding length of 25.4 mm is shown in Fig. 3.19.

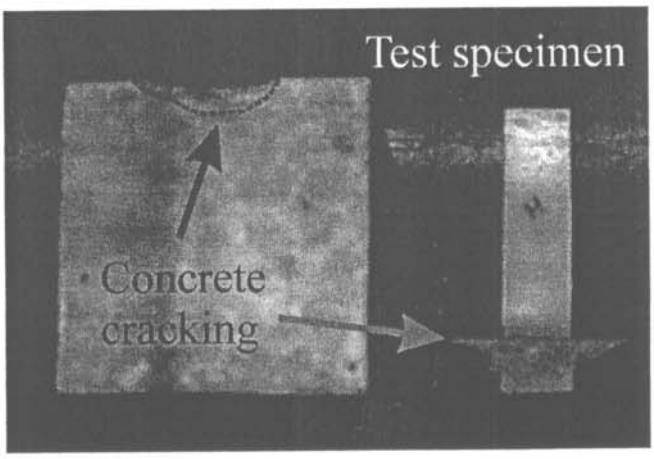

Figure 3.19. Failure mode of the single lap-joint shear test specimen.

The concrete cracking beneath the bonding region is a typical failure mode of the composite/concrete system. Since concrete possesses a very low tensile strength compared to the epoxy and glass fibre composite, cracks in the concrete may be easily formed when pushing force is applied on the composite strip, which is bonded directly on the concrete surface unless sufficient bonded length is used. This bonded length must ensure that the maximum shear and tensile stresses in adhesive and concrete materials, respectively must not excess its ultimate allowable stress limit. Therefore, the failure of the whole strengthening system becomes dominating by the allowable tensile stress of the composite strip.

3.4 Optical-fibre Embedded Composite Structures

3.4.1 Introduction

Optical fibre strain sensors are used to measure strain for the composite strengthened concrete structure in current research. The sensors are embedded into the concrete and composite to measure internal strain when they are loaded statically. The dimension of the optical fibre ($d \approx 250\mu m$) is relatively small compared to the concrete structure. Therefore, it is assumed that no significant influence of the mechanical strength to the sensor-embedded structure. However, for the composite structure, particularly for very thin composite laminate, the influence to its mechanical strength after embedding the optical fibre becomes significance. To apply the strain sensing technology by using optical fibre sensor, an understanding on the effects of this sensor to the composite laminating structure is essential. Two common experimental studies in investigating the internal strength of the optical fibre embedded composite structure have been conducted, which include: (1) short beam shear and (2) flexural strength tests.

3.4.2 Short Beam Shear Test (ASTM D 2334)

Short beam shear (SBS) test is designed to measure interlaminar shear strength parallel to the fibre direction. The strength may be affected by the weakness of the matrix and fibre-matrix bond, which is due to the inappropriate fibre coating system (result of weakening the

matrix bonding characterisation), intrinsic impurity and residual stress induced inside the structure during manufacturing process. This method is relatively simple, fast and economical, and so that it is a most common test for examining the matrix performance in composite structures, in particular the interlaminar shear properties. However, translaminar and interlaminar fractures, which are due to the load nose stress concentration can also be examined by performing this test. Although this test can not be used to exactly determine the shear properties of the fibre-matrix system, it can provide a very useful comparative information to the different composite structures.

Fig. 3.20 shows the dimension of the testing specimen and the experiment set-up of the short beam shear test. The method consists of applying 3-point bending load to a small piece of composite specimen with the dimension of 12 mm x 10 mm x 2 mm. It requires approximately six layers of composite laminate to achieve the thickness of 2 mm ($v_f \approx$ 22%). The optical fibres (a fibre that is used to make the FBG sensor) were embedded inside the glass fibre composite at the interface between different laminate layers in both the longitudinal and lateral directions. The dimension of the specimen is set to control the failure of the test pieces initiating only in shear before any flexural breakage of the fibre at the bottom surface occurs. The interlaminar shear strength, τ_{12} is determined by the following equation

$$\tau_{12} = \frac{3P}{4bd} \tag{3.7}$$

where P, b and d denote the applied load, depth and width of the specimen, respectively.

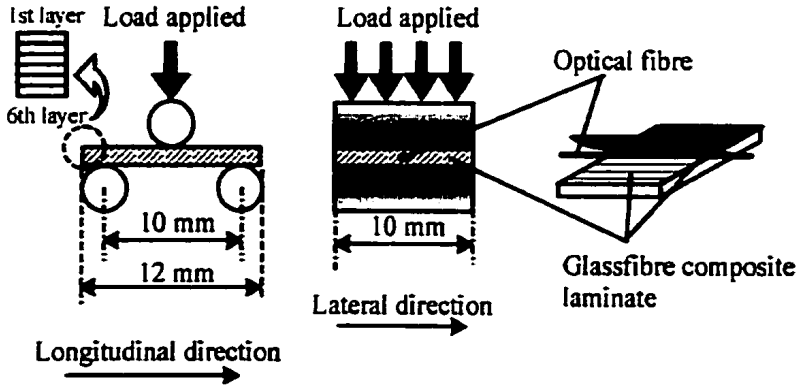

Figure 3.20 The short beam shear test for optical-fibre embedded composite structure.

3.4.3 Flexural Strength Test (ASTM D 790)

The test is designed to measure the laminate flexural strength under 3-point bending load. The recommended span to depth ratio of 40:1 is chosen to ensure true flexural failure and to minimise the effects of shear stress and transverse crushing by the loading anvils [Rubin 1991]. The experiment set-up is similar to that for the short beam shear test. The dimension of the testing specimen was 120mm x 10mm x 2mm. The distance between two roller supports was 100mm. The optical fibres were also embedded into the specimen in either the longitudinal or lateral directions at different interlaminate layers during lay-up process. The flexural strength, σ_f of the specimen after testing is estimated by

$$\sigma_f = \frac{3PL}{2bd^2} \tag{3.8}$$

where L is the span of the test specimen.

3.4.4 Results Interpretation

A total of 160 test specimens have been used and ten specimens were required for each individual test to ensure reliability of the testing results. Table 3.6 lists all experimental results for both the short beam shear and flexural strength tests for the optical fibre embedded composite structures. According to the testing results, it is obviously shown that there are no significant effects to the composite structure when the optical fibre is embedded longitudinally in terms of its short beam shear and flexural strengths. Reduction of flexural strength to 12% is resulted when the optical fibre is embedded laterally at the interface between the 1st and 2nd layers of glass fibre composite laminate. Only slight reduction in the short beam shear strength for the composite with the embedment of optical fibre in lateral direction.

Table 3.6 Experimental results of the short beam shear and flexural strength tests for the optical fibre embedded glass fibre composite specimens.

Optical fibre in	Short beam shear test (MPa)				Flexural strength test (MPa)			
	Lateral		Longitudinal		Lateral		Longitudinal	
	Mean	S.D.	Mean	S.D.	Mean	S.D.	Mean	S.D.
Sensor located at								
1^{st} and 2^{nd} layer	17.75	0.54	18.72	0.27	159.1	4.54	203.8	2.18
3^{rd} and 4^{th} layer	17.94	0.26	18.66	0.36	188.6	3.56	200.3	3.94
5^{th} and 6^{th} layer	18.91	0.43	18.52	0.12	190.9	3.79	198.7	2.96
No sensor specimen	18.82	0.15	18.82	0.14	202.1	2.13	202.1	2.36

CHAPTER 4

CONCRETE CONFINED BY COMPOSITE WRAP

4.1 Introduction

This chapter presents the mechanical behaviour of concrete cylinder wrapped by glass fibre composite laminates. Laboratory-sized concrete cylinders with a diameter, d of 100 mm and height, h of 200 mm were used in the present study. All fabrication procedures were similar to the plain concrete cylinder as described in Chapter 3.2. Two types of specimens were used in the study, which include plain and notched concrete cylinders. Balanced type (0°/90°) glass fibre composite laminates were laid-up directly on the circumference of the concrete surface to activate the constraint action when the concrete is subjected to compression load. Sand blasting and vacuuming were required on all bonding surfaces in order to remove un-bonded particles and dusts. Lay-up process was performed after 28 days of curing of the concrete. All wrapped concrete cylinders were then subjected to an uni-axial compression test. Surface mounted strain gauges were used to measure strain in both the longitudinal (loading) and lateral (hoop) directions. Three testing specimens were used for each individual test, i.e. specimens were made at the same day and controlled environment. In later section, finite element method (FEM) was adopted to investigate the mechanical behaviour of composite wrapped concrete cylinder with different wrapping materials and bonding dimensions. Bonding length was defined as the length of composite that is used to wrap the cylinder in longitudinal direction. The composite laminate was symmetrically wrapped on the concrete cylinder about the mid-height axis ($h/2$).

4.2 Plain and Notched Concrete Cylinders Wrapped by Glass Fibre Composite

4.2.1 Experimental Study

The plain concrete cylinders were wrapped by different layers of the glass fibre composite with two different bonding dimensions. E-glass (0°/90°) woven fabric and Araldite MY750 epoxy resin were used to form glass fibre reinforced plastic (GFRP) composites. Both warp and weft fibres were aligned along the cylinder longitudinal and hoop directions, respectively. A notch was made with a ratio of 0.2 to the diameter of the cylinder for some testing specimens in order to simulate the existence of a crack. The distance between two inner notches surface was 2 mm apart. All the GFRP composite laminates were laid –up with one-quarter overlap length after one successful wrap. This method was used to avoid spitting failure at the weakest joint region, i.e. end to end connection of the laminates. Plastic film with pre-smeared releasing agent onto inner surface was used to cover the laid-up composite in order to avoid contamination and water absorption during the curing process.

The size of the wrapping laminate for the notched concrete cylinder was gradually decreased with increasing the number of laminate layers in order to minimise the interlaminar shear and peel-off stresses at bond end regions. Fig. 4.1 illustrates the plain and notched concrete cylinders wrapped by the GFRP composite laminate. The dimension and wrapping layers of composite of all testing cylinders are listed in Table 4.1.

The experiment set-up was same as the uni-axial compression test for the plain concrete cylinder as mentioned in Chapter 3. Both compression surfaces of the cylinders were polished before laying-up the composite. Steel platens were used in compression-testing machine. Transparency plastic plate was placed in front of the testing chamber in order to avoid injury due to explosive action of the testing cylinders. External bonded strain gauges were used to measure surface strains of the composite when it was subjected to compression load. Strain and load values were recorded up to the condition when the ultimate load of the testing cylinder was reached.

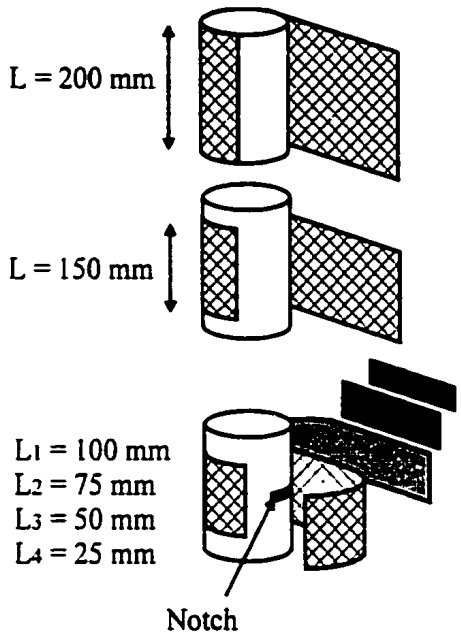

Figure 4.1 A schematic diagram of the plain and notched concrete cylinders wrapped by glass fibre composite laminate.

Table. 4.1 Details of all testing specimens.

Code	Cylinder type	Wrapping layer	Bonding length (mm)	Bonding pattern
CWC200-1 CWC200-2 CWC200-3	Plain	1 2 3	200 200 200	Fully covered the whole circumference of the cylinder.
CWC150-3 CWC150-5 CWC150-10	Plain	3 5 10	150 150 150	Partly covered the circumference of the cylinder.
NC100 CWNC100-15	Notched	— 15	— 100,75,50, 25	— The first three layers: L=100 mm, θ=360°. The second four layers: L=75 mm, θ=280°. The third four layers: L=50 mm, θ=200°. The last four layers: L=25 mm, θ=106°.

CWC: Composite wrapped concrete.
NC: Notched concrete.
CWNC: Composite wrapped notched concrete.

The experiment results of the wrapped concrete cylinders after testing are plotted in Figs. 4.2 to 4.4. All strains shown in the plots are average values, which are obtained from three strain gauges attached at as the positions indicated in Fig. 3.5.

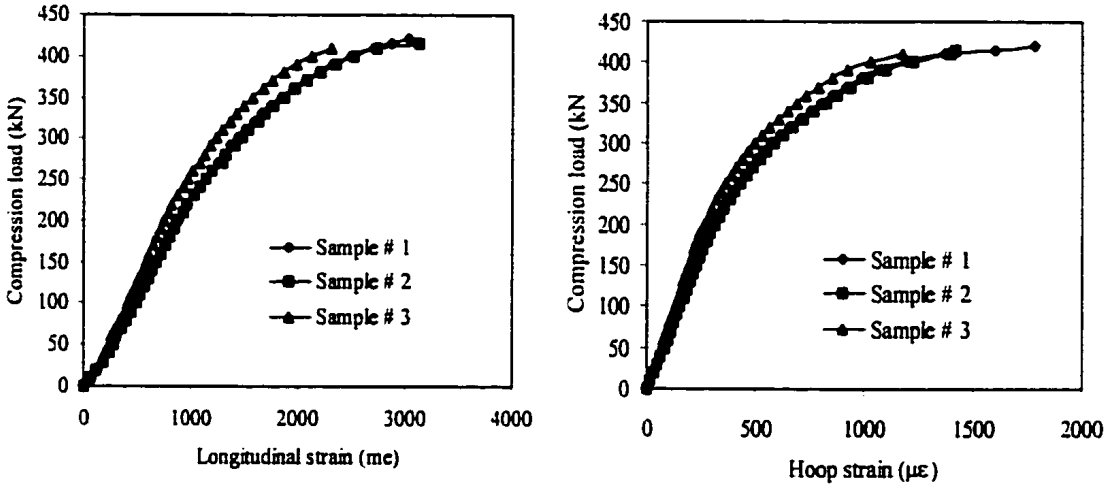

Figures 4.2a and b Experimental results of the test specimens CWC200-1after compression test.

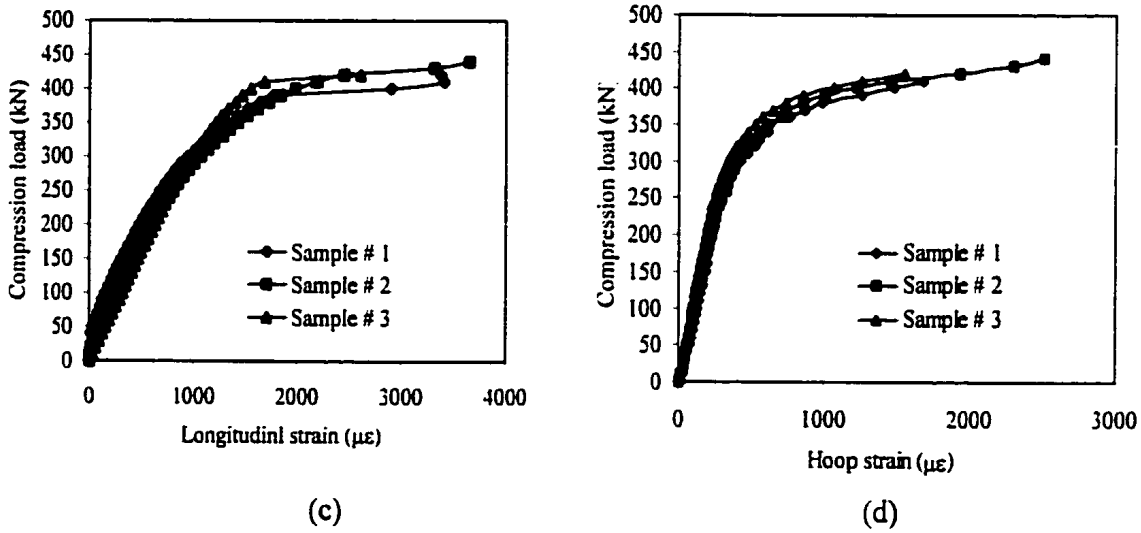

Figures 4.2c and d. Experimental results of the test specimens CWC200-2 after compression test.

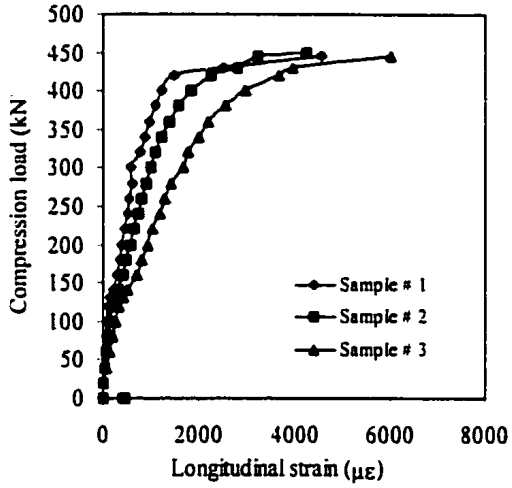

(e)

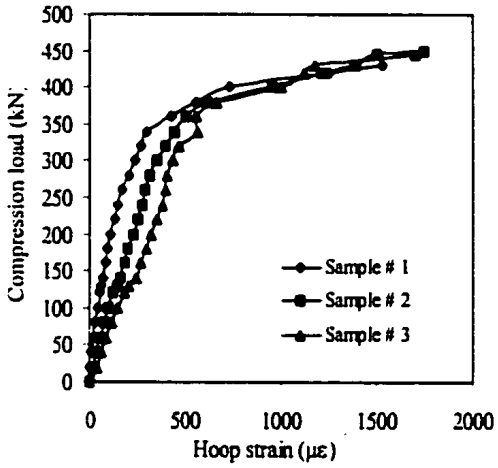

(f)

Figures 4.2e and f. Experimental results of the test specimens CWC200-3 after compression test.

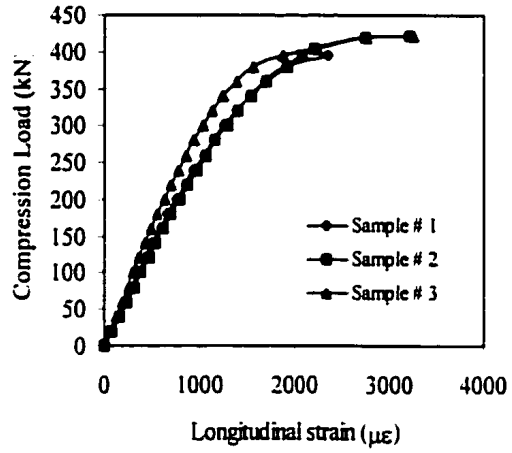

(a)

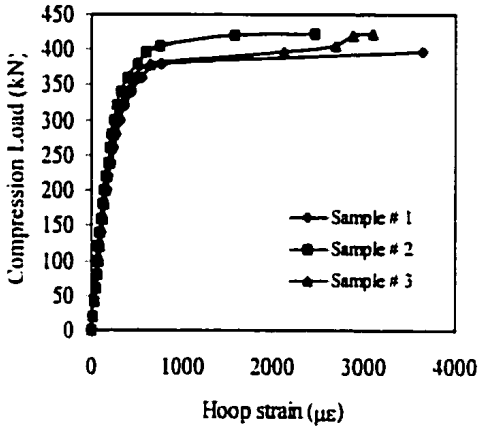

(b)

Figures 4.3a and b. Experimental results of the test specimens CWC150-3 after compression test.

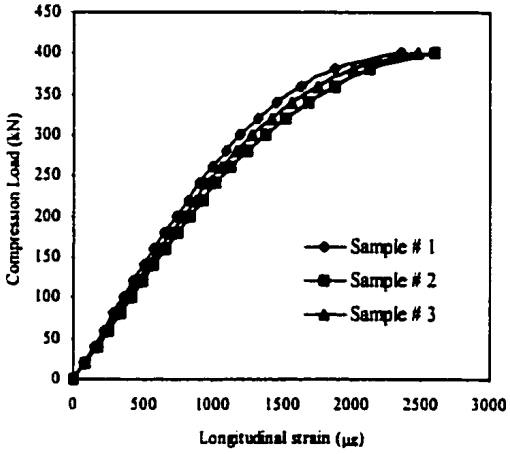

(c)

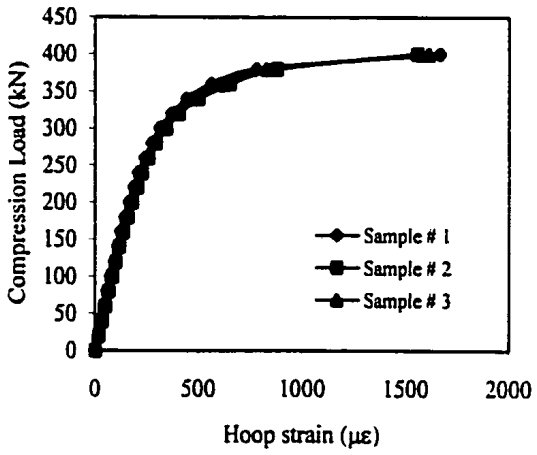

(d)

Figures 4.3c and d. Experimental results of the test specimens CWC150-5 after compression test.

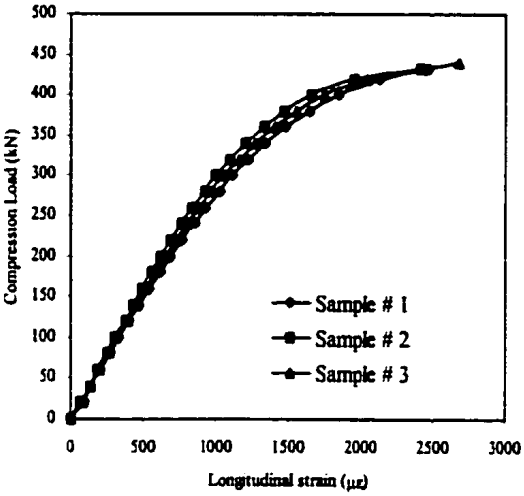

(e)

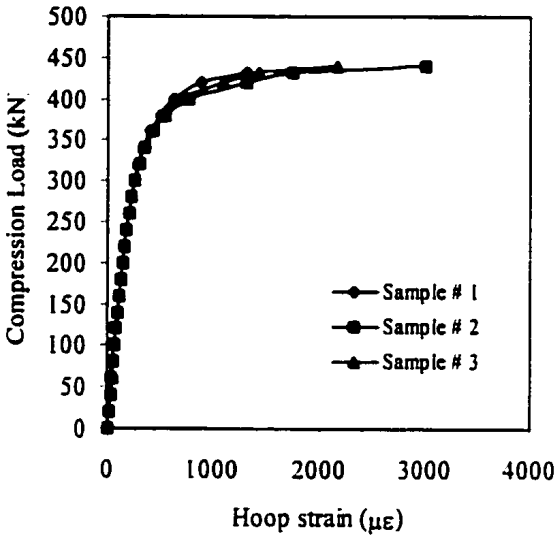

(f)

Figures 4.3e and f. Experimental results of the test specimens CWC150-10 after compression test.

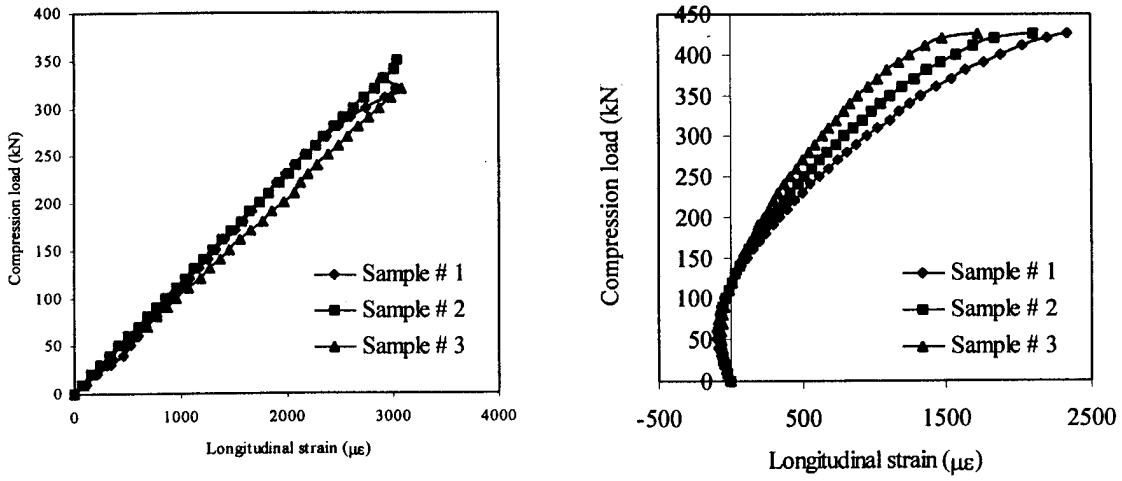

(a) (b)

Figures 4.4a and b. Experimental results of the test (notched) specimens NC100 and CWNC100-15 after compression test.

4.2.2 Result Discussions

The test results of the concrete cylinders with and without strengthening by glass fibre composite wraps under the applied compressive load indicate that the ultimate compressive loads increase with increasing the number of wrapping layers for the wrapped cylinder with the same bonding length. The average values of all testing results are summarised in Tables 4.2 to 4.4.

From the tables, it is obviously shown that the strength of the wrapped concrete cylinder increase with an increase of the stiffness as well compared with the plain concrete cylinder. The load strain relationship in lateral direction was found similarly and remains approximately unchanged in load up to 75% of its ultimate load value. The combined plots are shown in Fig. 4.5.

The load-strain relationships vary when further increasing the compression load. It is suspected that micro-cracks and debonding between aggregate and cement occurred beyond this limit. However, the comparison of the results of the wrapped cylinders with two different bonding lengths shows that the use of a long bonding length for concrete confinement

may give a better strengthening characteristic compared with a concrete cylinder with a short bonding length. The ultimate compressive strength of the test specimen with 10 layers of the composite wrap and the bonding length of 150 mm is similar that from the test specimen with 3 layers of composite wrap and the bonding length of 200 mm.

Table 4.2. The average ultimate compressive load of the test cylinders with the bonding length of 200 mm. (Specimens types: Plain, CWC200-1 to 3)

Sample Number	1	2	3	Avergae	S. D.
Plain cylinder	390	385	400	391.66667	7.64
Wrapped by 1 layer GFRP	410	415	420	415	5
Wrapped by 2 layers GFRP	420	440	440	433.33333	11.5
Wrapped by 3 layears GFRp	445	450	445	446.66667	2.88

Table 4.3. The average ultimate compressive load of the test cylinders with the bonding length of 150 mm (Specimen types: Plain, CWC150-3, 5 and 10).

Sample Number	1	2	3	Avergae	S.D.
Plain cylinder	390	385	400	391.66667	7.64
Wrapped by 3 layers GFRP	395	422.4	415	410.8	14.17
Wrapped by 5 layers GFRP	400	415	433	416	16.5
Wrapped by 10 layears GFRp	431.5	440	440	437.16667	4.32

Table 4.4. The average ultimate compressive load of the notched concrete with and without wrapping by glass fibre composite. The bonding lengths were varied to the thickness (Specimen types: Plain and notched (NC100 and CWNC100-15) cylinders).

Sample Number	1	2	3	Avergae	S.D.
Plain cylinder	390	385	400	391.66667	7.64
Notched cylinder	320	350	330	333.33333	15.27
Wrapped notched cylinder	425	430	440	431.66667	7.63

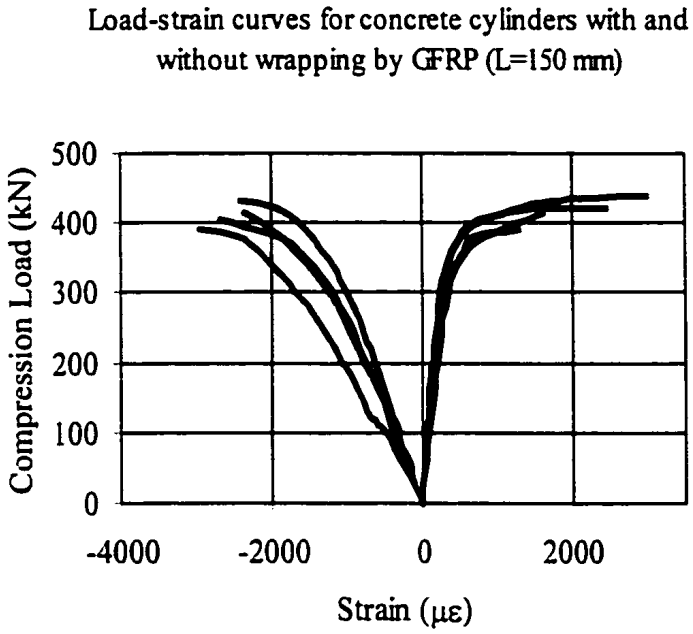

(a)

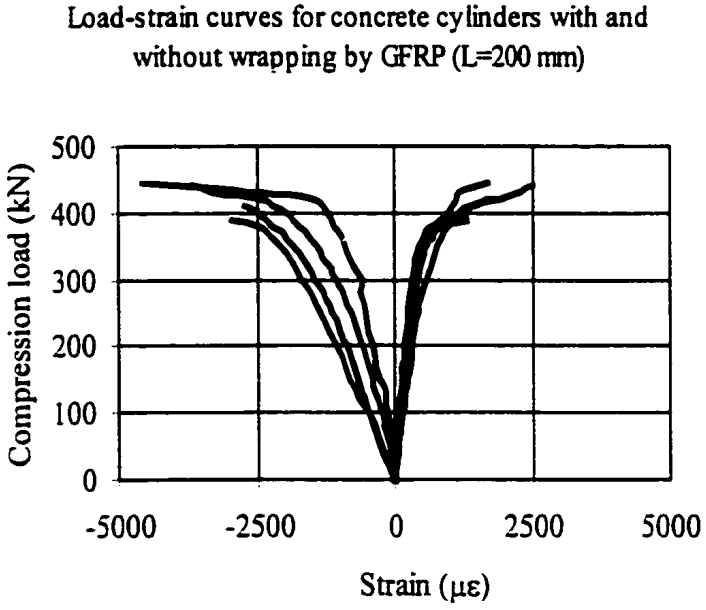

(b)

Figure 4.5 Load-strain relationships of two different types of test specimens: CWC150 (a) and CWC200 (b).

At the peak loading condition, several visible white track lines, which might be due to the formation of micro-cracks on the concrete surface, were observed. Split-off failures in the composite laminates occurred when further applying the compression load to failure condition. Cracks in composite were initiated at the middle height of the cylinder for thin layer wrapped cylinders and propagated toward both ends of the wrapping laminate in the direction of the applied load. For the 5 and 10 layers wrapped cylinders, unlike the thin composite wrapped cylinder, cracks were started at both ends of the wrapping laminate. Explosive failure occurred in very short time after crack was initiated. The failure modes of the test specimens with thin and thick composite wraps are shown in Figs. 4.6 and 4.7.

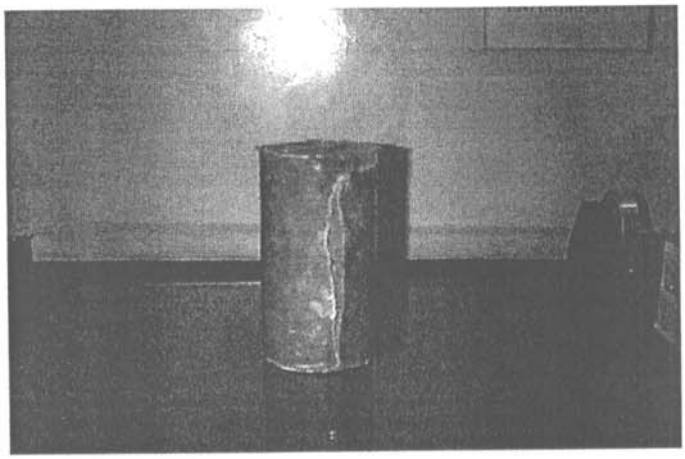

(a)

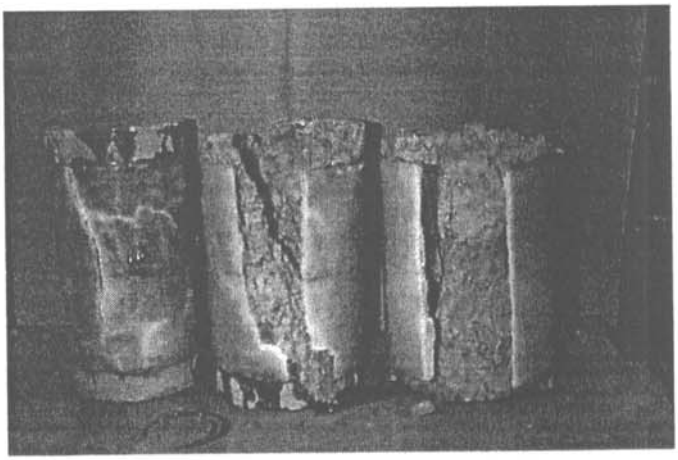

(b)

Figure 4.6 Failure modes of the test specimens with thin (a) and thick (b) layers of composite wraps.

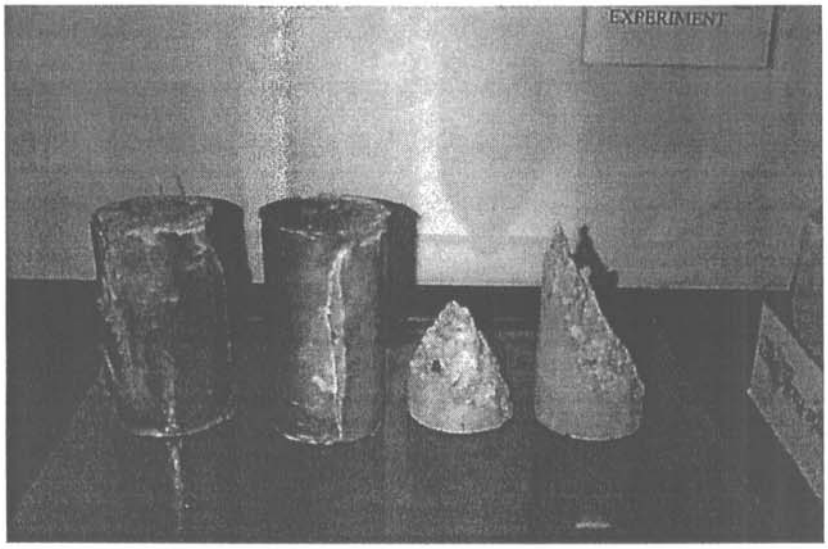

Figure 4.7 Comparison of tested cylinders with and without wrapping by the GFRP composites.

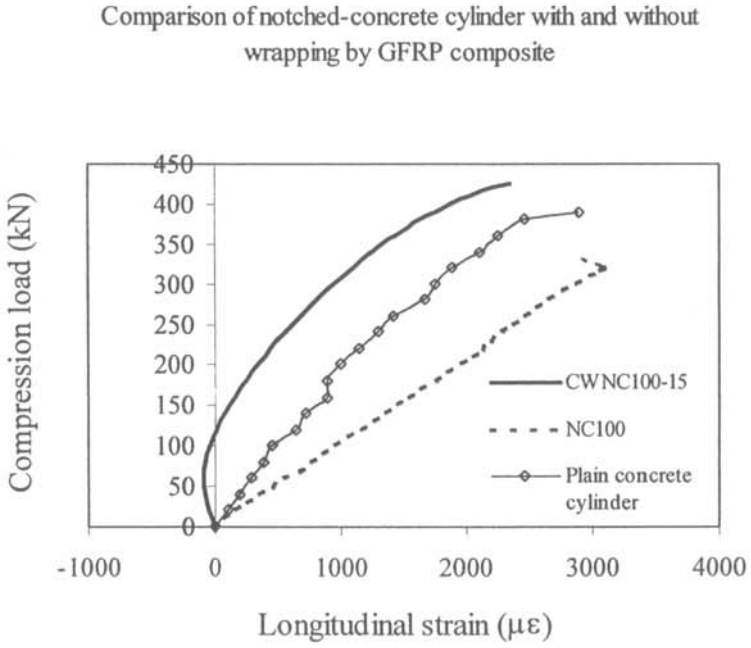

Figure 4.8 Load-strain curves for plain (middle line), notched (bottom line) and strengthened notched concrete cylinders (top line) subjected to uni-axial compression load.

The ultimate loads of the notched concrete cylinders with and without wrapping by the GFRP composite laminates are 331 kN and 431 kN, respectively as indicated in Table. 4.4. It is shown that the ultimate load of the notched concrete cylinder after wrapping by the GFRP composite is increased to 31% and 11% compared to its notched and plain statuses. The combined plots of the plain, notched and GFRP wrapped-notched concrete cylinders are shown in Fig. 4.8.

For the notched concrete cylinder, crack was initiated at notch-tip and extensively propagated toward both compression surfaces of the cylinder (see Fig.4.9). According to the experimental results and observations during the experiments, it is found that the GFRP composite material can be used as strengthening medium for concrete cylinders with and without crack formation. The ultimate load capacity is increased by using the GFRP composite wrap technique. For the notched concrete cylinder, the load capacity even can be restored to its plain status with the appropriate number of composite wraps.

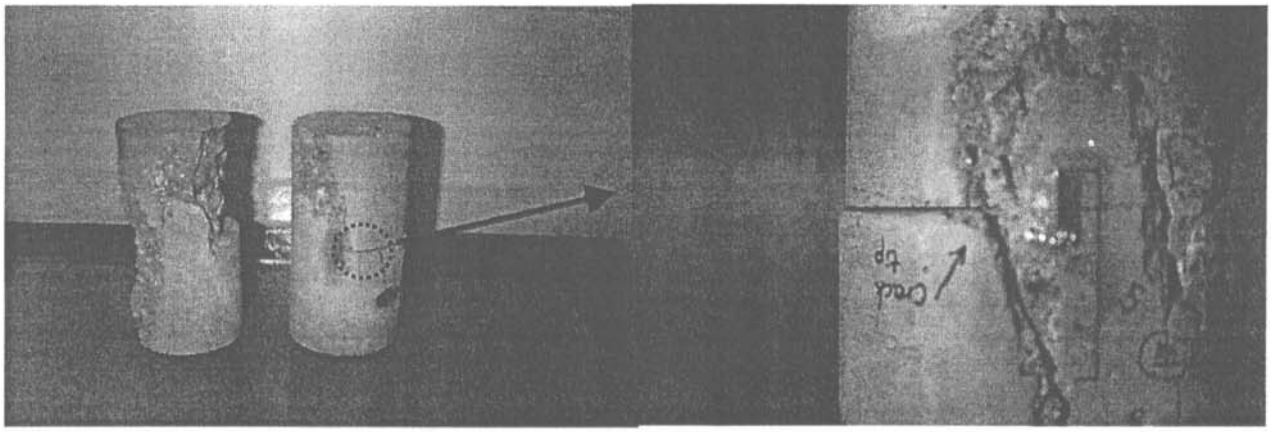

Figure 4.9 Failure patterns of the notched concrete cylinder

The failure mode of the wrapped concrete cylinders with 5 and 10 layers of composite wraps show that the hand lay-up technique by using epoxy resin do provide a very strong bonding between the concrete and composite. Nearly all materials inside the concrete were exploded-off when the wrapped cylinder reached its failure load condition. However, the wrapping composite laminate could remain adhere the concrete tightly without substantial failures by debonding or peeling-off. Fig. 4.10 gives photographs of the wrapped concrete cylinder after exploding by compression load.

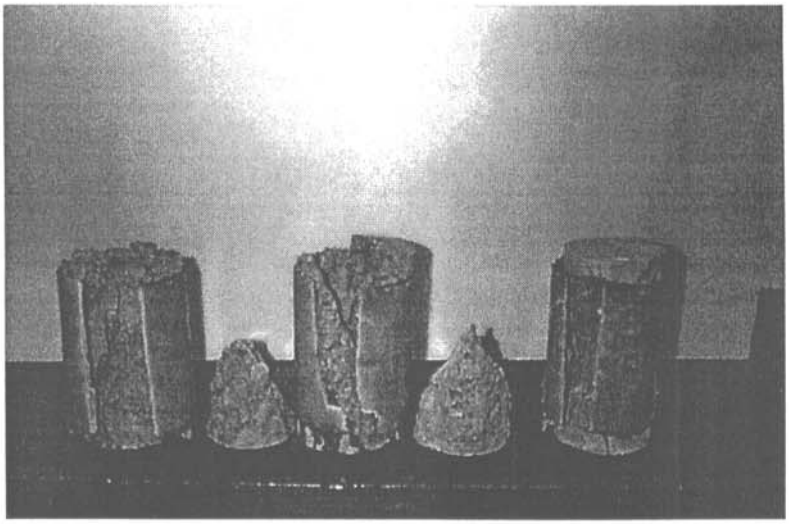

(a)

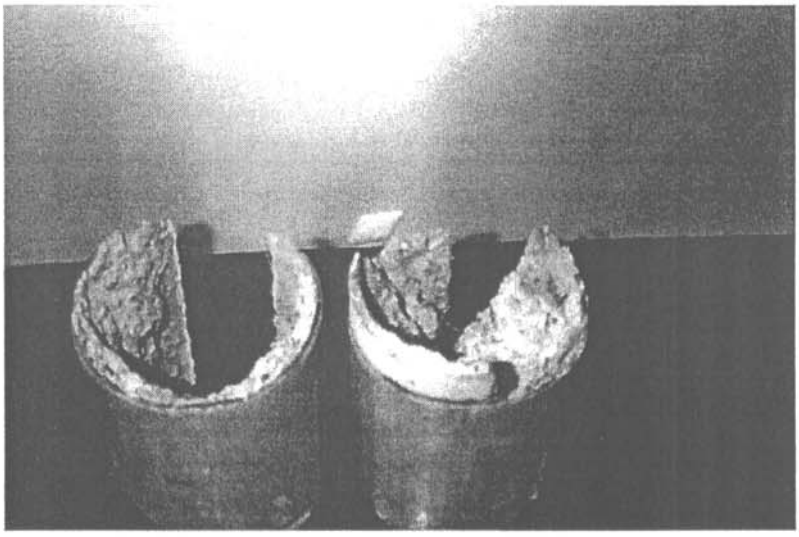

(b)

Figure 4.10 Photographs of the wrapped concrete cylinders after uniaxial compression test: (a) failure was happened explosively and (b) concrete and glass fibre composites failed as a single unit.

4.3 Numerical Study on Composite-wrapped Concrete Cylinders

4.3.1 Introduction

This Chapter aims to discuss the mechanical behaviour of plain concrete cylinder wrapped by composite or other high strength materials in order to achieve an efficient strengthening characteristic using finite element and analytical methods. The model used in current study is targeted on laboratory-sized concrete cylinder. The effects due to the use of shear rebars and embedded steel reinforcement, and the failure patterns due to the size effects are not included in the Chapter. In this Chapter, several significant effects in the field of concrete confinement by using either steel jacketing or composite wrapping techniques are addressed.

It is well known that the load carrying capacity of the wrapped concrete cylinder should be increased compared with its virgin status without considering its degradation due to the chemical interactions between concrete and wrapping materials. However, the stress distributions in the wrapping material with different mechanical properties and bonding dimensions of the wrapped concrete cylinder are always ignored by many researchers and engineers. Therefore, this Chapter intends to point out these effects by numerical and analytical methods.

4.3.2 Characterisation of Wrapped Concrete System

Karbhari et al (1997) and Zhang et al. (1998) found that the stress-strain response of the wrapped concrete cylinder under uniaxial compression load shows a bi-linear characteristic i.e. the initial response is almost linear up to a point, which is called "kink point". At this point, the wrapping sheet starts to activate the confining action. The concrete began to fail beyond this point, and the curve continues almost in liner manner with a reduction of slope. After the kink point, substantial visible cracks in the concrete and debonds at the interface between composite and concrete appear [Christropher, 1994]. Figure 4.11 shows the typical

stress-strain response of the glass-fibre composite wrapped concrete cylinder subjected to uniaxial compression load [Toutanji, et a. 1998].

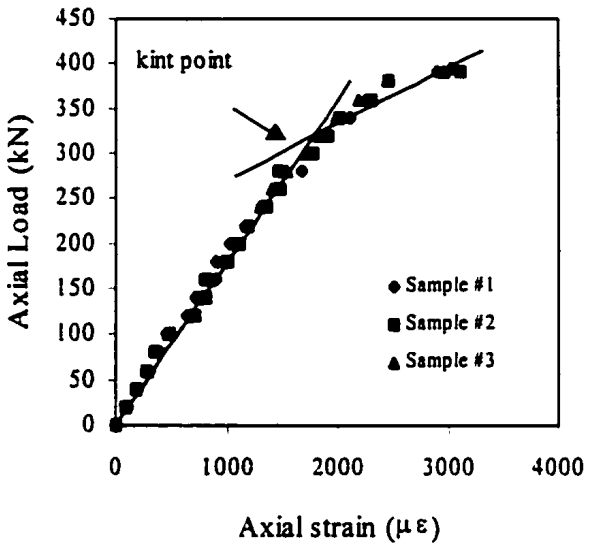

Figure 4.11 Stress-strain response for E-glass fibre composite wrapped concrete cylinder subjected to uni-axial compression load.

The load-deformation response of the typical civil concrete structure is shown in Fig. 4.12. The stress-strain behaves in a linear fashion up to yield stress and rapidly reaches its ultimate stress (called the compressive strength). Following this is a descending branch, which is normally called the softening region. The axial strain of the concrete cylinder continues to increase as the compressive stress decreases. At a stress level of approximately 70% of the peak-strength, lateral deformation raises rapidly and many extensive vertical cracks appear, the value of Poisson's ratio at peak being equal to 0.5 [Neville 1995].

Figure 4.13 shows the deformation of the plain concrete cylinder subjected to uni-axial compression load with different platen materials. It is demonstrated that the radial expansion of the column is highly dependent on the modulus and Poisson's ratio of the wrapping material. Therefore, in designing the wrapping system, attention should be paid to the real practical situation, particularly at the load bearing joint and connection of the wrapped concrete structure in order to achieve the maximum strengthening capacity of the structure.

Steel and composite wrapped systems are used to constrain the expansion of the concrete structure in order to maintain its structural integrity by minimising crack formation.

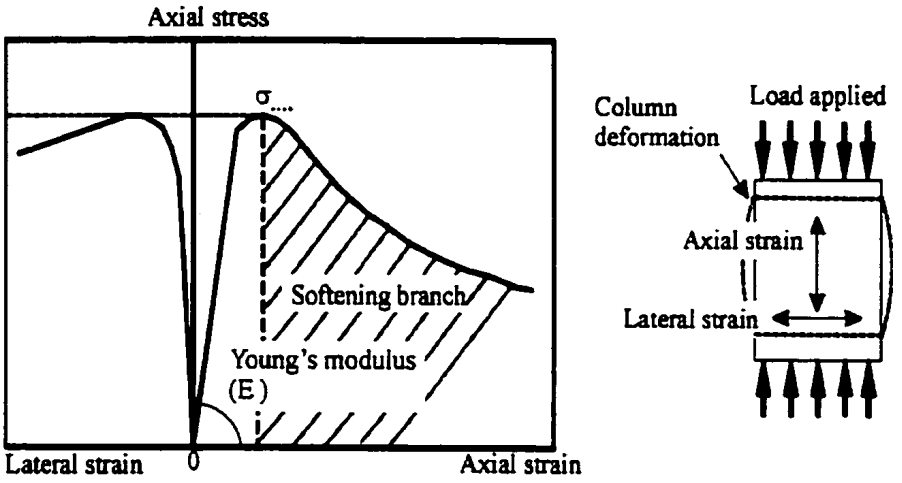

Figure 4.12 Stress and strain curve for plain cylinder subjected to uniaxial compression load.

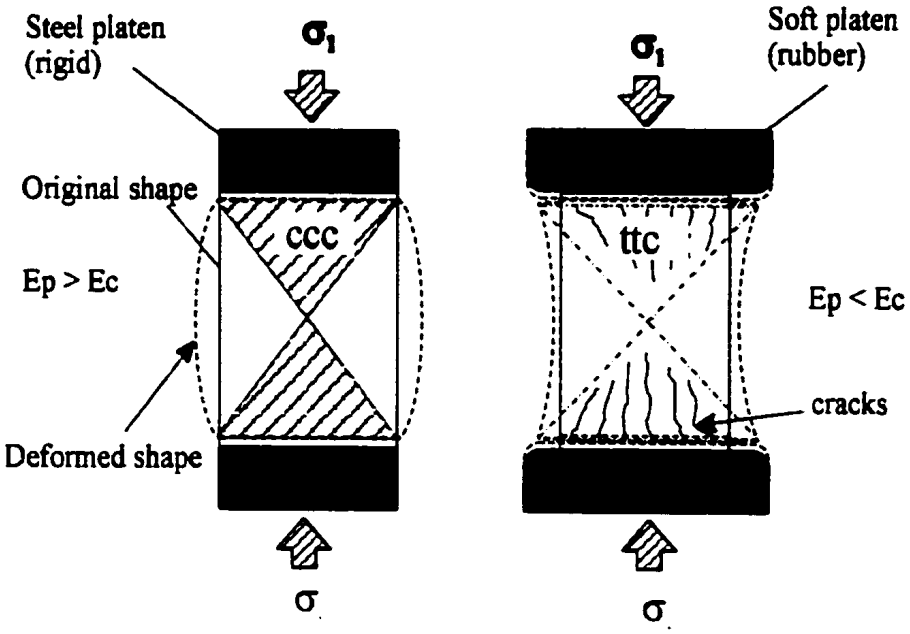

ccc = region of triaxial compression
ttc = region of triaxial tension-tension-compression

Figure 4.13 Effects of deformation on concrete cylinder under compression with different platen properties, (a) hard platen and (b) soft platen.

Zhang et al. (1998) found experimentally that splitting failure in the hoop direction of the wrapped concrete cylinder starts at both ends of the wrapping sheet and propagates toward the middle of the column. The failure mode of the composites wrapped concrete cylinder is shown in Fig.4.6. The failure mechanism of the wrapped column after testing is schematically illustrated in Fig.4.14. The column was wrapped by thick E-glass woven composites and tested under steel platen, i.e. the top and bottom-centre regions inside the concrete were subjected to tri-axial compression stress so that no deformation would occur in either radial or hoop direction. According to the test result shown above, it is worth to investigate in depth the mechanical behaviours of this wrapped concrete system, particularly at the bond-end regions.

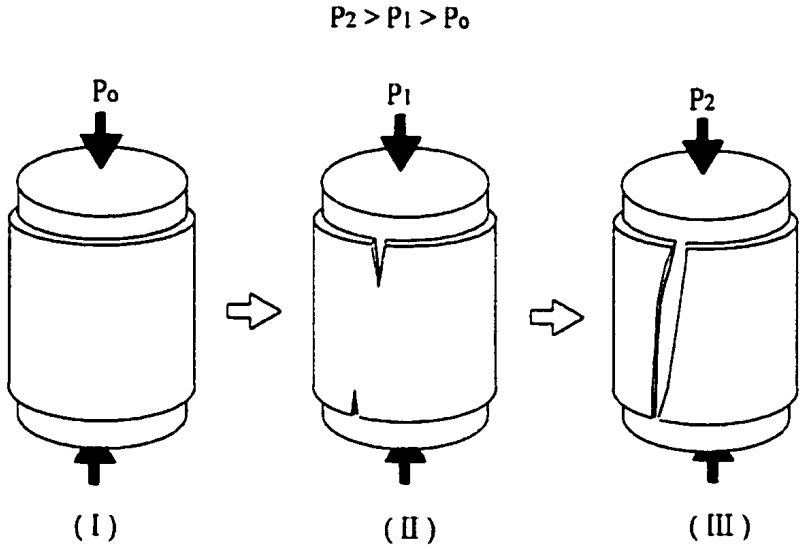

(I) Load is applied the surface of the wrapped concrete column.
(II) Cracks are initially started at both ends of the reinforced plate.
(III) Cracks are propagated toward the middle of the wrapped column.

Figure 4.14 Failure mechanism of wrapped concrete cylinder subjected to compression load.

In the section, a FEM method has been used to investigate the mechanical responses of the concrete cylinder wrapped by different wrapping materials, bonding lengths and thicknesses. A theoretical equation has been established to determine the shear stress distribution along the bonding line of an adhesive material. The results are then compared with the FEM solutions.

4.3.3 Numerical Analysis

4.3.3.1 Finite element model

The wrapped concrete cylinder is modelled as an axis-symmetrical cylinder. The size of the plain concrete cylinder is 100 mm in diameter (D) and 200 mm in height (h_o). A global co-ordinate system is used: x, y and z-axes represent the radial, hoop and axial directions of the wrapped column respectively. MSC/Nastran FEM Package was used to model the geometry. The element used to mesh the column was Parabolic Tria6 (Fig. 4.15).

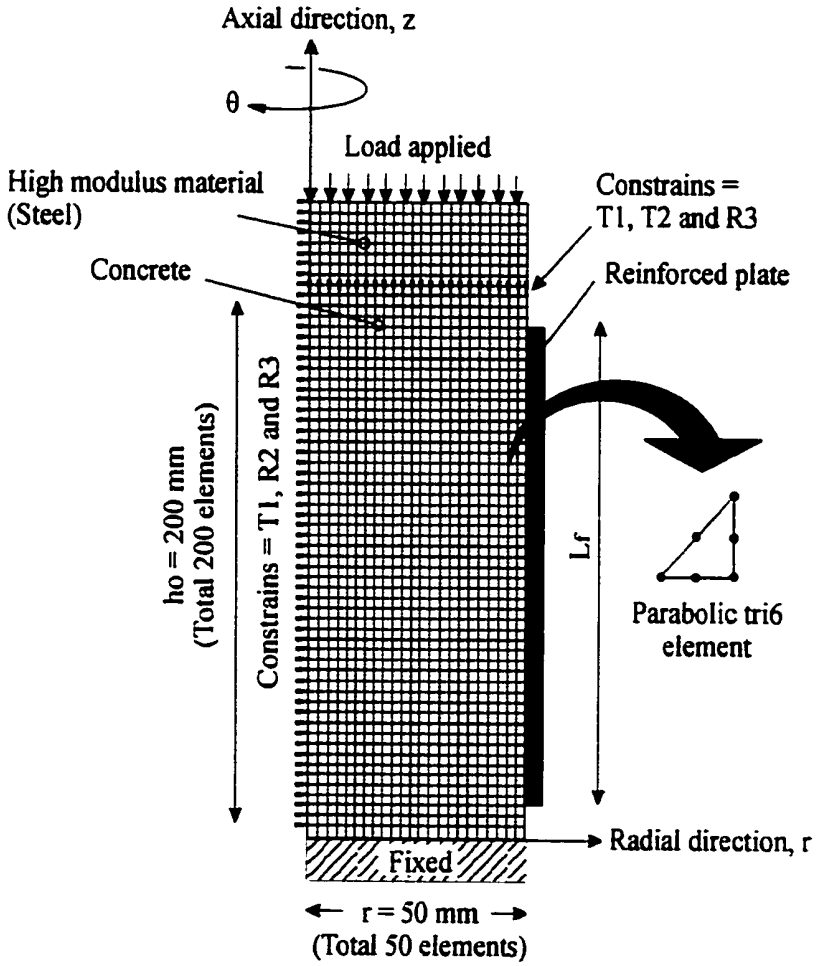

Figure 4.15 Finite element model for wrapped concrete cylinder

Three nodes are distributed along the three edges of each parabolic triangular element. The mesh consists of 50 elements and 200 elements in the radial and axial directions, respectively. Steel platen is modelled at the top of the wrapped concrete cylinder. A uniform pressure is applied on the top of the platen in order to simulate the real testing condition and to prevent stress concentration at the top surface of the concrete cylinder. The top surface of the wrapped concrete cylinder is constrained in the radial and hoop directions while the bottom surface is fixed. The centre line of the column is allowed to move vertically.

Different bonding lengths, wrapping materials and sheet thicknesses have been modelled individually to observe the mechanical responses under the same loading condition. The kink load is determined by applying the load to its critical axial deformation value δ^* of the plain concrete cylinder, i.e. the deflection of plain concrete cylinder at yield condition [Zhang et al, .

The FEM model was verified by the experiment for the concrete cylinder with wrapping by 3 and 10 layers of glass fibre composite laminates. The results of comparison are plotted in Fig. 4.16 and these results have a good agreement with the experimental data. It is noted that the experimental results of 3 layers composite wrapped concrete cylinder have a small scatter range, and the predicted results are relatively closer to the experiment data.

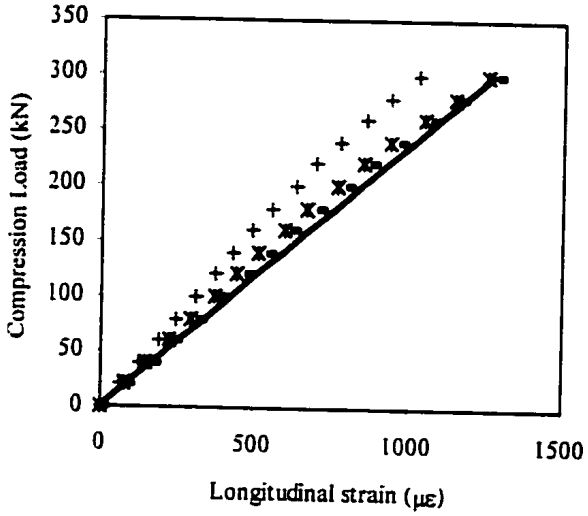

(a)

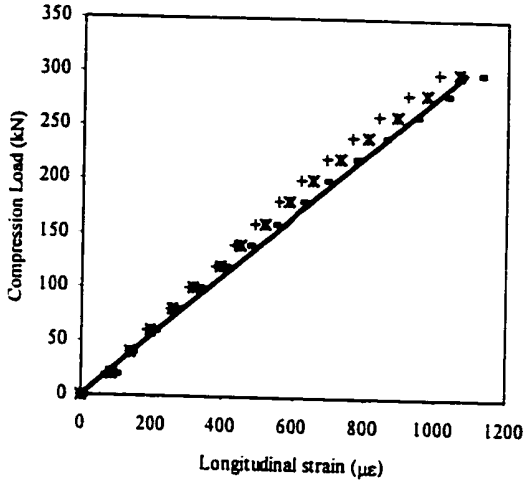

(b)

Figure 4.16 Comparison of FEM simulation and experimental data for the concrete cylinders with wrapping by 3 layers (a) and 10 layers (b) glass fibre composite laminates.

4.3.3.2 Axial deflection (δ^*) of wrapped concrete cylinder

The axial deformations of the wrapped concrete cylinder are plotted in Fig. 4.17. The figure shows that increasing the bonding length of the wrapping sheet greatly reduces the axial deformation of the wrapped concrete cylinder, especially when a high modulus wrapping sheet is used. A thick wrapping sheet also provides a better holding force to the concrete cylinder compared to thin wrapping sheet. In turn, the low modulus material does not influence the structure significantly regardless of the bonding length or the thickness of the material.

4.3.3.3 Kink load and wrapping efficiency

The plots of the kink load versus modulus of the wrapping material are shown in Fig. 4.18. The kink load increases significantly as the bonding length increases. For the E_p = 200 GPa with a bonding length of 200 mm, the value of the kink load measures almost twice as the same model with a bonding length of 50 mm under the same loading condition. However, for the E_p = 11 GPa, the kink load also increases with the bonding length but the increase is

less significant. The wrapping efficiency η_w presented in percentage can be expressed as [Zhang et al. 1998]

$$\eta_w = \frac{k_o - k_\delta^*}{k_\delta^*} \cdot 100\% \tag{4.1}$$

where k_δ^* and k_o denote the kink load for the plain and wrapped concrete cylinders at δ^* condition, respectively.

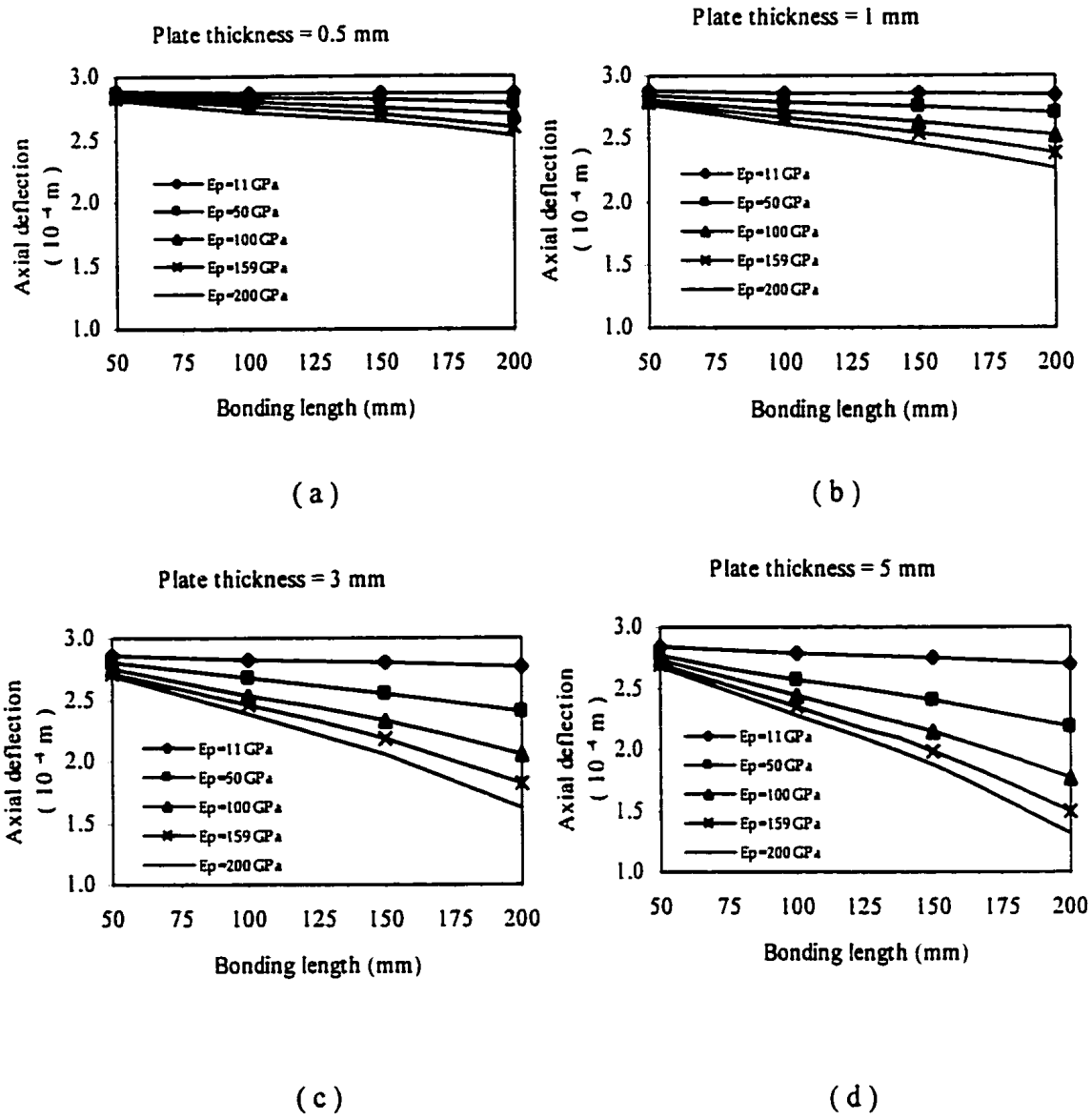

Figure 4.17. Deflection vs different bonding length of wrapped concrete column for tp = 0.5 mm (a); 1 mm (b); 3 mm (c) and 5 mm (d).

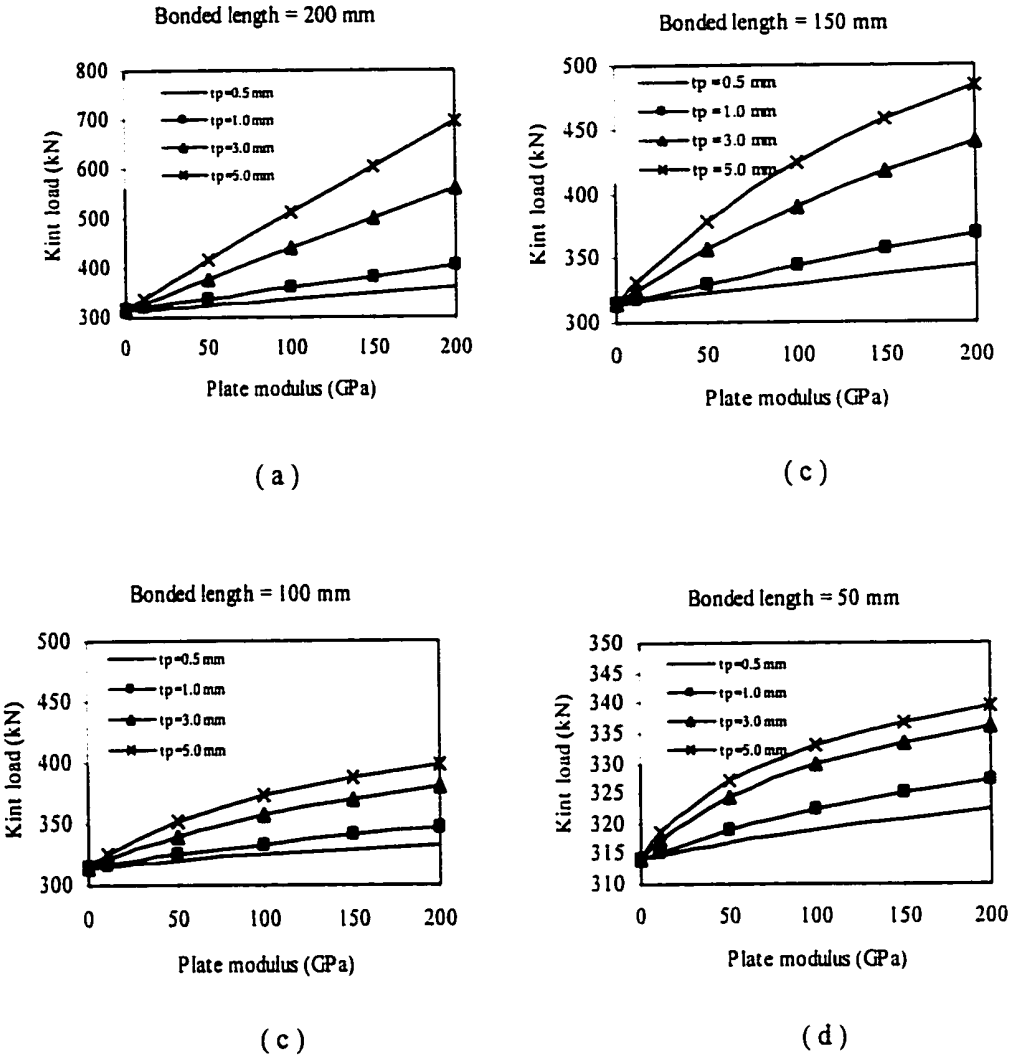

Figure 4.18. Kint load vs different reinforcement modulus of wrapped concrete column for L_f = 200 mm (a); 150 mm (b); 100 mm (c) and 50 mm (d).

4.3.3.4 Hoop stress of the wrapping sheet

The phenomena of splitting failure at both ends in the wrapping sheet can be explained by the result obtained from the FEM. Negative hoop stress is observed for the models with long bonding length and high wrapping material modulus. However, this does not happen

with short bonding length and low wrapping material modulus (and low Poisson's ratio). Maximum hoop stress is measured at both ends of the bond in the wrapping sheet. Figure 4.19 shows the plots of the hoop stress along the bonding length from z = 0 with different wrapping sheet moduli. High hoop stress is found at the end of the wrapping sheet ($z/L_f = 0$) and gradually decreases towards the middle of the column ($z/L_f = 0.5$). For the wrapping sheet with $E_p = 11$ GPa and $\nu = 0.13$, the hoop stress is positive for bonding lengths from L_f = 50 mm to 150 mm. However, for the plots of L_f = 100 mm and 150 mm, negative hoop stress is measured closed to the middle of the column for the wrapping sheets with modulus $E_p \geq 50$ GPa. This implies that the wrapping sheet may not provide the constraint action in the hoop direction throughout the whole wrapping system. Part of the concrete cylinder, particularly closed to the middle of the column, sustains the tensile stress rather than constraint force from the wrapping sheet. However, the lateral strain measured experimentally of the wrapped concrete specimen shows a positive value due to the Poisson's effect

$$\varepsilon_\theta^p(z) = \frac{1}{E_p}\left[\sigma_\theta^p - \nu^p\left(\sigma_z^p + \sigma_r^p\right)\right]. \tag{4.2}$$

The axial compressive stress of the wrapping sheet reaches maximality at the middle of the column. The Poisson's expansion in the hoop direction due to the large compressive stress in the wrapping sheet becomes the main contribution to the hoop strain (ε_θ^p) of the whole wrapping system. Thereupon, the hoop stresses in concrete and wrapping material are dependent on the difference of Poisson's ratio and axial compressive stress in both materials. For the wrapping sheet with high modulus and Poisson's ratio, a large part of the axial load is taken by the wrapping sheet, and therefore, the Poisson's expansion in the wrapping sheet becomes greater than that in the concrete. Eventually, the negative hoop stress occurs due to the existence of these differential Poisson's and modulus effects. The schematic diagram of this Poisson's effects at the middle of the wrapped column is shown in Fig. 4.20.

(a)

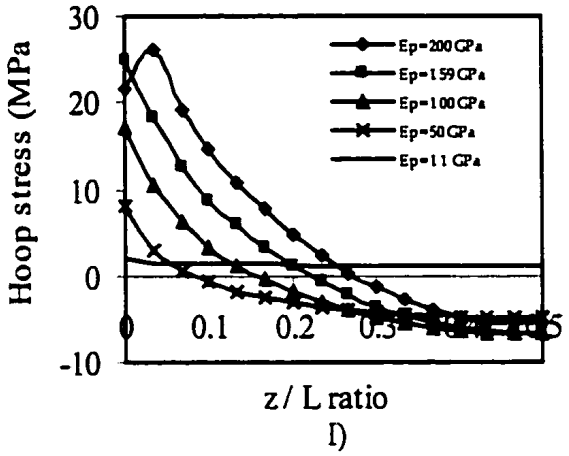

I)

(b)

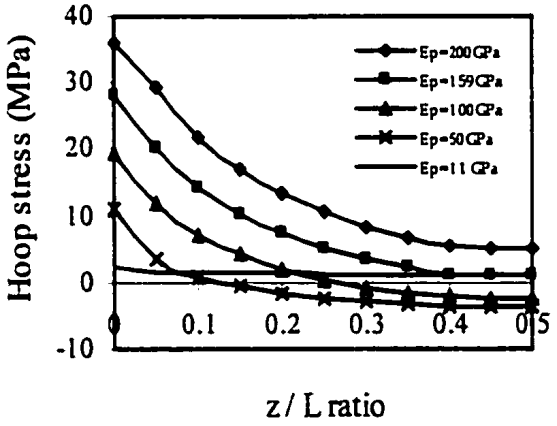

(c)

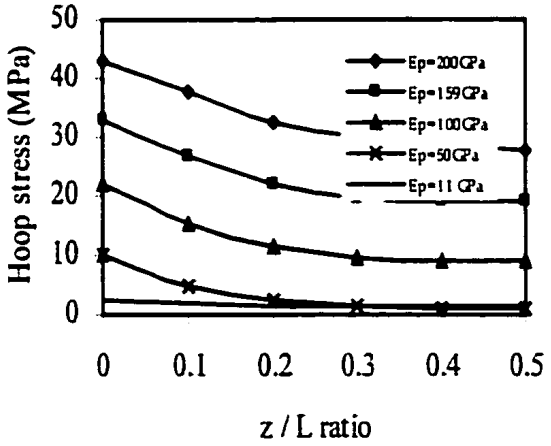

Figure 4.19. Hoop stress distribution along the bonded line of wrapping material with tp = 3 mm and L_f = 150 mm (a); 100 mm (b) and 50 mm (c).

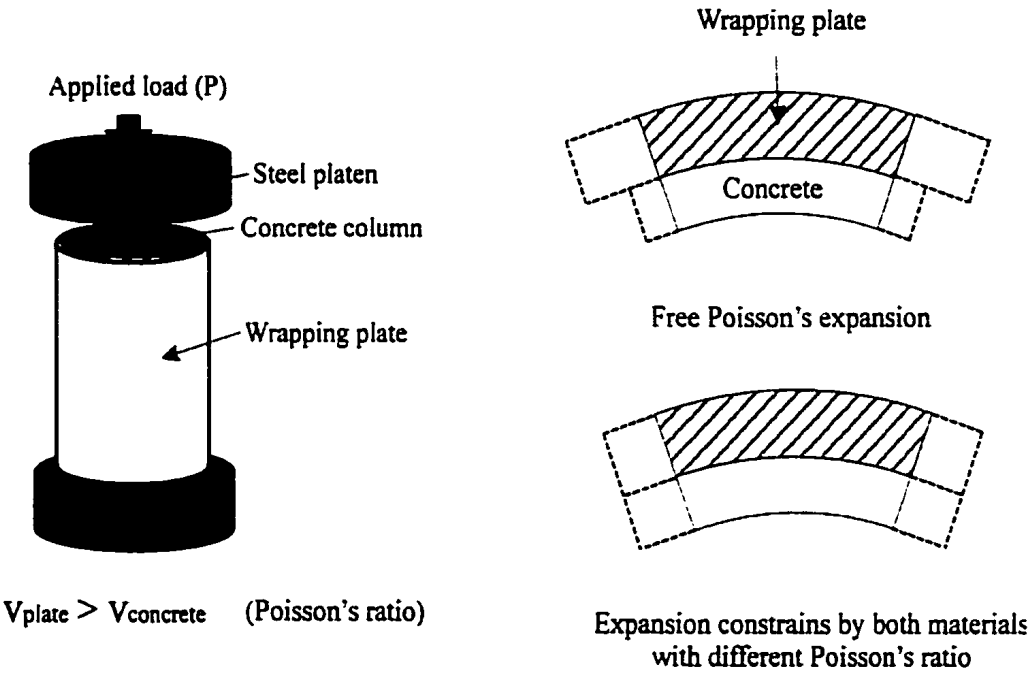

Figure 4.20. Poisson's effects of the wrapped concrete column.

The maximum hoop stress in the wrapping sheet and the distance of zero hoop stress from the bond end increase as the modulus of the wrapping sheet and the bonding length decreases, respectively. This infers that the effect of negative hoop stress can be minimised by reducing the bonding length to some critical limit. Figure 4.21 shows that the maximum hoop stress of L_f=150 mm with a modulus of wrapping sheet of 200 GPa is almost twice as measured for the same wrapping system with the modulus of 100 GPa.

The optimisation of this phenomenon can be achieved by plotting the diagram, which indicates the location of zero hoop stress z_o versus different bonding length (see Fig. 4.10). The diagram indicates that no negative hoop stress occurs when the bonding length L_f is less than $0.35h_o$, where h_o is the height of the column.

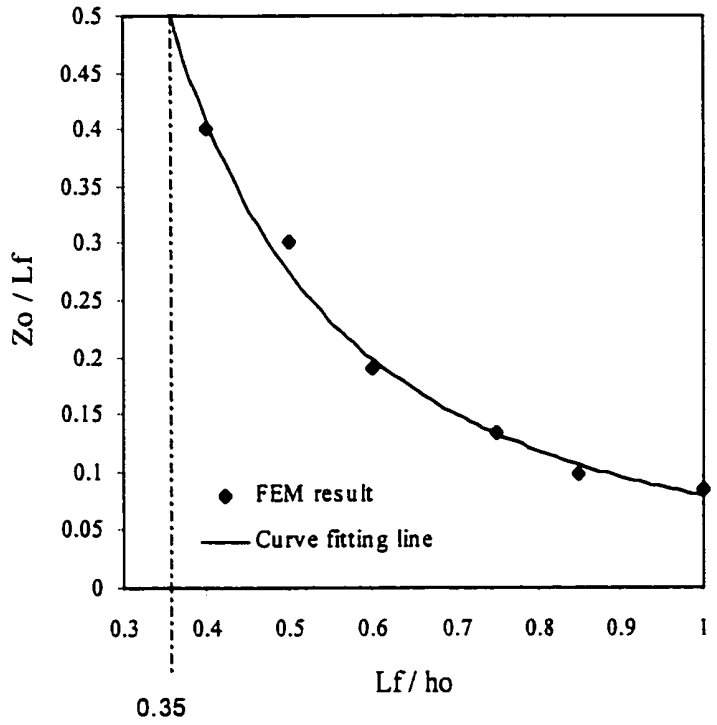

Figure 4.21 Plot of the location of zero hoop stress z_o measured from FEM (E_p=200 GPa; t_p=5 mm and P=40 MPa)

Hoop stresses of the concrete cylinders wrapped by different modulus of wrapping sheets are shown in Figs.4.22 and 4.23. They are clearly shown that the hoop stress increases with an increase of wrapping modulus while the location of zero hoop stress measured from the sheet end is decreased.

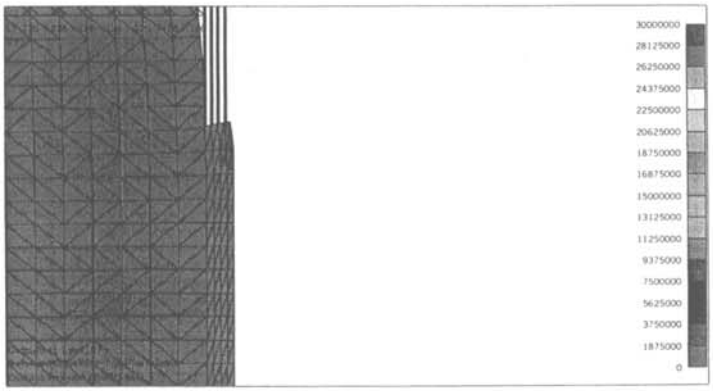

(a)

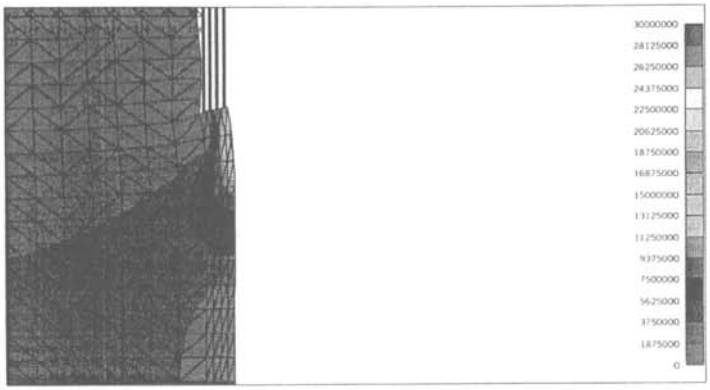

(b)

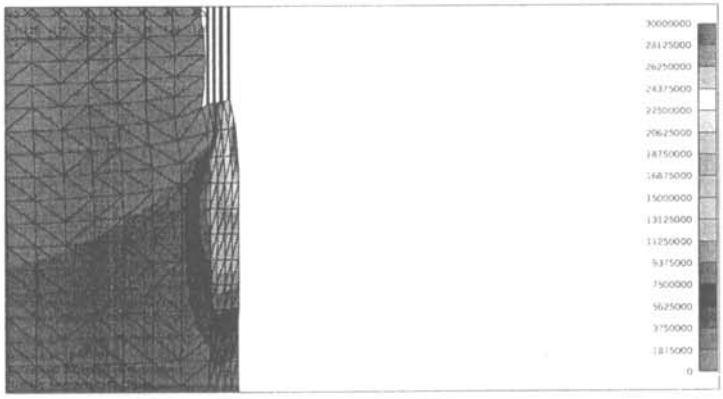

(c)

Figure 4.22 Contour of hoop stress extracted from the FEM for wrapped concrete cylinders with t_p = 5mm. E_p=11 GPa (a), E_p=100 GPa and E_p=200 GPa.

(a)

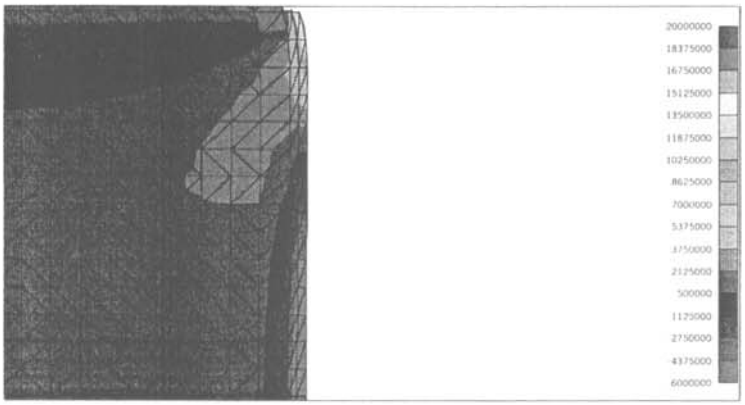

(b)

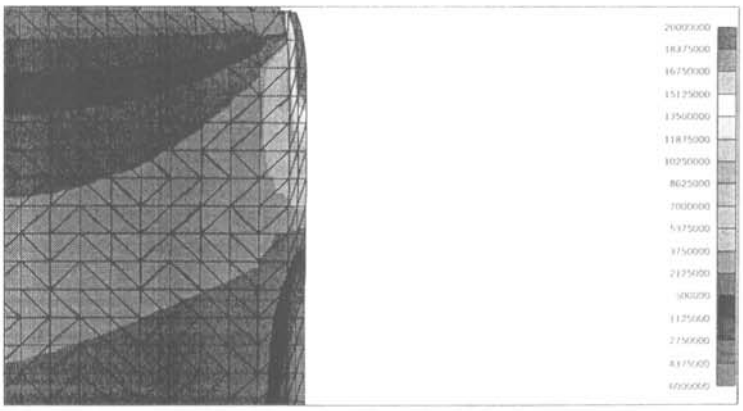

(c)

Figure 4.23 Contour of hoop stress extracted from the FEM for wrapped concrete cylinders with t_p = 3mm. E_p=11 GPa (a), E_p=100 GPa and E_p=200 GPa.

4.3.4 Theoretical Approach (adhesive shear stress)

Current literature in the field tends to pay little attention to the effect of adhesive shear stress in the wrapped concrete system. However, the adhesive material plays a very important role in the wrapping system. It must function to fully transfer stress from the concrete cylinder to the wrapping sheet without failure. Otherwise, the effective bonding length of the wrapping sheet is reduced. However, in some particular case, a bond is not required for seismic retrofit [Seible et al, 1997].

Figure 4.24 shows a theoretical model for determining the adhesive shear stress in the axial direction. The subscripts po and co denote the condition of the concrete and the wrapping sheet at the middle of the wrapped concrete cylinder, respectively. σ and L_f represent the axial stress and total wrapped length, respectively. To simplify the procedure of analysis, several assumptions are used, which include:(1) the stresses in the adhesive layer do not change with the thickness; (2) all materials behave elastically and iso-tropically under loading condition; (3) no slipping occurs at the interfaces between all bonded layers and (4) the axial strains in different materials distribute uniformly through the depth of each section.

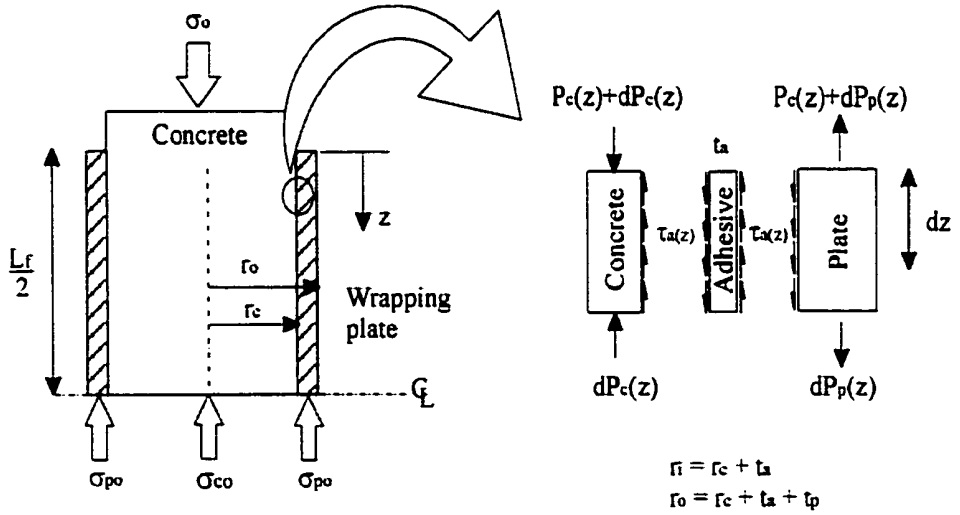

Figure 4.24 Theoretical model for evaluating the shear stress distribution of an adhesive material along the bonded line.

The adhesive shear stress $\tau_a(z)$ is expressed as the product of shear modulus G_a and shear strain $\gamma_a(z)$ of the adhesive material in any particular position, z along the bonding line:

$$\tau_a(z) = G_a\gamma_a(z) \tag{4.3}$$

and $\gamma_a(z)$ can be expressed as

$$\gamma_a(z) = \frac{\omega_p(z) - \omega_c(z)}{t_a} \tag{4.4}$$

where $\omega_p(z)$ and $\omega_c(z)$ denote the axial displacements of the wrapping sheet and the concrete, respectively. Substituting Eq.(4.4) into Eq.(4.3), the following expression is obtained after differentiating Eq. (4.3) and considering the strain compatibility:

$$\frac{d\tau_a(z)}{dz} = \frac{G_a}{t_a}\left(\frac{d\omega_p(z)}{dz} - \frac{d\omega_c(z)}{dz}\right) = \frac{G_a}{t_a}\left[\varepsilon_p(z) - \varepsilon_c(z)\right] \tag{4.5}$$

where $\varepsilon_p(z)$ and $\varepsilon_c(z)$ denote the axial strains of the wrapping sheet and concrete. The axial loads in the concrete and wrapping sheet are given by

$$\frac{dP_p(z)}{dz} = \tau_a(z)b_p \tag{4.6}$$

$$\frac{dP_c(z)}{dz} = \tau_a(z)b_c \tag{4.7}$$

where $b_p(z) = 2\pi r_i$ and $b_c(z) = 2\pi r_c$. Differentiating the Eq. (4.5) again after substituting Eqs. (4.6) and (4.7) yields

$$\frac{d^2\tau_a(z)}{dz^2} = \frac{G_a}{t_a}\left(\frac{2r_i}{E_p\left(r_o^2 - r_i^2\right)} + \frac{2}{E_c r_c}\right)\tau_a(z). \tag{4.8}$$

The solution to Eq.(4.8) is given by

$$\tau_a(z) = C_1 \cosh(\beta z) + C_2 \sinh(\beta z) \tag{4.9}$$

where
$$\beta = \sqrt{\frac{2G_a}{t_a}\left(\frac{r_i}{E_p(r_o^2 - r_i^2)} + \frac{1}{E_c r_c}\right)}. \tag{4.10}$$

Two boundary conditions are needed to determine the constants C_1 and C_2:

$$P_p(0) = 0 \qquad \text{and} \qquad \begin{matrix} P_p(L_f) = P_o \\ \tau_a(L_f) = 0 \end{matrix} \tag{4.11}$$

in which P_o is the maximum axial load of the wrapping sheet and can be evaluated by applying the strain compatibility condition at the middle of the wrapped concrete cylinder, i.e. $\varepsilon_c(L_f) = \varepsilon_p(L_f)$:

$$P_o = \frac{PA_p}{\frac{E_c}{E_p}A_c + A_p} \tag{4.12}$$

where P, A_p and A_c denote the applied load on the concrete surface, cross section area of the wrapping sheet and concrete cylinder, respectively. The constants C_1 and C_2 are obtained as

$$C_1 = \frac{P_o\beta}{b_p(1 - e^{-\beta L_f})} \qquad \text{and} \qquad C_2 = C_1 \tag{4.13}$$

Therefore, the axial stress in the wrapping sheet at $z = L_f$ and shear stress distribution in the adhesive layer along the bonding line can be given by

$$\sigma_{po} = \frac{P}{\alpha\eta + 1} \tag{4.14}$$

$$\tau_a(z) = \frac{P_o\beta}{b_p(1 - e^{-\beta L_f})} e^{-\beta z} \tag{4.15}$$

where α ($=E_c/E_p$) and η ($=A_c/A_p$) represent the modulus and area ratios of the concrete to wrapping sheet, respectively. In Eq. (4.15), it is obviously shown that the maximum shear stress of the adhesive material is reached when z=0. It is then possible to write Eq. (4.15) as

$$\tau_{a,\max} = \frac{P_o \beta}{b_p (1 - e^{-\beta L_f})} \tag{4.16}$$

The results from Eqs.(4.14) and (4.16) and FEM are plotted in Figs.4.25 and 4.26. The theoretical results give good agreement with the FEM solutions. The axial stress in the wrapping sheet increases as the thickness and modulus of the wrapping sheet increase. This implies that a part of the axial load is shared by the wrapping sheet and therefore, the dilation of the concrete cylinder can be minimised. This phenomenon is true only when the wrap is covered along whole cylinder, and therefore a part of the load is directly applied to the end of wrapping sheet. In turn, for a shorter bond length of the wrap, this phenomenon is valid up to a point where the axial stress does not increase continuously with increasing the thickness and modulus. It is due to the failure of the concrete in unwrapped area.

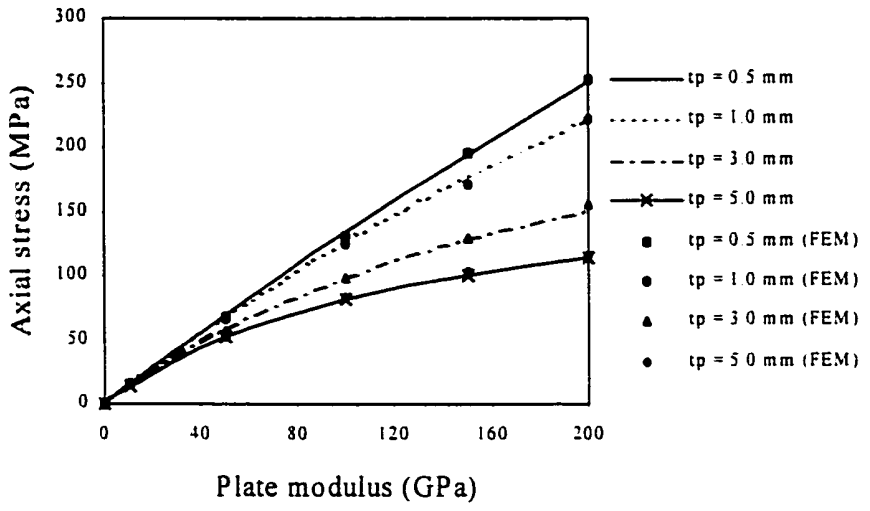

Figure 4.25 The axial compression stress of the wrapping material with different wrapping thickness and modulus.

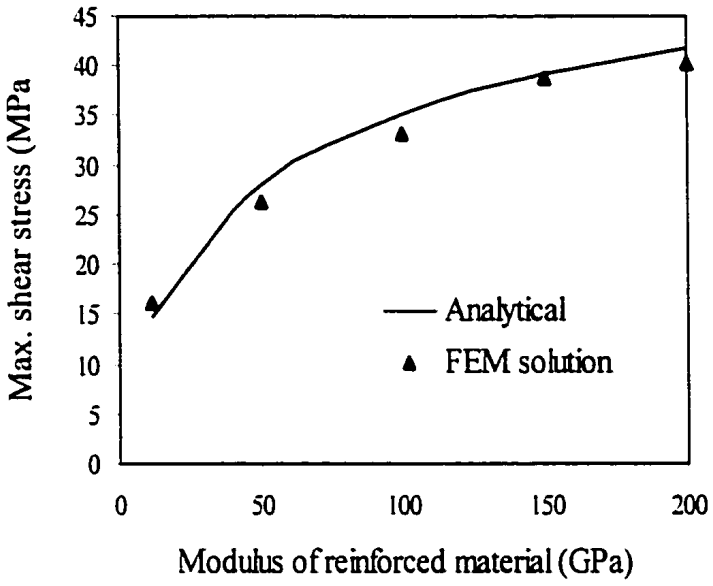

Figure 4.26 Maximum shear stress in the adhesive material with different wrapping sheet properties.

However, for the low modulus of wrapping sheet, the effect caused by the wrapping thickness becomes less significant. The maximum adhesive shear stress $\tau_{a,max}$ increases with the modulus of the wrapping sheet, and decreases with the adhesive thickness. In general, modulus and strength are the dominating factors that are used to select the material for confining the concrete structure. However, adhesive shear stress increases with the use of thick, high modulus wrapping sheet. Once the failure of the adhesive material occurs, the effective bonded length of the wrapping sheet is reduced subsequently. Eventually, the increases of the hoop stress in the wrapping sheet and axial deformation of the wrapped concrete cylinder and the decrease of the wrapping efficiency in the wrapped concrete system are resulted.

4.3.5 Summary

The Chapter discusses several failure mechanisms of the wrapped concrete cylinder with different bonding length, sheet thickness and wrapping materials through experimental in-

vestigations, numerical analysis and theoretical study. Several conclusions can be drawn as follows:

1. The ultimate load capacity of the concrete cylinder increases with the use of composite wrap technology. It is increased with increasing the number of wrapping layer and bonding length. Also, no slipping and debond failure were observed when ultimate load was reached.
2. The load carrying capacity of the wrapped concrete structure is governed by the mechanical properties, such as modulus and Poisson's ratio, of the wrapping sheet.
3. The deflection of the wrapped concrete cylinder in the load direction decreases as the modulus of the wrapping sheet, bonding length and thickness increase, bringing higher wrapping efficiency (η_w).
4. However, negative hoop stress may be resulted by using thick and high modulus of wrapping sheet, and with long bonding length for the wrapped concrete system.
5. The maximum hoop stress is located at both ends of the wrapping sheet. The initiation of cracks at both ends of the wrapping sheet and splitting-off failure were observed in the experiments. Furthermore, adhesive shear stress increases with the use of high modulus and thick wrapping sheet.
6. The optimised bond length of the wrap can be evaluated using the method shown in Fig. 4.21. However, too short bonding length may increases the maximum hoop stress in the wrapping sheet.

CHAPTER 5

COMPOSITE BONDED CONCRETE BEAMS

5.1 Experimental Study

5.1.1 Introduction

In this chapter, the mechanical behaviours of concrete beam with and without strengthening by externally bonded glass fibre composite plates are investigated. Rectangular concrete beams were manufactured for standard three point bending test. Notches were made in some of the rectangular concrete beams with notch-to-depth ratio of 0.2 in tension surface. This functions to simulate damaged structure for later repair process.

Five different types of beam configurations were tested in present study, which include (1) plain concrete beam, (2) notched concrete beam, (3) plain concrete beam with externally bonded glass fibre composite, (4) notched concrete beam with pre-filled epoxy resin inside the notch, and (5) same as (4) with strengthening by glass fibre composite. All the beams were then subjected to three point bending test in order to investigate their mechanical responses after strengthening.

5.1.2 Specimen Fabrication and Experiment Set-up

Total 54 rectangular concrete beams were made for three point bending test. Three standard size steel moulds were made to manufacture the concrete beams. Releasing agent was applied to all inner surfaces of the steel mould in order to make ease for de-moulding. All moulded concrete beams were removed from the mould after 24 hours and placed inside a temperature controlled water bath as shown in Fig. 3.2 for extra 28 days for curing. Notches were made in some rectangular beams on its tension (bottom) surface by using high speed

cutting disc with a notch-to-depth ratio of 0.2 in order to simulate damaged concrete structure for repair. The width of the notch was 2 mm apart from both inner surfaces. Total three concrete specimens were used for each individual test. The configurations of all testing specimens are summarised in Table 5.1 and the abbreviations of the specimen code are illustrated in Fig. 5.1.

Table 5.1 Descriptions of all testing beams for three point bending test.

Code	Type of concrete specimen	Strengthening status	No. of laminate layer(s)	Descriptions
PC	Plain	None	----	Same as Chapter 3.2.1.3.
PC3L3		Tension surface (pre-cured plate bonding)	3 – 3"	Glass fibre composite plate was fabricated before bonding on the concrete surface.
PC3L6			3 – 6"	
PC3L10			3 – 10"	
PC6L3			6 – 3"	
PC6L6			6 – 6"	
PC6L10			6 – 10"	
PC10L3			10 – 10"	
PC10L6			10 – 10"	
PC10L10			10 – 10"	
PC3L10H		Hand lay-up	3 – 10"	Glass fibre composite laminate was laid up directly on the concrete surface.
NC	Notched	None	----	
NCF		Epoxy filled	----	Epoxy resin was filled inside the notch.
NCF1LT16*		Tension surface	1 – 16"	
NCF2LT16*		Tension surface	2 – 16"	
NCF1LS16-W*		Shear surfaces	1 – 16"	Plates were bonded on whole side surfaces.
NCF2LS16-W*		Shear surfaces	2 – 16"	
NCF6L3FV*		Three faces	6	Plates were bonded on both tension and shear surfaces. The bonding lengths varies with thickness.

* All glass fibre composites were laid-up directly on the concrete surfaces and notches were filled by epoxy resin.

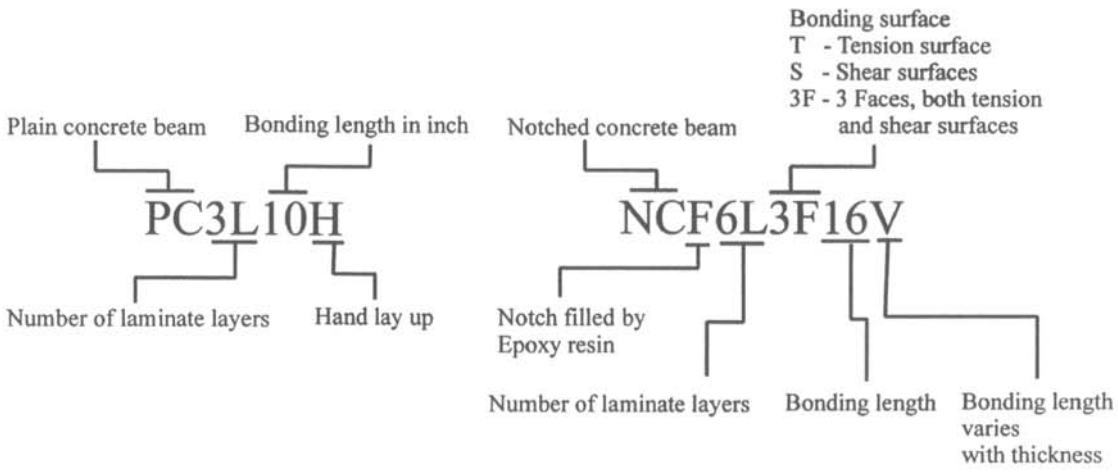

Figure 5.1 Abbreviations of all testing specimen codes.

Experiment set-up for the present study was similar to that the experiment for the plain rectangular concrete beam under three point bending test as mentioned in Chapter 3. The MTS 810 tensile and compression testing machine with pre-installed 100kN load cell was used and the loading rate was set as 0.5 mm/min. Machine was stopped automatically when the strengthened beam was failed. The experiment set-up and schematic illustration for all testing beams are shown in Figs. 5.2 and 5.3.

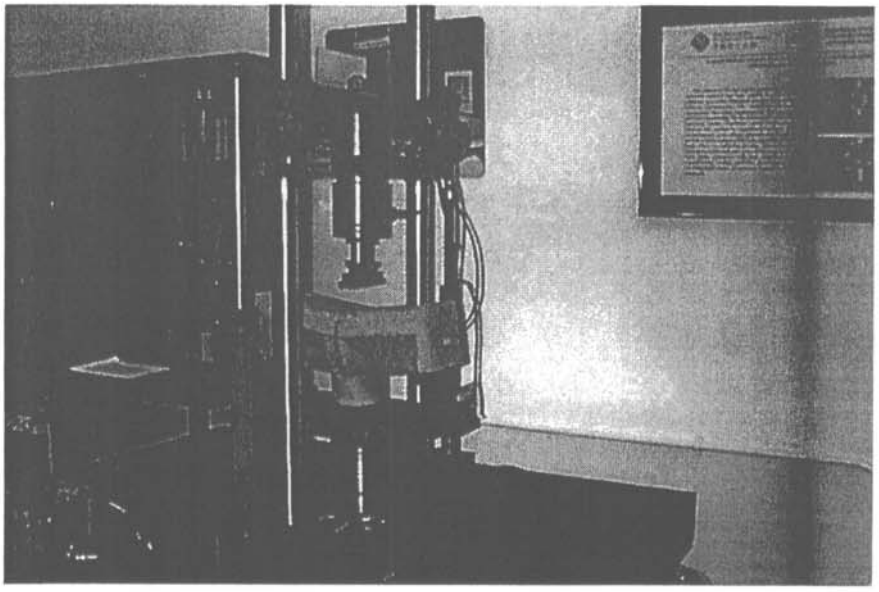

Figure 5.2 MTS 810 tension and compression testing machine with a 100kN load cell.

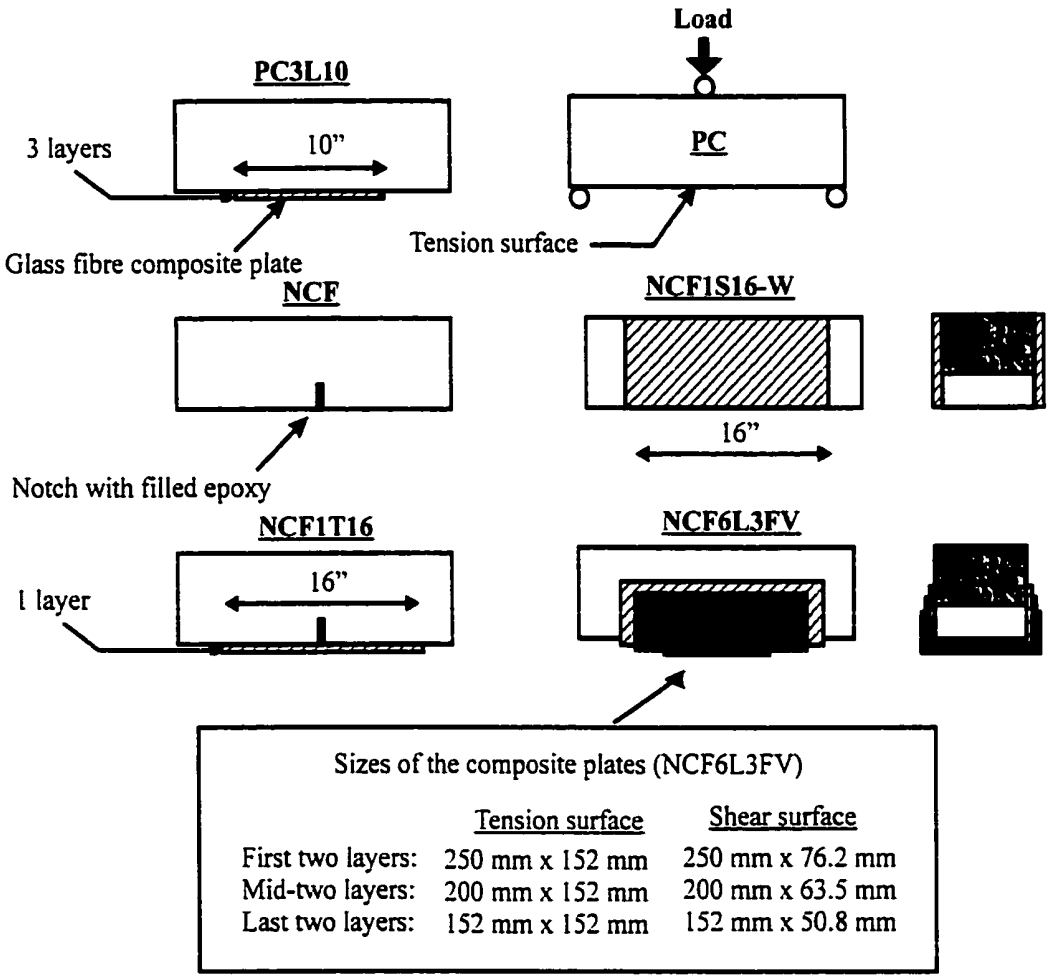

Figure 5.3 A schematic illustration of all testing beams.

All pre-cured glass fibre composite plates were fabricated by using hand lay-up method and then cured by pressure compaction method. Post-curing was used by placing all the plates into oven with temperature setting of 80°C for another 8 hours to ensure strength and quality of the composite. Epoxy adhesive was used to fill the notch of the notched rectangular concrete beams and bond the composite plate on the pre-treated concrete surfaces. All the composite plates were rested for 48 hours for bonding under applied pressure of 5 kPa to ensure uniform adhesive thickness of the resultant strengthening structure. Releasing film was placed between the glass fibre composite and flat compaction platen to avoid bonding between both materials.

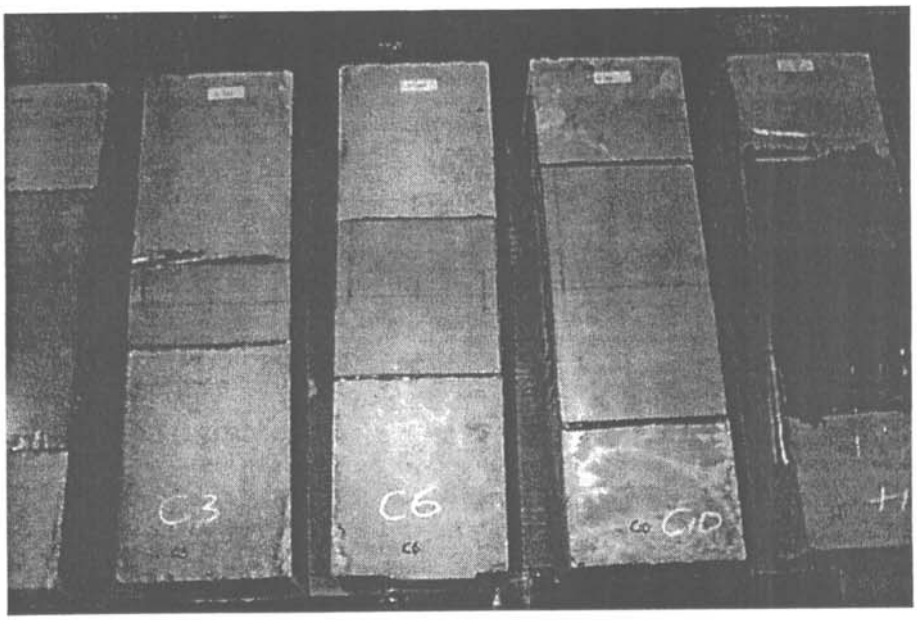

Figure 5.4 The PC10 series specimens before testing.

In Fig. 5.4, the plain concrete beams (PC series) with the externally bonded pre-cured glass fibre composite plates with different bonding lengths are shown. In Fig. 5.5, a notched concrete beam with pre-filled epoxy resin inside the notch is shown. Three point bending test was performed to compare their mechanical responses with the virgin notched beam without strengthening. In the diagram, it is clearly seen that the notch on the top of the rectangular beam was filled by epoxy.

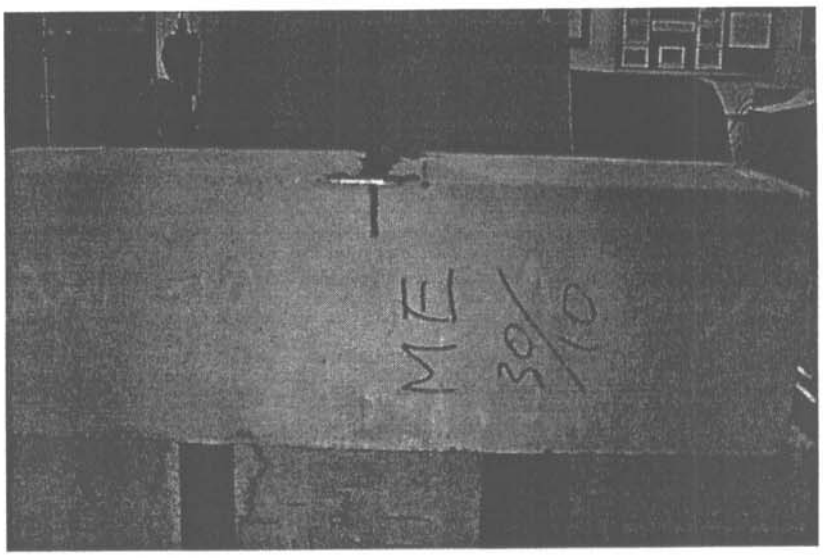

Figure 5.5 Notched rectangular concrete beam with epoxy filled inside the notch.

5.1.3 Results and Discussions

The ultimate flexural loads for all composite strengthened beams are summarised in Table 5.2 and the combined curves (maximum value) are plotted in Figs. 5.6 to 5.9. The results shown in the table are given by the average (mean) values from three similar specimens under the same testing condition.

Table 5.2a The ultimate flexural loads for the plain, notched and epoxy filled notched concrete beams subjected to three point bending test.

Specimen code	Sample 1 (kN)	Sample 2 (kN)	Sample 3 (kN)	Mean value (kN)	S.D. (kN)
PC	21.28	21.4	22.03	21.57	0.42
NC	16.05	17.61	16.65	16.77	0.78
NCF	21.80	21.10	22.2	21.71	0.56

Table 5.2b The ultimate flexural loads for the glass fibre composite strengthened plain concrete beams subjected to three point bending test.

Specimen code	Sample 1 (kN)	Sample 2 (kN)	Sample 3 (kN)	Mean value (kN)	S.D. (kN)
PC3L3	29.4	29.17	29.53	29.4	0.182
PC3L6	33.3	34	33.06	33.45	0.488
PC3L10	33.03	33	34.35	33.46	0.77
PC6L3	35.4	33.2	34.03	34.21	1.11
PC6L6	36.25	34.5	34.36	35.64	1.05
PC6L10	36.768	38.07	36.26	37.1	0.935
PC10L3	33.758	34.5	32.4	33.55	1.06
PC10L6	35.2	34.8	36.3	35.66	1.4
PC10L10	39.5	37.2	36.8	38.2	1.16

Table 5.2c The comparison of the ultimate flexural loads for the plain concrete beams strengthening by glass fibre composite with pre-cured plate bonding and hand lay-up techniques.

Specimen code	Sample 1 (kN)	Sample 2 (kN)	Sample 3 (kN)	Mean value (kN)	S.D. (kN)
PC3L10	33.03	33	34.35	33.46	0.77
PC3L10H	37.13	35.26	33.1	35.16	2.01

Table 5.2d The ultimate flexural loads for the glass fibre composite strengthened notched-concrete beams subjected to three point bending test.

Specimen code	Sample 1 (kN)	Sample 2 (kN)	Sample 3 (kN)	Mean value (kN)	S.D. (kN)
NCF1T16	31.25	32.42	33.15	32.90	0.958
NCF2T16	36.54	35.46	35.68	35.89	0.57
NCF1S16-W	22.36	22.13	20.36	21.91	0.53
NCF2S16-W	22.89	24.15	23.23	23.18	1.46
NCF6L3FV	38.93	39.21	39.00	39.01	0.15

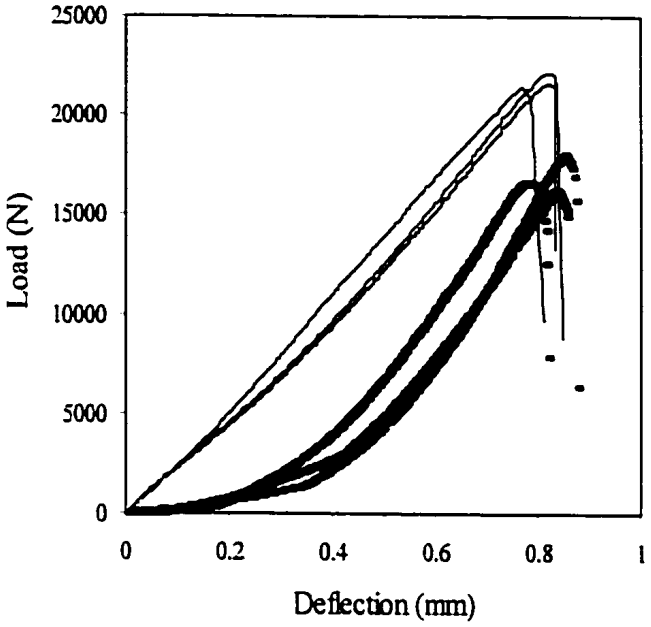

(a)

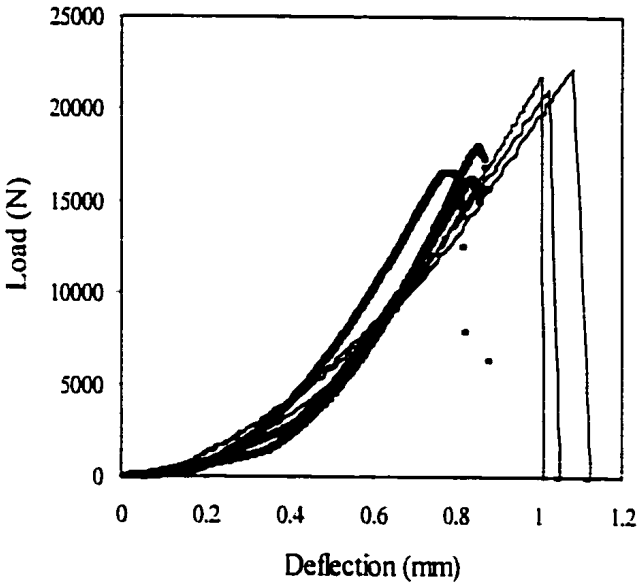

(b)

Figure 5.6 Load-deflection curves extracted from the experiments for the (a) plain and notched concrete beams, and (b) the notched concrete beams with and without filling by epoxy inside the notch.

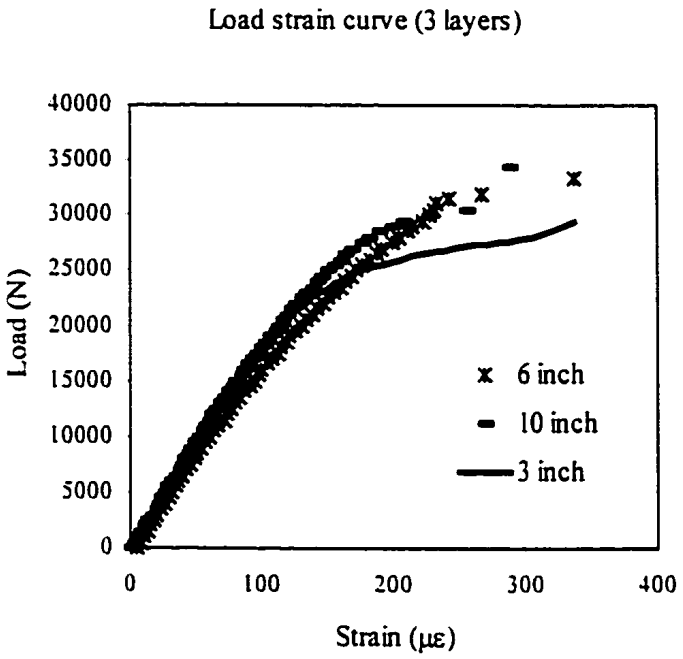
Load strain curve (3 layers)
40000
35000
30000
25000
20000
15000
10000
5000
0
Load (N)
0
100
200
300
400
Strain (με)
6 inch
10 inch
3 inch

(a)

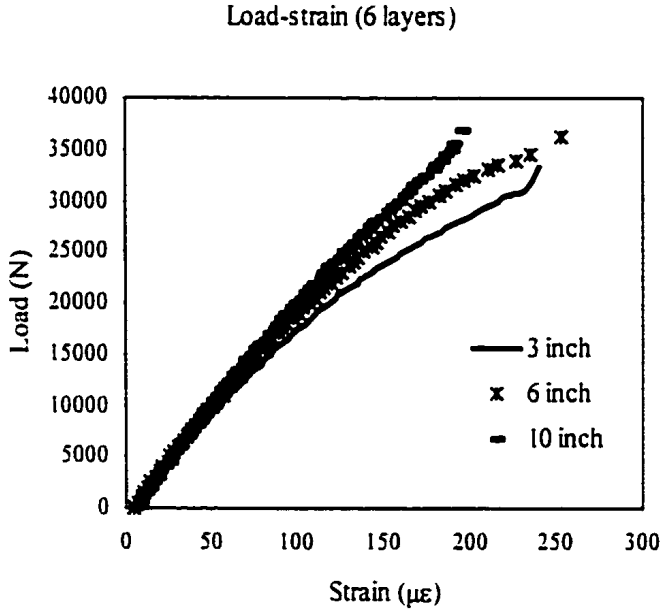
Load-strain (6 layers)
40000
35000
30000
25000
20000
15000
10000
5000
0
Load (N)
0
50
100
150
200
250
300
Strain (με)
3 inch
6 inch
10 inch

(b)

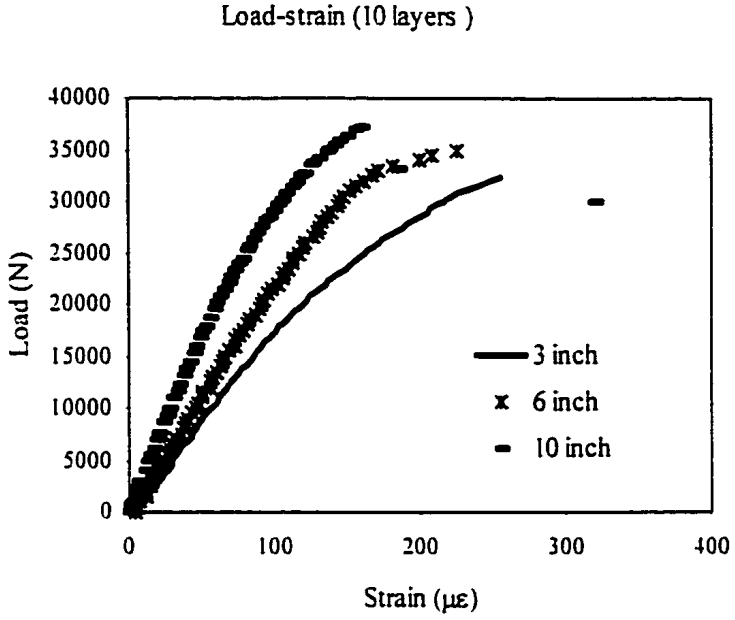

(c)

Figure 5.7 Load-strain (measured at the middle of the beam) curves of the plain concrete beams strengthened by glass fibre composite with different bonding lengths and layers. (a) 3 layers, (b) 6 layers and (c) 10 layers.

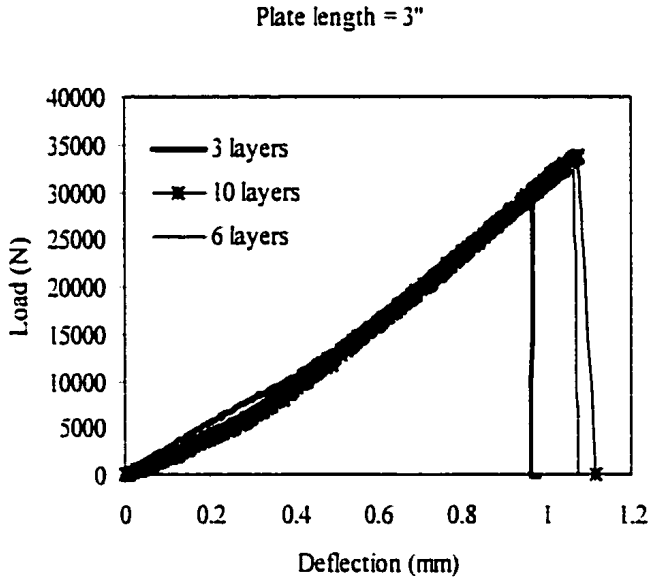

(a)

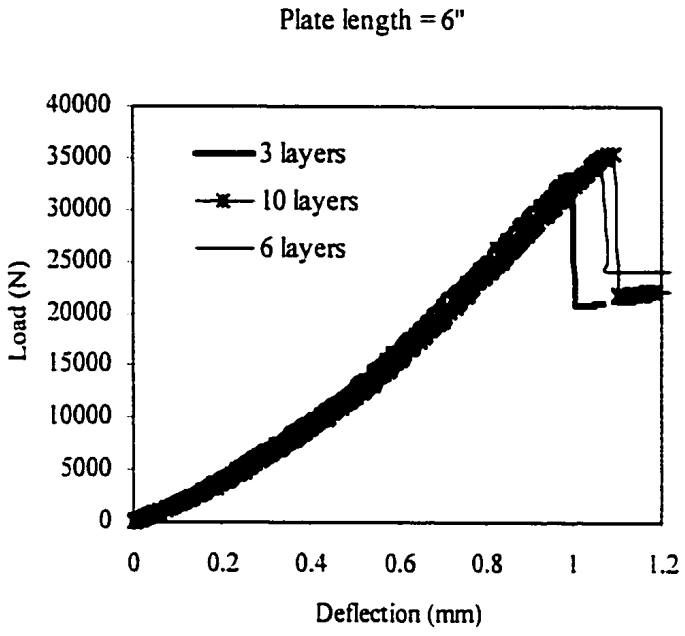

(b)

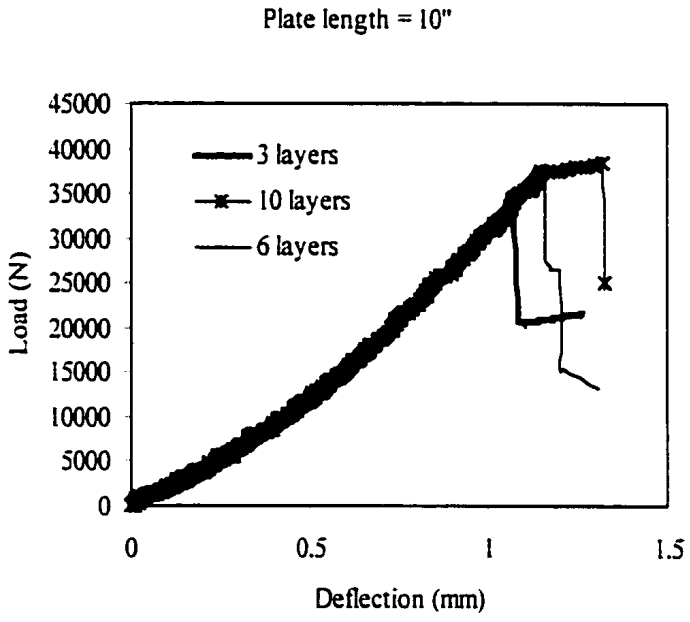

(c)

Figure 5.8 Load-deflection curves of the plain concrete beams strengthened by glass fibre composite with different bonding lengths and number of laminate layers. (a) 3-inches, (b) 6-inches and (c) 10-inches.

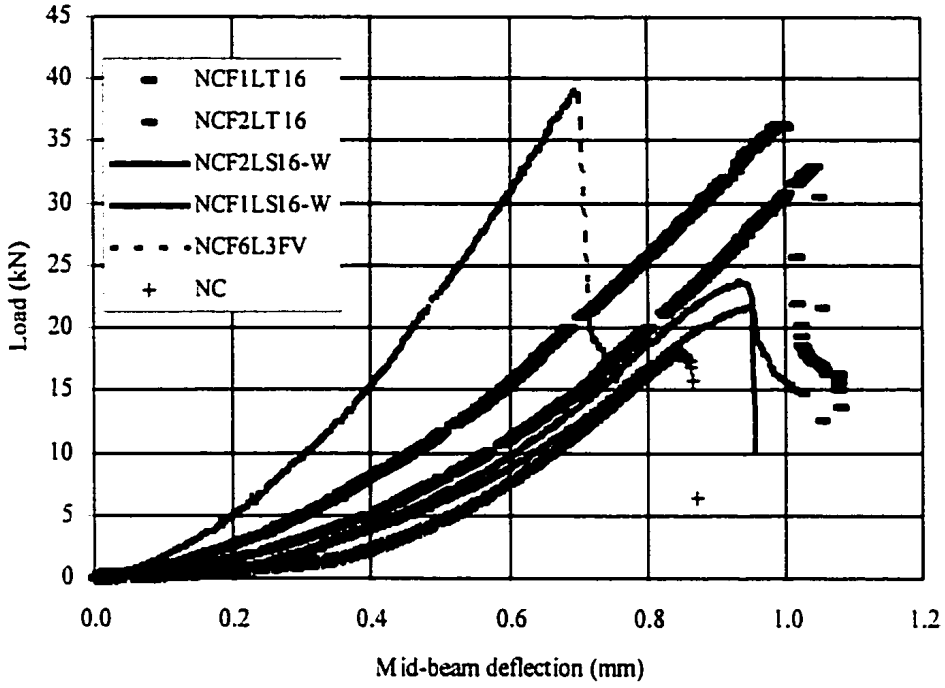

Figure 5.9 Load-deflection curves of the notched concrete beams strengthened by glass fibre composite with different bonding patterns.

According to the results showed in Table 5.2a, it is found that the reduction of the ultimate flexural load of the notched concrete (NC) beam is 22% compared with the plain concrete beam (PC). However, the increase of the ultimate flexural load is 20% if the notch is filled by the epoxy resin. Since the concrete is a low tensile strength material, the filled epoxy resin could sustain tensile stress much higher than that the concrete and therefore prolong the maximum allowable beam deflection as indicated in Fig. 5.6b. In Fig. 5.10, it is clearly showed that the crack of the epoxy filled notched concrete beam was initiated beside the notch region, unlike the notched concrete beam, crack was started at the notch-tip and failed catastrophically. The tensile strengths of the concrete and adhesive materials are about 3 MPa and 90 MPa, respectively.

Fig.5.6 shows that the load-deflection curve for the notched concrete beam is initially in linear fashion with a small slope pattern. The slope then increases when the load reaches approximately 3 kN. In Fig. 5.6b, it is indicated that the epoxy filled notched concrete beam

has higher ultimate flexural load capacity as well as beam deflection compared with the notched beam. The epoxy acted as a strong bonding medium to hold both notch inner surfaces together and restricted the opening action at notch mouth region.

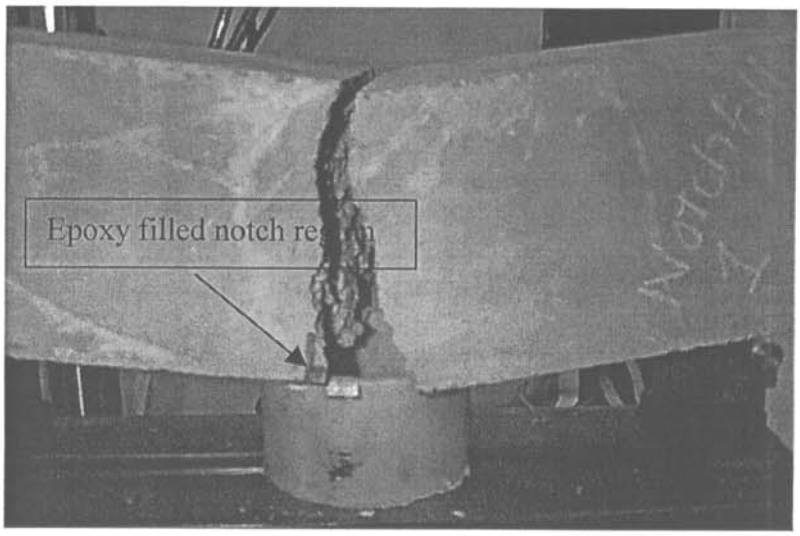

Figure 5.10 Failure pattern of the epoxy filled notched-concrete beam.

In Table 5.2b, the experimental results for the plain concrete beam strengthening by different glass fibre composite layers and bonding lengths are shown. For the beams strengthened by the composite plate with the bonding lengths of 3 inches, the results of the specimens PC3L3, PC6L3 and PC10L3 are not significantly different to each other. It is found during the experiment that the failures of the strengthened beam are dominated by the allowable shear and tensile strengths of the concrete rather than externally bonded composite plate. In Fig. 5.11, a failure mode of the plain concrete beam with the bonding length of 3 inches is shown and a crack was found at the plate end region.

However, for the plain concrete beams with the plate bonding lengths of 6 and 10 inches, the ultimate flexural loads increase with increasing the number of composite layers. The maximum value of 38.2 kN was achieved for the beam with the bonding lengths of 10 inches and bonding layers of 10. For these specimens, they were failed by tension cracking in the concrete within the composite covering regions. Several small cracks were initially appeared on the concrete surface at the mid-beam region. Large cracks were then appeared

at the region closed to the plate end when further applying the load. In Fig. 5.12, the failed specimens for PC6L6 and PC10L10 are shown. The plots of Fig 5.7 clearly show that the beam stiffness after strengthening by externally bonded glass fibre composite increases with increasing the number of bonding layers. However, for the same number of bonding layers with different bonding length, the ultimate flexural load also increases with increasing the bonding lengths of composite plate.

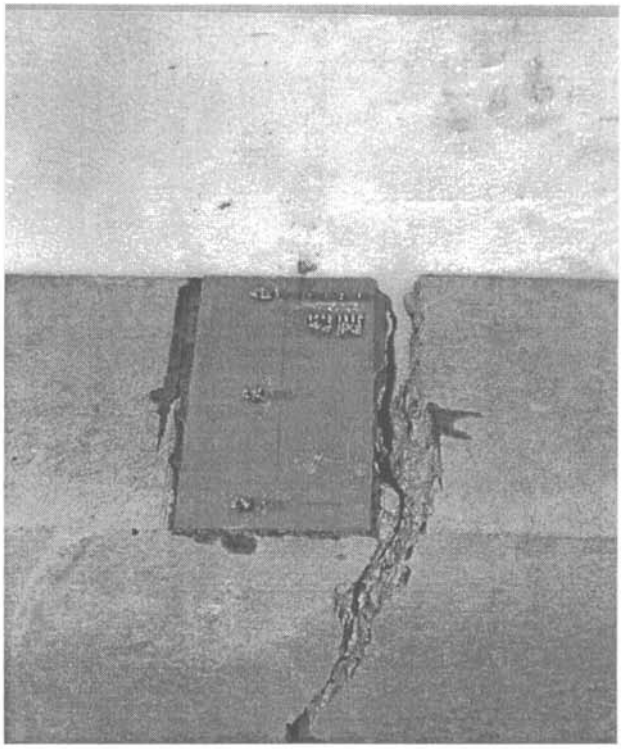

Figure 5.11 Failure pattern of the specimen PC10L3.

In table 5.2c, it is indicated that the hand-lay up method gives better strengthening characteristic in term of the flexural load capacity compared with the specimen, which has a same configuration but the composite plate were bonded by pre-cured plate bonding method. During the bonding process, it was found that part of resin have been absorbed into the concrete by using hand lay-up process. Therefore, it is difficult to control the fibre volume fraction of final finished composite plate.

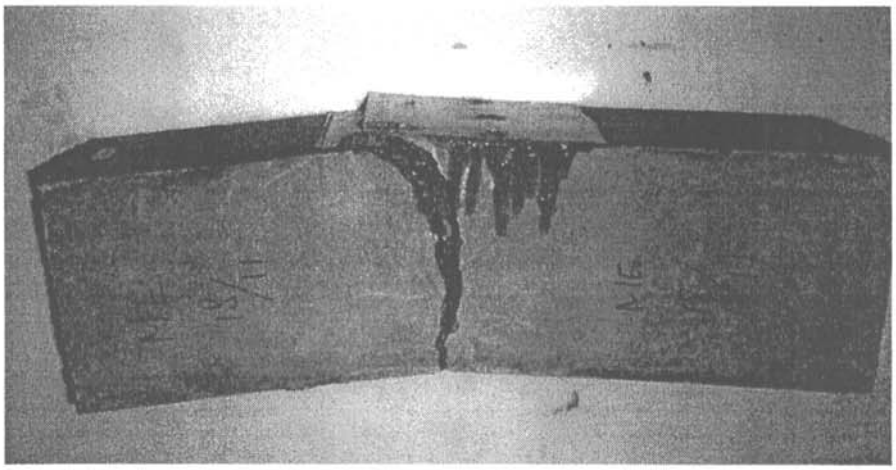

(a)

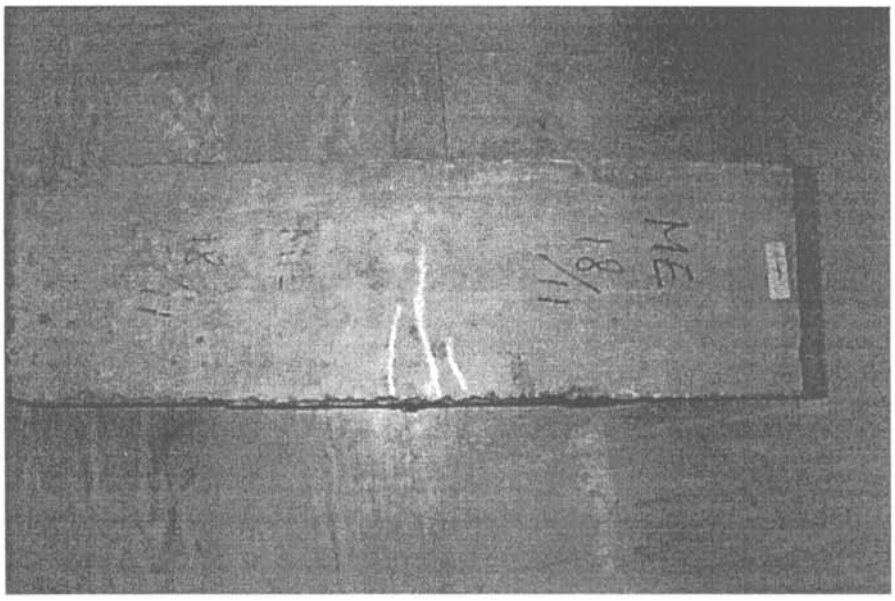

(b)

Figure 5.12 The failed specimens of PC6L6 and PC10L10 after three point bending test. Failure of the specimen of PC6L6 in tensile and shear cracks (a) and many small cracks (white lines) appeared in tension side of the specimen PC10L10 (b) at ultimate flexural load condition.

The pre-cured plate bonding technique could not guarantee the perfect bond between the concrete and the composite plate due to the existence of voids and irregular contour on the concrete surface. However, the hand lay-up technique becomes more applicable since a good bonding in all contact surfaces can be achieved. The composite laminate is able to lay up along the contour of the bonding surface. The failure pattern of the PC3L10 bonded by hand lay-up is shown in Fig. 5.13. Many small cracks appeared on the concrete surface and a longer cracks was found at mid-beam region at ultimate load condition.

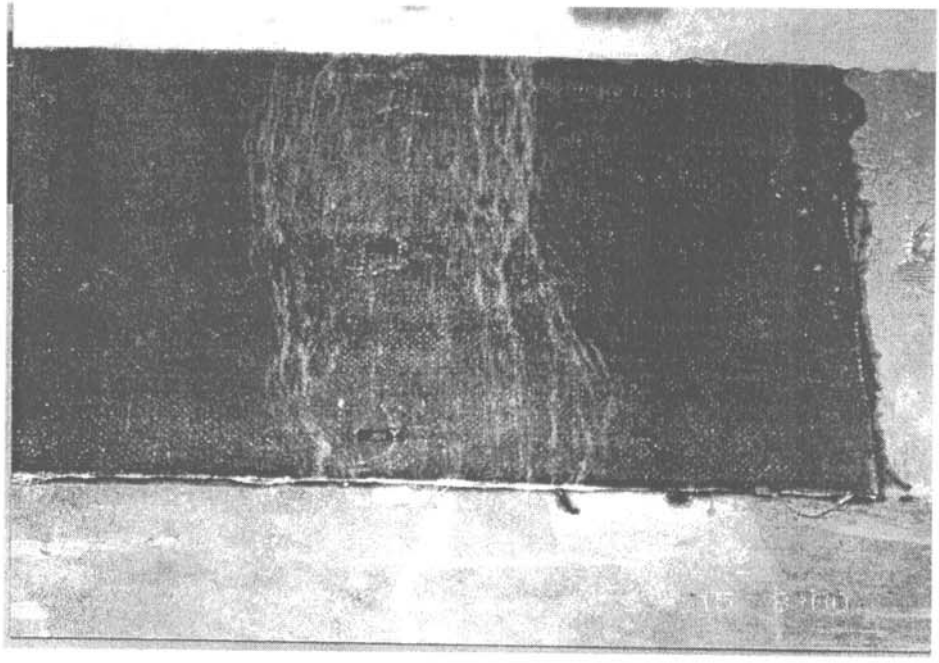

Figure 5.13 Failure pattern of the specimens PL3L10H.

For the composite strengthened notched-concrete beam, the ultimate flexural load increases with the use of externally bonded glass fibre composite. The glass fibre composite laminates were laid–up directly on the concrete surface by hand lay-up method. According to the result shown in Table 5.2d, it is found that the shear surface strengthening method is less significance compared with that by bonding the composite plate on the tension surface.

The percentage increases of the strengthened notched beam compared to the original and notched concrete specimens is listed in Table 5.3.

Table 5.3 Comparison of the results for notched concrete specimens after strengthening by externally bonded glass fibre composite laminates.

Specimen code	Ultimate flexural load (kN)	Percentage increase compared with PC (%)	Percentage increase compared with NC (%)
PC	21.57	0	28.6
NC	16.77	-22.25	0
NCF	21.7	0.61	29.41
NCF1LT16	32.90	52.5	96.18
NCF2LT16	35.89	66.4	214
NCF1LS16-W	21.91	1.57	30.6
NCF2LS16-W	23.08	7.00	35.21
NCF6L3FV	39.01	80.8	232

The failure patterns of all strengthened-notched concrete specimen show that no crack was initiated at the notch-tip. The filled epoxy resin provides a strong bonding between the notch inner surfaces. Cracks were found beside the notch at the failure condition. In Fig. 5.14, a photo for a specimen of NCF1T16 is shown. It is obviously revealed that many small cracks appeared on the tension surface of the concrete and just beside the notch-mouth region. Fig. 5.15 also shows the failure pattern of the specimen of NCF6L3FV. Debond and cracks were not found at the mid-beam region of the strengthened concrete beam. The use of thick composite plate at mid-beam region gave better strengthening characteristic in the concrete beam. However, the failure in peel-off at the plate end region was observed at ultimate load condition.

A plot in Fig. 5.9 shows that the beam stiffness increases with strengthening by the externally bonded composite plates. However, the side bonding technique cannot be effectively used to restore the original strength of the structure after damage.

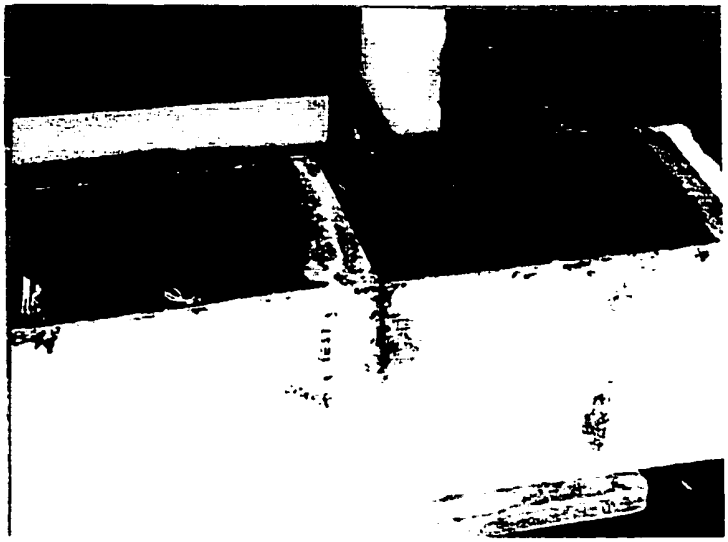

Figure 5.14 Failure pattern of the specimen NCF1T16.

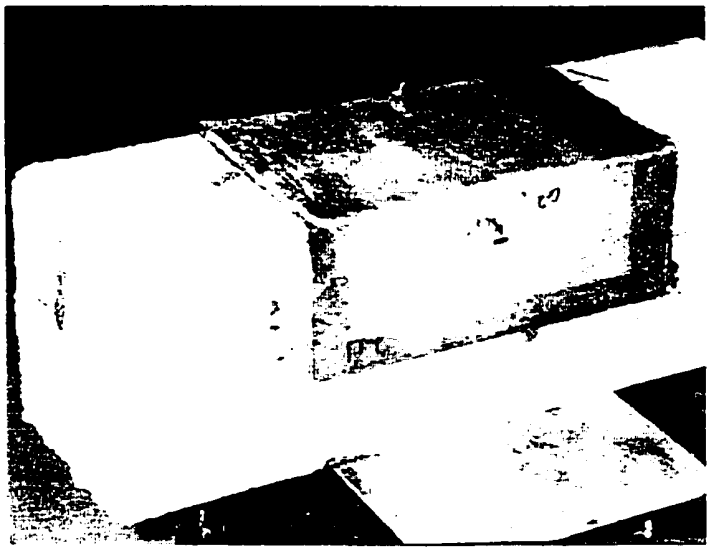

Figure 5.15 Peel-off failure occurred at the plate end region of the specimen NCF6L3FV.

5.2 Theoretical Prediction of the Composite Plate Bonded Beam

5.2.1 Introduction

In the previous section, the mechanical behaviours of the rectangular concrete beam strengthened by composite plate have been discussed according to experimental results. Tension face strengthening method gives better mechanical performance of the concrete beam when the beam is subjected to three-point bending compared with shear surface strengthening method. Since the use of tension face strengthening method becomes an important issue in concrete rehabilitation, a better understanding on the stress transferring mechanism is essential. In this Chapter, a simple theoretical model to estimate shear and peel-off stresses is proposed. Axial stresses in a FRP strengthened concrete beam are considered including the variation in FRP plate fibre orientations, laminate layers and mechanical properties.

The plate bonded method has been well recognised as an effective solution to reinforce and strengthen the concrete beam in order to minimise the risk of concrete cracking, which results the corrosion of embedded steel reinforcement. Eventually, surface concrete spalling may happen due to the volumetric expansion of the corroded steel material. Many researches revealed that the common failure of the plate-bonded concrete is due to the externally bonded plate peel-off and deformation in bending of the plate with using a high modulus material [Triantafillou, 1998]. However, high plate modulus materials are popularly utilised because it can provide a substantial strengthening properties to the structure.

A model, which is used for the present theoretical analysis is shown in Fig.5.16. Several assumptions stated below are to simplify the procedure in calculation. These include:

1. Mechanical properties of all materials involved in present study behave elastically, linearally and isotropically until failure.

2. No slip is allowed at the interface of bond (perfect bond between the composite and concrete).
3. Stresses in the adhesive layer and composite laminate do not change with thickness because both the adhesive and composite materials are very thin.
4. Bending stiffness of the concrete beam that to be strengthened is much greater than the stiffness of the composite plate.

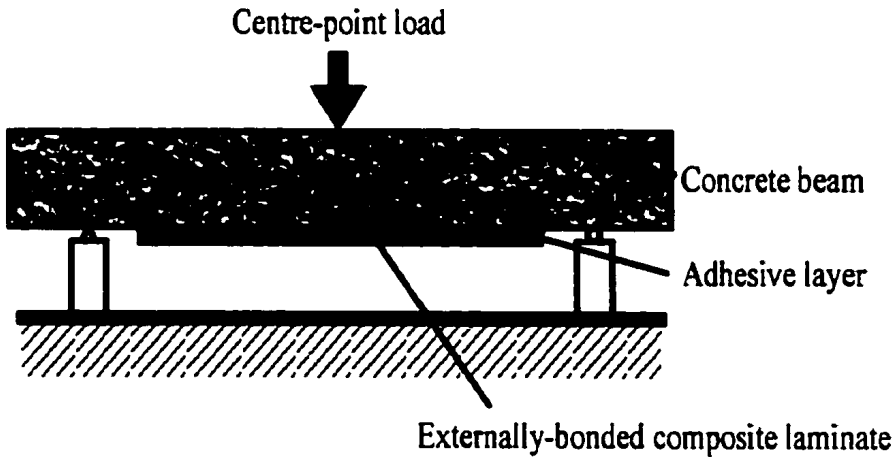

Figure 5.16 Rectangular concrete beam strengthened by externally-bonded composite laminate onto the beam tension surface.

5.2.2 Adhesive Shear Stress

Adhesive shear failure is one of the most common failure patterns that may happen in plate bonded concrete structure as illustrated in Fig. 2.2. Excess of an applied shear stress in the adhesive layer leads to the failure at the interface between the concrete beam and composite, and results in the reduction of effective bonding length of the plate. Fig. 5.17 illustrates the theoretical model for evaluating the adhesive stress transfer properties for current study. From the diagram, the compatibility expression for the shear stress in the adhesive layer at any section x is given by

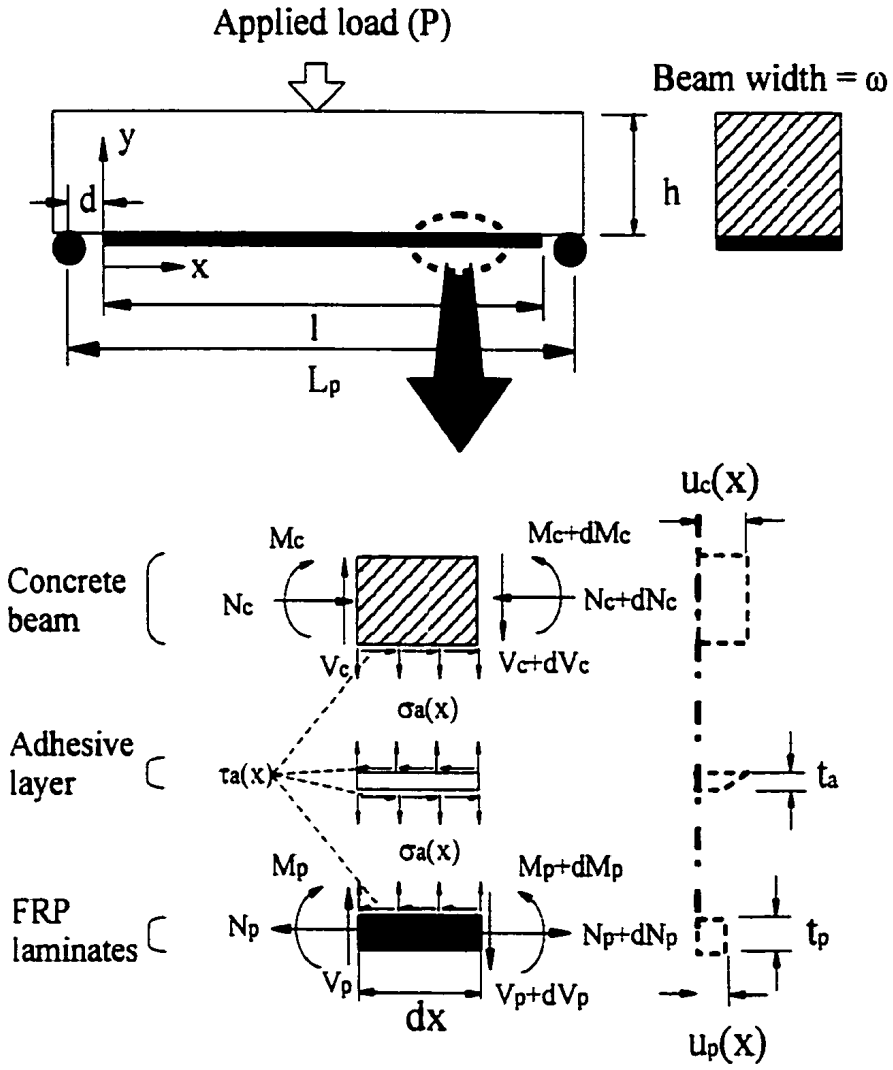

Figure 5.17 A model of the strengthened rectangular beam

$$\tau_a(x) = \frac{G_a}{t_a}\left(u_p(x) - u_c(x)\right) \tag{5.1}$$

where G_a, t_a, u_c and u_p denote shear modulus, thickness of the adhesive material, displacements of the concrete and externally bonded composite plate at the boundary of bond, respectively.

Eq.(5.1) can be expressed in terms of mechanical strains of the concrete, $\varepsilon_c(x)$ and composite plate $\varepsilon_p(x)$ after differentiating with respect to x, i.e.

$$\frac{d\tau_a(x)}{dx} = \frac{G_a}{t_a}\left(\varepsilon_p(x) - \varepsilon_c(x)\right) \tag{5.2}$$

where

$$\frac{du_c(x)}{dx} = \varepsilon_c(x) \quad \text{and} \quad \frac{du_p(x)}{dx} = \varepsilon_p(x) \tag{5.3a,b}$$

The tensile strain at the bottom of the beam is induced by two basic stress components including (1) tensile stress induced by the bending moment, $M_c(x)$ in the beam and (2) axial stress induced by the adhesive shear stress, $N_c(x)$ at the bond interface. Therefore, Eqs. (5.3a) and (5.3b) can be written as

$$\varepsilon_c(x) = \frac{1}{E_c \omega h^2}\left(6M_c(x) - N_c(x)h\right). \tag{5.4}$$

and

$$\varepsilon_p(x) = \frac{N_p(x)}{\omega t_p E_{eff}} \tag{5.5}$$

where, t_p and E_{eff} represent the thickness and effective modulus of the composite plate. Since the composite laminate is an orthotropic material, its material properties are varied from layer to layer. In current study, the laminate theory is used to determine the stress and strain behaviours of the externally bonded composite plate in order to investigate the whole mechanical performance of the composite strengthened structure. Since the effective modulus of the composite laminate vary with the orientation of the fibre directions and arrangements of the laminate patterns, Eq.(5.5) is only valid for the plate in which the mechanical properties behave iso-tropically and homogeneously. Therefore, the laminate theory is used to estimate the strain of the composite plate [Hyer 1998], i.e.

$$\begin{Bmatrix} \varepsilon^o \\ M \end{Bmatrix} = \begin{bmatrix} A^x & B^x \\ C^x & D^x \end{bmatrix} \begin{Bmatrix} N \\ k \end{Bmatrix} \tag{5.6}$$

where

$[A^x]$: $[A^{-1}]$

$[B^x]$: $[A^{-1}][B]$

$[C^x]$: $[B][A^{-1}]$

$[D^x]$: $[D]-[B][A^{-1}][B]$

and

$$A_{ij} = \sum_{k=1}^{n} \left(\bar{Q}_{ij} \right)_k (z_k - z_{k-1}), \qquad \text{Extensional matrix (5.6a)}$$

$$B_{ij} = \frac{1}{2} \sum_{k=1}^{n} \left(\bar{Q}_{ij} \right)_k \left({z_k}^2 - {z^2}_{k-1} \right), \qquad \text{Extensional-bending coupled matrix (5.6b)}$$

$$D_{ij} = \frac{1}{3} \sum_{k=1}^{n} \left(\bar{Q}_{ij} \right)_k \left({z_k}^3 - {z^3}_{k-1} \right). \qquad \text{Flexural matrix (5.6c)}$$

Subscription *n* represents a number of laminate layers of the FRP plate. Parameter $\bar{Q}_{ij}$ can be estimated by using the off-axis orthotropic ply theory. A schematic diagram in illustrating the laminate theory for composite plate is shown in Fig. 5.18. By assuming that the ply arrangement of the plate is symmetrical with respect to the mid-plane axis z=0, a great simplification in laminate analysis occurs by assuming the coupling matrix, B is identically zero [RMIT 1996]. Furthermore, it is assumed that no external bending moment is applied to the plate. Eq.(5.6) is therefore simplified to the following matrix form for the plate with a width of ω:

$$\{\varepsilon^o\} = [A^x]\{N\}_p \tag{5.7}$$

where

$$\{\varepsilon_o\} = \begin{Bmatrix} \varepsilon_x \\ \varepsilon_y \\ \varepsilon_{xy} \end{Bmatrix} \quad \text{and} \quad \{N\}_p = \begin{Bmatrix} N_x \\ N_y \\ N_{xy} \end{Bmatrix}_p \tag{5.8}$$

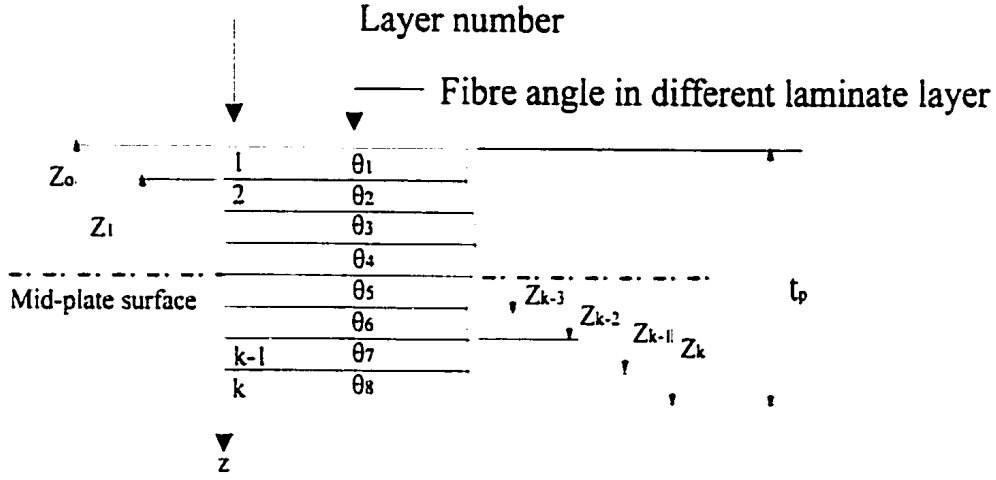

Geometry of an N-layered of FRP laminate

Figure 5.18 Multi-layered laminate geometry

In the present study, only an axial load in the beam longitudinal axis is considered, i.e. $N_y = N_{xy} = 0$. Therefore, Eq.(5.7) can then be simplified to

$$\varepsilon_p(x) = A_{11}^{\varepsilon} N_{\varepsilon} \frac{1}{\omega} \tag{5.9}$$

Differentiating the Eq.(5.2) again by considering the strains given by Eqs.(5.4) and (5.9) gives

$$\frac{d\tau_a^2(x)}{dx^2} = \frac{G_a}{t_a}\left[\frac{A_{11}^{\varepsilon}}{\omega}\frac{dN_p(x)}{dx} - \left(\frac{6}{\omega h^2}\frac{dM_c(x)}{dx} - \frac{1}{\omega h^2}\frac{dN_c(x)}{dx}\right)\right] \tag{5.10}$$

The bending moment in the beam, $M_c(x)$ is determined by the sum of an external applied moment due to the centre load, P and a moment induced by the adhesive shear force:

$$dM_c(x) = R_b dx - \tau_a(x)\omega dx \frac{h}{2} \tag{5.11}$$

where R_b is the reaction force at the support. For a three point bending case, $R_b = P/2$. The axial load applied in the concrete is

$$dN_c(x) = \tau_a(x)\omega dx \tag{5.12a}$$

The magnitude of the tensile stress of the composite plate is determined by the amount of adhesive shear stress transfer from the concrete beam to the externally bonded plate, i.e.

$$dN_p(x) = \tau_a(x)\omega dx \tag{5.12b}$$

By substituting Eqns (5.11) and (5.12) into (5.10), a following equation is obtained:

$$\frac{d^2\tau_a(x)}{dx^2} = \frac{G_a\omega}{t_a}\left(\frac{A_{11}^{\varepsilon}}{\omega} + \frac{4}{\omega h E_c}\right)\tau_a(x) - \frac{6R_b G_a}{E_c \omega h^2 t_a} \tag{5.13}$$

The mathematical solution for the Eqn.(5.13) is

$$\tau_a(x) = C_1 \cosh(\beta x) + C_2 \sinh(\beta x) + \eta_a \tag{5.14}$$

where

$$\beta = \sqrt{\frac{G_a\omega}{t_a}\left(\frac{A_{11}^{\varepsilon}}{\omega} + \frac{4}{\omega h E_c}\right)} \tag{5.15a}$$

and

$$\eta_a = \frac{6R_b G_a}{E_c \omega h^2 t_a \beta^2}. \tag{5.15b}$$

C_1 and C_2 are arbitrary constants, which are determined by using appropriate boundary conditions. The first and second derivatives of Eq. (5.14) with respect to x are given by

$$\frac{d\tau_a(x)}{dx} = C_1 \beta \sinh(\beta x) + C_2 \beta \cosh(\beta x) \tag{5.16}$$

$$\frac{d^2\tau_a(x)}{dx^2} = C_1 \beta^2 \cosh(\beta x) + C_2 \beta^2 \sinh(\beta x). \tag{5.17}$$

For the three-point bending test model, it is shown that there is no axial component force, which is induced by the adhesive shear stress as indicated in Eq.(5.13) in beam longitudinal direction at z=0 in the concrete and composite plate, i.e. $N_p(0) = N_c(0) = 0$. However the bending moment, M_c at the plate end region is equal to the vertical reaction force, R_b at the support multiplied by the distance measured from the support to the plate end, d. By considering the first boundary condition, the first derivative of the Eq.(5.2) is obtained:

$$\frac{d\tau_a(x)}{dx} = \frac{G_a}{t_a}\left[\frac{A_{11}{}^x}{\omega} N_p(0) - \frac{1}{E_c}\left(\frac{6}{\omega h^2} M_c(0) - \frac{1}{\omega h} N_c(0)\right)\right]$$

$$= C_1 \beta \sinh(\beta \cdot 0) + C_2 \beta \cosh(\beta \cdot 0) \tag{5.18a,b}$$

and the coefficient C_2 is given by

$$C_2 = -\frac{6G_a R_b d}{E_c t_a \omega h^2 \beta} \tag{5.19}$$

Since the model being symmetrical about middle-axis of the beam, the adhesive shear stress. $\tau_a(x)$ is theoretically equal to zero when $x=l/2$. Therefore, the second boundary condition is given by:

$$\tau_a\left(\frac{l}{2}\right)=0. \tag{5.20}$$

From Eq.(5.14), it is obtained that

$$C_1\cosh\left(\beta\frac{l}{2}\right)+C_2\sinh\left(\beta\frac{l}{2}\right)+\eta_o=0 \tag{5.21}$$

and therefore

$$C_1+C_2\tanh\left(\beta\frac{l}{2}\right)-\frac{\eta_o}{\cosh\left(\beta\frac{l}{2}\right)}=0. \tag{5.22}$$

Since the third terms in Eq.(5.22) can be neglected (≈ 0), the coefficient C_1 is given by

$$C_1=\frac{6G_aR_bd}{E_ct_a\omega h^2\beta}\tanh\left(\frac{\beta l}{2}\right). \tag{5.23}$$

Hence, the full equation of the adhesive shear stress distribution along the bond line measured from the plate end (x=0) can be written as

$$\tau_a(x)=\frac{6G_aR_bd}{E_ct_a\omega h^2\beta}\tanh\left(\frac{\beta l}{2}\right)(\cosh(\beta x)-\sinh(\beta x))+\eta_a. \tag{5.24}$$

The parabolic functions of cosh(βx) and sinh(βx) can be expressed in exponential forms:

$$\cosh(\beta x)=\frac{e^{\beta x}+e^{-\beta x}}{2} \tag{5.25a}$$

and $$\sinh(\beta x)=\frac{e^{\beta x}-e^{-\beta x}}{2}. \tag{5.25b}$$

Therefore, Eq.(5.24) can be simplified to

$$\tau_a(x)=\frac{6G_aR_bd}{E_ct_a\omega h^2\beta}\tanh\left(\frac{\beta l}{2}\right)e^{-\beta x}+\eta_o \tag{5.26}$$

The axial force in the composite plate in the beam direction, $N_p(x)$ can be determined by integrating the Eq.(5.12b) with the substitution of Eq.(5.26). The same boundary condition is used at the plate end region, i.e. $N_p(0) = 0$, it results:

$$N_p(x)=\frac{6G_aR_bd}{E_ct_a\omega h^2\beta}\tanh\left(\frac{\beta l}{2}\right)\left(\frac{\omega}{\beta}\left(1-e^{-\beta x}\right)+\frac{\omega}{d\beta}x\right). \tag{5.27}$$

In general, the maximum adhesive shear stress is located at the short end (x=0) of the externally bonded composite plate while the maximum tensile load added on the plate is located at the middle of the beam (x=l/2) region. It is then possible to write the Eq.(5.26) and (5.27) when they achieve the ultimate stress and load conditions as

$$\tau_{a,\max}=\frac{6G_aR_bd}{E_ct_a\omega h^2\beta}\tanh\left(\frac{\beta l}{2}\right)+\eta_o \tag{5.28a}$$

$$N_{p,\max}=\frac{6G_aR_bd}{E_ct_ah^2\beta^2}\tanh\left(\frac{\beta l}{2}\right)\left(1+\frac{l}{2d}\right). \tag{5.28b}$$

Eq.(5.28) shows that the maximum adhesive shear stress is only dependent on the coefficient of C_1. It means that the shear stress increases with increasing the shear modulus and decreasing the thickness of the adhesive material.

5.2.3 Adhesive Peel-off Stress

Peel-off is another popular mode of failures for the externally plate bonded concrete structure when it is subjected to bending. Therefore, in-depth investigation on the mechanical performance, particularly for the adhesive peel-off stress of the plate-bonded structure is essential.

The peel-off stress in the adhesive layer at any section of x can be simply defined as:

$$\sigma_a^z(x) = E_a \frac{v_p^z(x) - v_c^z(x)}{t_a} \tag{5.29}$$

where σ_a^z, E_a and v represent peel-off stress and tensile modulus of the adhesive material, and the deformation of material in z direction. Subscripts p, c and a denote the externally bonded FRP plate, concrete and adhesive materials, respectively. Super-subscript z represents the direction of deformation. The bending moment in a small element of the externally bonded plate with a length and thickness of dx and t_a as showed in Fig.5.19 is given by:

$$dM_p(x) = V_p^z(x)dx - \tau_a(x)\omega\frac{t_p}{2}dx \tag{5.30}$$

where $V_p^z(x)$ is a shear force, which is measured from the shear force diagram as indicated in Fig. 5.20 of the externally bonded plate at any section of x. Differentiating Eq.(5.30) yields

$$\frac{d^2M_p(x)}{dx^2} = \frac{dV_p^z(x)}{dx} - \frac{d\tau_a(x)}{dx}\frac{t_p}{2}\omega. \tag{5.31}$$

By considering force equilibrium condition, the shear force, $V_p^z(x)$ at a small element shown in Fig. 5.20 is determined by

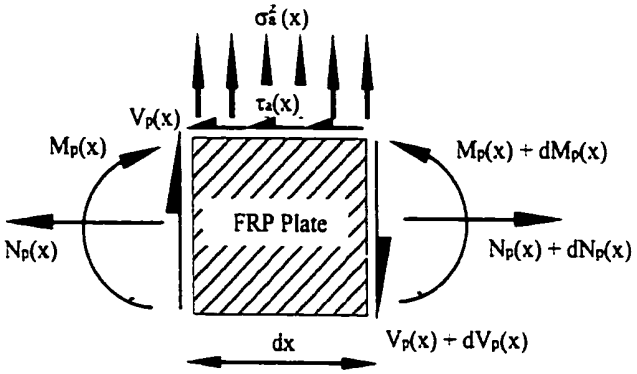

Figure. 5.19 A small element of FRP plate with a length of dx.

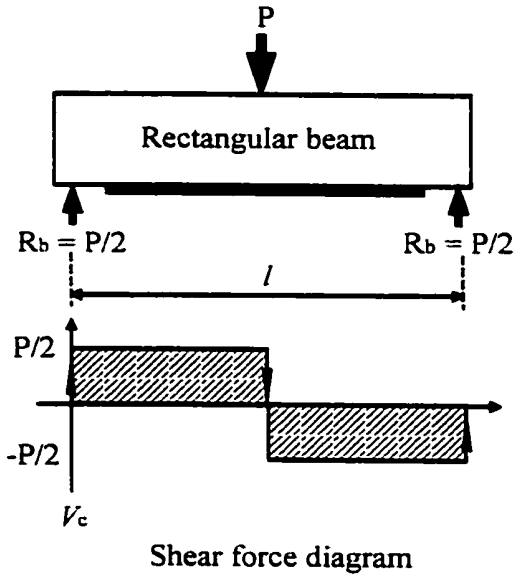

Figure 5.20. The shear force diagram of rectangular beam subjected to three point bending.

$$dV_p^z(x) = \sigma_a^z(x)\omega dx . \tag{5.32}$$

Then, the Eq.(5.31) can be rewritten as following form:

$$\frac{d^2M_p(x)}{dx^2} = \sigma_a^z(x)\omega - \frac{d\tau_a(x)}{dx}\frac{\omega t_p}{2}. \tag{5.33}$$

The second derivatives of the bending moment of the FRP plate can be expressed as

$$\frac{d^2 M_p(x)}{dx^2} = -\frac{d^4 v_p^z(x)}{dx^4} E_{eff} I_p \tag{5.34a}$$

where

$$E_{eff} = \frac{1}{\omega t_p A_{11}^{-1}}. \tag{5.34b}$$

By considering condition Eq.(5.29), Eq.(5.33) can then be expressed as

$$\frac{d^4 v_p^z(x)}{dx^4} \frac{I_p}{t_p \omega A_{11}^{-1}} + \frac{E_a \omega}{t_a} v_p^z(x) = \frac{E_a \omega}{t_a} v_c^z(x) + \frac{d\tau_a(x)}{dx} \frac{\omega t_p}{2}. \tag{5.35}$$

By substituting the first derivative of the shear stress function in Eq.(5.26) into Eq.(5.35), the Eq.(5.35) can be simplified to the following form:

$$\frac{d^4 v_p^z(x)}{dx^4} + 4\lambda^4 v_p^z(x) = 4\lambda^4 v_c^z(x) - \frac{C_1 \beta (\omega t_p)^2 e^{-\beta x} A_{11}^{-1}}{2 I_p} \tag{5.36}$$

where

$$\lambda^4 = \frac{1}{4}\left\{\frac{E_a \omega^2 t_p A_{11}^{-1}}{I_p t_a}\right\} \tag{5.37}$$

For the concrete beam, the axial deflection of the concrete in z-direction can be evaluated in term of its internal bending moment, $M_c(x)$ at any section of x:

$$v_c^z(x) = -\frac{1}{E_c I_c} \iint M_c(x) dx \cdot dx \tag{5.38}$$

and the bending moment in the concrete is

$$M_c(x) = \iint \left(R_b - \tau_a(x)\frac{\omega h}{2} \right) \cdot dx . \tag{5.39}$$

By substituting Eq.(5.26) into Eq.(5.39), we obtain

$$M_c(x) = R_b x + \frac{1}{\beta} C_1 e^{-\beta x} - \eta_a x + D \tag{5.40}$$

where D is a arbitrary constant, which can be determined by using a appropriate boundary condition. At the plate end region, x=0, the bending moment in the concrete beam is $M_c(0) = R_b d$. Then, the constant D is given by

$$D = R_b d - \frac{\omega h C_1}{2\beta} . \tag{5.41}$$

Eq.(5.38) can be written as

$$v_c''(x) = -\frac{1}{E_c I_c} \left\{ \frac{1}{6} R_b x^3 + \frac{\omega h}{2\beta^3} C_1 e^{-\beta x} - \frac{\omega h}{12} \eta_a x^3 + \frac{1}{2} D x^2 + F x + G \right\} \tag{5.42}$$

where F and G are arbitrary constants. Two boundary conditions are used to solve the constants, F and G:

$$v_c''(-d) = 0 \tag{5.43a}$$

and

$$v_c''(0) = -\frac{R_b \left(3l^2 d - 4d^3 \right)}{24 E_c I_c} . \tag{5.43b}$$

The constants F and G are obtained as

$$F = -\frac{1}{d}\left\{\frac{1}{6}R_b d^3 - \frac{\omega h}{2\beta^3}C_1 e^{\beta d} - \frac{\omega h}{12}\eta_o d^3 - \frac{1}{2}Dd^2 - G\right\} \tag{5.44a}$$

and

$$G = \frac{R_b\left(3l^2 d - 4d^3\right)}{24} + \frac{\omega h}{2\beta^3}C_1 . \tag{5.44b}$$

By substituting Eqs.(5.42) and (5.44) into the R.H.S. of Eq.(5.36), the R.H.S. of the Eq. (5.36) can be rewritten as

$$4\lambda^4 v_c^*(x) - \frac{C_1\beta\left(\omega t_p\right)^2 e^{-\beta x} A_{11}^{-1}}{2I_p} = v_o(x). \tag{5.45}$$

where

$$v_o(x) = 4\lambda^4 \xi_{v1}(x) + 4\lambda^4 \xi_{v2} e^{-\beta x} + \xi_{v3} e^{-\beta x} \tag{5.46}$$

and

$$\xi_{v1}(x) = -\frac{1}{E_c I_c}\left(\frac{1}{6}R_b x^3 - \frac{\omega h}{12}\eta_o x^3 + \frac{1}{2}Dx^2 + Fx + G\right) \tag{5.47a}$$

$$\xi_{v2} = -\frac{1}{E_c I_c}\left(\frac{\omega h}{2\beta^3}C_1\right) \tag{5.47b}$$

$$\xi_{v3} = -\frac{C_1\beta\left(\omega t_p\right)^2 A_{11}^{-1}}{2I_p} . \tag{5.47c}$$

A coefficient of C_1 is given by Eq. (5.23). The Eq.(5.36) can then be shortened as

$$\frac{d^4 v_p^z(x)}{dx^4} + 4\lambda^4 v_p^z(x) = v_o(x). \tag{5.48}$$

The solution of Eq.(5.48) is

$$v_p^z(x) = H_1 e^{-\lambda x}\cos(\lambda x) + H_2 e^{-\lambda x}\sin(\lambda x) + v_\lambda(x). \tag{5.49}$$

where v_λ can be determined by substituting all derivatives of Eq.(5.49) into Eq.(5.48), i.e.

$$\frac{dv_p^z(x)}{dx} = H_1\left\{-\lambda e^{-\lambda x}(C_{\lambda x} + S_{\lambda x})\right\} - H_2\left\{\lambda e^{-\lambda x}(S_{\lambda x} - C_{\lambda x})\right\} + \frac{dv_\lambda(x)}{dx}$$

$$\frac{d^2 v_p^z(x)}{dx^2} = 2H_1\lambda^2 e^{-\lambda x}S_{\lambda x} - 2H_2\lambda^2 e^{-\lambda x}C_{\lambda x} + \frac{d^2 v_\lambda(x)}{dx^2}$$

$$\frac{d^3 v_p^z(x)}{dx^3} = 2H_1\lambda^3 e^{-\lambda x}(C_{\lambda x} - S_{\lambda x}) + 2H_2\lambda^2 e^{-\lambda x}(C_{\lambda x} + S_{\lambda x}) + \frac{d^3 v_\lambda(x)}{dx^3}$$

$$\frac{d^4 v_p^z(x)}{dx^4} = -4H_1\lambda^4 e^{-\lambda x}C_{\lambda x} - 4H_2\lambda^4 e^{-\lambda x}S_{\lambda x} + \frac{d^4 v_\lambda(x)}{dx^4} \tag{5.50 a-d}$$

where

$$C_{\lambda x} = \cos(\lambda x) \quad \text{and} \quad S_{\lambda x} = \sin(\lambda x). \tag{5.51}$$

Let $v_\lambda(x)$ is written as the following form:

$$v_\lambda(x) = K_1\xi_{v1}(x) + K_2\xi_{v2}e^{-\beta x} + K_3\xi_{v3}e^{-\beta x}. \tag{5.52}$$

A solution of the forth derivative of the Eq.(5.52) becomes

$$\frac{d^4 v_\lambda(x)}{dx^4} = K_2 \beta \xi_{v2} e^{-\beta x} + K_3 \beta^4 \xi_{v3} e^{-\beta x}. \tag{5.53}$$

Substituting Eqs.(5.50a-d) into Eq.(5.48) and comparing to the Eq.(5.46) give:

$$K_2\left(\lambda^4 \xi_{v2} e^{-\beta x} + \beta^4 \xi_{v2} e^{-\beta x}\right) + K_3\left(4\lambda^4 \xi_{v3} e^{-\beta x} + \beta^4 \xi_{v3} e^{-\beta x}\right) = 4\lambda^4 \xi_{v2} e^{-\beta x} + \xi_{v3} e^{-\beta x} \tag{5.54}$$

and therefore, the coefficients K_1. K_2 and K_3 are obtained as

$$K_1 = 1; \quad K_2 = \frac{4\lambda^4}{4\lambda^4 + \beta^4} \quad \text{and} \quad K_3 = \frac{1}{4\lambda^4 + \beta^4}. \tag{5.55}$$

The function of $v_\lambda(x)$ is then obtained as follows

$$v_\lambda(x) = -\frac{1}{E_c I_c}\left(\frac{1}{6} R_b x^3 - \frac{\omega h}{12}\eta_o x^3 + \frac{1}{2} D x^2 + F x + G\right) - \frac{4\lambda^4}{4\lambda^4 + \beta^4}\frac{1}{E_c I_c}\left(\frac{\omega h}{2\beta^3} C_1\right) e^{-\beta x}$$
$$- \frac{1}{4\lambda^4 + \beta^4}\frac{C_1 \beta (\omega t_p)^2 A_{11}^{-1}}{2 I_p} e^{-\beta x} \tag{5.56}$$

To solve Eq.(5.49), another two boundary conditions are required. Since the bending moment at the plate end region, x=0 is theoretically equal to zero, then

$$\frac{d^2 v_p^{=}(x)}{dx^2} E_c I_c = -M_P(x)\big|_{x=0} = 0 \tag{5.57}$$

and the shear force, $V_p(x)$ is assumed to be zero when x<0, and the shear stress in the bond line is assumed to reach its maximum value when x=0. The magnitude of this force can then be calculated from Eq.(5.30), since

$$\frac{d^3 v_p^z(x)}{dx^3} = \frac{\omega t_p A_{11}^{-1}}{I_p} \frac{dM_p(x)}{dx}\bigg|_{x=0} = -\frac{(\omega t_p)^2 A_{11}^{-1}}{2I_p} \tau_{a,\max}\bigg|_{x=0} . \tag{5.58}$$

Consider the first condition,

$$\frac{d^2 v_p^z(x)}{dx^2} = -2H_2\lambda^2 - \frac{1}{E_c I_c}\left(R_b d - \frac{\omega h C_1}{2\beta}\right) + \frac{\beta^2}{4\lambda^4+\beta^4}\left(\begin{array}{l}\dfrac{4\lambda^4}{E_c I_c}\left(\dfrac{\omega h}{2\beta^3}C_1\right)e^{-\beta x} \\ +\dfrac{C_1\beta(\omega t_p)^2 A_{11}^{-1}}{2I_p}e^{-\beta x}\end{array}\right) = 0 , \tag{5.59}$$

the coefficient H_2 is calculated

$$H_2 = \frac{1}{2\lambda^2}\left(\frac{\beta^2}{4\lambda^4+\beta^4}\left(\frac{4\lambda^4}{E_c I_c}\left(\frac{\omega h}{2\beta^3}C_1\right) - \frac{C_1\beta(\omega t_p)^2 A_{11}^{-1}}{2I_p}\right) - \frac{1}{E_c I_c}\left(R_b d - \frac{\omega h C_1}{2\beta}\right)\right). \tag{5.60}$$

For the second boundary conditions, the third derivative of Eq.(5.49) with respect to x is

$$\begin{aligned} &2H_1\lambda^3 e^{-\pi x}(C_{\lambda x} - S_{\lambda x}) + 2H_2\lambda^3 e^{-\lambda x}(C_{\lambda x} + S_{\lambda x}) - \frac{1}{E_c I_c}\left(R_b + \frac{\omega h}{2}\eta_o\right) + \\ &\frac{4\lambda^4\beta^3 e^{-\beta x}}{4\lambda^4+\beta^4}\frac{\omega h}{2\beta^3 E_c I_c}C_1 + \frac{\beta^3 e^{-\beta x}}{4\lambda^4+\beta^4}\frac{\beta(\omega t_p)^2 A_{11}^{-1}}{2I_p} = \frac{(\omega t_p)^2}{2I_p}\tau_{a,\max} \end{aligned} \tag{5.61}$$

The coefficient H_1 is then obtained

$$H_1 = \frac{1}{2\lambda^3}\left\{\frac{(\omega t_p)^2}{2I_p}(C_1+\eta_o) - 2H_2\lambda^3 - \frac{\xi_{v1}}{E_c I_c} - \frac{\beta^3}{4\lambda^4+\beta^4}\left(4\lambda^4\xi_{v2} + \xi_{v3}\right)\right\}. \tag{5.62}$$

Therefore, the peel-off stress of the adhesive material at any section of x can be estimated as following equation:

$$\sigma_a^{\bar{}}(x)=\frac{E_a}{t_a}\left\{\begin{array}{l}\frac{1}{2\lambda^3}\left\{\frac{(\omega x_p)^2}{2I_p}(C_1+\eta_o)-2H_2\lambda^3-\frac{\xi_{v1}}{E_cI_c}-\frac{\beta^3}{4\lambda^4+\beta^4}\left(4\lambda^4\xi_{v2}+\xi_{v3}\right)\right\}e^{-\lambda x}\cos(\lambda x)- \\ \frac{1}{2\lambda^2}\left(\frac{\beta^2}{4\lambda^4+\beta^4}\left(\frac{4\lambda^4}{E_cI_c}\left(\frac{\omega h}{2\beta^3}C_1\right)-\frac{C_1\beta(\omega x_p)^2A_{11}^{-1}}{2I_p}\right)\frac{1}{E_cI_c}\left(R_bd-\frac{\omega hC_1}{2\beta}\right)e^{-\lambda x}\sin(\lambda x)+\right) \\ +K_1\xi_{v1}(x)+K_2\xi_{v2}e^{-\beta x}+K_3\xi_{v3}e^{-\beta x}+ \\ \frac{1}{E_cI_c}\left\{\frac{1}{6}R_bx^3+\frac{\omega h}{2\beta^3}C_1e^{-\beta x}-\frac{\omega h}{12}\eta_ox^3+\frac{1}{2}Dx^2+Fx+G\right\}\end{array}\right\} \tag{5.63}$$

5.2.4 Result Interpretation

The adhesive shear and peeling off stresses can be estimated by Eqs.(5.28) and (5.63). It is shown that the maximum adhesive shear stress is dominated by the coefficient of C_1, which is given in Eq.(5.23). The tendency of the shear stress distribution and stress transfer length in the adhesive layer for the plate bonded concrete beam is controlled by the factor of β. Both the C_1 and β are the functions of the material properties and geometry of the concrete, adhesive and externally bonded composite. Furthermore, the fibre orientation in different laminate layers is also considered in the equation. Any one of these parameters would influence the whole adhesive shear stress distribution along the bond line.

The determination of the adhesive peel-off stress along the bond line is comparatively more complicated than the determination of shear stress distribution. Both the beam and plate deformations under bending conditions are considered as factors that affect the adhesive peel-off stress in the whole system. In fact, the fundamental principle of the adhesive peel-off stress is estimated by Eq.(5.29). Several parameters such as λ, ξ_{v1}, ξ_{v2}, ξ_{v3}, K_1, K_2 and K_3 are factors that would influence the resultant adhesive peel-off stress along the bond line.

Plots of the adhesive shear stress with different fibre orientations, adhesive shear and composite plate moduli, adhesive thickness and number of laminate layers are shown in Figs

5.21 to 5.25. The mechanical properties and geometrical dimensions for present example are listed in table 5.4.

Table 5.4 Dimensions and material data used in present example.

E_a (GPa)	G_a (GPa)	t_a (mm)	E_p (GPa)	E_c (GPa)	h (mm)	ω (mm)	t_p (mm)	d (mm)	L (mm)	P (kN)
3.3	1.15	0.1 | 5	20 | 200	27.8	0.15	0.15	0.8 | 8	0.025	0.35	17

According to the results shown as above, it is clearly indicate that the maximum adhesive shear stress increases with increasing the strengthened plate tensile and adhesive shear moduli, thickness of strengthened plate, and decreasing thickness of the adhesive layer. The maximum adhesive shear stress also increases with aligning all high strength fibres in the composite plate in beam longitudinal direction, x. In Figs. 5.21 to 5.25, it can be seen that the maximum adhesive shear stress locates at plate end region, x=0 and rapidly vanishes with increasing length toward the centre of the beam. In Fig. 5.26, a comparison of the maximum adhesive shear stress with different number of laminate layers, adhesive shear and plate moduli are shown.

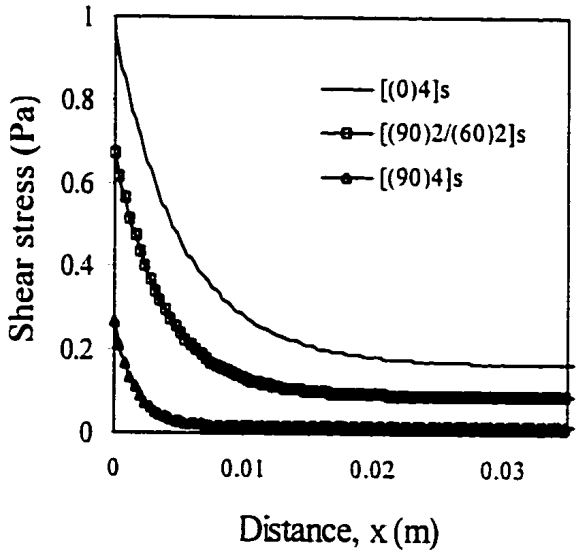

Figure 5.21 The adhesive shear stress along the bond line with different fibre orientations in composite laminate. The modulus of the composite with an orientation of $[(0)_4]_s$ is 159 GPa (Carbon fibre composite).

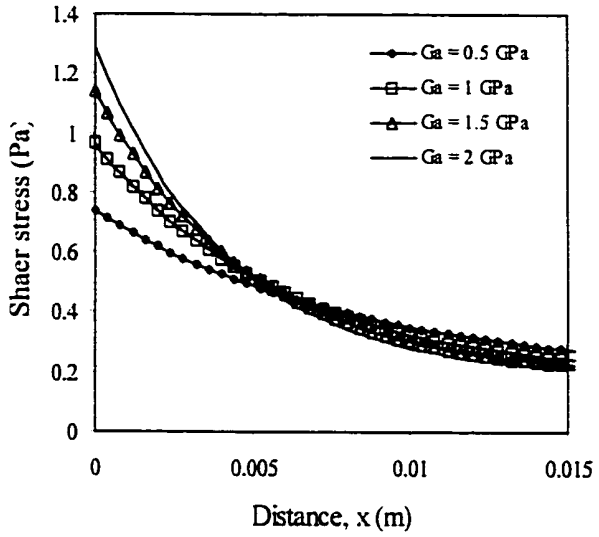

Figure 5.22 The adhesive shear stress along the bond line for the strengthened beam with different adhesive shear moduli.

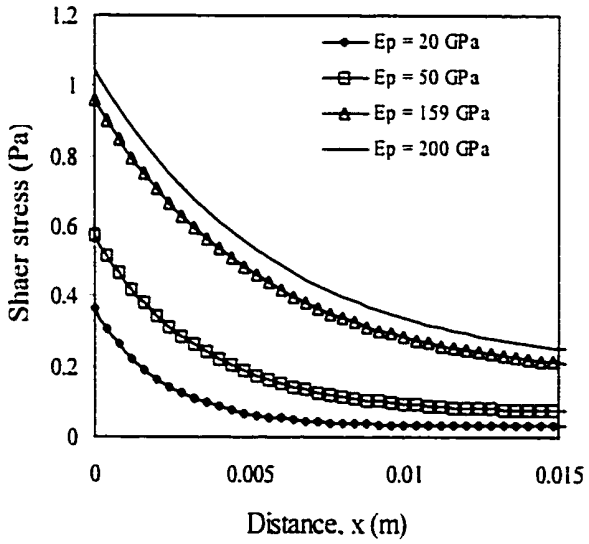

Figure 5.23 The adhesive shear stress along the bond line for the strengthened beam with different bonding plate moduli.

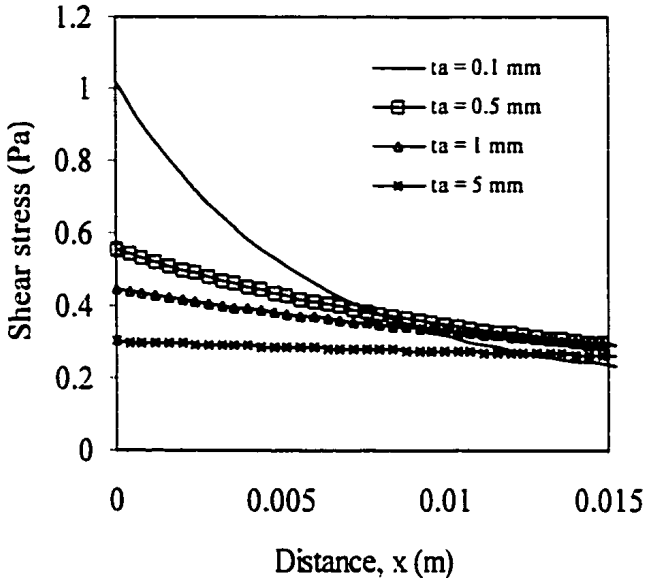

Figure 5.24 The adhesive shear stress along the bond line for the strengthened beam with different adhesive thicknesses.

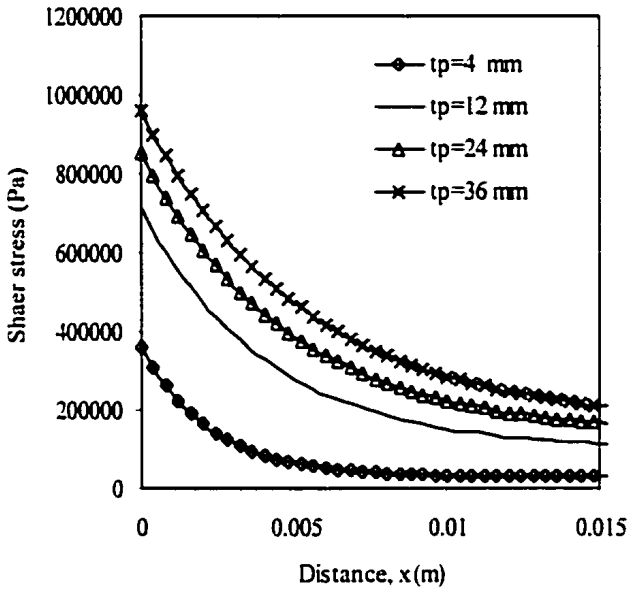

Figure 5.25 The adhesive shear stress along the bond line for the strengthened beam with different bonding plate thicknesses.

For the adhesive peel-off stress with the different fibre orientations, strengthened plate and adhesive shear moduli, thickness of the adhesive layer and number of laminate layers are plotted in Figs. 5.27 to 5.31.

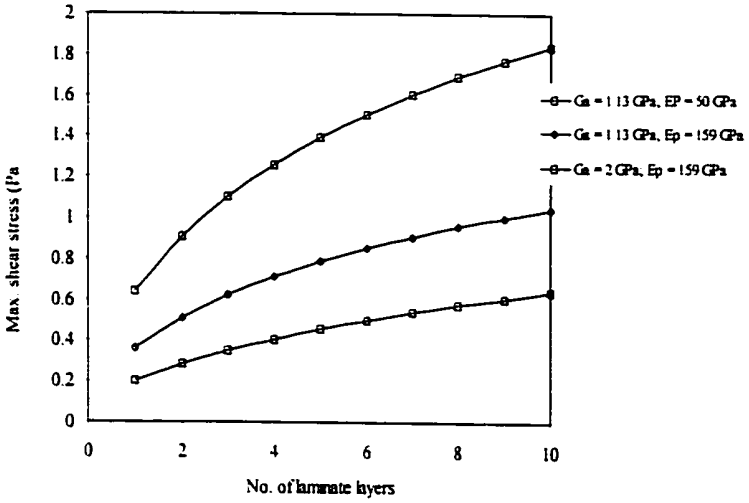

Figure 5.26 A comparison of the maximum adhesive shear stress with different number of laminate layers, adhesive shear and plate moduli.

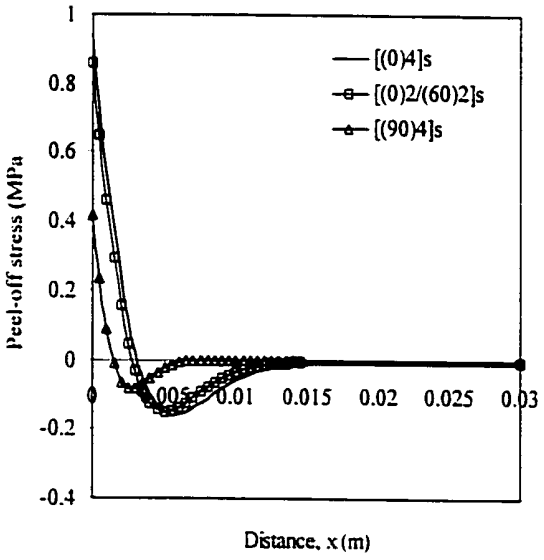

Figure 5.27 The adhesive peel-off stress along the bond line for the strengthened beam with different fibre orientations in composite laminate.

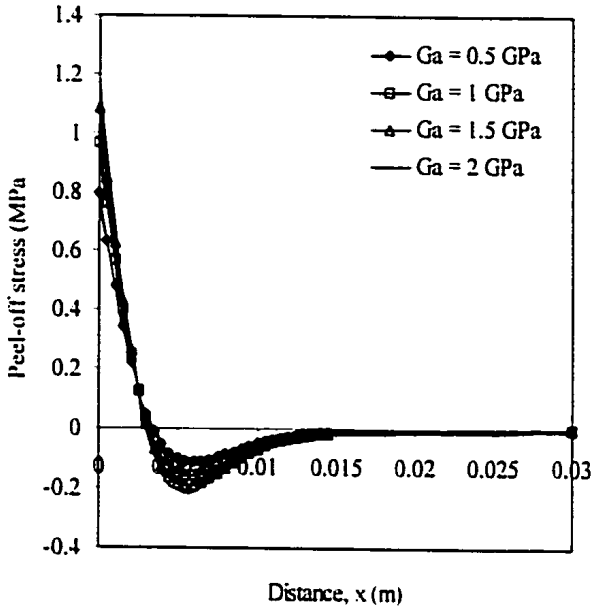

Figure 5.28 The adhesive peel-off stress along the bond line for the strengthened beam with different adhesive shear moduli.

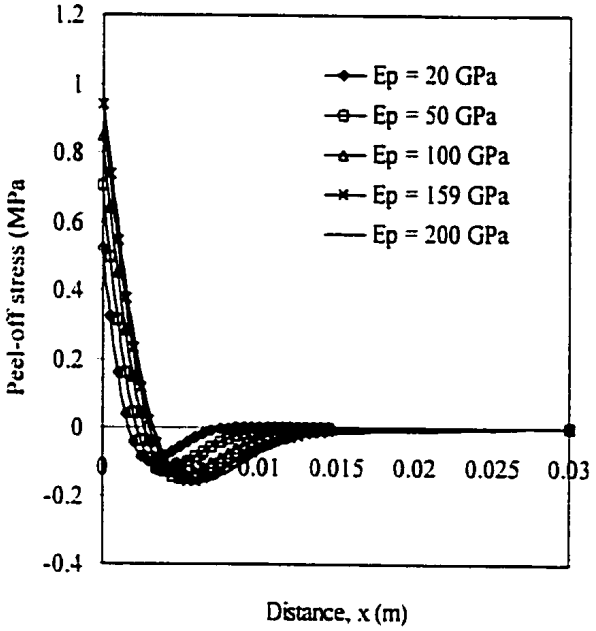

Figure 5.29 The adhesive peel-off stress along the bond line for the strengthened beam with different strengthened plate moduli.

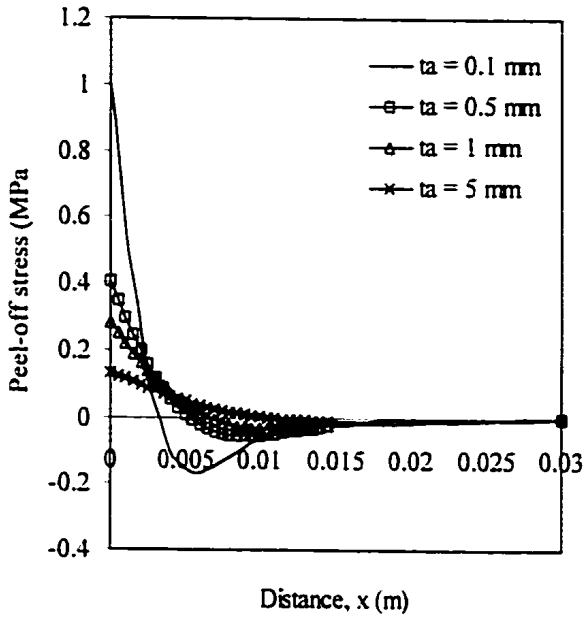

Figure 5.30 The adhesive peel-off stress along the bond line for the strengthened beam with different thicknesses of the adhesive layer.

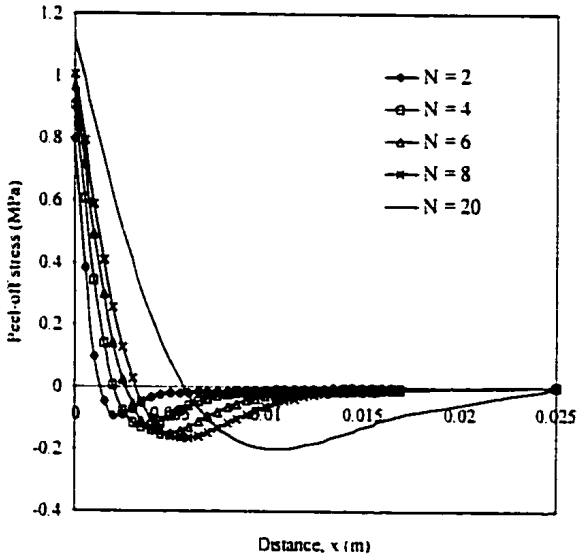

Figure 5.31 The adhesive peel-off stress along the bond line for the strengthened beam with different number of laminate layers.

According to the predicted results, the adhesive peel-off stress increases with increasing the strengthened plate tensile and adhesive shear moduli, number of laminate layers, and decreasing the thickness of the adhesive layer. The maximum adhesive peel-off stress is reached at the plate end region then rapidly decreases to negative value in general. Near zero stress is obtained when further moving toward the centre of the beam. The stress affecting zone is highly dependent on the material properties and geometrical factors. The formation of a negative peel-off stress region is due to the upward bending of externally bonded plate with high adhesive shear stress at the plate end region.

In general, a high modulus plate has been used for concrete rehabilitation and repair. However, the induced adhesive shear and peel-off stresses cannot be ignored. These stresses may cause premature failure at a load, which is below the estimated maximum strength of the strengthened structure.

The use of the composite plate with different fibre orientations results in changing the effective modulus, E_{eff} of the strengthened plate. All high strength fibres aligned in beam direction would maximise the modulus of the strengthened plate while the fibres aligned perpendicularly to the beam axis would greatly reduce the plate modulus. The effects on adhesive shear stress with different fibre orientation measured from the beam longitudinal direction are shown in Fig. 5.32.

5.2.5 Result Validation

Finite element method (FEM) was used to validate the results from the theoretical prediction. Msc/Nastran 4.0 commercial FEM package was used to model and analyse the rectangular beam strengthened by externally bonded composite plate subjected to three point bending load. The tensile modulus of the concrete and composite plate, and the shear modulus of the adhesive material of 27.8 GPa, 159 GPa and 1.125 GPa were modelled to study the stress transferring properties in the adhesive material with a centre applied load of 17 kN. The thicknesses of the adhesive layer and plate are 0.1 mm and 1.6 mm, respec-

tively. Since the beam is symmetrical about its centre axis, only half of the beam with appropriate constraints at the centreline was modelled.

In the present study, different mesh sizes in the adhesive layer were used to test the convergence and the resultant adhesive shear stresses at plate end are listed in Table.5.5. To compromise the processing time and accuracy of the results, plate elements (Quad 4) with a mesh size of 156.2 μm was selected at the plate end region. The FEM model for validating the theoretical result is illustrated in Fig. 5.33.

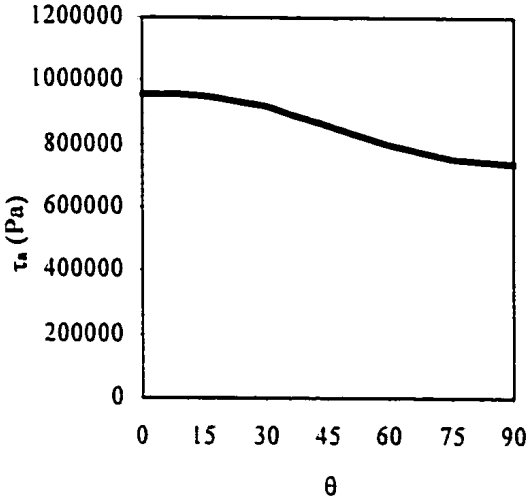

Figure 5.32 Effects on the adhesive shear stress with different fibre orientations (through all laminate layers) measured from the beam longitudinal axis

Table 5.5 Results from the convergence test for different mesh sizes FEM model.

Mesh size (mm)	0.625	0.3125	0.15625	0.78125	0.03915
$\tau_{a,\,max}$ (MPa)	0.752	0.821	0.957	0.971	0.981

The results from the FEM analysis together with the theoretical prediction for interfacial shear and peel-off stresses of the strengthened plate are shown in Fig.5.34 (a) and (b), respectively. It can be concluded that only a very fine mesh can show the descending branch in the shear stress very close to the plate end region.

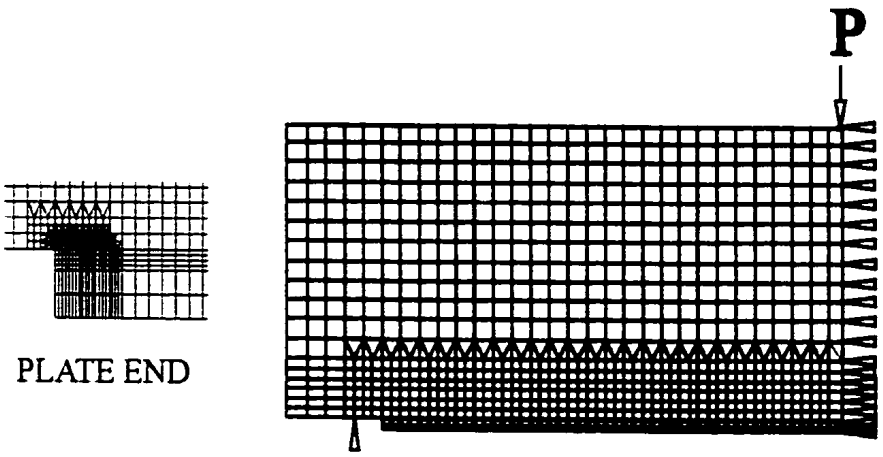

Figure 5.33 A FEM model for validating results from theoretical prediction.

The result from the adhesive shear stress shows slightly deviation from the FEM solution at the plate end region. However, at the location of maximum stress, which is used for design, the agreement between the FEM result and present method is good as can be seen from Fig. 5.34(a).

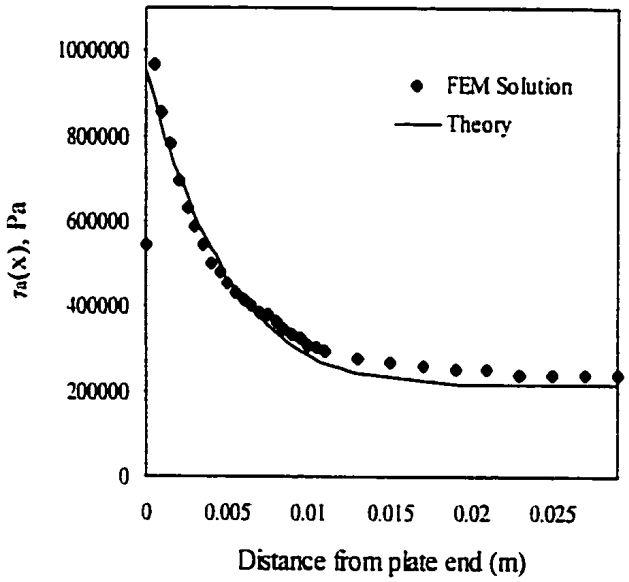

(a)

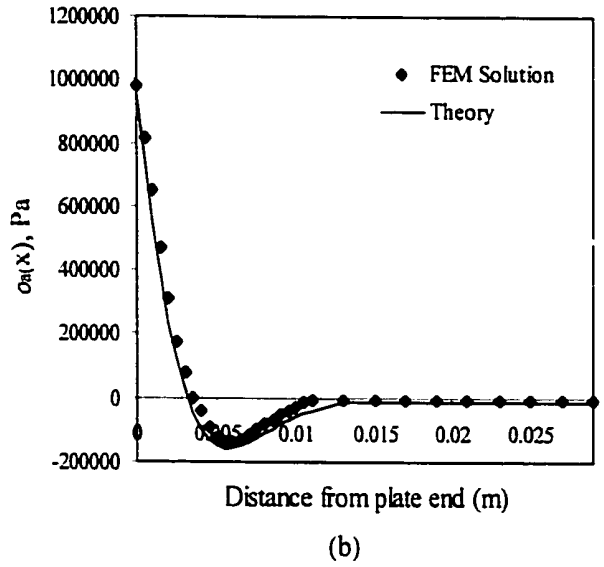

(b)

Figure 5.34 Comparison of the results obtained from the FEM analysis and theoretical prediction for a strengthened plate with a modulus of 159 GPa.

In general, both the adhesive shear and peel-off stresses estimated from the theoretical study are well compare well with the FEM solutions. In this study, It is possible to calculate the critical stress levels for the adhesive material at the end of the outer strengthened plate by using linear elastic theory. In deed, the mechanical properties of fibre reinforced polymeric composite materials behave in orthotropic forms. However, Malek et al. (1998) pointed out that the variation of elastic modulus in transverse direction does not have a significant effect on shear and peel-off stresses of the composite strengthened beam system. Therefore, the present theoretical prediction is valid to estimate the critical stress in the adhesive materials.

5.3 Stress Intensity Factor for Composite Strengthened Beam

5.3.1 Introduction

In previous section, a theoretical model for estimating the adhesive shear and peel-off stresses, and axial stress for strengthened plate for plain concrete beam strengthened by externally bonded composite plate are given. However, these equations cannot be used for determination of normal stress of the plate if crack exists at mid-beam region. In this Chapter, a simple superposition method with appropriate assumption is presented to estimate stress intensity factor, K_I and normal stress of the strengthened plate, σ_p with different crack length, plate thickness and properties.

Although a numerous of study has been conducted into cracking of concrete beams with steel bar reinforcement, there has been limited research into the cracking of concrete beams strengthened by an externally bonded reinforcement. A model for solving the fracture problem of steel RC beam using the superposition method was first proposed by *Carpinteri* (1986) as shown in Fig.5.35.

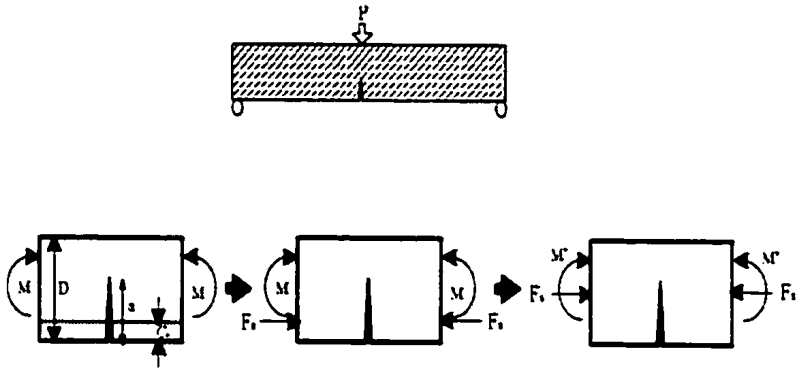

$$K_I = K_M - K_S$$

Figure. 5.35 The LEFM model established by Carprinteri's (1986) for the RC beam.

The stress intensity factor K_I, of the RC beam was determined by two independent factors: (1) stress intensity factor K_M due to the load P applied at the middle of the cracked-beam. (2) stress intensity factor K_F due to the tensile force F_s (closing force) from the embedded reinforced steel bar. However, F_s was estimated from the ultimate tensile or yield stresses of the steel bar, which implies that the failure of the structure is dominated by the steel bar rather than the concrete beam itself. Since F_s is an assumed value and not directly related to the external applied force P, this method may not practicable to determine K_I and F_s as a function of P.

A recent improved model by Baluch (1992) assumed that the strain is linear along the depth of the RC beam and proportional to the distance measured from the beam neutral axis as shown in Fig.5.36. In this method, the critical crack length a_c and F_s are initially assumed. F_s and M can then be computed by iteration method until the results converge. This improved model provides a more realistic solution than that from the *Carpinteri* method. However, the numerical analysis verifies that the strain distribution along the depth of the cracked RC beam is not linear in form, especially at the crack section. Therefore, this improved model cannot be used to accurately predict the stresses of the strengthened cracked beam with external reinforced FRP plate.

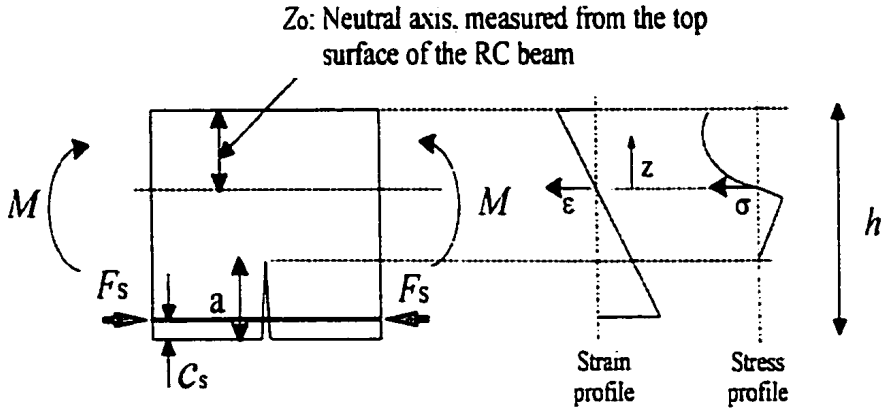

Figure 5.36 Improved model by Baluch (1992); strain and stress distribution along the depth of the beam.

In realistic engineering application, K_I is a factor that most engineers should take into account when designing and maintaining real concrete structures. Consequently, the stresses in the concrete beam and reinforced plate/bar become the major factors in investigating the failure modes of the structures. From this discussion, the magnitude of F_s cannot be found directly by using the strain continuity method. Therefore, it is necessary to develop a simple and more convenience method to predict the failure stress of the strengthened beam.

5.3.2 Methodology

This Chapter introduces a simple method for determining the stress intensity factor K_{IA} of a rectangular cracked-concrete beam strengthened by externally bonding a plate onto the tension surface. Fig. 5.37 shows a diagrammatic representation of a rectangular concrete beam with a crack of depth a_e at the mid-section. The depth of the crack is assumed uniform throughout the width ω of the beam. The composite plate is fixed to the tension surface of the beam by an adhesive material with uniform thickness throughout the whole bonding length. The mechanical properties of both concrete and externally bonded plate are linear elastic. A perfect bond at the interface between the concrete and reinforced plate is assumed, i.e. there is no crack formation along the bonded interface.

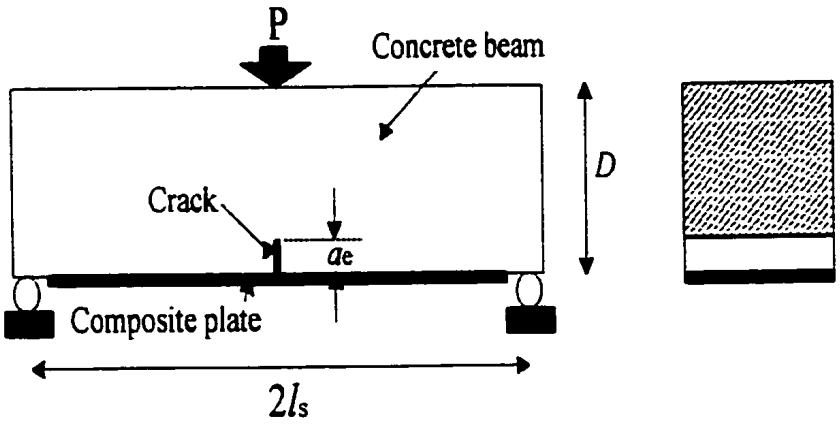

Figure 5.37 Schematic model of a rectangular cracked concrete beam strengthened by an externally bonded plate.

A super-position method is proposed to evaluate the value of K_I at the crack tip of the beam when it is subjected to three point bending. The method treats an edge crack problem as a centre crack in order to determine the value of K_I, which cannot be directly solved by existing closed-form solution. Figs.5.38 and 5.39 give a step by step illustration of the method used in present study. It can be separated into three stages as follows:

a) Determination of the stress function $\sigma_c(x)$ with respect to the material properties and geometrical factors for both the concrete and reinforced plate of the strengthened cracked-beam as indicated in Fig. 5.38. It is assumed that the stress function along the crack surface is same as that determined for the whole system.

b) Evaluation of the K_{IA} by treating the existing edge-crack problem as a centre crack since both crack tips have zero-displacement constraints in the beam longitudinal direction. The stress function on the crack surface is determined from stage (a). Only the crack, which is furthest from the plate is interested, i.e. point "A" in Fig. 5.

c) Determination of plate normal force F_P. The well-known super-position method for estimating the value of K_F by de-composting the actions of the tensile force in the plate and bending moment of the beam is illustrated in Fig.5.39.

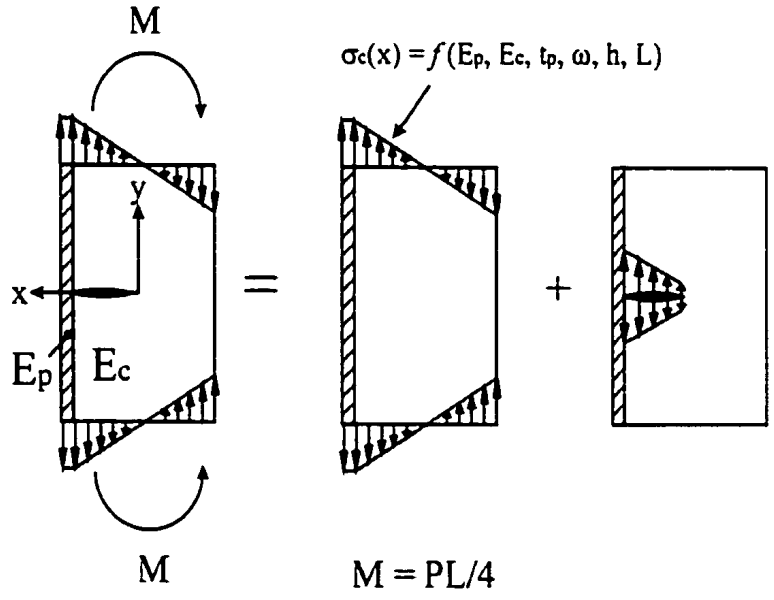

Figure 5.38 Schematic diagram of the supposition method to interpret the stress distribution along the crack surface.

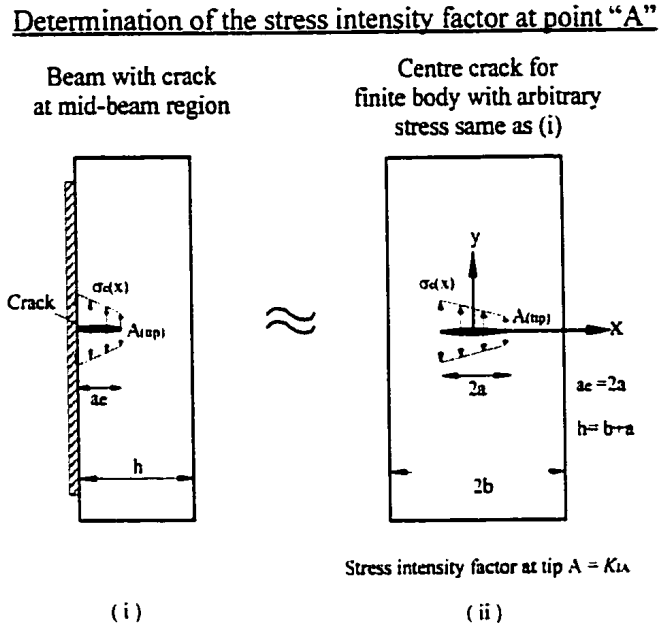

(a)

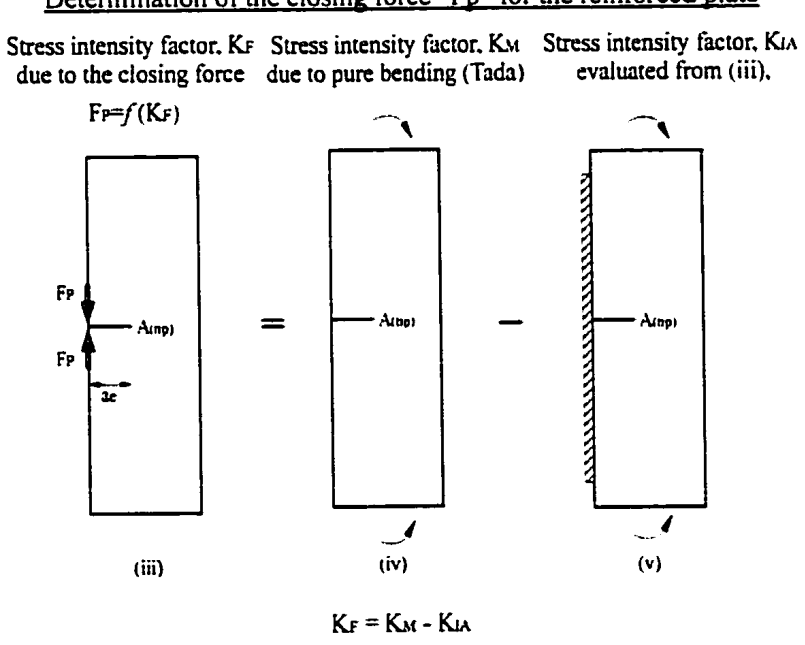

(b)

Figure 5.39 Model to treat an edge-crack problem as an inner crack problem (a). Superposition method for evaluation of stress intensity factor at point A; and (b) for the beam with a pair of edge closing forces F_p.

The major focus of the present study is to evaluate K_{IA} in a cracked concrete beam after strengthening by an externally bonded plate on the tension surface. The original edge-crack problem of the beam is considered as an inner-crack problem after strengthening since both ends of the crack have a zero-displacement characteristic, i.e. the displacement at the crack tips in the beam longitudinal direction is equal to zero when $\theta = 0°$. The stress distribution along the crack surface can be estimated by superimposing method given by *Rooke et al* (1981), i.e. the stress distribution along the crack surface is equal to the determined from the whole system without cracking within the region $-a \le x \le a$ under the same loading condition. Effects arising from the plate with different mechanical properties to the beam under the centre point loading are overcome by the stress function estimated from the same strengthened beam without cracking. However, a tip (point "A"), which is remote from the boundary of bond, is assumed to have no significant influence by the stress induced due to the bi-material effect at the bonding region.

5.3.3 Stress Function of the Strengthened Concrete Beam without Crack

In the initial stage, the stress distribution along the centreline of the concrete structure without cracking but with the externally bonded reinforcement is evaluated. Since the thickness of the reinforced plate is normally much smaller than the depth of the beam to be reinforced, the uniform axial strain of the plate is assumed through its thickness, t_p. The stress profile along the depth of the beam is linear. The bottom surface is under tension while the top surface is in compression. As the beam is symmetrical about its centre-axis (y=0), the shear deformation of an adhesive material is theoretically equal to zero at the centre region (y=0). The strain of the reinforced plate ε_p at the mid-beam section should be same as the surface strain of the concrete ε_o, at the bonding region, i.e. at $(x,y)=(X_o,0)$,

$$\left.\frac{\sigma_o}{E_c}\right|_{y=0,x=X_0} = \left.\frac{\sigma_p}{E_p}\right|_{y=o,x=X_0} \tag{5.64}$$

where σ_o, σ_p, E_c and E_p denote the maximum tension stress of the concrete beam and reinforced plate, the tensile moduli of the concrete and reinforced plate, respectively. Accord-

ingly, the normal stress distribution along the lateral direction (x,0) at the mid-beam section can be expressed as

$$\sigma_c(x,0) = \sigma_o \frac{x}{X_o} = \sigma_p \frac{E_c}{E_p} \frac{x}{X_0} = \left. \frac{F_p \beta x}{t_p \omega X_o} \right|_{y=0} \tag{5.65}$$

where β is the Young's modulus ratio of the concrete and reinforced plate ($\beta = E_c/E_p$) and F_P is the closing force (in beam longitudinal direction) induced by the reinforced plate at the mid-beam region. The location of zero stress ($\sigma_c(x)=0$), of the strengthened beam is called neutral axis X_o, which can be evaluated using the force balance equation, $\sum F_y = 0$, thus.

$$F_p + \int_{-(h-Xo)}^{Xo} \sigma_c(x,0)\omega \cdot dx = 0 \Big|_{y=0}. \tag{5.66}$$

Substituting Eq.(5.65) into Eq.(5.66) yields

$$X_o = \frac{\beta h^2}{2(\beta h + t_p)}. \tag{5.67}$$

The maximum tensile stress σ_0 in the concrete material can be estimated by using the moment-equilibrium method, i.e. $\sum M=0$:

$$F_p X_o + \int_{(h-Xo)}^{Xo} \sigma_c(x,o)\omega x dx = \frac{PL}{4} \Big|_{y=0}. \tag{5.68}$$

By substituting Eq.(5.65) into Eq.(5.68), σ_0 can be expressed as following

$$\sigma_o = \frac{PL\beta}{4t_p\omega\left(X_o + \frac{\beta}{3t_p X_o}\left(X_o^3 + (h - X_o)^3\right)\right)}. \tag{5.69}$$

5.3.4 Stress Intensity Factor K_{IA}

Whereas the boundaries of both sides of the crack have tips with zero displacement, the problem can be considered essentially a centre-crack problem as mentioned previously and only a tip at the concrete region is of interest. Therefore, the effective crack length a for the centre-crack problem is equal to $a_e/2$ and the origin (0,0) is shifted to the centre of the crack. The direction of the x-axis is also reversed. The crack tips are now located at the co-ordinated x = $\pm a$. For the strengthened cracked-beam, the stress function of the beam along the crack surface can be treated as the same stress function obtained from Eq.(5.65) but only the region of crack is of interest. Then, the stress function along the crack surface is calculated by

$$\sigma_c(x) = \sigma_o\left(1 - \frac{x+a}{X_o}\right) \qquad -a \le x \le a \ . \tag{5.70}$$

For the finite plate under a point loading condition as illustrated in Fig.5.40, stress intensity factor K can be given by Sih (1973)

$$\begin{Bmatrix} K_I \\ K_{II} \\ K_{III} \end{Bmatrix}_B = \frac{1}{\sqrt{2b}} \begin{bmatrix} P \\ Q \\ T \end{bmatrix} \begin{Bmatrix} F(a/b, c/a) \\ F(a/b, c/a) \\ F_{III}(a/b, c/a) \end{Bmatrix}_B \tag{5.71}$$

in which

$$\{F(a/b, c/a)\}_B = \left\{1 + \left(\frac{\pi}{\sqrt{\pi^2 - 4}} - 1\right)\sqrt{1 - \left(\frac{c}{a}\right)^2}\left(1 - \cos\left(\frac{\pi a}{2b}\right)\right)\right\}\{F_{III}(a/b, c/a)\}_B \tag{5.72}$$

$$\{F_{III}(a/b,c/a\}_B = \sqrt{\tan\left(\frac{\pi a}{2b}\right)} \frac{1-\left(\dfrac{\sin\left(\dfrac{\pi c}{2b}\right)}{\sin\left(\dfrac{\pi a}{2b}\right)}\right)}{\sqrt{1-\left(\dfrac{\cos\left(\dfrac{\pi a}{2b}\right)^2}{\cos\left(\dfrac{\pi c}{2b}\right)^2}\right)}}. \tag{5.73}$$

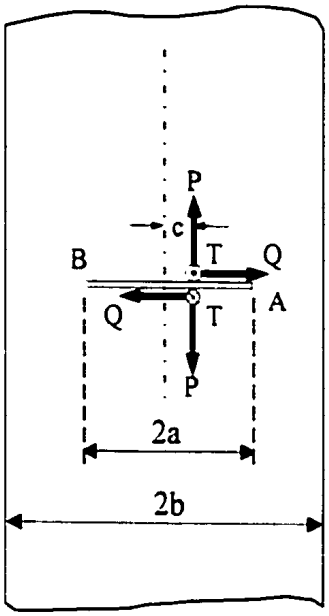

Figure 5.40 Schematic diagram of the finite plate geometry with a concentrated point load.

The foregoing solution can be extensively applied to the finite body with the applied arbitrary load distribution along the crack surface by integrating the stress and geometry functions within the region of $-a \le x \le +a$. The stress intensity factor K_{IA} of the beam becomes

$$K_{IA} = \frac{1}{\sqrt{2b}} \int_{-a}^{a} \sigma_c(x)\{F(a/b,x/a)\}dx \tag{5.74}$$

and *F(a/b,x/a)* is given by Eq.(5.72).

5.3.5 Closing Force F_p of the Reinforced Plate

The final step is to estimate the closing force F_P of the reinforced plate at the crack mouth region. Consider the model mentioned previously in Fig.5.39, from which it is obtained that

$$K_{IA} = K_M - K_F \tag{5.75}$$

where K_M is the stress intensity factor for the rectangular beam with the edge crack at the mid-beam region when it is subjected to three-point bending load. It can be evaluated by using the well-known closed form solution given by

$$K_M = \frac{3PL}{2b\omega^2}\sqrt{\omega} f_m(\alpha) \tag{5.76}$$

where $f_m(\alpha)$ is the shape function for the beam with notch formation under three point bending and α is the notch to depth ratio a/h. K_F is given by Tada et al. (1985)

$$K_F = \frac{2F_p}{\omega\sqrt{\pi a_e}} f_F(\alpha) \tag{5.77}$$

where

$$f_F(\alpha) = \frac{0.46 + 3.06\alpha + 0.84(1-\alpha)^5 + 0.66\alpha^2(1-\alpha)^2}{(1-\alpha)^{3/2}}. \tag{5.78}$$

From Eqs.(5.74-5.77), the closing force F_P induced by the centre point load P can be calculated by

$$F_p = \frac{\omega\sqrt{\pi a_e}}{2f_F(\alpha)}\{K_M - K_{IA}\}. \tag{5.79}$$

5.3.6 Results Verification

The result obtained from the proposed method was verified by comparing it with the numerical analysis solution using finite element method (FEM). Msc/Nastran FEM package was used for investigating the stress concentration at the crack-tip and tensile stress in the reinforced plate. The area close to the crack-tip and at the mid-beam section of the reinforced plate were meshed into very fine element size (QUAD4 element with 0.00015625 m each side) in order to obtain more accurate results. A schematic illustration of the model is given in Fig. 5.41. Since the strengthened beam is symmetrical to its central axis, only half of the beam was modelled. The load P is applied vertically on the top and aligned at the centre of the beam to simulate the real three point bending test. Boundary constrains were applied at the nodes along the centre line of the beam so that only vertical movement was permitted. Vertical movement was not permitted at the bottom supporting point (S). Linear elastic properties were assumed for both concrete and reinforced plate. The thickness and modulus of the reinforced plate ranging from 1 mm to 2.5 mm and 50 GPa to 200 GPa, respectively were used to compare the results obtained from the proposed method. All details of the simulated model are shown in Table.5.6.

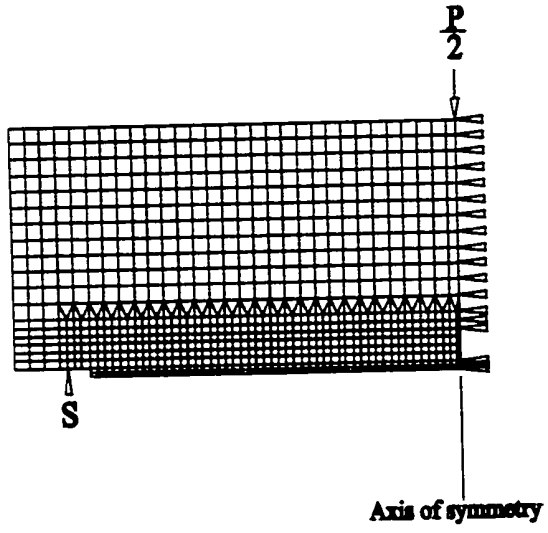

Figure 5.41 FEM model for estimating the parameters K_I and F_p.

Table 5.6 The details of the beam model for analytical and numerical analyses

Sample	P (kN)	Ec (GPa)	Ep (GPa)	tp (mm)	h (m)	l (m)	d (m)	α
1	0 | 20	27.8	50 | 200	1.0 | 2.5	0.15	0.2175	0.0125	0.2

The FEM model has been validated by comparing it with the experimental data for the concrete specimen bonded to glass fibre composite plate. The plate normal strain was measured directly in the experiment for the cracked-concrete beam strengthened by 6 layers of glass fibre composite laminate by using externally bonded strain gauge. The crack was made during moulding process by placing a plastic film with a depth of pre-determined crack length inside the mould. The concrete beam with a pre-filled plastic film before and after strengthening by glass fibre composite laminate is shown in Fig. 5.42 and 5.43.

Figure 5.42 A crack made by placing a plastic film inside the mould.

Figure 5.43 A cracked beam strengthened by 6 layers of glass fibre composite laminates.

The experimental results for the plain rectangular concrete beam with a crack on its tension surface under three point bending is plotted in Fig. 5.44. The curve in the figure is extracted from a specimen with higher failure strength from three similar specimens.

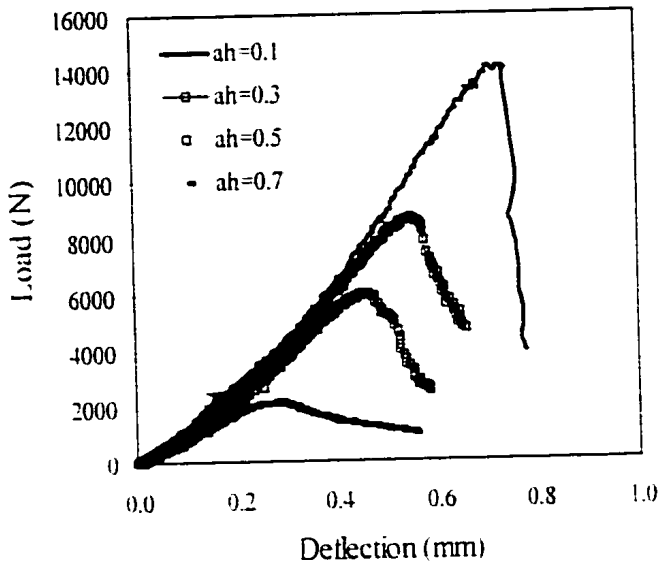

Figure 5.44 Load-deflection curves for cracked concrete beam with different crack-depth ratio.

The results for all cracked-beams after strengthening by 6 layers of glass fibre composite plate are plotted in Fig. 5.45. It is clearly demonstrated that the ultimate flexural load of the strengthened cracked concrete beam is increased substantially by using the glass fibre composite plate. However, the ultimate flexural loads of the test specimens are not proportional to the crack depth of the beam. The average ultimate flexural load from three similar tested beams with crack-depth ratio of 0.1, 0.3, 0.5 and 0.7 are 19.8kN, 19.5 kN, 24.9kN and 25.6kN, respectively.

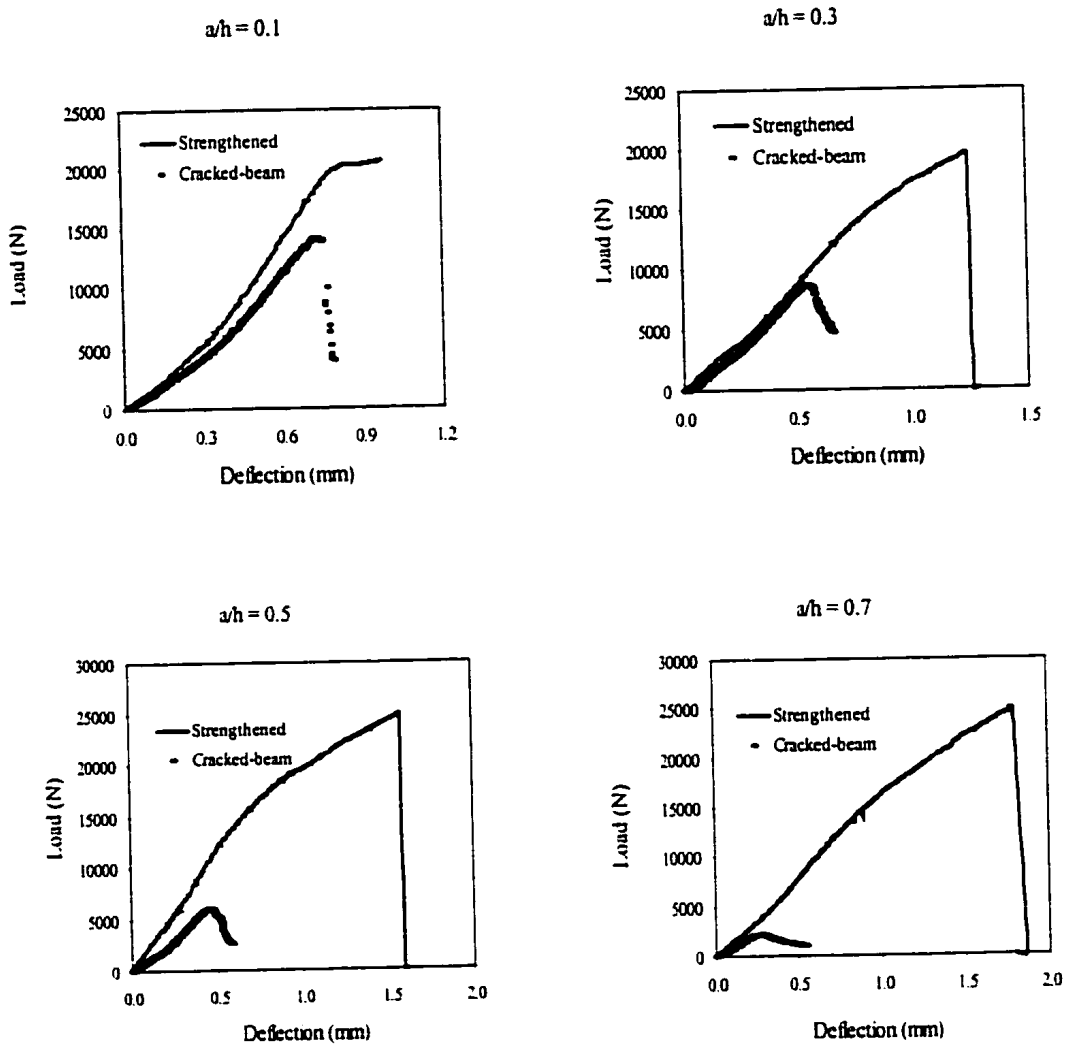

Figure 5.45 Experimental results for all glass fibre composite-strengthened cracked-beam subjected to three point bending test.

The comparison of the results from the experiment and FEM analysis at an applied load of 10 kN is plotted in Fig.5.46. Strains on the surface of glass fibre composite plate were measured by three surface mounted strain gauges. It is shown that the strains measured from the experiment agree well with the FEM solution. Therefore, it can be concluded that the FEM result is able to be used as real experimental data for predicting the stress distribution of the strengthened beam with different bonding plate materials.

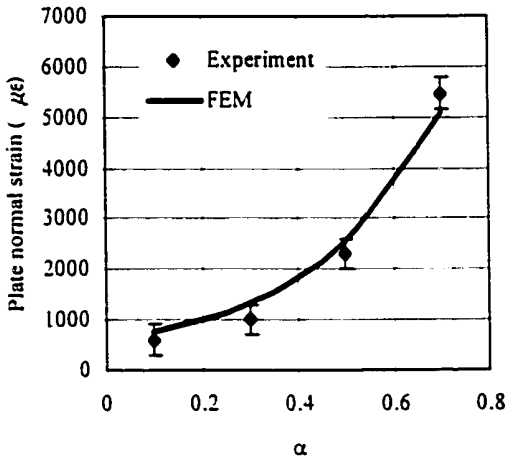

Figure 5.46 The comparison of plate normal strain measured from the experiment and FEM solution.

The stress intensity factor of K_I can be estimated by measuring displacements at two nodes closest to the crack-tip in the FEM model. Assuming that the beam was subjected to the load at the plane strain condition, the following empirical equation was used [Aliabadi and Rooke (1991)].

$$\begin{Bmatrix} u \\ v \end{Bmatrix} = \frac{K_I}{\mu\left(\frac{1}{1-\nu}\right)}\sqrt{\frac{r}{2\pi}}\begin{Bmatrix} \cos\left(\frac{\theta}{2}\right)\left(\left(\frac{1-2\nu}{1-\nu}\right)+\left(\frac{1}{1-\nu}\right)\sin^2\left(\frac{\theta}{2}\right)\right) \\ \sin\left(\frac{\theta}{2}\right)\left(2-\left(\frac{1}{1-\nu}\right)\cos^2\left(\frac{\theta}{2}\right)\right) \end{Bmatrix}. \tag{5.80}$$

5.3.7 Results and Discussions

The results obtained from the FEM and proposed method are plotted in Figs.5.47 and 5.48. Accordingly, it is found that the values of K_{IA} and F_P obtained from the proposed solution compare well with the FEM for the model with α of 0.2. The relative error is less than 4%. The tensile force of the reinforced plate increases with increasing its thickness. The corresponding stress intensity factor K_{IA} decreases when the thickness of the plate is increased. This implies that by using the thick reinforced material would reduce the chance of failure by cracking in the concrete material. A high modulus material used as the reinforced plate would reduce the value of K_I, while the maximum normal stress at the plate is increased. Figures 5.49 and 5.50 show the effect of the applied load, P to the values of K_{IA} and F_P. Both show a good agreement with FEM results.

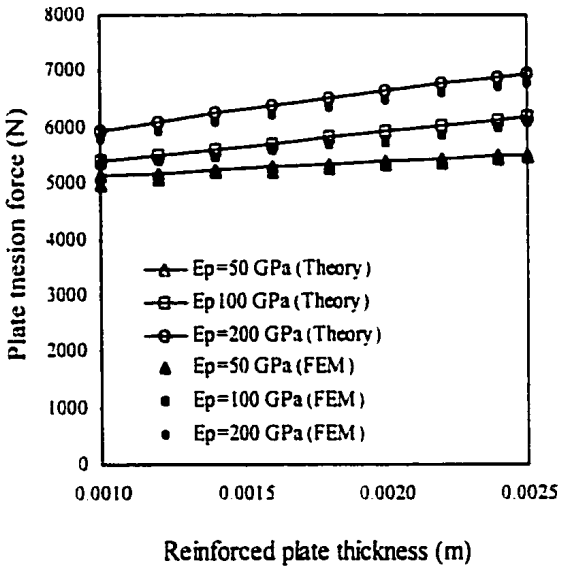

Figure 5.47 The normal force, F_p of the reinforced plate plotted against different plate thicknesses used for the strengthened beam model.

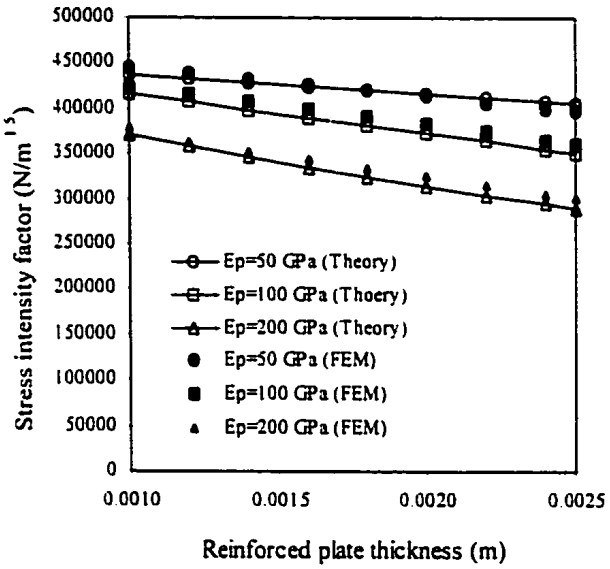

Figure 5.48 The stress intensity factor, K_{IA} of the strengthened beam plotted against different plate thicknesses used for the strengthened beam model.

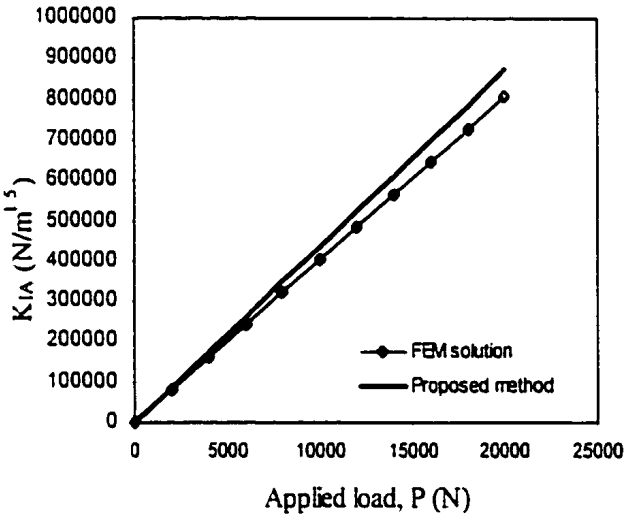

Figure 5.49 The results of load against stress intensity factor from FEM results and theoretical prediction.

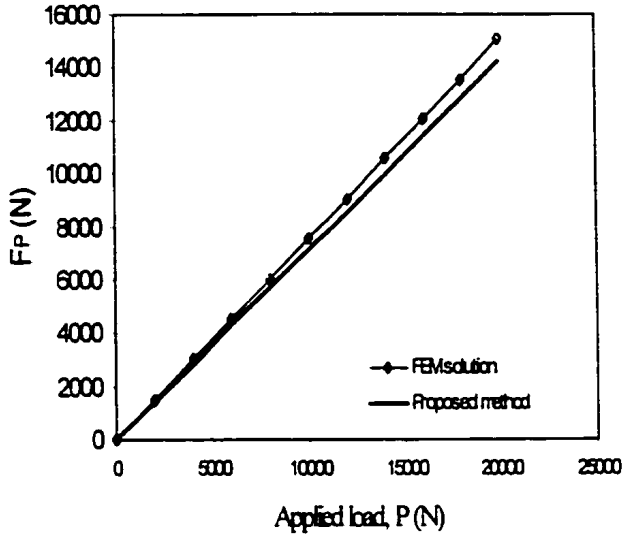

Figure 5.50 The results of load against normal force in strengthened plate curve from FEM results and theoretical prediction.

The present method provides a simple but accurate tool for estimating the values of K_{IA} and F_P accurately for the strengthened beam with β=7.2 when the a/h ratio is less than 0.45. The effects are clearly demonstrated in Fig.5.51. The result shows that the errors are within 6% compared with the FEM solution. According to the results shown in Fig.5.51, it is also demonstrated that the maximum K_{IA} reaches at $\alpha \approx 0.2$. Beyond this limit, the K_{IA} decreases with increasing the crack length. The failure mechanism of the structure is dominated by the mechanical properties and geometrical factors of the external bonded reinforcement.

Table 5.7. The details of the beam model for evaluating the K_I with different α ratio

Curve	Modulus of plate (E_P), GPa		Modulus of concrete (E_c), GPa		β
# 1	30	Glass fibre composites	30	Medium strength	1
# 2	120	Graphite composites	30	Medium strength	4
# 3	200	Steel plate	30	Medium strength	7.2
# 4	200	Steel plate	10	Low strength	20
# 5	300	High strength material	10	Low strength	30

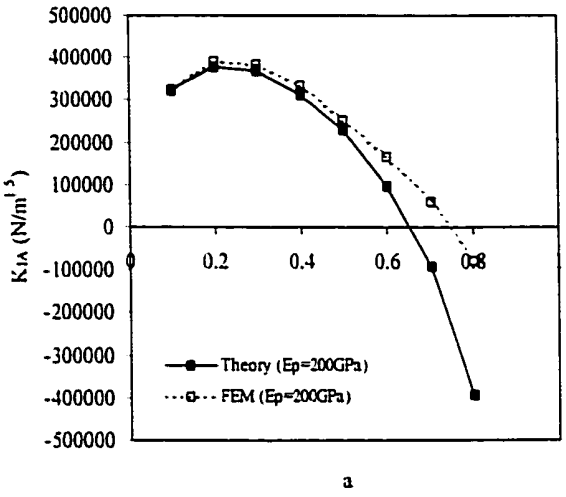

Figure 5.51 Plot of K_{IA} against α for E_p=200GPa under applied load of 17 kN.

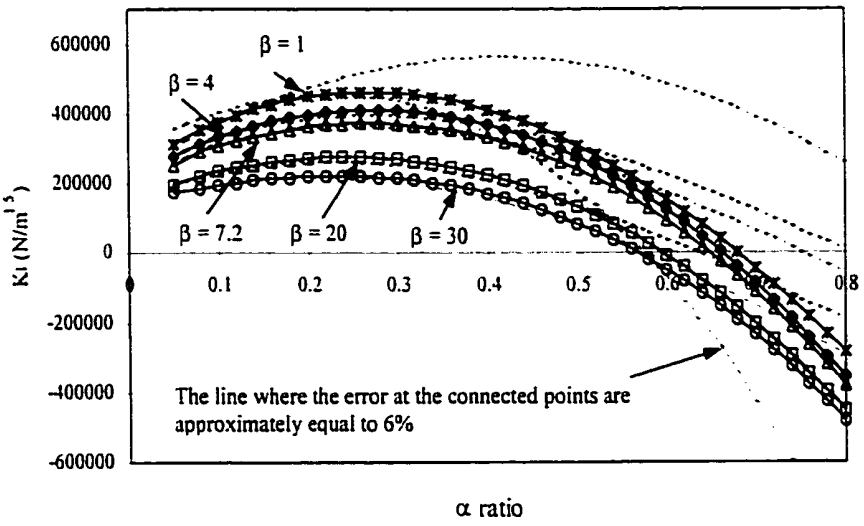

Figure 5.52 Plots of stress intensity factor (K_{IA}) against crack-depth ratio (α) of different modulus ratio (β) between the strengthened plate and concrete materials.

The stress intensity factor K_I of the strengthened beam against the notch-depth ratio α for different modulus ratio of β is plotted in Fig.5.52. The details of the beam model are listed in Table. 5.7. Fig.5.52 obviously shows that the difference between the theoretical prediction and numerical analysis increases with increasing the ratio of β and increasing the ratio of α. This may be due to the following factors:

i In general, the tensile modulus of the reinforced plate is larger than the beam to be strengthened, i.e. $\beta \leq 1$. For the reinforced plate with high tensile modulus, it is strong enough to constrain the crack mouth (crack tip at the interface of bond between the concrete and plate) opening and maintain the assumption of inner crack characteristic. However, a low tensile modulus plate cannot give the same characteristic and therefore, high K_I is resulted from the FEM solution.

ii For further increase of the ratio of α, the difference between the analytical and FEM results at the decreasing branch is increased because the neutral axis (X_o) determined by the structure without cracking is normally shorter than that from the cracked-structure. Therefore, the internal compressive stress at the crack-tip appears earlier from the theoretical solution than that from the FEM results.

The validity of the present method is plotted in Fig.5.53. All data points are extracted from the calculated results for different ratio of E_p/E_c on condition that the error between the theoretical prediction and FEM result at each data point is approximately equal to 6%. The smooth curve is plotted after fitting all data points. Fig.5.53 demonstrates that the current proposed method is able to accurately evaluate K_I for the value of α up to 0.5 when the ratio of E_p/E_c is larger than 13. However, for a reinforcement with low tensile modulus, such as balanced type glassfibre composites ($E_p \leq 20$GPa), the proposed method is also available for value of α up to 0.2. The limitation of using the current analytical method to evaluate the values of K_I and F_p is shown as follows:

$$\alpha \le 0.13Ln\left(\frac{E_p}{E_c}\right)+0.17. \tag{5.81}$$

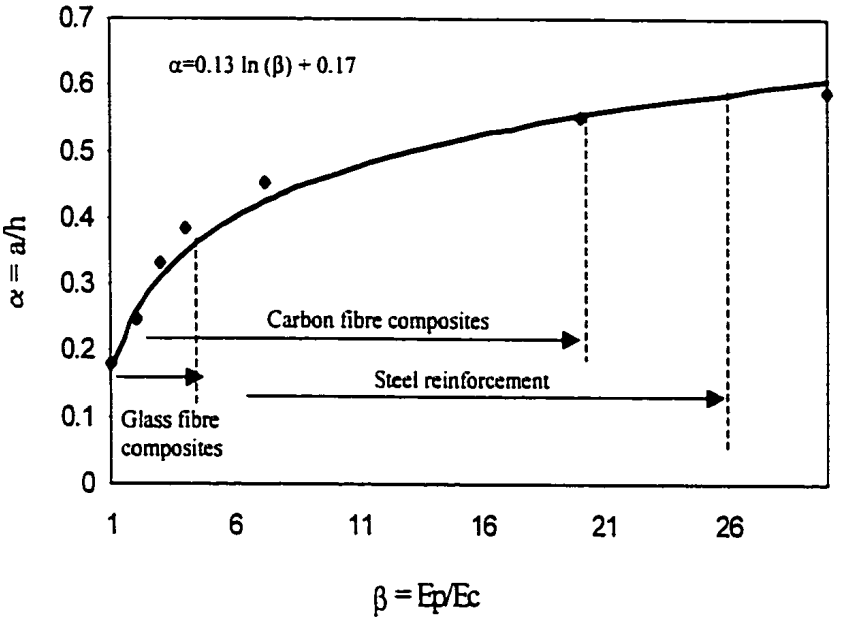

Figure 5.53 Validity of the theoretical method

Eq. (5.81) shows that the accuracy of using the current analytical method increases with increasing the plate modulus. Therefore, for a large β ratio, the proposed equation is not valid for estimating the value of K_I in a strengthened-concrete beam. However, the proposed method provides good predictions of K_I and F_p for the small cracked-structure in an engineering application. A deeply cracked beam would normally not be used for a realistic concrete structures. Figs.5.54 and 5.55 show four pictures captured from the FEM analysis. A load of 30kN was applied to the FEM model, and the modulus of the strengthened plate was given as 11GPa and 200GPa. Crack-depth ratios of 0.2 and 0.5 were selected for the analysis. The pictures indicate that the normal stress at the crack-tip decreases with decreasing the modulus of the strengthened plate. However, the increase of the crack-depth of the strengthened crack model could not reduce the normal stress in the crack-tip region. It is well matched with the experimental observation as shown in Fig. 5.45.

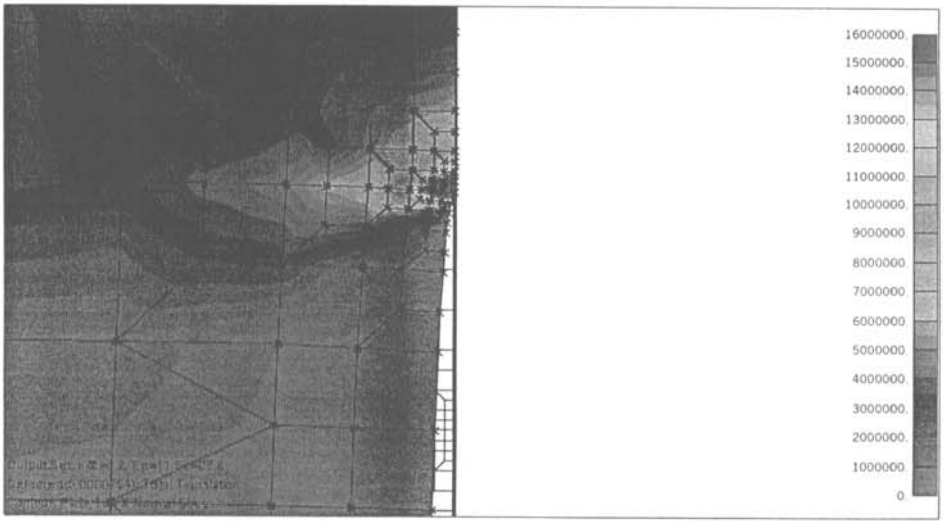

(a)

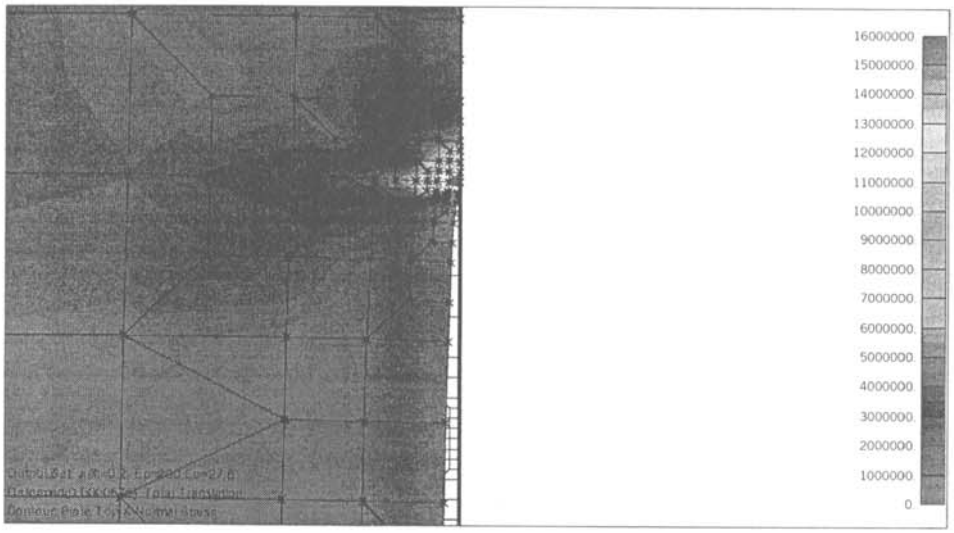

(b)

Figure 5.54 Normal stress contour captured from the FEM, the modulus of the strengthened of 11GPa (a) and 200 GPa (b) are used for the cracked-beam with a/h = 0.2.

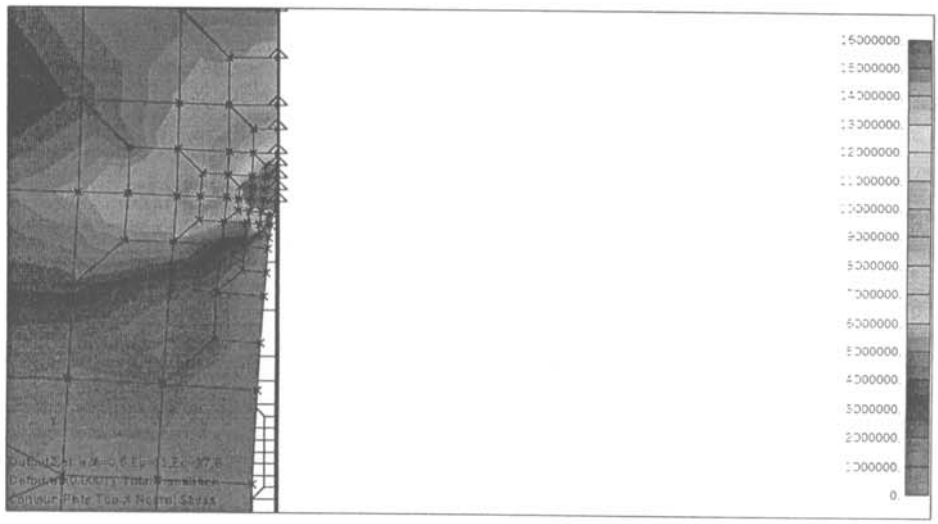

(a)

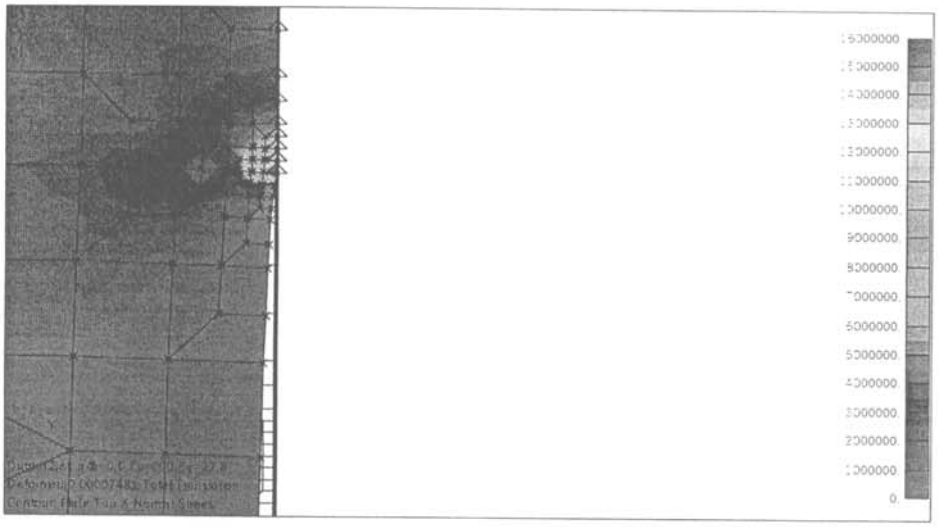

(b)

Figure 5.55 Normal stress contour captured from the FEM, the modulus of the strengthened of 11GPa (a) and 200 GPa (b) are used for the cracked-beam with a/h = 0.5.

5.4 Summary

In this Chapter, the mechanical behaviours of the composite strengthened concrete beams have been investigated through the experimental studies, theoretical and numerical analyses. The experiment results provide a valuable information for strengthening technique of the civil concrete structures with a notch formation on its tension surface by using glass fibre composites. The adhesive shear and peel-off stresses, and normal stress of the strengthened composite plate could be estimated by using predictive theoretical equations as indicated in Eqs.(5.63) and (5.28). The stress intensity factor of the cracked concrete structure can also be determined by using a simple superposition method with the appropriate initial assumptions. Throughout the whole Chapter, several conclusion are drawn as follows:

1. The flexural strength of the notched-rectangular concrete beam increases substantially by bonding the glass fibre composite on the concrete surfaces, particularly strengthening on tension surface.
2. Failures in the adhesive and concrete materials may occur by using thick strengthened composite plate.
3. Filling the epoxy resin inside the notch-region also increases the flexural load capacity of the notched concrete beam. Epoxy provides a strong bonding characteristic in both inner surfaces of the notch.
4. The proposed theoretical model shown in Eqs.(5.63) and (5.28) can be used to estimate the adhesive shear and peel-off stresses, and normal stress of the strengthened plate. The results are well compared with the experimentally validated finite element method.
5. The maximum adhesive shear and peel-off stresses increase with increasing the modulus and thickness of the strengthened plate, and decreasing the thickness of the adhesive layer. However, the stress transferring length from the plate end decreases with increasing the maximum shear stress.
6. The proposed superposition method as discussed in Section 5.3 is simple and can be effectively used for the evaluations of stress intensity factor K_I and maximum tensile

stress σ_p in the concrete beam and externally bonded reinforcement, respectively when it is satisfied to Eq.(5.81).

7. The use of high modulus and thick materials as the reinforced plate for the strengthened cracked-beam reduces the value of K_I. However, the value of σ_p increases as the modulus and thickness of the plate increase.
8. The failure mode of the strengthened beam is highly dependent on the modulus ratio of the concrete and reinforced materials, thickness of the reinforced plate and the crack-length of the structure.

CHAPTER 6

STRAIN MONITORING USING FBG SENSORS

6.1 Introduction

Fibre-optic Bragg grating (FBG) sensor has been extensively adapted as a new non-destructive evaluation (NDE) technique in monitoring strain and temperature profiles of structures under service conditions [Huang et al. 1998]. The specialty of using FBG sensor for strain sensing application is that it is able to measure strains locally with high resolution and accuracy. As the physical size of an optical fibre is extremely small compared with other strain measuring components, it enables to be embedded into the structures for determining the strain distributions without influencing the mechanical properties of the host materials [Maaskant et al 1997].

The precision of the measurement by using the FBG strain sensor is highly dependent on the bonding characteristics among the fibre core, protective coating, adhesive layer and host material. The principle of the FBG technology is to gauge the light reflective signal from the grating (the region where the sensor is located) region when it is subjected to strain. Ideally, the embedded sensor should provide the straining signal that is equivalent to the strain of the host structure to the operator. However, the existence of the adhesive layer and protective coating would absorb part of energy when the structure is under loading. Therefore, the strains experienced by host material are not wholly transferred to the bare fibre and some of them may be lost through interface shear transfer within the protective coating and adhesive layer.

In this section, a theoretical model to evaluate the differential strains between the bare fibre and host material with different adhesive thickness and modulus of the protective coating of

the embedded FBG sensor is firstly introduced. The results are then compared with numerical analysis by using finite element method (FEM). The later part is to perform experimental investigations on using the FBG sensors as internal strain measuring device for glass fibre composite strengthened concrete structure. Single and multiplexed FBG sensors have been used in present study.

6.2 Theoretical Approaches

6.2.1 Load Transfer Properties

6.2.1.1 Constant load applied along fibre longitudinal direction

For the practical problem mentioned above, the bonding characterisation at the interfaces between the host material and adhesive layer, adhesive layer and protective coating, and protective coating and bare fibre (the actual segment from that the strain is measured) would influence the true strain measured from the FBG sensor. The adhesive layer and the protective coating would absorb part of energy and therefore, shear deformation results [Ansari and Yuan, 1998]. Besides, the total embedding length ($2L_f$) of the fibre would affect the accuracy of measurement by using the FBG sensor because the shear stress concentration exists at the fibre ends. Fig.6.1 shows a four-cylinder model for the analysis of the stress transfer. The cross-section microscopy photograph of a typical sensor embedded in specimen is given in Fig. 6.2. The longitudinal axis z represents the direction (fibre direction) of the applied load. Transverse direction r represents the distance measured from the centre (r=0) of the fibre core. In Fig. 6.1. subscripts c, p, a and h denote the bare fibre, protective coating, adhesive layer and host material, respectively. Tensile and shear moduli are given by E and G, respectively. $\tau_a(z,r)$ and $\tau_{ap}(z,r)$ denote the shear stresses along the axial direction at the interfaces between the host material and adhesive layer and between the adhesive layer and protective coating, respectively. The symbols r_h, r_{ap}, and r_c represent the inner radius of the host material, the outer radii of the protective coating and the bare fibre, respectively measured from the centre of the fibre core. The axial loads are applied on the host material, adhesive layer, protective coating and bare fibre along the given model by N_h, N_a, N_p and N_c, re-

spectively. Because of the symmetry about both r and z-axises, only a quarter section of the embedding fibre system is considered for the strain analysis.

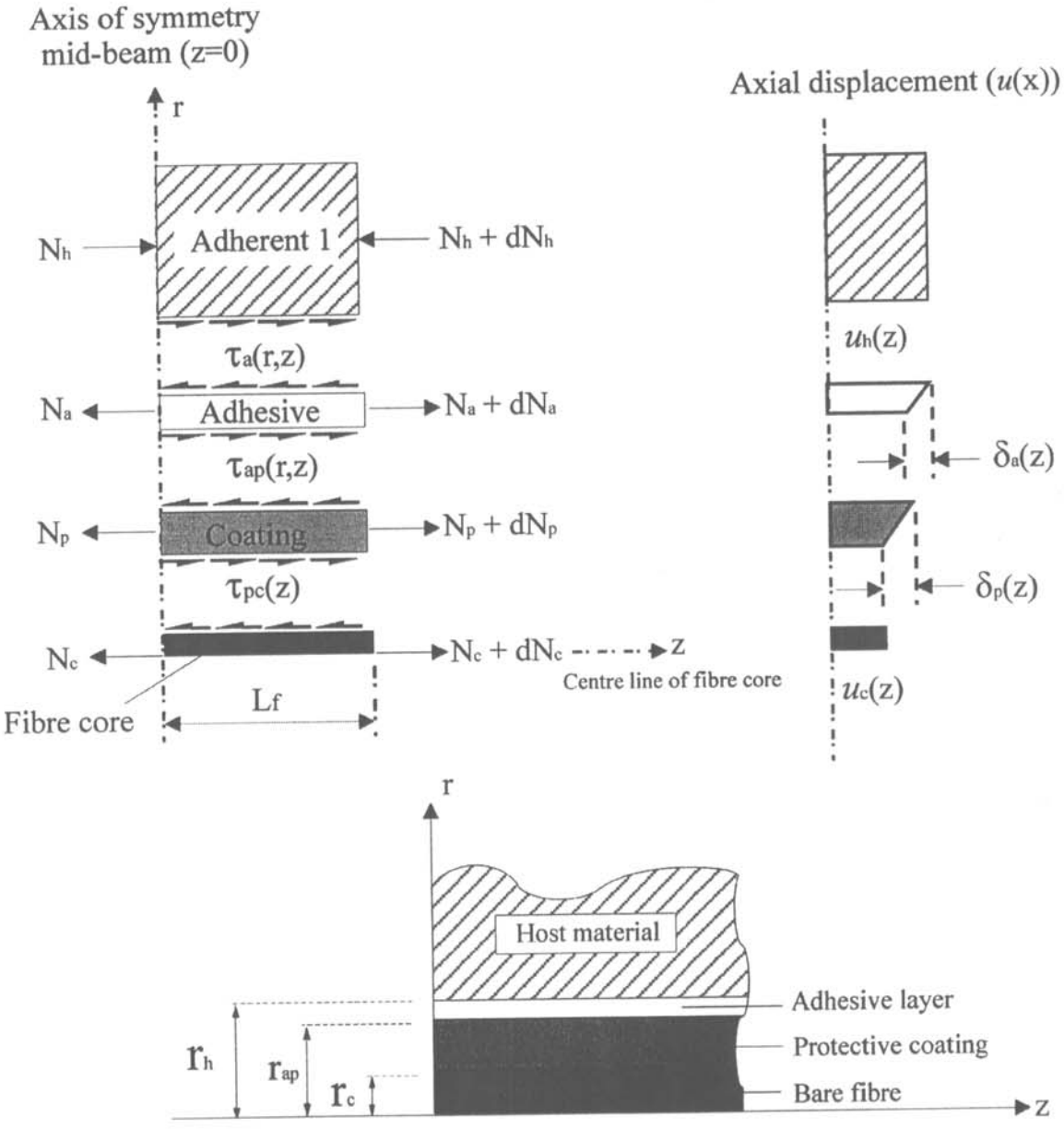

Figure 6.1 Four-cylinder model for the present study.

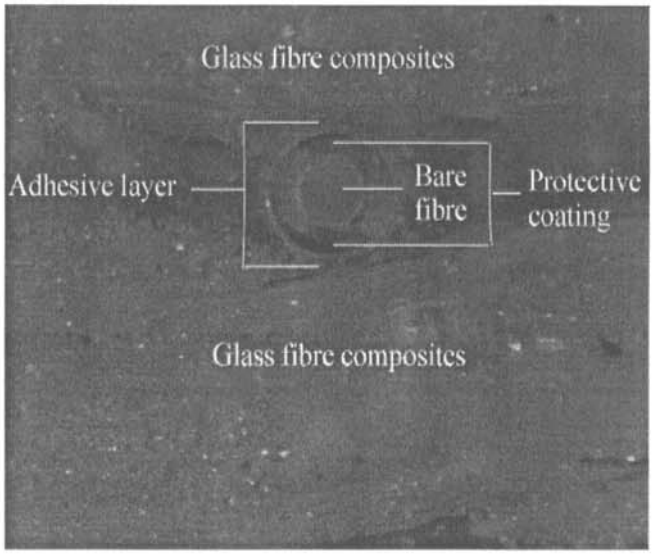

Figure 6.2 Cross-section view (microscopic scale) of the composite structure with the embedded optical fibre sensor.

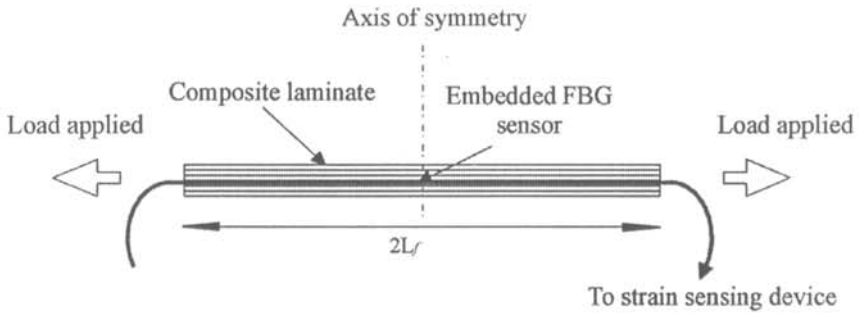

Figure 6.3 A beam model of the composite laminate with the embedment of an optical fibre.

Table 6.1 lists the mechanical properties and geometrical factors for current theoretical study. A typical composite laminate with an embedded FBG sensor is shown in Fig.6.3. The following basic assumptions are made to simplify the case of current study:

1. Mechanical behaviours of the bare fibre, protective coating, adhesive layer and host material are linear, elastic and isotropic.
2. All interfaces are perfectly bonded. Therefore, the displacement conditions are described by:

$$u(z)=\begin{cases} u_h(r,z)=u_a(r,z) & for \quad r=r_h \\ u_a(r,z)=u_p(r,z) & for \quad r=r_{ap} \\ u_p(r,z)=u_c(r,z) & for \quad r=r_c \end{cases}. \tag{6.1}$$

The relative displacements (δ) of the adhesive material and the protective coating due to shear deformation are given by:

$$\delta_a(z) = u_a(r_h,z)-u_a(r_{ap},z) \tag{6.2}$$

At the mid-beam region (z=0), the strains for all elements are mathematically identical, i.e.

$$\varepsilon_h(0,r)=\varepsilon_a(0,r)=\varepsilon_{ap}(0,r)=\varepsilon_c(0,r) \tag{6.3}$$

3. No thermal load is applied in the system. The strain evaluated at the core region only responds the strain induced by the load applied axially.

Table 6.1 Mechanical properties and geometrical factor for current theoretical study.

Description	Symbols	Values
Diameter of bare fibre (μm)	r_c	125
Outer diameter of protective coating (μm)	r_{ap}	250
Young's modulus (GPa)		
- fibre core	E_c	72
- protective coating	E_p	0.1
- adhesive material	E_a	3.3
- Concrete	E_h	27.8
Shear modulus (GPa)		
- adhesive material	G_a	1.2
- protective coating	G_p	0.037
Thickness of an adhesive layer (mm)	t_a	0.1

By considering the force equilibrium for the element of the protective coating in the loading direction shown in Fig.6.1, the shear stress in the protecting coating can be approximately obtained by using the following relationship:

$$\pi\left(r^2 - r_c^2\right)\sigma_p + 2\pi r_c \int_0^{L_f} \tau_{ap}(z, r_c)dz - 2\pi r \int_0^{L_f} \tau(z, r)dz = 0 \tag{6.4}$$

where σ_p is the axial stress in the protective coating material in z direction. Equation (6.4) can then be rewritten in the following form:

$$\frac{1}{L_f}\int_0^{L_f}\left(r^2 - r_c^2\right)\sigma_p dz + 2r_c \int_0^{L_f} \tau_{ap}(z, r_c)dz - 2r\int_0^{L_f} \tau(z, r)dz = 0 \tag{6.5}$$

Hence, Eq.(6.5) is alternatively written as the following format:

$$\frac{1}{L_f}\left(r^2 - r_c^2\right)\sigma_p + 2r_c\tau_{ap}(z, r_c) - 2r\tau(z, r) = 0 \tag{6.6}$$

In general case, the embedding length of the optical fibre is greater than the fibre diameter, L >> r, so that the first term in Eq.(6.6) becomes very small compared to anther terms in the equation and therefore, this term can be neglected in current calculation. This results in the relationship between the shear stress in the coating and the core at any section x as

$$\tau(z, r) = \frac{r_{ap}}{r}\tau_{ap}(z, r) \qquad r_c \le r \le r_{ap} \tag{6.7}$$

Similarly, the shear stress in the adhesive material is expressed by

$$\tau(z, r) = \frac{r_{ap}}{r}\tau_{ap}(z, r) \qquad r_{ap} \le r \le r_h \tag{6.8}$$

The axial displacement of the host material can be obtained by considering the condition of compatibility for all elements shown in Fig.6.1:

$$u_h(z) = \delta_a(z) + \delta_p(z) + u_c(z) \tag{6.9}$$

in which the relative displacement of the adhesive layer is determined by

$$\delta_a(z) = \frac{1}{G_a} \int_{r_{ap}}^{r_h} \tau(z,r)dr \tag{6.10}$$

and the relative displacement of the protective coating is given by

$$\delta_p(z) = \frac{1}{G_p} \int_{r_c}^{r_{ap}} \tau(z,r)dr \tag{6.11}$$

For the host material and the bare fibre, the axial displacements are given by

$$u_h(z) = \int_0^z \frac{\sigma_h(z)}{E_h} dz \tag{6.12}$$

and

$$u_c(z) = \int_0^z \frac{\sigma_c(z)}{E_c} dz \tag{6.13}$$

The tensile force of the fibre core can be expressed as

$$N_c(z) = \pi r_c^2 \sigma_c - 2\pi r_c \int_0^z \tau_{pc}(z,r_c)dz = \pi r_c^2 \sigma_c - 2\pi r_{ap} \int_0^z \tau_{ap}(z,r_{ap})dz \tag{6.14}$$

where σ_c is the axial stress of the bare fibre at mid-beam section (z=0). Substituting Eqs. (6.10-6.13) into Eq. (6.9) yields the following integral equation:

$$\int_0^z \frac{\sigma_h}{E_h} dz = \frac{r_{ap}}{G_a}\tau_{ap}(z, r_{ap}) \ln\left(\frac{r_h}{r_{ap}}\right) + \frac{r_{ap}}{G_p}\tau_{ap}(z, r_{ap}) \ln\left(\frac{r_{ap}}{r_c}\right) + \frac{1}{E_c \pi r_c^2} \int_0^z \left[\sigma_c \pi r_c^2 - 2\pi r_{ap} \int_0^\xi \tau_{ap}(\xi, r_{ap}) d\xi\right] dz \tag{6.15}$$

By differentiating Eq (6.15) and combining the compatibility condition (6.3), the equation is simplified as

$$\frac{-2r_{ap}}{E_c r_c^2} \int_0^z \tau_{ap}(z, r_{ap}) dz + \left\{\frac{r_{ap}}{G_a} \ln\left(\frac{r_h}{r_{ap}}\right) + \frac{r_{ap}}{G_p} \ln\left(\frac{r_{ap}}{r_c}\right)\right\} \frac{\partial \tau_{ap}(z, r_{ap})}{\partial z} = 0 \tag{6.16}$$

Further differentiating Eq (6.16) gives

$$\frac{\partial^2 \tau_{ap}(z, r_{ap})}{\partial z^2} - \lambda^2 \tau_{ap}(z, r_{ap}) = 0 \tag{6.17}$$

where

$$\lambda = \sqrt{\frac{2r_{ap}}{E_c r_c^2 \left(\frac{r_{ap}}{G_a} \ln\left(\frac{r_h}{r_{ap}}\right) + \frac{r_{ap}}{G_p} \ln\left(\frac{r_{ap}}{r_c}\right)\right)}} \tag{6.18}$$

The solution to Eq (6.17) is given by

$$\tau_{ap}(z, r_{ap}) = C_1 \cosh(\lambda z) + C_2 \sinh(\lambda z) \tag{6.19}$$

Two unknowns C_1 and C_2 are determined using two boundary conditions. The first boundary condition is evaluated at z=0. The axial load (N_c) at the bare fibre is determined by the compatibility condition (Eq (6.3)). The strain of the fibre core at the mid-beam region is equal to the strain of the host material. The second boundary condition is evaluated at the point where the axial load of the fibre core is zero, i.e.

$$N_c(0) = \sigma_h \pi r_c^2 \frac{E_c}{E_h} \quad \text{and} \quad N_c(L_f) = 0 \tag{6.20}$$

in which L_f is the distance measured from the mid-beam (z=0) to the point of zero axial load of the fibre. Using above boundary conditions, the constants C_1 and C_2 are obtained by

$$C_1 = \frac{\sigma_c r_c \lambda}{2\sinh(\lambda L_f)} \quad \text{and} \quad C_2 = 0 \tag{6.21}$$

Combining Eqs (6.19) and (6.21) yields the final form of shear stress distribution at the interface between the adhesive layer and protective coating:

$$\tau_{ap}(z, r_{ap}) = \frac{\sigma_c r_c \lambda}{2\sinh(\lambda L_f)} \cosh(\lambda z) \tag{6.22}$$

Further, the axial stress of the bare fibre, $\sigma_c(z)$, can be determined by substituting the Eq. (6.22) into Eq. (6.14):

$$\sigma_c(z) = \frac{1}{\pi r_c^2}\left\{\sigma_c \pi r_c^2 - 2\pi r_c \left\{\frac{C_1}{\lambda}\sinh(\lambda z)\right\}\right\} \tag{6.23}$$

Considering the compatibility condition (Eq (6.3)), the axial strain, $\varepsilon_c(z)$, in the fibre core region is given by

$$\varepsilon_c(z) = \varepsilon_0\left(1 - \frac{\sinh(\lambda z)}{\sinh(\lambda L_f)}\right) \tag{6.24}$$

where, ε_0 is the axial strain of the host material at z=0. From Eq (6.24), it is clearly shown that the strain distribution along the axial direction is dominated by the constant variable λ. This parameter is a function of the material properties and geometric factor of the adhesive layer, protective coating and bare optical fibre. Any changes of these properties and factor would influence the stress distribution at bonded ends due to the existent of hyperbolic function ($\sinh(\lambda z)$). The Eq (6.24) also shows that the maximum strain of the fibre is equal to the maximum strain of the host material at z = 0.

The axial strains of the bare optical fibre along the bonded length are plotted in Fig.6.4 for the different bonded lengths (L_f), tensile moduli of the protective coating (E_p) and thicknesses of the adhesive layer ($t_a = r_h - r_{ap}$).

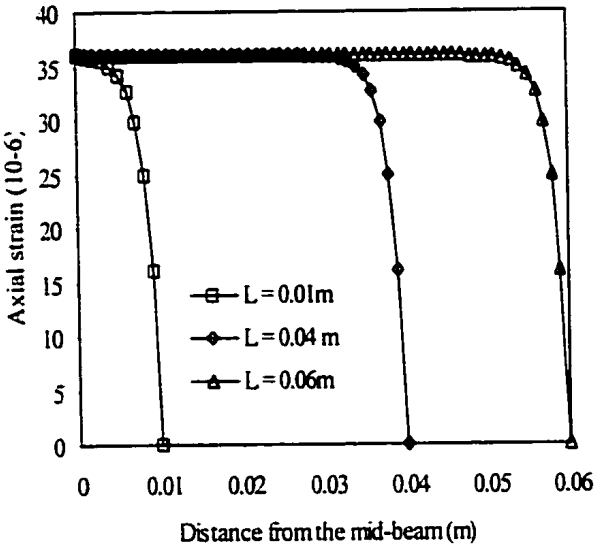

Figure 6.4a Axial strain of the bare fibre against the distance measured from the axis of symmetry (z=0) with different embedding lengths.

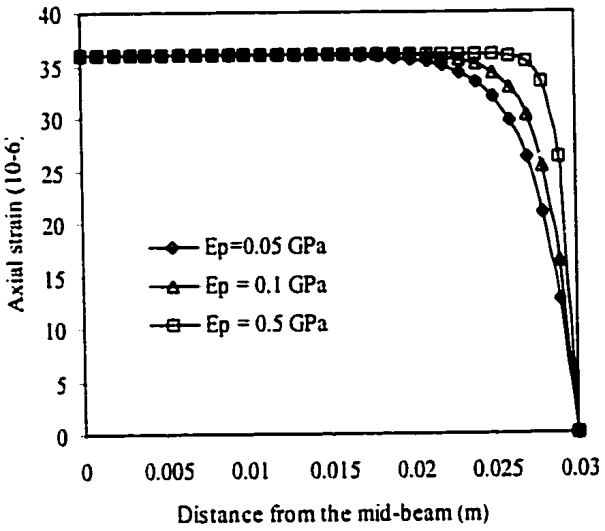

Figure 6.4b Axial strain of the bare fibre against the distance measured from the axis of symmetry (z=0) with different moduli of protective coating material.

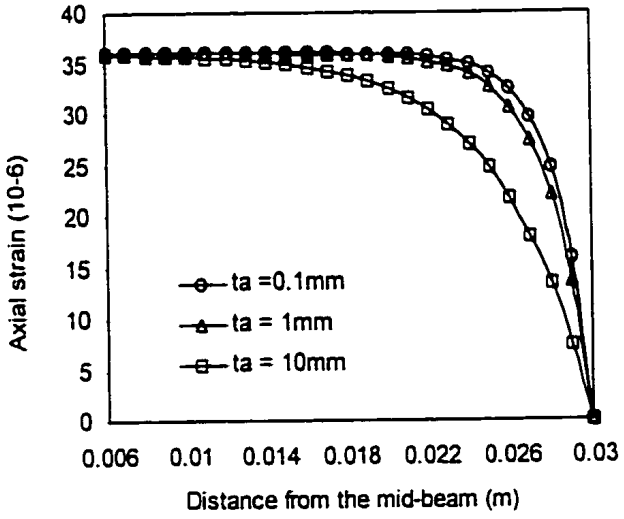

Figure 6.4b Axial strain of the bare fibre against the distance measured from the axis of symmetry (z=0) with different adhesive thicknesses.

In Fig. 6.4, it is apparently demonstrated that a steady strain measurement can be achieved at the fibre core region only when a long bonded length is used. The axial strain of the bare fibre for the different moduli of the protective coating material and thickness of the adhe-

sive layer are plotted. The results indicate that if a high modulus material is used as a fiber protective coating and thin adhesive layer is used as a bond interface layer, it requires a shorter load transfer distance to transfer the load from the host material to the fibre core region. Conversely, a longer distance is required to transfer all loads to the fibre core by using low modulus material and thick adhesive layer. A large part of the energy is converted into shear deformations at the coating and adhesive materials. The axial shear stresses ($\tau_{ap}(z,r_{ap})$) are shown in Fig.6.5 for different adhesive thicknesses.

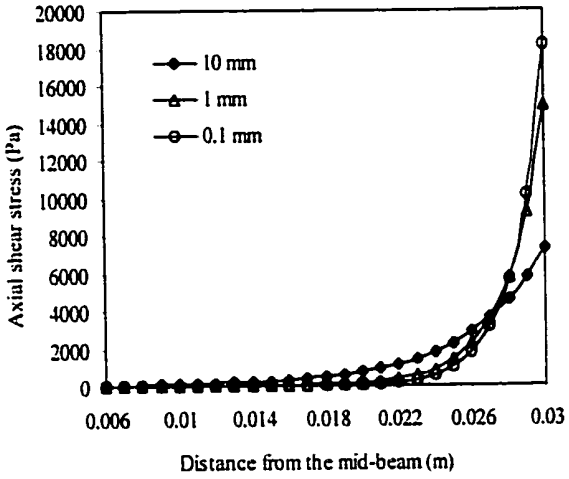

Figure 6.5 Shear stress against the distance measured from the axis of symmetry (z=0) with different adhesive thicknesses.

The shear stress concentration at the bonded end region rapidly vanishes with increasing distance toward the mid-beam (z=0) region. The high shear stress region reduces with decreasing thickness of the adhesive layer. However, the maximum shear stress $\tau_{ap}(z,r_{ap})$ increases with increasing adhesive thickness. Increasing the thickness of the adhesive layer would prolong the shear stress concentration region at the bonded end region.

In Eq. (6.25), it is obviously indicated that the maximum strain of the fibre core (ε_c) at z=0 is same as the strain measured at the host material (ε_h) due to the basic assumption (N_a=N_p=0). However, it may not be true when a thicker adhesive layer is used. During the adhesion process, a thin adhesive layer cannot be in general precisely controlled. The thick-

ness of an adhesive layer is normally beyond the desired limit. A thick adhesive layer, in turn may take up part of the axial load from the host material. The strain measured from the fibre core region is slightly less than the strain of the host material. Therefore, the Eq (6.24) should be rewritten in the following form:

$$\varepsilon_c = A_1 \varepsilon_o \left\{ 1 - \frac{\sinh(\lambda z)}{\sinh(\lambda L_f)} \right\} \tag{6.25}$$

where A_1 is the function of the material and geometric constants of the adhesive layer, protective coating, bare fibre and host material. It is assumed that a part of the axial load is taken up by an adhesive layer (N_p). By considering the force equilibrium at mid-beam region (z=0) and substituting the compatibility condition (6.3), the maximum strain of the bare optical fibre at the mid-beam region is obtained by:

$$\varepsilon_c = \varepsilon_o \frac{1}{\left\{ \frac{E_h}{E_c} + \frac{E_a}{E_c} \left(\frac{r_h^2 - r_{ap}^2}{r_{ho}^2 - r_h^2} \right) + \left(\frac{r_c^2}{r_{ho}^2 - r_h^2} \right) \right\}} \tag{6.26}$$

where r_{ho} is the outside radius of the host material.

6.2.1.2 Bending load added along fibre longitudinal direction

In this section, optical fibre embedded in the structure, which is subjected to non-uniform stress distribution along the fibre direction is investigated theoretically. Fig 6.6 illustrates the structure with the embedment of the FBG sensor at the middle region (z=0) of the fibre , which is subjected to three point bending load.

In the diagram, it is obviously shown that the maximum bending moment is reached at the mid-beam section. It can be evaluated by multiplying the reaction load in the support ($P/2$) to the distance between the support and mid-beam (L_f). To determine the stress transferring

properties for the system shown as above, the same initial procedure as Eqs (6.1) to (6.14) is followed. The bending moment at any section along the beam longitudinal axis can be expressed by

$$M_b(z) = \frac{P}{2}(L_f - z). \tag{6.27}$$

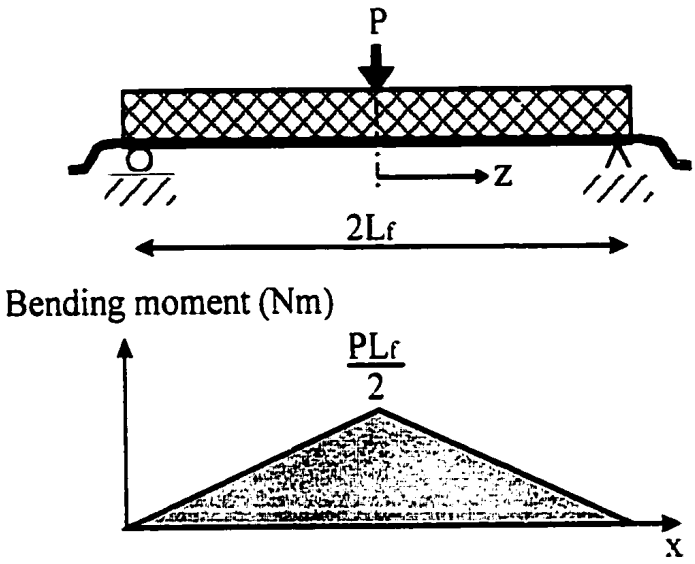

Figure 6.6 Schematic diagram for the structure with the embedment of optical fibre sensor subjected to three point bending load.

The normal tensile stress at the bottom of the beam at any point measured from the mid-beam, z is given by

$$\sigma_h(z) = \frac{3P}{bh^2}(L_f - z). \tag{6.28}$$

Assume that σ_{ho} is the maximum tensile stress at the mid-beam (z=0) of the structure. Eq (6.28) can then be rewritten to the form:

$$\sigma_h(z) = \sigma_{ho} - \frac{3Pz}{bh^2}. \tag{6.29}$$

Then, the Eq (6.16) for the condition of uniform applied load of the structure along the optical fibre direction can be alternated to the following form for the structure subjected to three point bending load, i.e. tensile stress of the structure is expressed as a function of z:

$$\left\{\frac{r_{ap}}{G_a}\ln\left(\frac{r_h}{r_{ap}}\right)+\frac{r_{ap}}{G_p}\ln\left(\frac{r_{ap}}{r_c}\right)\right\}\frac{\partial\tau_{ap}(z,r_{ap})}{\partial z}+\frac{\sigma_c}{E_c}-\frac{2r_{ap}}{E_c r_c^{\,2}}\int_0^z\tau_{ap}(z,r_{ap})dz=\frac{\sigma_h}{E_h}-\frac{3Pz}{E_h bh^2} \tag{6.30}$$

By considering the strain compatibility condition at the mid-beam region (z=0), the Eq (6.30) can then be simplified after differentiation:

$$-\frac{3P}{E_h bh^2}=\left\{\frac{r_{ap}}{G_a}\ln\left(\frac{r_h}{r_{ap}}\right)+\frac{r_{ap}}{G_p}\ln\left(\frac{r_{ap}}{r_c}\right)\right\}\frac{\partial^2\tau_{ap}(z,r_{ap})}{\partial z^2}-\frac{2r_{ap}}{r_c^{\,2}E_c}\tau_{ap}(z,r_{ap}). \tag{6.31}$$

The Eq. (6.31) can then be expressed as

$$\frac{\partial^2\tau_{ap}(z,r_{ap})}{\partial z^2}-\lambda^2\tau_{ap}(z,r_{ap})+\eta=0 \tag{6.32}$$

where

$$\eta=\frac{3P}{E_h bh^2\left(\frac{r_{ap}}{G_a}\ln\left(\frac{r_h}{r_{ap}}\right)+\frac{r_{ap}}{G_p}\ln\left(\frac{r_{ap}}{r_c}\right)\right)}. \tag{6.33}$$

The solution of Eq (6.33) is given by

$$\tau_{ap}(z,r_{ap})=C_1\cosh(\lambda z)+C_2\sinh(\lambda z)+\phi_o \tag{6.34}$$

For the above equation, two different boundary conditions are required to determine the parameters C_1 and C_2. The last term in the equation can be evaluated by substituting the first and second derivatives of the Eq (6.34) into Eq (6.32). The parameter ϕ_o can then be expressed as

$$\phi_o = \frac{3P}{E_h b h^2 \lambda^2 \left(\frac{r_{ap}}{G_a} \ln\left(\frac{r_h}{r_{ap}}\right) + \frac{r_{ap}}{G_p} \ln\left(\frac{r_{ap}}{r_c}\right) \right)}. \tag{6.35}$$

At the mid-beam region (z=0), the axial force acted on the fibre core along its fibre direction should be equal to $N_c(0) = \sigma_c \pi r_c^2$ while zero axial force is obtained at the plate end region, i.e. $N_c(L_f) = 0$. By using the above boundary conditions, two parameters C_1 and C_2 are then obtained by

$$C_1 = \left(\frac{\sigma_c r_c^2}{2 r_{ap}} - \phi_o L_f \right) \frac{\lambda}{\sinh(\lambda L_f)} \quad \text{and} \quad C_2 = 0 \tag{6.36}$$

Therefore, the Eq (6.34) becomes

$$\tau_{ap}(z, r_{ap}) = \lambda \left(\frac{r_c^2 \sigma_c}{2 r_{ap}} - \phi_o L_f \right) \frac{\cosh(\lambda z)}{\sinh(\lambda L_f)} + \phi_o \tag{6.37}$$

Similarly, the axial stress and strain in the fibre core at any distance z along the fibre direction can be determined by

$$\sigma_c(z) = \sigma_{co} - \frac{2 r_{ap}}{r_c^2} \left(\frac{C_1}{\lambda} \sinh(\lambda z) + \phi_o z \right) \tag{6.38}$$

$$\varepsilon_c(z) = \varepsilon_{co} - \frac{\sigma_{co}}{E_c}\frac{\sinh(\lambda z)}{\sinh(\lambda L_f)} - \frac{2r_{ap}}{E_c r_c^2}\phi_o z \tag{6.39}$$

The axial stress in the fibre core region with different embedding length and modulus of protective coating material, and the shear stress along the coating material ($\tau_{ap}(z,r_{ap})$) with different embedding length are plotted in Fig. 6.7.

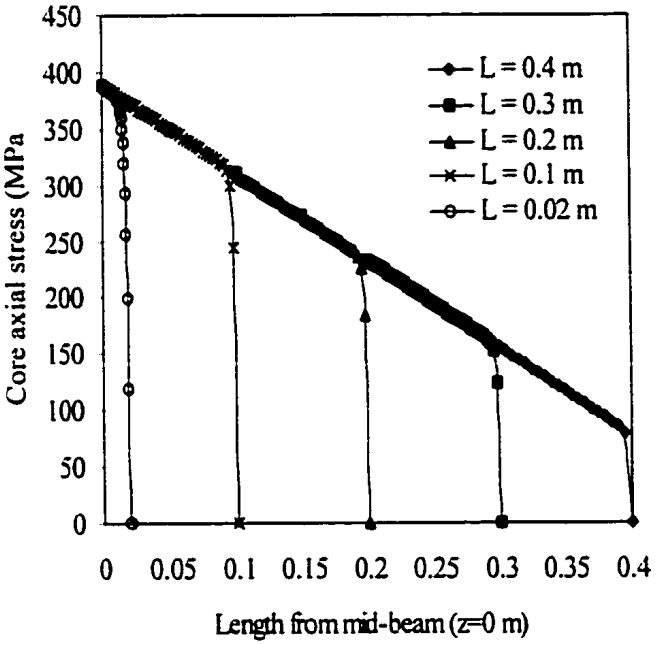

Figure 6.7a. Fibre core axial stress against different embedding lengths.

It is shown in the diagrams that the stress transferring length increases with increasing the modulus of protective coating. Since high modulus coating material reduces the shear deformation in the coating layer, it allows the stress to be fully transferred from the host material to the fibre core within a short distance. The stress transferring length is mainly dependent on the hyperbolic function showed in the Eq. (6.37). High coating shear stress is resulted when decreasing the overall embedding length of the fibre. It may be due to the increases of tensile stress at the bottom of the beam when the distance from the mid-beam is reduced.

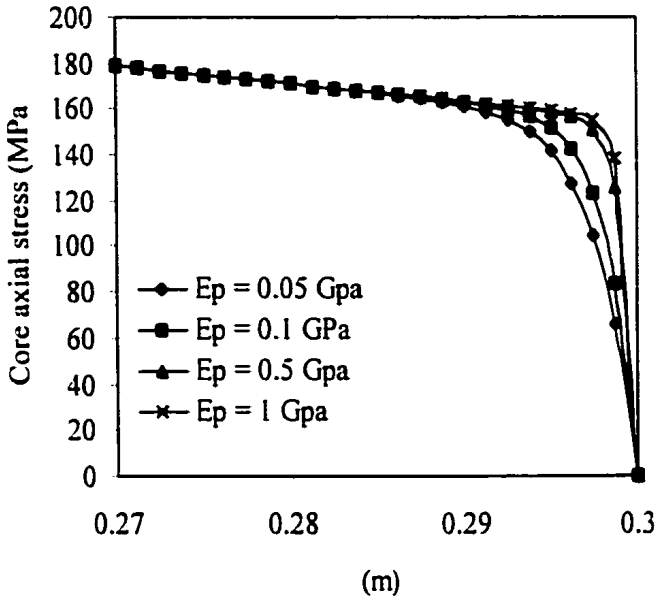

Figure 6.7b Fibre core axial stress against different moduli of protective coating material.

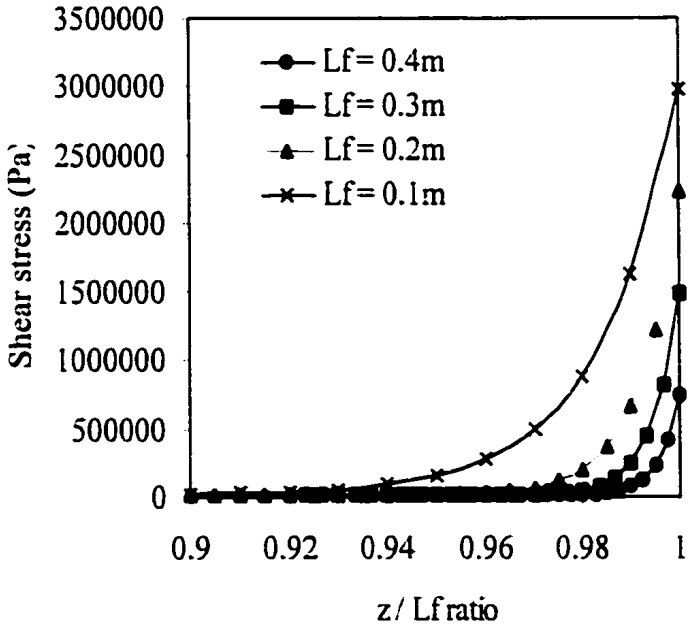

Figure 6.7c Shear stress against different embedding lengths of the fibre sensor.

6.2.1.3 Minimum fibre embedding length

In the Eqs. (6.22) and (6.37), it is observed that the stress transferring length of the optical strain sensor is highly influenced by its embedding length L_f. In order to determine the reasonable embedded optical fibre length in relation to the length of the grating L_g, an approximate method with the error less than 1 % is introduced. To avoid any stress concentration occurred within the fibre grating region, all stresses are assumed to be fully transferred from the structure to the fibre core beyond this region. The hyperbolic function in the Eq (6.22) is then reversed as the following form by using the tolerance of 0.01:

$$L_f = \frac{1}{\lambda}\sinh^{-1}\left\{\frac{1}{0.01}\sinh(\lambda L_g)\right\} \tag{6.40}$$

The minimum embedding length of the optical fibre with different grating lengths and values of λ, which is evaluated from Eq (6.18) is plotted Fig. 6.8. It is shown that the value of minimum embedding length increases with increasing the length of grating region, L_g. The required embedding length increases rapidly when the value of λ is decreased from 400 m^{-1}. Steady decrease of required embedding length is observed when further increasing the value of λ beyond 400m^{-1}.

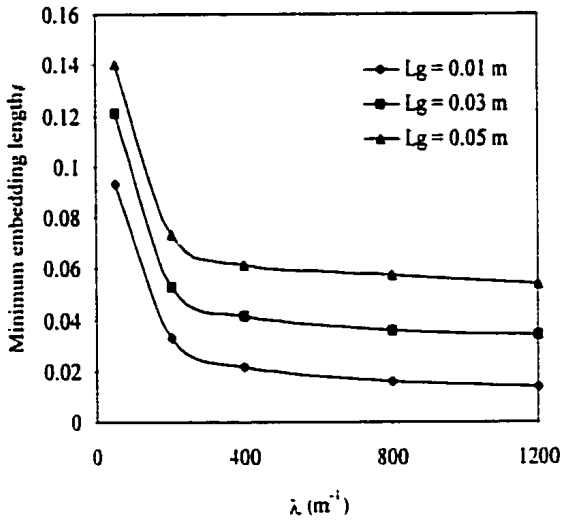

Figure 6.8 Plot of minimum embedding length of the fibre-optic strain sensing with different lengths of grating region and the value of λ.

6.2.1.4 Result verification

The solution from the theoretical study is now verified by the finite element method (FEM) using commercial package of Msc/Nastran. 6 nodes (Traia6) elements were used to generate meshes. Fine mesh was used at the fibre end region to measure the shear stress distribution in the protective coating layer. Since the model is bi-symmetric about its r- and z-axes, only a quarter segment is considered. Three boundary constrains are applied. These include $v|_{r=0} = 0$ and $u|_{z=0} = 0$, where u and v are the displacements along r and z directions, respectively and the point of origin (z=0 and r=0) is fixed. Load is applied on the surface of the model with an uniform pressure of 1 MPa.

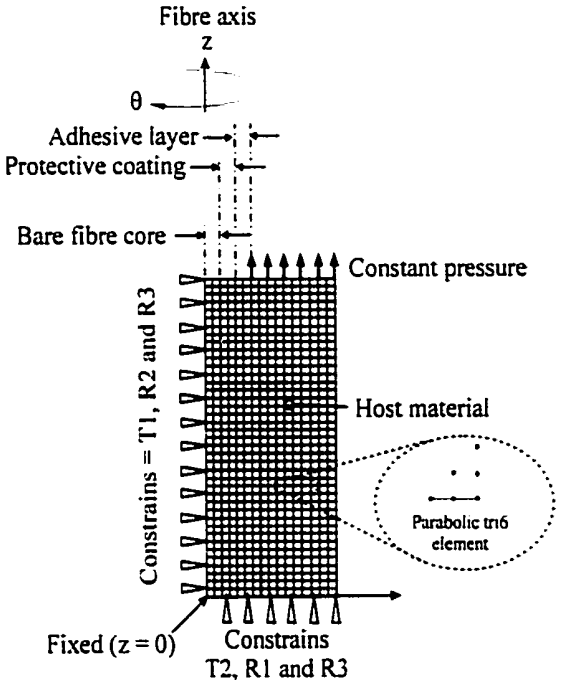

Figure 6.9. The FEM model for comparison of the theoretical analysis.

Details of the mechanical properties and geometry factor used in the model are listed in Table 6.1. Fig. 6.9 illustrates the FEM model for analysing the stress transferring properties of the optical fibre embedded system and to compare the result from theory.

The results evaluated from the Eqns (6.22), (6.24) and (6.26) and FEM are plotted in Fig.6.10. It is shown that the theoretical solutions are in a good agreement with the FEM results. High magnitudes of the axial strain in the fibre core region and shear stress in the protective coating layer are measured at the fibre end region ($z=L_f$) and rapidly vanished with increasing the distance towards the axis of symmetry ($z=0$).

In Fig.6.10c, it is demonstrated that the axial strain at the fibre core region decreases with increasing the thickness of the adhesive layer. The result indicates that the thickness of the adhesive layer should be carefully controlled to avoid the happening of mis-measurement. The comparison of the result also shows that the equation (6.26) is able to predict the difference of strain between the fibre core and the host material for the determined thickness of an adhesive layer.

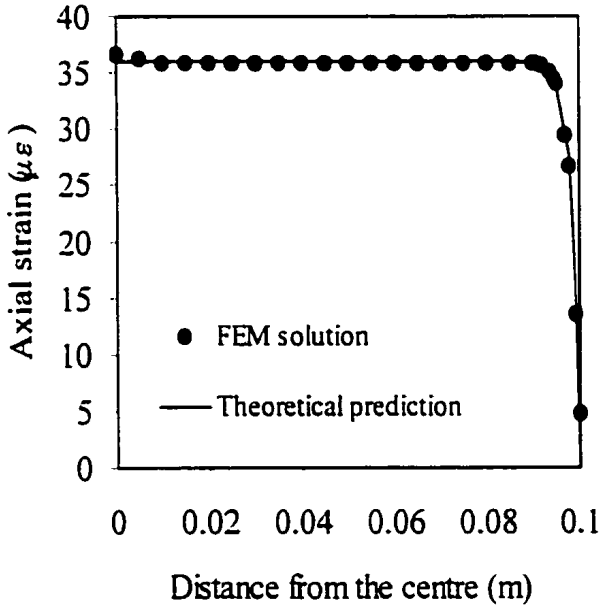

(a)

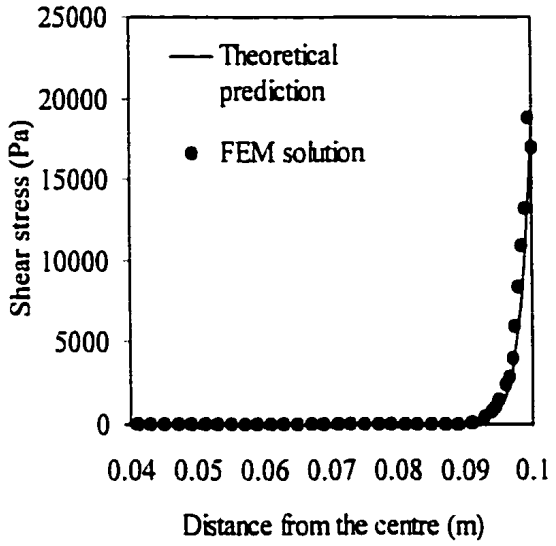

(b)

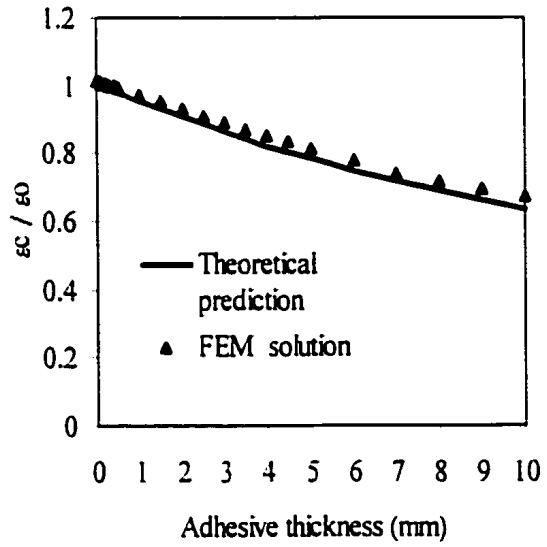

(c)

Figure 6.10. The comparison of the results between the analytical and FEM model for (a) the axial strain of the bare fibre and (b) shear stress of the protective coating against the distance measured from the axis of symmetry (z=0), and (c) the relative strain ($\varepsilon_c/\varepsilon_o$) against the adhesive thickness.

6.2.2 Thermal Effects on Embedded Grating Sensor

In this section, a simple theoretical model is introduced to investigate the mechanical behaviour of the embedded FBG sensor for strain measurement under different ambient temperature environments. The magnitude of the maximum shear stress in the protective coating layer is highly influenced with the values of the coefficient of thermal expansion (CTE) of silica fibre and composite materials. The compaction pressure distribution along the circumference of the coating layer is also varied with temperature.

Investigation on the interfacial properties of the embedded optical fibre system is an important issue since the interface between the optical fibre and surrounding material has to allow stress from the host material to fully transfer to the fibre core region. Composite materials possess different thermal properties, which are dependent on the type of fibre and resin used. A carbon fibre owns a negative value of CTE while glass fibre has a positive value of CTE. The resultant CTE of the composite system is based on several factors, which include (1) fibre volume fraction, (2) CTEs in resin and fibre materials and (3) fibre arrangement inside the composite laminates. For the unidirectional type of composite plate with all fibres aligned in axial direction, the CTE of the composite, α is given by [Mallick, 1997]

$$\alpha = \frac{v_f(\alpha_f - \beta\alpha_m) + \beta\alpha_m}{v_f(1-\beta) + \beta} \tag{6.41}$$

where v_f, α_f, α_m and β represent fibre volume fraction of composite, fibre and matrix longitudinal CTEs, and moduli ratio of the fibre and matrix, E_f/E_m, respectively. It is obviously shown in Eq.(6.41) that the expansion of the composite subjected to the change of temperature is highly influenced by the thermal properties of mixed constituents. For the carbon fibre composite with a high fibre volume fraction, the CTE value is negative. Therefore, the differential axial deformations between the composite and embedded sensor vary with tem-

perature.

A cylinder model, which consists of three different elements including (1) silica fibre core, (2) polyimide protective coating and (3) surrounding composite laminate as shown in Fig. 6.11. Axial loads are applied to the host material, protective coating and bare fibre along the x axis by N_h, N_p and N_c, respectively. E and G represent tensile and shear moduli of the materials. $\tau_p(x,r)$ denotes the shear stresses along the axial direction at the interfaces between the fibre core and protective coating. The symbol r_c, r_p and r_h denote the radial distances measured from the centre of the fibre core to the outside boundaries of fibre core, protective coating and composite cylinder, respectively. Since the model is symmetry about both r- and x-axes, only a quarter section of the cylinder is modelled.

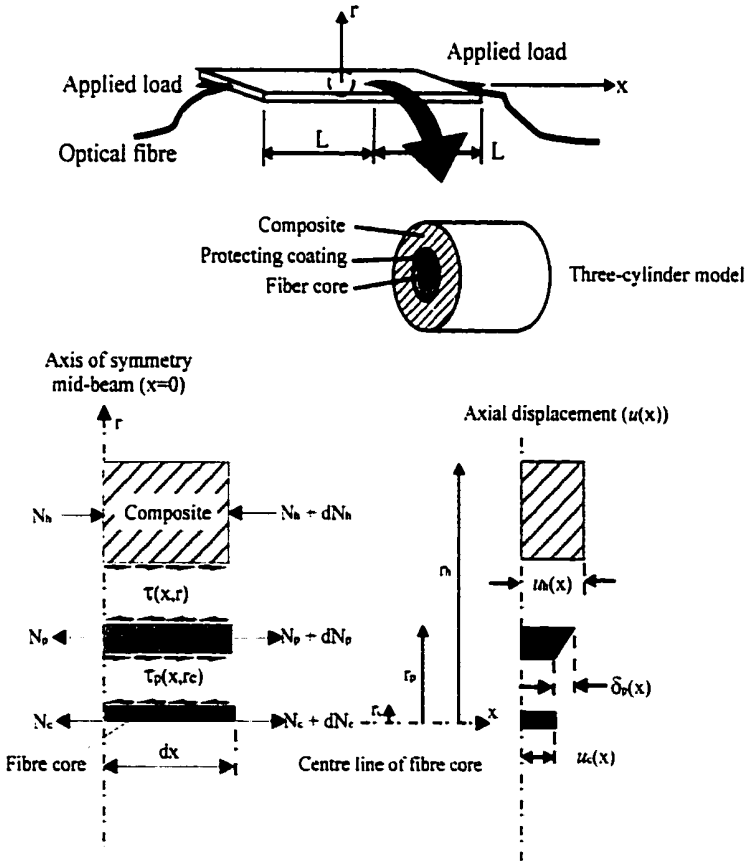

Figure 6.11 A schematic illustration of three-cylinder model

To simplify the procedure of calculation, several common used assumptions are addressed as follows for the current study:

1. Mechanical behaviours of the silica fibre, protective coating layer and composite cylinder are linear and elastic. The mechanical properties of the fibre core and cladding materials are treated as the same [Lo and Xiao, 1998], and they are referred as the fibre core. In reality, the mechanical properties of the fibre core and cladding are only slightly different. The relative refractive index for the fibre core n_{core} and cladding $n_{cladding}$ are 1.46 and 1.45, respectively.
2. Temperature inside the fibre core, coating layer and composite are identical and uniform.
3. Interfaces between the coating and composite are bonded perfectly and no slip happens at the interface between the fibre core and protective coating. Therefore, the displacement conditions are described by

$$\begin{matrix} u_h(x,r_p) = u_p(x,r_p) \\ u_p(x,r_c) = u_c(x,r_c) \end{matrix} \quad \text{for} \quad \begin{matrix} r = r_p \\ r = r_c \end{matrix}. \tag{6.42}$$

By considering the equilibrium condition in a small element dx from the free body diagram showed in Fig. 6.1, the sum of total axial force in the coating segment at any radius of r is equal to zero, i.e.

$$\frac{d\sigma_p(x)}{dx}\frac{\left(r^2 - r_c^2\right)}{2} + \tau_p(x,r_c)r_c - \tau(x,r)r = 0 \tag{6.43}$$

where $\sigma_p(x)$ represents axial stress in the protective coating layer at any section of x. Integrating of Eq.(6.43) yields:

$$\frac{\sigma_p(x)}{2}\left(r^2 - r_c^2\right) + \int_0^x \tau_p(x, r_c) r_c dx - \int_0^x \tau(x, r) r dx = 0 \tag{6.44}$$

Since the protective coating is typically made by a very low modulus material compared with the fibre core itself, it is reasonably assumed that no axial load is taken by the protective coating layer at any section of x [Duck and LeBlanc, 2000], i.e.

$$\frac{\sigma_p(x)}{2}\left(r^2 - r_c^2\right) \approx 0 \tag{6.45}$$

Therefore, the first term in Eq.(6.44) can be ignored in the study. The shear stress in the coating layer at any section x can be expressed in the following format:

$$\tau(x, r_c) = \frac{r_c}{r}\tau_p(x, r) \tag{6.46}$$

Considering the condition of compatibility for all elements shown in Fig. 6.1, the axial displacement of the composite material can be obtained by

$$u_h(x) = \delta_p(x) + u_c(x) \tag{6.47}$$

where δ_p, u_h and u_c represents relative displacement of the protective coating, axial displacements of the composite material and fibre core, respectively. By taking into account the thermal induced strains in the axial direction, the strains of the composite material and fibre core can be expressed as

$$\varepsilon_h(x) = \frac{\sigma_h(x)}{E_h} + \alpha_h \Delta T_h \tag{6.48a}$$

and

$$\varepsilon_c(x) = \frac{\sigma_c(x)}{E_c} + \alpha_c \Delta T_c \tag{6.48b}$$

where $\alpha_h(x)$ and $\alpha_c(x)$ represent the CTEs of the composite (host) material and fibre core in the optical fibre, respectively. ΔT_h and ΔT_c denote the differential temperature of the composite and fibre core, respectively. The axial displacements of the composite material and fibre core are then given by

$$u_h(x) = \int_0^x \left(\frac{\sigma_h(x)}{E_h} + \alpha_h \Delta T_h \right) dx \tag{6.49a}$$

and

$$u_c(x) = \int_0^x \left(\frac{\sigma_c(x)}{E_c} + \alpha_c \Delta T_c \right) dx \tag{6.49b}$$

The relative displacement of $\delta_p(x)$ at any section x can be determined by

$$\delta_p(x) = \frac{1}{G_p} \int_{r_c}^{r_p} \tau(x,r) dr \,. \tag{6.50}$$

The axial load $N_c(x)$ in the fibre core at any distance measured from the mid-cylinder x is then expressed as

$$N_c(x) = \sigma_{co} \pi r_c^2 - 2\pi r_c \int_0^x \tau_p(x, r_c) dx \,. \tag{6.51}$$

where σ_{co} is a axial stress in the fibre core at mid-cylinder region. i.e. x=0. By substituting Eq.(6.51) into Eq.(6.49b), the axial displacement in the fibre core can then be written as

$$u_c(x)=\int_0^x\left\{\frac{1}{\pi r_c^2 E_c}\left\{\sigma_{co}\pi r_c^2-2\pi r_c\int_0^{\xi}\tau_c(\xi,r_c)d\xi\right\}+\alpha_c\Delta T_c\right\}dx \tag{6.52}$$

Substituting Eqs.(6.49a), (6.50) and (6.52) into Eq.(6.47) yields

$$\int_0^x\left(\frac{\sigma_h(x)}{E_h}+\alpha_h\Delta T_h\right)dx=\int_0^x\left\{\frac{1}{\pi r_c^2 E_c}\left\{\sigma_{co}\pi r_c^2-2\pi r_c\int_0^{\xi}\tau_c(\xi,r_c)d\xi\right\}+\alpha_c\Delta T_c\right\}dx+\frac{r_c}{G_p}\tau_p(x,r_c)\ln\left(\frac{r_p}{r_c}\right) \tag{6.53}$$

By differentiating Eq.(6.53) and considering the compatibility strain condition at mid-cylinder section, i.e.

$$\varepsilon_c(0,r)=\varepsilon_p(0,r)=\varepsilon_h(0,r), \tag{6.54}$$

the following relationship is formed:

$$-\frac{2}{r_c E_c}\int_0^x\tau_p(x,r_c)dx+\frac{r_c}{G_p}\frac{\partial\tau_p(x,r_c)}{\partial x}+(\alpha_c\Delta T_c-\alpha_h\Delta T_h)=0 \tag{6.55}$$

Hence, the governing differential equation for the shear stress in the coating layer after differentiating Eq.(6.55) can be expressed as:

$$\frac{\partial^2\tau_p(x,r_c)}{\partial x^2}-\omega^2\tau_p(x,r_c)+\eta=0 \tag{6.56}$$

where

$$\omega=\sqrt{\frac{2G_p}{r_c^2 E_c\ln\left(\frac{r_p}{r_c}\right)}} \tag{6.57a}$$

$$\eta = \frac{\alpha_c \Delta T_c - \alpha_h \Delta T_h}{r_c \ln\left(\frac{r_p}{r_c}\right)}. \tag{6.57b}$$

The solution to Eq.(6.56) is given by

$$\tau_p(x, r_c) = C_1 \cosh(\omega x) + C_2 \sinh(\omega x) + k \tag{6.58}$$

where $k = \eta/\omega^2$. Two boundary conditions are required to solve two constant values of C_1 and C_2. The first boundary condition is evaluated at x=0. The axial load in the fibre core can be evaluated by considering the strain compatibility condition, which is explained in Eq.(6.54). The axial strain in the fibre core region is theoretically equal to the strain of the composite material. It is based on the assumption that no axial load is taken by the coating layer in the embedded optical fibre system. Although this assumption may not be applicable for the optical fibre coated with high strength material such as copper for corrosion detection sensor [Lo and Xiao, 1998], it is well accepted to be used for general strain and temperature measuring sensors, which are coated by low tensile modulus material. The second boundary condition is evaluated at the end point of the cylinder, i.e. x = L. The axial load in the fibre core is equal to zero, i.e. no load is transferred from the host material to the fibre core region, i.e.

$$N_c(0, r_c) = \pi r_c^2 \sigma_{co} \quad \text{and} \quad N_c(L, r_c) = 0. \tag{6.59}$$

Therefore, the constant values of C_1 and C_2 are obtained by

$$C_1 = \frac{\sigma_{co} r_c \omega}{2(\sinh(\omega L) + k\omega L)} \quad \text{and} \quad C_2 = 0. \tag{6.60}$$

The final equation of the shear stress distribution along the protective coating layer is then

given by

$$\tau_p(x) = \frac{\sigma_{co} r_c \omega}{2(\sinh(\omega L) + k\omega L)} \cosh(\omega x) + k. \tag{6.61}$$

The equations of the axial load and strain in the fibre core region at any section of x are further obtained as

$$N_c(x) = \pi r_c^2 \left\{ \sigma_{co} - \frac{2}{r_c} \left(\frac{\sigma_{co} r_c \omega}{2(\sinh(\omega L) + k\omega L)} \sinh(\omega x) + kx \right) \right\}. \tag{6.62}$$

and

$$\varepsilon_c(x) = \varepsilon_{co} \left(1 - \frac{2}{r_c} \left(\frac{r_c \omega}{2(\sinh(\omega L) + k\omega L)} \sinh(\omega x) + \frac{kx}{\sigma_{co}} \right) \right) \tag{6.63}$$

where ε_{co} denotes axial strain in the fibre core at the mid-cylinder region. According to the Eq.(6.61), it is obviously shown that the stress transfer properties from the surrounding composite materials to the fibre core region are highly influenced by a hyperbolic function. cosh(ωx). ω is a function of mechanical properties and geometrical factors of the protective coating and fibre core materials. The second term in Eq.(6.62) expresses the thermal effects from both the composite and fibre core materials. Therefore, any changes of the fibre core. coating and composite materials and temperatures may result in changing the stress transfer behaviour and magnitude of the maximum shear stress in the coating layer. In the current study, carbon/epoxy, Kelvar/epoxy and E-glass/vinyl ester composites are used as the surrounding material for the embedded optical fibre system to compare their stress transfer behaviours under a same loading and temperature conditions. All mechanical and geometrical properties are listed in Table 6.2. An axial stress of 100 MPa is applied on the end of the composite cylinder with the differential temperature variation ranging from 0°C (RT) to 80°C. In the study, it is assumed that the differential temperature in the fibre core and host

material is same, i.e. $\Delta T_c = \Delta T_h$.

The shear stress distribution in the protective coating layer estimated from the theoretical prediction are plotted in Figs.6.12 to 6.14. It is shown in the figures that the maximum shear stress decreases with increasing the differential temperature ΔT if the optical fibre is embedded into the carbon/epoxy (Fig.6.11) and Kelvar/epoxy (Fig.6.13) composites. In contrary, the maximum shear stress decreases with decreasing the differential temperature ΔT if the optical fibre is embedded into the E-glass/epoxy (Fig. 6.12) composite. This implies that the magnitude of the maximum shear stress in the coating material is dominated by the value of the CTE of the surrounding composite material.

Table 6.2 Mechanical and geometrical information for present study

	Silica fibre	Coating (Polyimide)	Carbon/ epoxy	Kelvar/ epoxy	E-glass/ vinly ester
Tensile modulus (GPa)	72	0.047	180	76.32	38.6
Thermal coefficient of Expansion (10^{-6} m/m/°C)	5	45	0.02	-1.1	8.6
Fibre volume fraction	—	—	0.6	0.6	0.6
r_c (μm)			62.5		
r_p (μm)			125		
r_h (μm)			500		
L (m)			0.2		

In Table 6.3, it is shown that the values of the CTE of the carbon and Kelvar fibres are negative while E-glass fibre is positive. This implies that the carbon and Kelvar composite materials contract with increasing the temperature, which results in reducing the resultant axial strain in the composite cylinder, $\varepsilon_h(x)$. i.e.

$$\varepsilon_{total}(x) = \varepsilon_{applied\ load}(x) - \varepsilon_{thermal\ contraction}(x) \tag{6.64}$$

The shear stress in the coating layer is then reduced in due course. Accordingly, the reverse shear action (gives negative shear stress value) may occur if the negative value of the CTE of the surrounding composite material reaches a critical limit, i.e. Kelvar/epoxy composite

with high fibre volume fraction. The optical fibre trends to protrude from the composite at the plate end region while the composite contracts as shown in Fig.6.15.

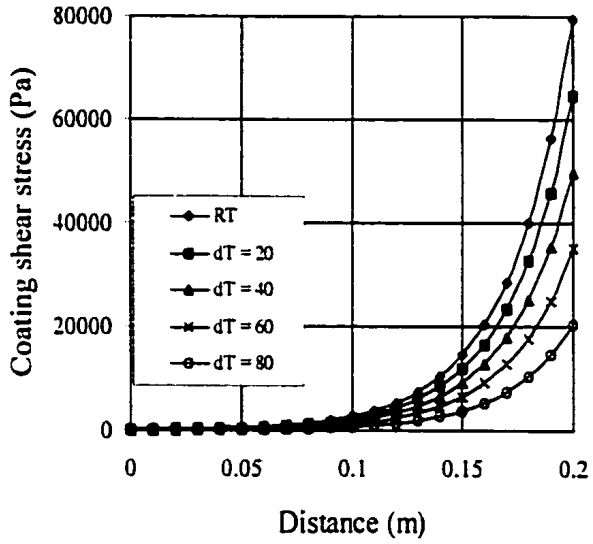

Figure 6.12. Shear stress in coating layer of the optical fibre surrounding by carbon/epoxy composite.

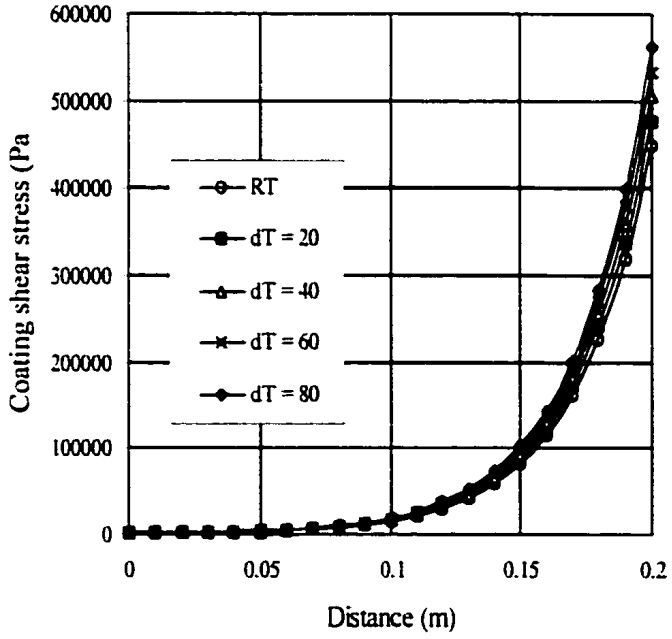

Figure 6.13. Shear stress in coating layer of the optical fibre surrounding by E-glass/vinlyester composite.

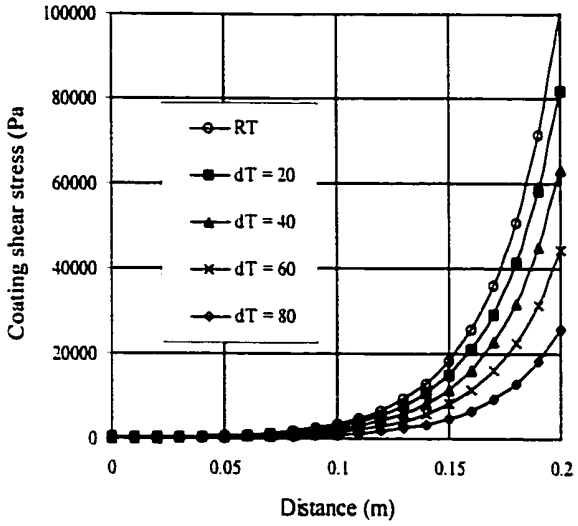

Figure 6.14. Shear stress in coating layer of the optical fibre surrounding by Kevlar/epoxy composite.

Table 6.3 Coefficients of thermal expansion for various fibre, matrix and composite materials.

Materials	Coefficient of thermal expansion (10^{-6} m/m/°C)
Fibres	
Graphite	-1.3
Kelvar	-5
E-glass	5
Matrix	
Epoxy	65
Vinylester	45
Advanced compsoites	
Graphite/epoxy ($v_f = 0.6$)	0.02
Glass/epoxy ($v_f = 0.25$)	14.25

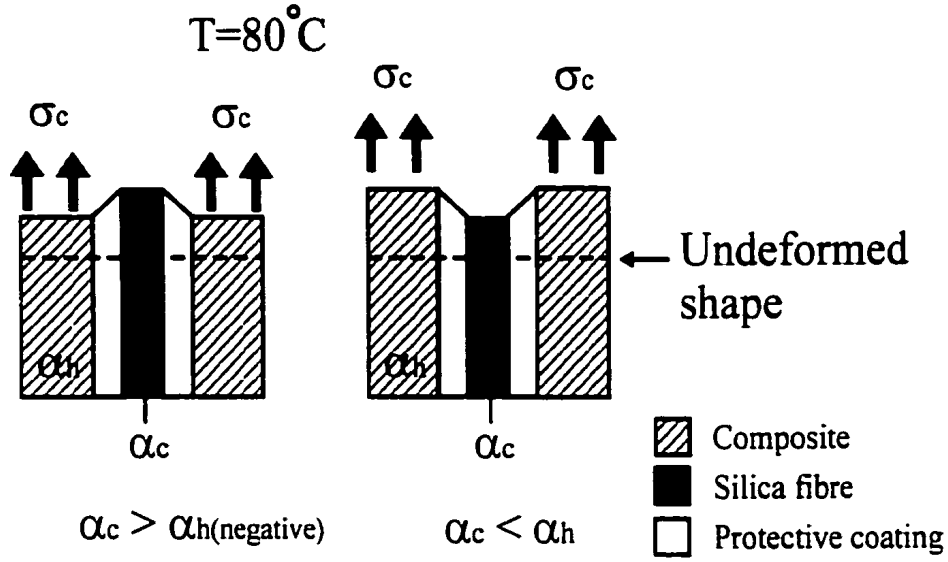

Figure 6.15. Deformation patterns of embedded optical fibre surrounding by composite materials with different CTE properties.

However, for the E-glass composite cylinder, the axial strain increases with the increase of temperature. This makes further expansion of the composite material and the resultant strain is much greater than that the strain induced by the applied load alone. It therefore gives highest shear stress in the coating materials when the temperature of the composite increases. The fibre core axial load against different embedding lengths is plotted in Fig. 6.16. It is found that the maximum axial load in the optical fibre core increases with increasing the temperature for the glass fibre composite material. The overall stress transferring length is almost unchanged with temperature. It is worth to note here that the selected embedding length of the optical fibre should be longer than the grating length of the FBG sensor. The grating should be laid inside the steady stress transfer region in order to provide an accurate strain measuring result.

The radial stress at the interface between the coating and composite due to the thermal expansion of the embedded optical fibre and surrounding composite materials can be evaluated by super-positioning the equations for thick walled cylinder [Yuan and Zhou, 1998a]

method. Figure 6.17 shows a two-dimensional model for investigating radial shrinkage pressure of the optical fibre due to thermal effect and external applied load.

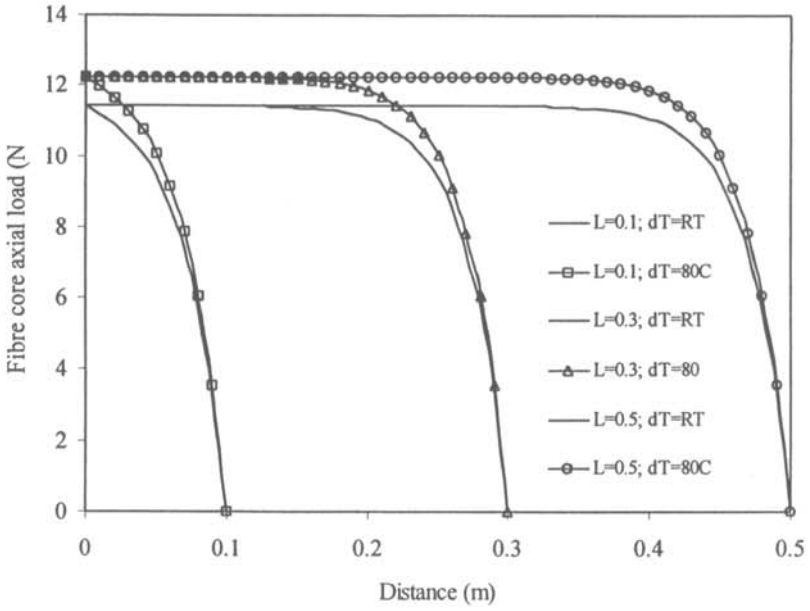

Figure 6.16. Fibre core axial load versus embedding length of the optical fibre.

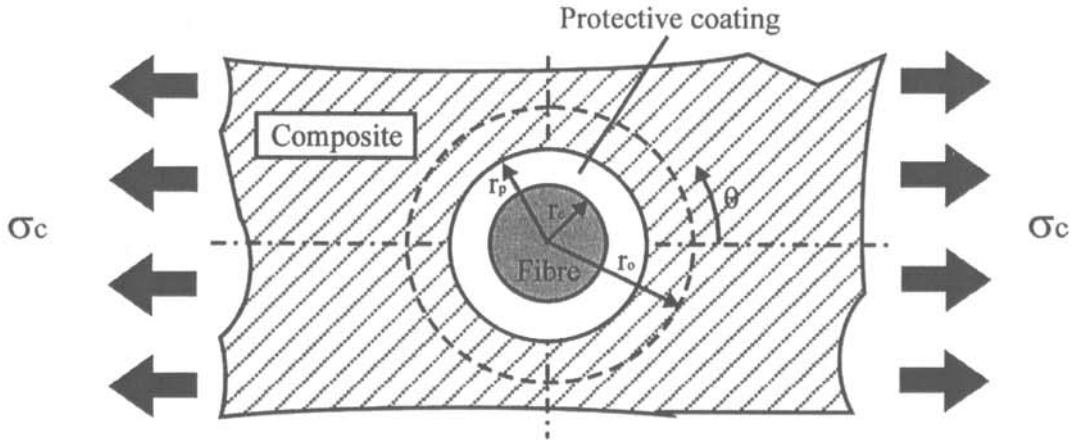

Figure 6.17. A 2-D model for interpretation of compaction pressure on coating surface.

The radial CTE of the composite cylinder is given by

$$\alpha_r = (1+v_f)\frac{\alpha_{fl}+\alpha_{fr}}{2}V_f + (1+v_m)\alpha_m(1-V_f) - \alpha v \tag{6.65}$$

where α_r denotes the composite transverse CTE; α_{fl} and α_{fr} represent the fibre longitudinal and radial CTEs; α_m is CTE of resin; V_f, v_f and v_m denote the fibre volume fraction, Poisson's ratio of fibre and matrix materials, respectively. The following equation was derived to estimate the compaction pressure on the coating surface of the embedded optical fibre sensor subjected to thermal effect and external applied load, σ_c:

$$\sigma_{cr}(\theta) = \frac{1}{2}\sigma_c(1+\cos(2\theta)) + \frac{(\alpha_r-\alpha_s)\Delta T}{\left[\frac{(1-v_s)r_p^2+(1+v_s)r_o^2}{E_s(r_p^2-r_o^2)}\right]+\left[\frac{(1-c_{cr})r_p^2+(1+v_{cr})r_c^2}{E_{cr}(r_c^2-r_p^2)}\right]} \tag{6.66}$$

where σ_{cr} and σ_c denote a compaction pressure on the coating surface and external applied load on the composite; v_s and v_{cr} represent the Poisson's ratio of the sensor and surrounding composite materials; E_s and E_{cr} denote the tensile modulus of the sensor and composite materials; α_r and α_s are the radial CTEs of the composite and sensor. A plot of the radial compaction pressure in the coating surface against different angle measured from the load-applied direction is shown in Fig. 6.18. It is found that the compaction pressure at θ=90° is no longer equal to zero. This is due to the shrinkage or expansion action of the sensor and composite at the interface between the coating surface and composite.

The solution from the theoretical prediction is verified by the finite element method (FEM) using the commercial package of Msc/Nastran. Six-node (Tria 6) elements were used to generate meshes. Small mesh size is used at the fibre end region in order to achieve more accurate result. Since the model is bi-symmetric about both the radial and fibre axes, only a

quarter segment is modelled for our investigation. The boundary conditions are $v\,|_{r=0}$ and $u\,|_{x=0}$, where v and u represent the displacements of a node along the fibre radial and longitudinal directions, respectively. Differential temperature of 40°C is applied to all elements including glass fibre composite, protective coating and fibre core materials. External applied pressure of 100 MPa is added on the end of the composite cylinder. The mechanical properties of the materials used in the current study are shown in Table 6.2. The results evaluated from the Eqs.(6.59) and (6.62) and the FEM analysis are plotted in Figs.6.19 and 6.20. In the figures, it is demonstrated that the coating shear stress and axial strain in the fibre core region evaluated from the theoretical predictions are well compared with the FEM solutions.

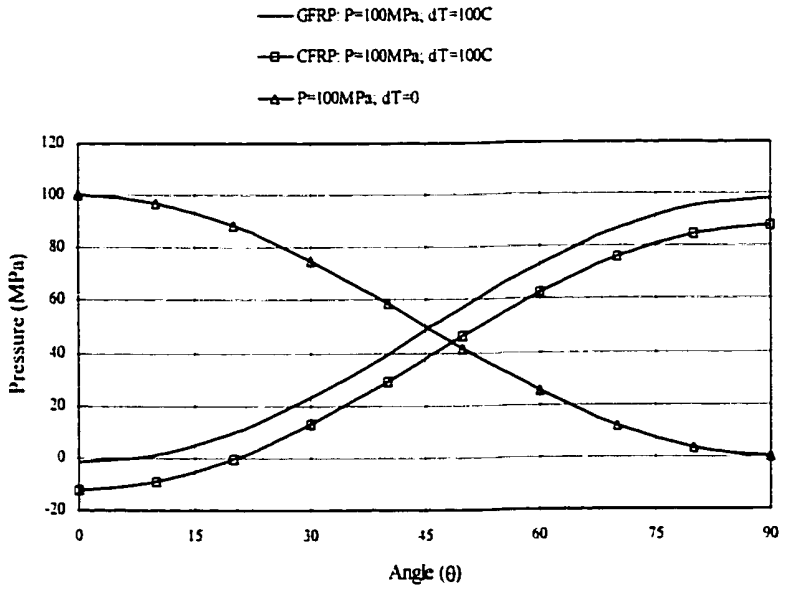

Figure 6.18. A plot of compaction pressure on the coating surface versus different angles of measurement, θ.

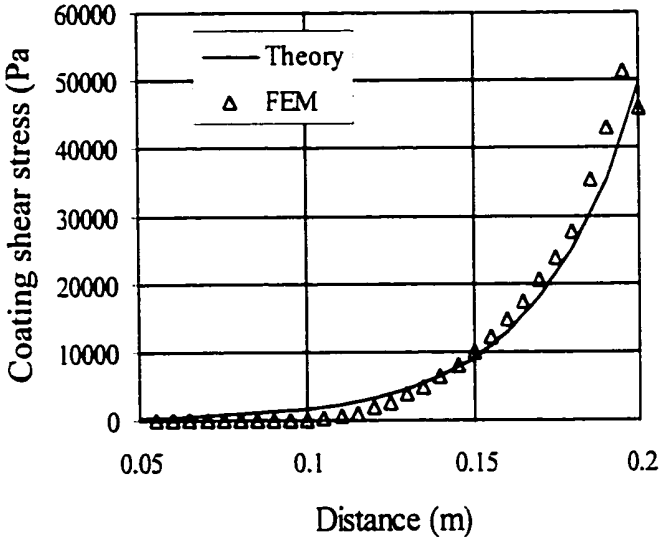

Figure 6.19. A comparison of the theoretical prediction with FEM result of coating shear stress.

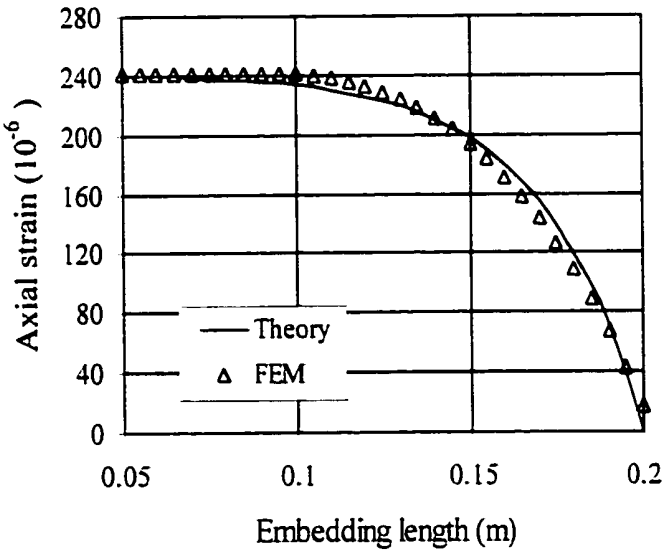

Figure 6.20. A comparison of the theoretical prediction with FEM result of fibre core axial strain.

6.3 Strain Measurements using Fibre-optic Bragg Grating (FBG) Sensors

6.3.1 Introduction

In this section, experimental studies on strain measurement by using embedded fibre optic Bragg grating sensor in concrete structures are presented. The principle of the FBG sensor has been introduced in Chapter 2.2.3. The FBG sensors have been installed either into the concrete or at the interface between the concrete and externally laid up composite materials. Conventional strain gauges were used to compare the strain reading from the sensors.

6.3.2 Single sensor Strain Measurement

6.3.2.1 Sensor calibration

A preliminary calibration test was performed to determine the coefficient K_ε, which is indicated in Eq.(2.5). A standard steel dog-bone shape specimen was used in a tensile strength test. The calibration factor pertains to the slope of the linear relationship between FBG reflective wavelength shift and strain measured by conventional strain gauge. Opposite the strain gauge, an FBG sensor has been adhered to the centre of the test specimen with epoxy. The grating length of the FBG sensor was 12 mm and total embedding length was 235mm. According to the theoretical prediction, the coefficient λ was calculated to be 600 m^{-1}, and the required minimum embedding length evaluated from Eq.(6.40) was 19.67 mm. Therefore, the sensor should provide a strain reading within the steady measuring region as the strain reading would not be influenced by the bonded end shear stress concentration. A schematic diagram of the testing specimen is shown in Fig. 6.21. The adhesive thickness was controlled evenly by using spring clamp and cushioned by a soft rubber chip. The strain reading for the strain gauge and the reflective wavelength signal from the sensor were recorded by the System 4000 data logger and optical spectrum analyser (OSA), respectively.

The testing specimen was held in the Sintech tensile testing machine for tensile testing. A loading rate of 0.5 mm/min was used in the test.

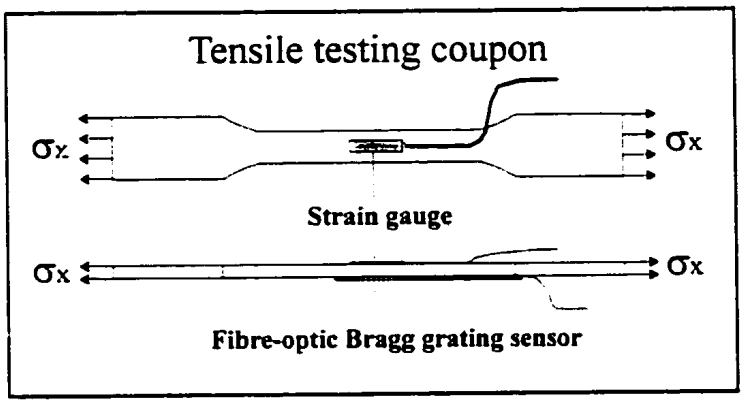

Figure 6.21 Tensile testing specimen for calibration test.

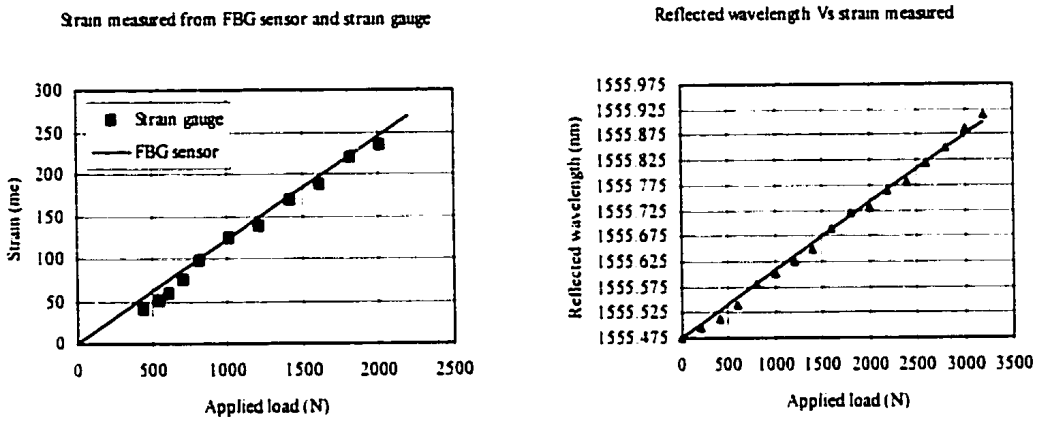

(a) (b)

Figure 6.22 Load-strain (a) and wavelength-strain (b) curves extracted from the calibration test. In the diagrams, diamond and triangular spots represent readings from the strain gauges while solid line represent readings from the FBG sensor.

The experimental results are shown in Fig. 6.22. For a silica fibre (optical fibre core), the wavelength-strain sensitivity is 1.55 μm. The selected Bragg wavelength used for present study was 1555 nm. The result obtained from the FBG sensor gives a good agreement compared with the strain gauge, which was bonded on the opposite side of the testing specimen. The value K^{-1} as indicated in Eq.(2.6) is determined by fitting a curve in Fig 6.22b and it was calculated as 947.55 nm^{-1}. This implies that each 947.55 nm^{-1} shift of the reflective

wavelength corresponds to 1 x 10^{-6} of strain change. The unit of reflective wavelength, λ_B is in nm. Thus, the Eq.(2.6) can be rewritten as

$$\varepsilon_f = 947.55\ \lambda_B - 1473917.45 \tag{6.41}$$

The function of OSA is to display in-coming wavelength signal from the sensor. The reading displayed on the screen of the OSA presents the peak reflective wavelength value and this value, eventually can be converted into the strain at the grating region. The spectrum, which was captured from the OSA during the experiment, is shown in Fig. 6.23.

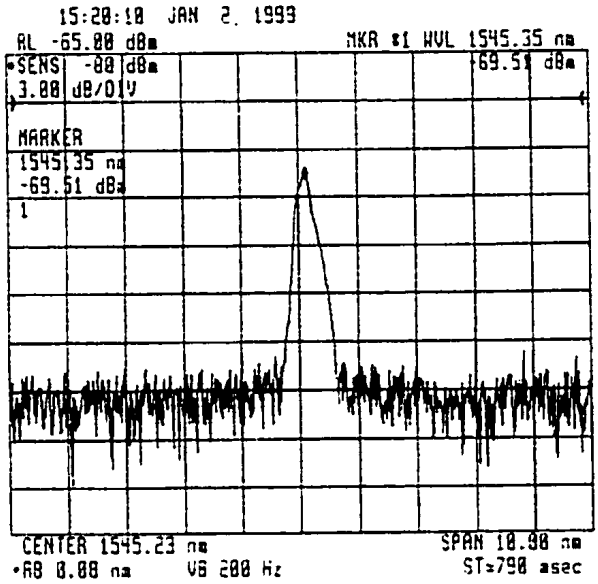

Figure 6.23 Reflective Bragg wavelength spectra (extra from OSA).

6.3.2.2 Strain measured in concrete cylinder

6.3.2.2.1 Experiment set up

The FBG sensors were installed in various forms in concrete cylinders with and without wrapping by glass fibre composite. These include: (1) embedded into the plain concrete cylinder (intrinsically); (2) bonded at the interface between the glass fibre composite and

concrete surface in parallel and perpendicular to the direction of compression loading; (3) embedded inside notched concrete cylinder and located in front of the notch-tip. Schematic diagrams of experiment set up in strain measurement by using FBG sensor, and the test specimens with the surface bonded strain gauges and embedded FBG sensor are shown in Figs. 6.24 and 6.25 respectively. The FBG sensors, which were used for measuring surface strain of the concrete for the wrapped concrete cylinder were pre-glued one day before laying up the composites.

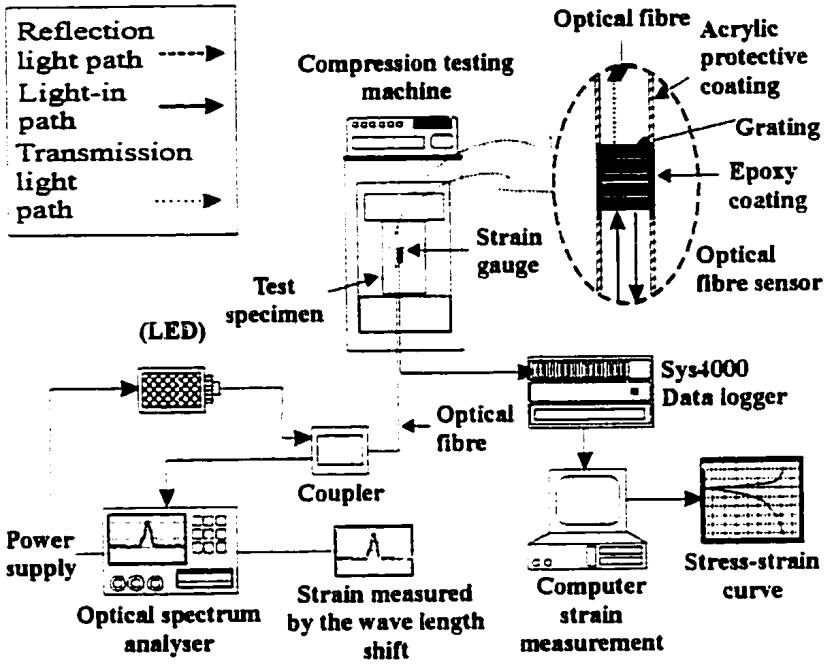

Figure 6.24 Schematic diagram of the experiment set-up for concrete cylinder with the embedment of FBG sensor and surface bonded strain gauges under uni-axial compression test.

To avoid damage of the fibre sensor during handling and moulding processes, a special supporting fixture for aligning and reinforcing the sensor is introduced. Thin and tough nylon string was used to align and guide the optical fibre in line parallel to the load direction. Both ends of the sensor were stuck on the string by using epoxy adhesive. High flexible rubber tubes were used to protect the fibre at both entrance and exit locations of the concrete cylinder to minimise the risk of fibre breakage due to the formation of sharp turning or other unexpected damage during moulding and de-moulding processes. Illustrations of the optical fibre installation technique and the photograph of the moulded concrete cylinder with the

optical fibre are shown in Fig.6.26. The experiment set up and notched concrete cylinder with the embedment of FBG sensor are shown in Fig. 6.27.

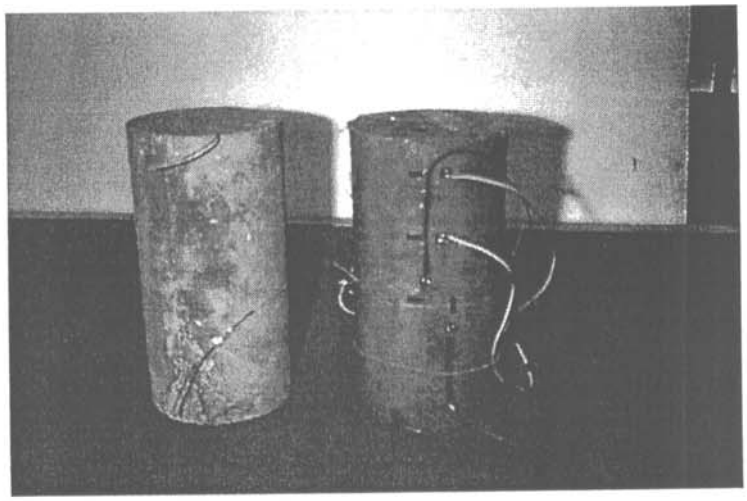

Figure 6.25 Schematic illustration of the FBG sensor embedded specimens.

Initial calibration of the embedded FBG sensor was performed in the early stage. The sensors were embedded into the plain concrete cylinder and at the interface between the concrete surface and external wrapped composite laminate of 1 layer glass fibre composite wrapped concrete cylinder. The specimens were then compressed to 1/3 of its ultimate load value of the plain concrete cylinder, for three repeated loading cycles. The test results of the FBG sensor compared with the surface bonded strain gauges are demonstrated in Fig. 6.28.

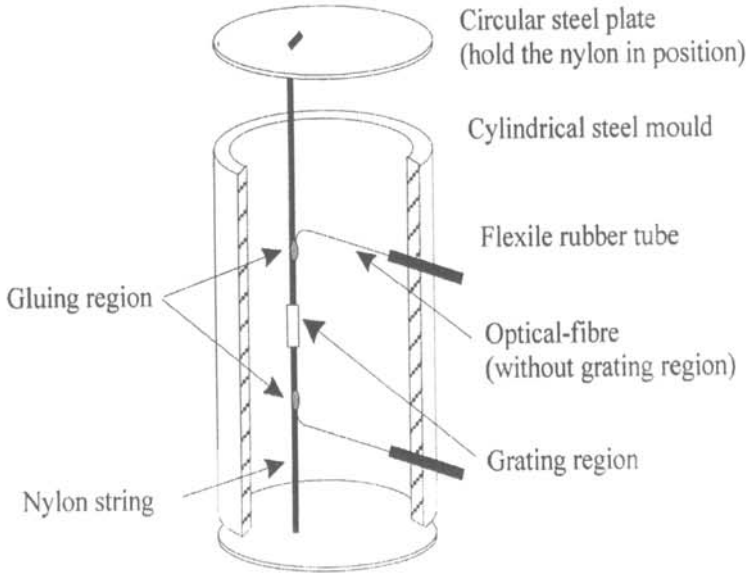

(a)

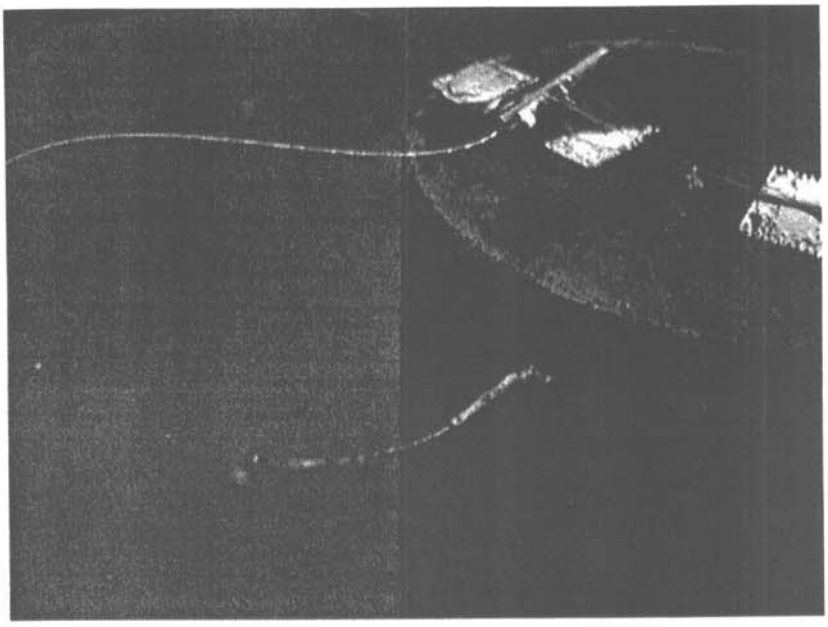

(b)

Figure 6.26 (a) Schematic diagram of the installation set-up for FBG embedding system and (b) photograph of the moulded concrete cylinder with the embedded FBG sensor.

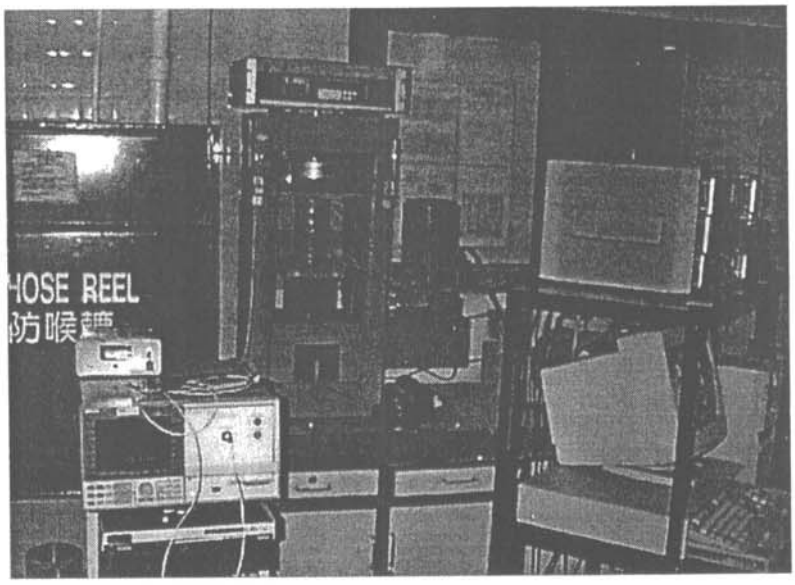

(a)

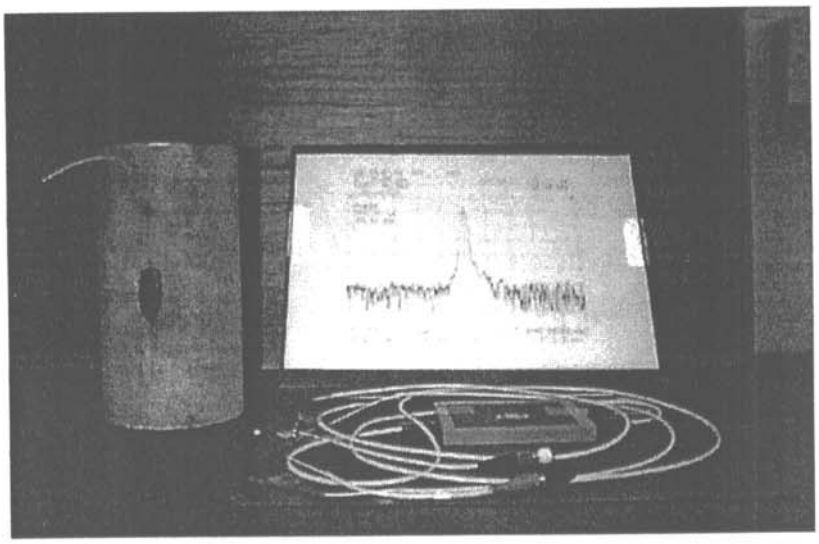

(b)

Figure 6.27 Photographs of the (a) experimental set-up and (b) notched-concrete cylinder with the embedment of FBG sensor.

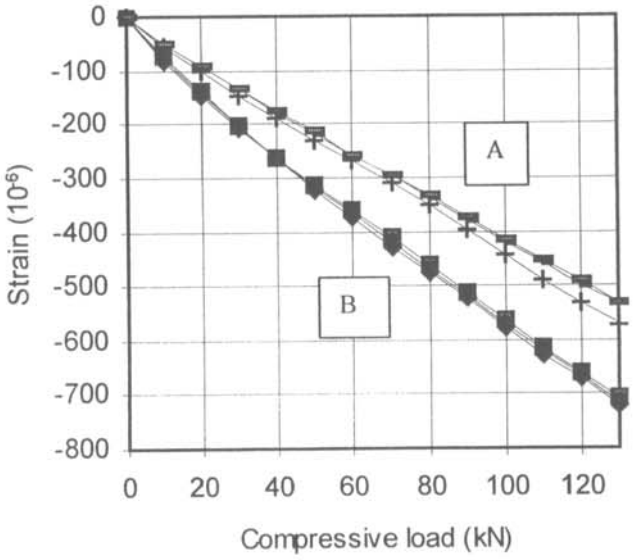

Figure 6.28 Experiment results of strain measured by using embedded FBG sensors (solid line) and surface bonded strain gauges (dot line). Result A: FBG sensor was embedded at the interface between concrete and composite of the wrapped concrete cylinder; Result B: Plain concrete cylinder with the embedment of FBG sensor.

6.3.2.2.2 Results and discussions

The strain readings from the sensor are well compared with the conventional strain gauge of the tested concrete cylinder with 1 layer of GFRP composite wrap. The result of the experiment is plotted in Fig. 6.29. The compressive strains measured from the test gave consistent reading between the FBG sensor and strain gauge when the compression load was applied up to 70% of its ultimate load value. The readings are diverged when the applied load continuously increases. It is speculated that the wrapped concrete cylinder develops considerably more cracks than that for the un-wrapped concrete specimen, particularly on the concrete surface, which is located inside the wrapping region.

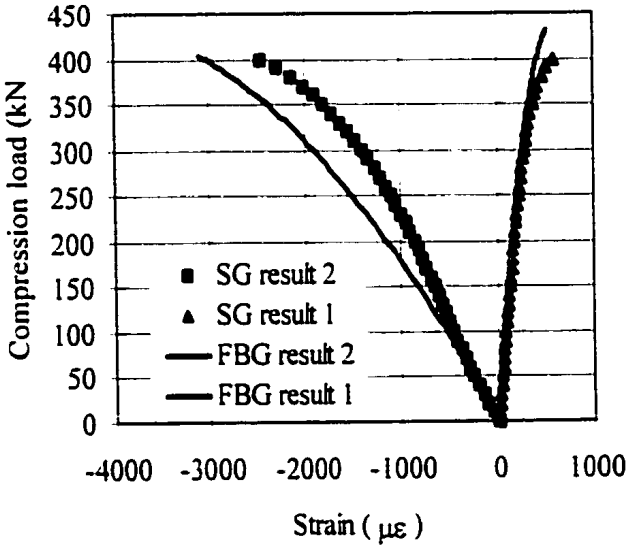

Figure 6.29 The strain measured by the FBG sensors and externally bonded strain gauges of the concrete cylinder with 1 layer of GFRP composite wrap. Readings from the strain gauge and FBG sensor are represented by dot and solid lines, respectively.

For the notched concrete cylinder, the strain measured from the FBG sensor was greater than that from the externally bonded strain gauge at ultimate load condition. It is revealed that the stress was still concentrated inside the concrete and in front of the notch-tip, where the sensor was embedded. The property changes in this region cannot be directly measured via externally bonded strain gauge. The results of the strain measured using FBG sensor and strain gauge for the wrapped notched concrete cylinder are plotted in Fig. 6.30. The micro-

graph of the wrapped concrete cylinder with the embedment of optical fibre is shown in Fig. 6.31. In the diagram, it is clearly shown that the aggregates are not uniformly distributed inside the concrete. The sensor is respectively bonded well on the concrete surface and inner face of glass fibre composite laminate.

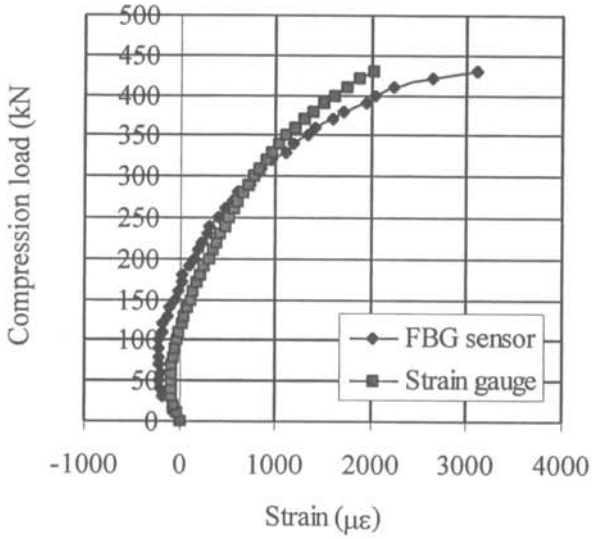

Figure 6.30 The strain measured at the notch-tip of the wrapped notched concrete cylinder from the embedded FBG sensor (solid line) and externally bonded strain gauge (dot line).

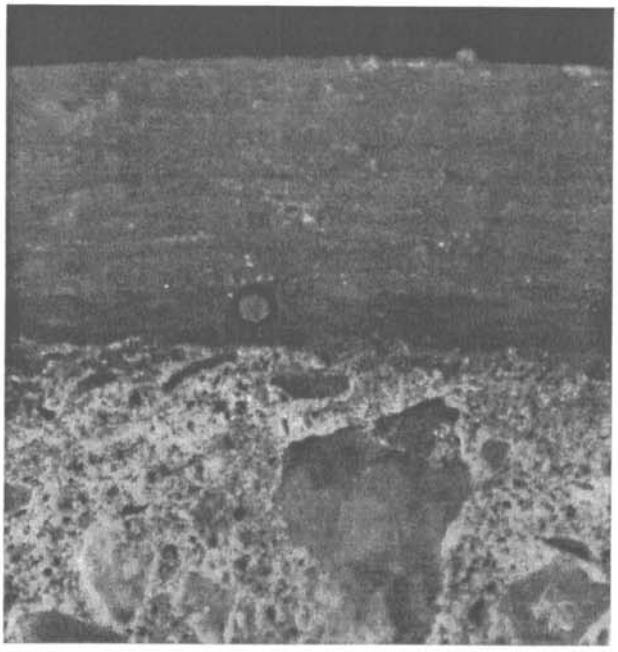

Figure 6.31 The cross section view of the embedded sensor at the interface between concrete and externally bonded glass fibre composite.

6.3.2.3 Strain measurement in composite bonded concrete beam

6.3.2.3.1 Experiment set up

Standard laboratory-sized rectangular concrete beams were made according to the ASTM C293-94 for three point bending test. The dimension of the beam is 154 mm x 154 mm x 500 mm. The mixture ratio and mechanical properties of the beam are same as the beam mentioned in Chapter 3. The beams were strengthened by bonding glass fibre composite laminate on either tension or shear surfaces. Notches were made on the tension side for all the beams with notch-to-depth ratio of 0.2 before strengthening. The notches were then filled with epoxy based resin to avoid any environmental attacks on notch-surfaces. The type of glass fibre composite was same as the wrapping material for concrete cylinder. Pre-treatment on all surfaces of bond was needed to ensure perfect bond between concrete and composite. Details of the testing specimens for present study are listed in table 6.4 and Fig. 6.32.

Table 6.4 Descriptions of all strengthened beams with the embedment of FBG sensors.

Code	Strengthening surface(s)	Number of layer(s)	Size of GFRP plate
SB-S1	Tension	1	250 mm x 152 mm
SB-S2	Tension	1	250 mm x 152 mm
	Shear	1	250 mm x 76.2 mm
SB-S3	Tension	6	250 mm x 152 mm (1^{st} 2 layers) 200 mm x 152 mm (2^{nd} two layers) 152 mm x 152 mm (last two layers)
	Shear	6	250 mm x 76.2 mm (1^{st} 2 layers) 200 mm x 63.5 mm (2^{nd} two layers) 152 mm x 50.8 mm (last two layers)

The strains of the composite strengthened rectangular notched concrete beams were measured by two different systems for the. whihc include FBG strain monitoring and externally bonded strain gauge measurements. The FBG sensor was attached on the concrete surface

before laying up the composites. The reflective wavelength from the sensor was recorded simultaneously during the test. The glass fibre composite laminate was made by laying-up directly on the surfaces of the concrete beam. All the strengthened beams were then rested for 24 hours for curing. Strain gauges were attached on the outer surface of composite laminate and at the same position where the sensors were embedded at the interface between concrete and composite. They were used to measure the surface strain condition of the externally bonded composite. All strain and load values were recorded automatically through the computer. The embedding length of the sensor was large enough to avoid shear strain loss at the bonded end region.

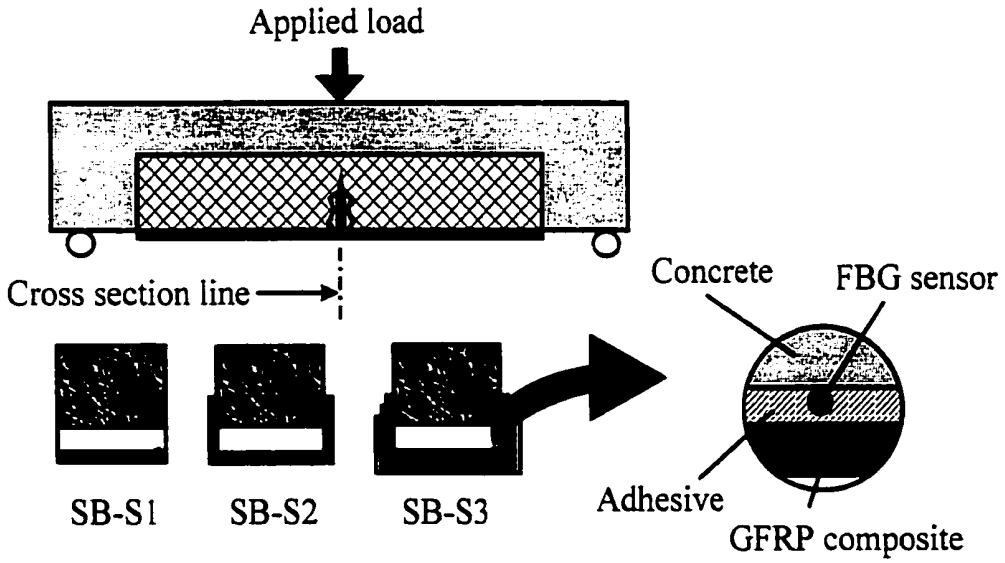

Figure 6.32 Schematic illustration of all strengthened beams with the embedment of FBG sensors at the interface between concrete surface and composite.

All the standard notched beams after strengthening were then subjected to three point bending load to investigate the strain behaviours. The load displacement rate was set as 0.5 mm/min. The experiment set-up of the whole strain measuring system and a photograph captured in site of the experiment is shown in Fig. 6.33.

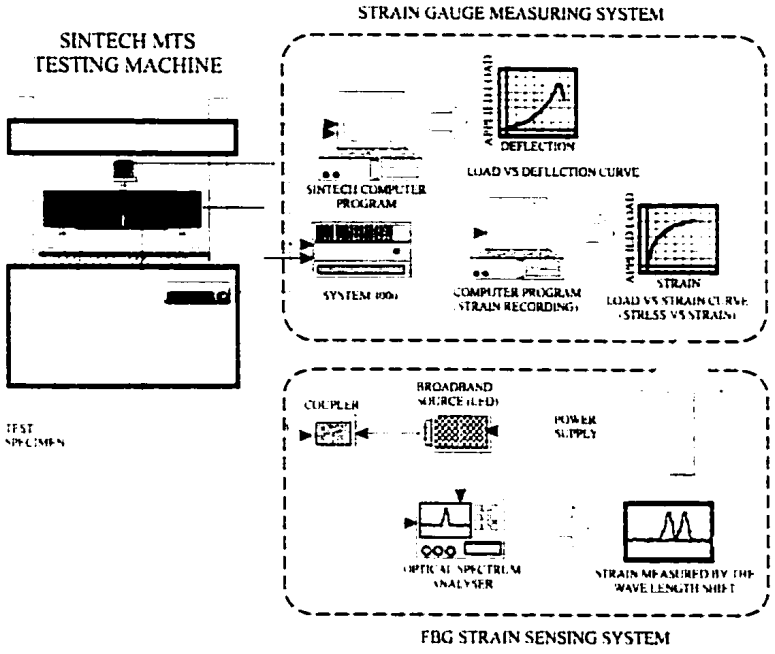

(a)

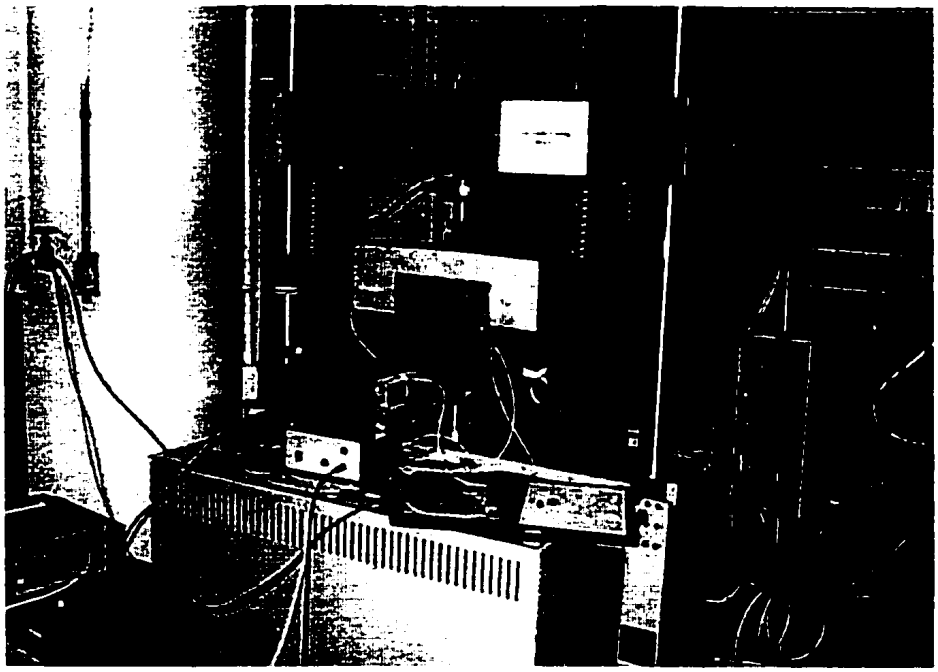

(b)

Figure 6.33 A schematic diagram (a) and photograph (b) of the experiment set-up for strain measurement of composite strengthened concrete beam using the FBG sensor and externally bonded strain gauge.

6.3.2.3.2 Results and discussions

The FBG sensors were installed at the interface between the concrete surfaces and externally bonded composites laminate of the composite bonded notched-concrete beam. The strains measured from the strain gauge and the FBG sensor are plotted in Fig. 6.34. It is obviously shown that the strain at the concrete surface is always higher than that at the surface of the externally bonded composite plate. The FBG sensor can monitor the strain condition of the concrete and detect the failure earlier than the strain gauge, which is mounted on the surface of outer reinforcement. The result of the specimen SB-S1 shows the rapid change of strains when the load is applied beyond 20 kN. During the experiment, several visible cracks and debonds were observed at adjacent areas near notch-mouth when the load reached 30 kN. Due to the formation of cracks, where beside the location of the sensor and strain gauge, the strain relaxation occurred when further increasing the applied load. This causes the regression of strain measured during the experiment.

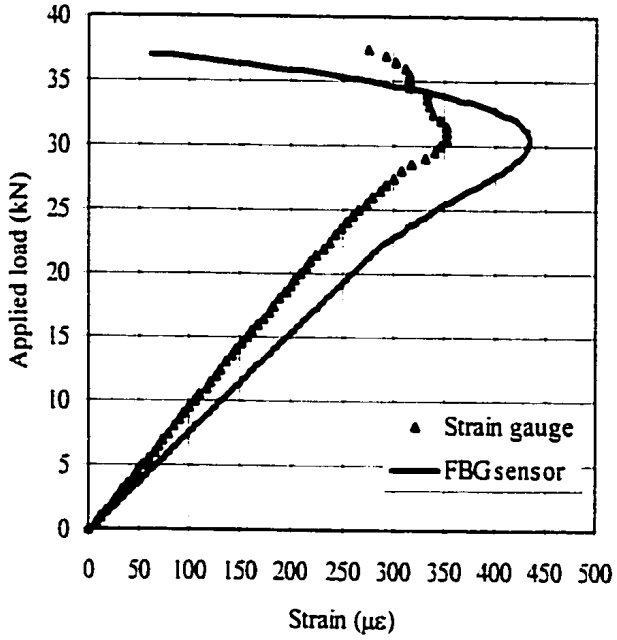

(a)

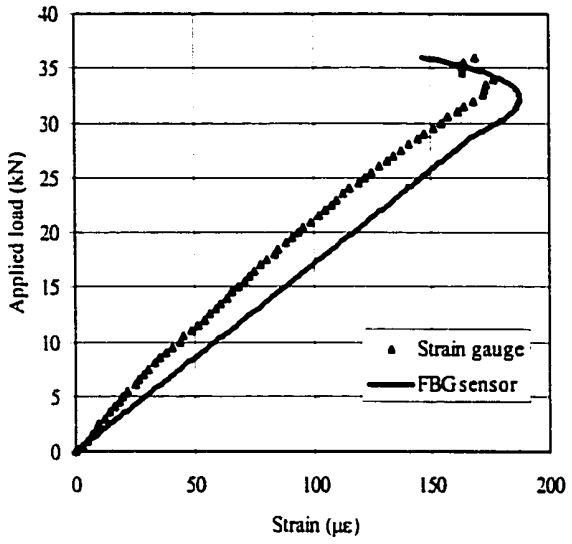

(b)

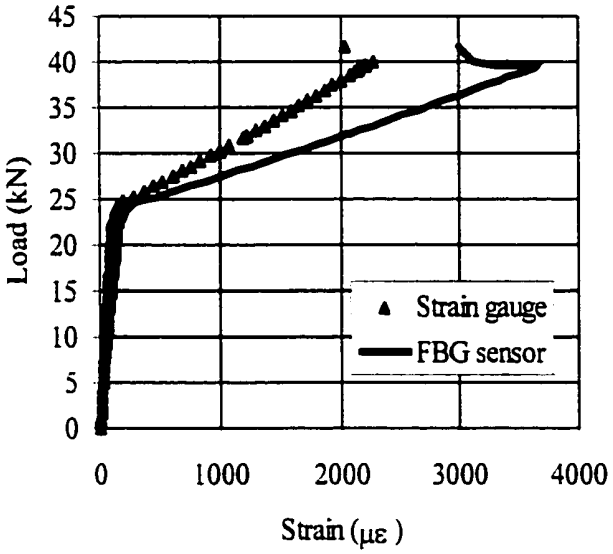

(c)

Figure 6.34 Strains measured by using the embedded FBG sensors and externally bonded strain gauges for the specimens (a) SB-S1, (b) SB-S2 and (c) and SB-S3.

However, this phenomenon may not influence strain on the outer surface of composite plate. Therefore, the strain measured from the FBG sensor is much more sensitive than that measured from surface mounted strain measuring device if internal debonds occurs at the sensor embedding region, particularly for the beam strengthened by thick reinforcement. The discrepancy of the strain measurement between the embedded FBG sensor and strain gauge for specimen with 6 layers of composite laminate (SB-S3) is higher than the specimen with only one layer of composite laminate (SB-S1) on the tension surface. The failure modes of all testing specimens are shown in Fig. 6.35 to 6.36.

Figure 6.35 White tracks represent the occurrence of debonds and small cracks on the concrete surface for specimen SB-S1.

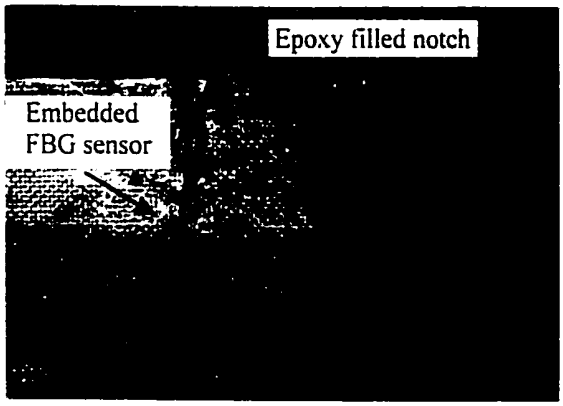

Figure 6.36 The embedded FBG sensor is located at the notch-tip region. A large portion of white shallow behind the sensor represents debond occurred in this region.

6.3.3 Multiplexing Strain Sensors

6.3.3.1 Glass fibre composite laminate

As described in Chapter 2, the FBG sensors can be arranged in multiplexing array to measure strains in different locations along a structure by only occupying one single optical fibre. In present study, Frequency modulated continuous wave (FMCW) multiplexing technique was used. The FBG sensors were embedded into 20 layers of balanced type glass fire composite laminates. Three FBG sensors were made in one single optical fibre. The sensors were located at the interfaces between first and second layer and between 19th and 20th layer. One sensor was used for reference signal. A four point bending test was performed to investigate strain responses measured from the sensors. External bonded strain gauges were used to compare the results from the FBG sensors. The testing set up and test specimen are shown in Figs. 6.37 and 6.38, respectively.

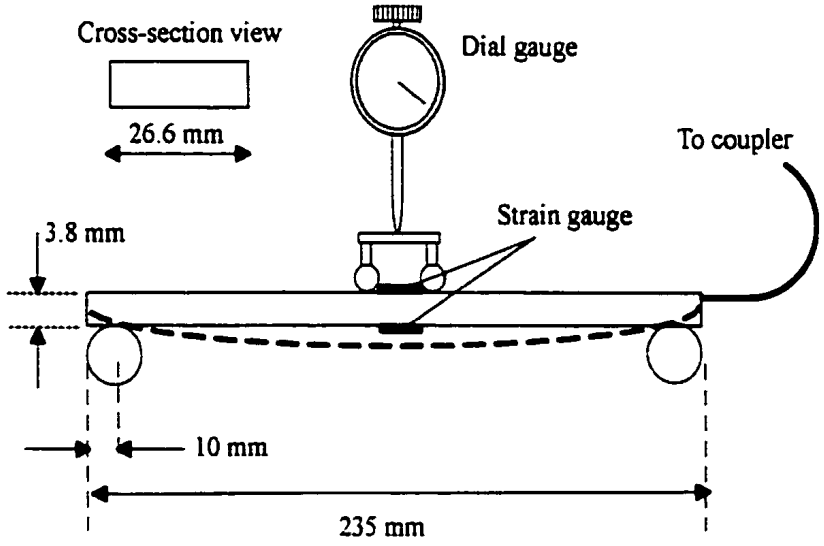

20 layers of glass fibre laminate (V_f = 42%)
FBG sensors are located at the interface between
- 1st and 2nd layers
- 19th and 20th layers

Figure 6.37 Experimental set up for the four point bending test.

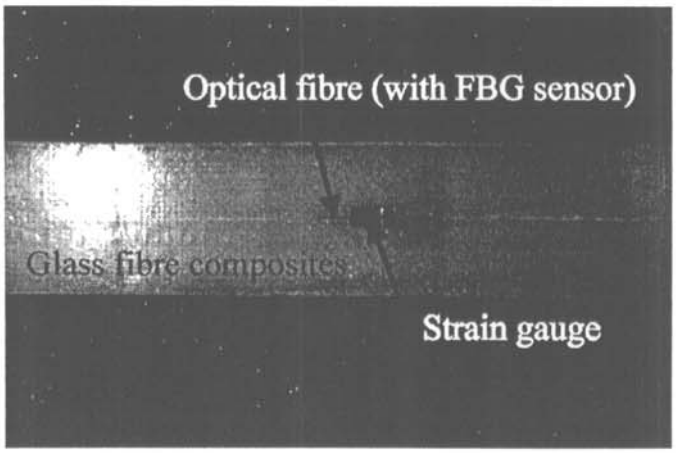

Figure 6.38 Photograph of the testing speicmen

A high fibre volume fraction ($v_f \approx 42\%$) composite plate was used to reduce adhesive thickness between the sensor and its surrounding materials. A high radio frequency (RF) spectrum analyser of 30 Hz resolution and the rate of frequency excursion of approximate 4 x 10^{11} Hz^2 were used in present study. The coefficient K_ε measured in the experiment for the sensor was 947.55 nm^{-1}. The selected wavelength and corresponding beat frequency in the experiment for sensors S_1, S2 and S_3 were 1556.3 nm, 1554.24 nm and 1554.24 nm, and 50 kHz, 75 kHz and 105 kHz, respectively. The separation between each sensor was 1 m, which is long sufficient enough to avoid the occurrence of coherent noise inside the fibre core. The spectrum extracted from the OSA is shown in Fig. 6.39. The total embedding length was satisfied to the Eq. (6.20).

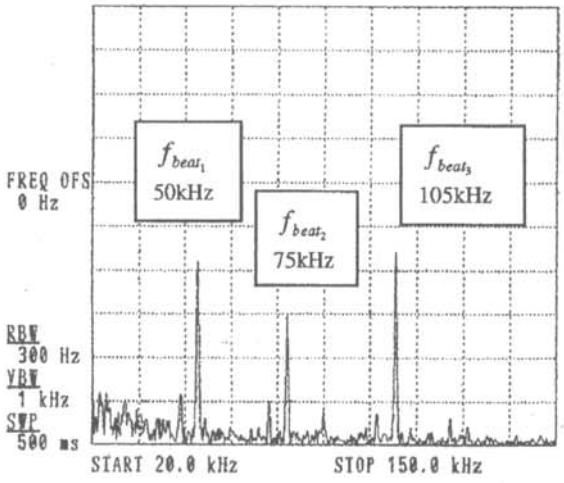

Figure 6.39 The beat frequencies for S_1, S_2 and S_3 sensors measured in the experiment.

The experimental results for the strain measured from both the FBG sensors and externally bonded strain gauges give a good agreement to each other. The result is plotted in Fig.6.40. The positive portion represents the tensile strain measured on the bottom surface while the negative portion is compressive strain measured on the top surface of the specimen.

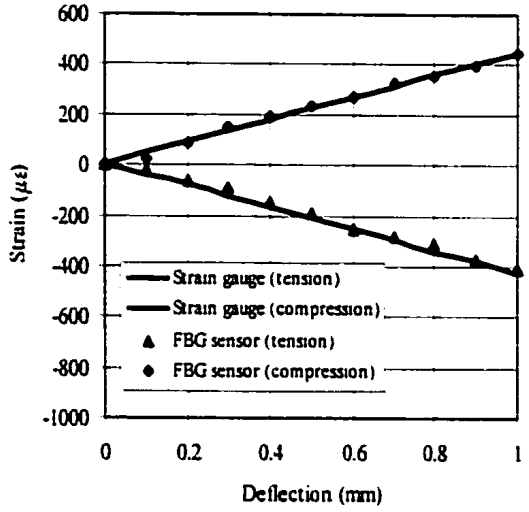

Figure 6.40 Comparison of the strains measured by FBG sensors and externally bonded strain gauge.

6.3.3.2 Strain measurement for composite wrapped concrete cylinder

6.3.3.2.1 Experiment set up

The testing specimen was similar to that described in Section 6.3.2.2. A concrete cylinder was wrapped by 5 layers of glass fibre composite laminate. A single optical fibre with three grating sensors was adhered on the concrete surface. Two sensors S_1 and S_2 were placed at the middle height of the cylinder in both the longitudinal and hoop directions to measure strains. The same parameters such as beat frequencies and selected wavelengths used for the composite plate in previous section for the FBG sensors were used in the experiment.

Externally bonded strain gauges were mounted on the surface of composite and at the same locations that the sensors were embedded. A schematic diagram of the test specimen is shown in Fig. 6.41.

Uni-axial compression test was then performed and the strains were measured up to its ultimate compression load value. The optical fibre was glued on the concrete surface by using epoxy resin, which is same as the type of matrix used to form composite. The composite lay-up process was performed after 24 hours.

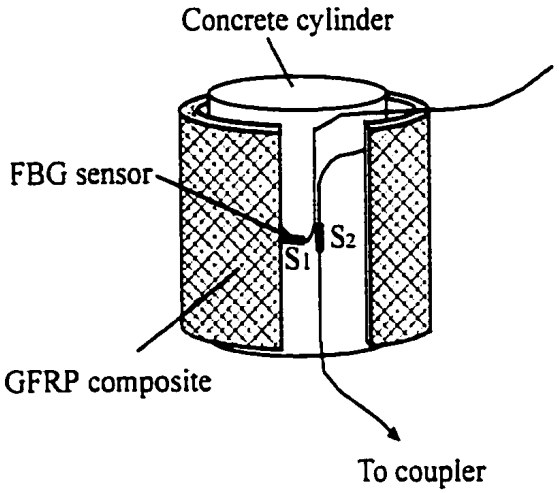

Figure 6.41 Composite wrapped concrete cylinder with the embedment of multiplexed FBG sensors.

6.3.3.2.2 Result and discussion

In Fig.6.42, experimental results for the wrapped concrete cylinder with the multiplexed FBG sensors, which were embedded at the interface between the concrete surface and wrapping laminate, are plotted. It is shown that the difference of the strains measured from the FBG sensors and strain gauges increases with increasing the applied compression load beyond 250kN. This phenomena implies that the axial deformation in concrete is larger than that of the outer surface of the wrapping composite. The differences of the strain measurement might be due to the existence of cracks on the concrete surface and high shear deformation in composite laminate (see Fig.6.43). However, the divergence of the result meas-

ured in the lateral direction is smaller compare to that measured in axial direction. Since there was no lateral shear deformation existed in the wrapping composite, the strains measured at the interface between the concrete and wrapping composite and on the surface of composite are closed to each other when the applied load is below 300kN. The difference increases with continuously increasing the applied load. It was suspected that internal cracks and debonds might occur in the concrete and at the bond interface, respectively.

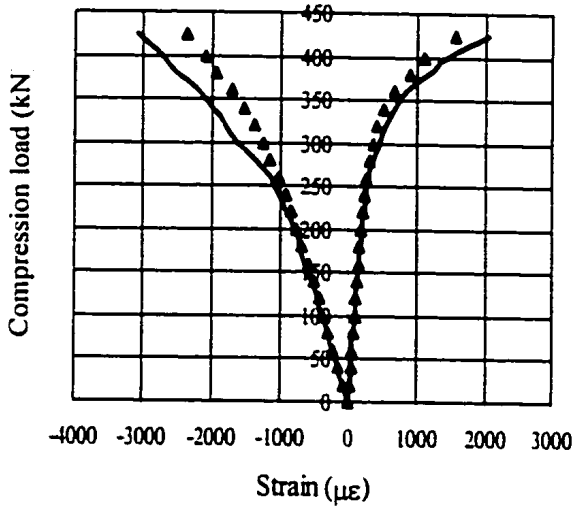

Figure. 6.42 Strains measured by the embedded FBG sensors with single optical fibre and surface mounted strain gauge for 6 layers of composite wrapped concrete cylinder.

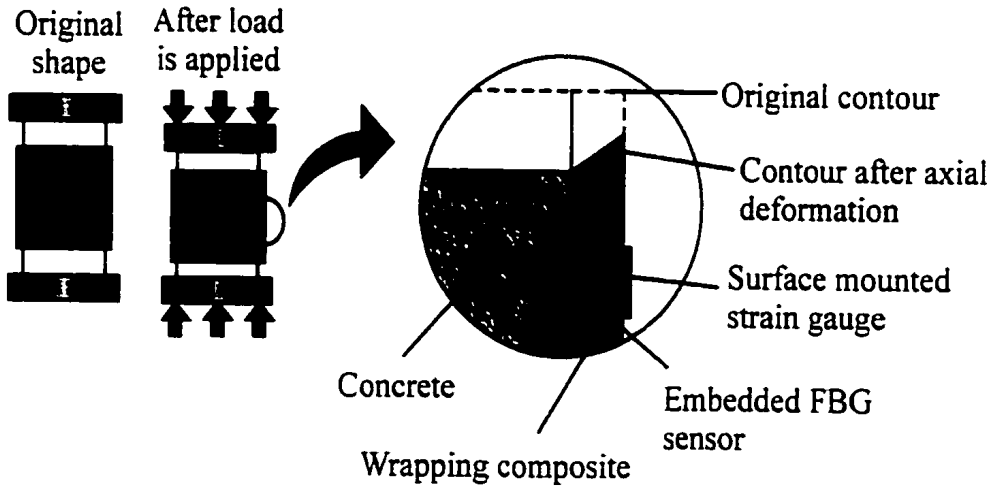

Figure 6.43 Schematic diagram of the composite wrapped concrete cylinder subjected to compression load. Relative high compressive strain on the surface of composite is measured due the existence of axial shear deformation in composite laminate.

6.3.3.3 Strain measurement for composite bonded concrete beam

6.3.3.3.1 Experiment set up

A standard laboratory sized rectangular notched-concrete beam with a notch-to-depth ratio of 0.2 was made. The notch was then filled by epoxy resin, which is same as that used for lay-up the glass fibre composite plate in the experiment. Three FBG sensors were glued by using epoxy base resin on three different locations as illustrated in Fig. 6.44. Sensor S_1 was located at 1 mm in front of the notch-tip region, which is suspected to be a highest stress area for the notched –beam without strengthening by external reinforcement. S_2 was located at the mid-beam bottom-edge while S_3 was at bottom-centre regions and in front of the notch-mouth. Sensors S_2 and S_3 were arrayed serially in a single optical fibre. All three sensors were located in parallel arrangement as shown in Figs. 6.44a and b. All composite laminates were laid up directly onto the surface of the concrete beam.

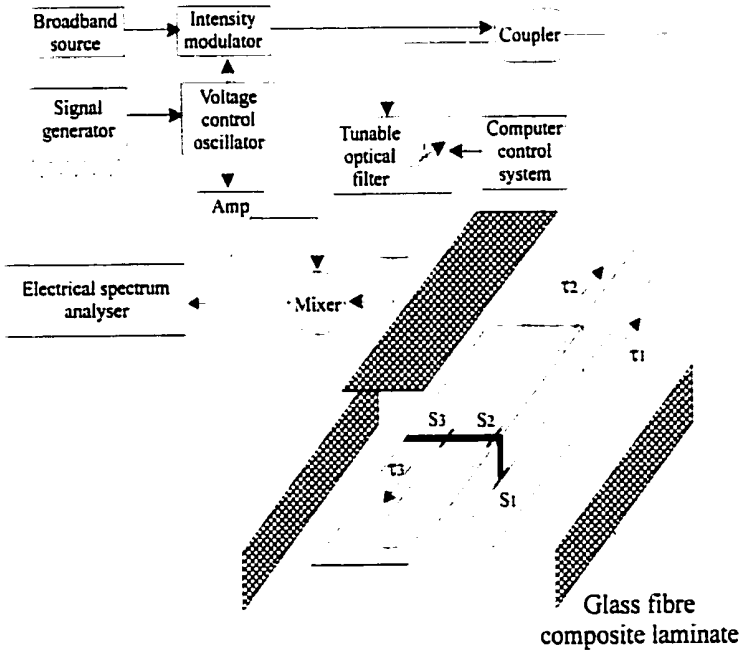

(a)

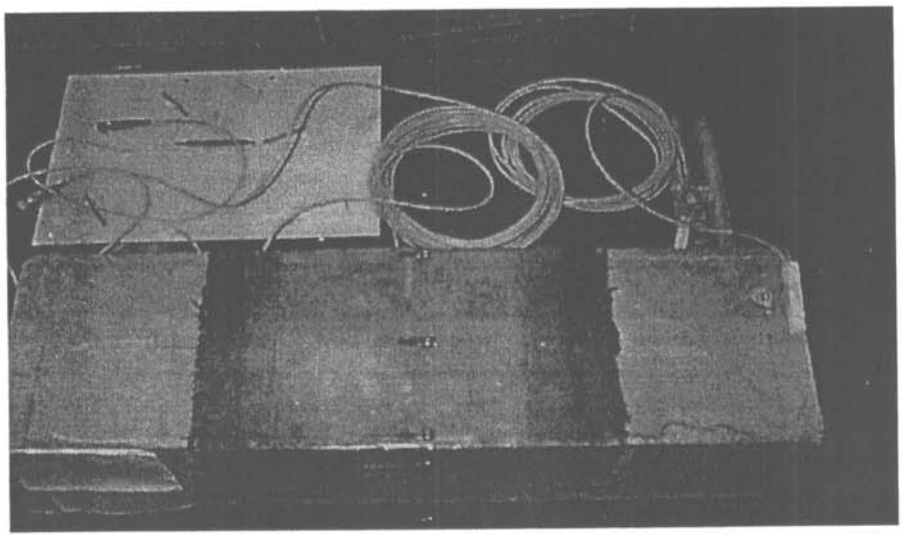

(b)

Figure 6.44 The FMCW multiplexing technique (a) in monitoring strain for strengthened rectangular concrete beam and (b) the test specimen for three point bending test.

6.3.3.3.2 Results and discussions

The results of the specimens subjected to the three point bending are shown in Fig.6.45. It is found that the difference of the strain measured by the external bonded strain gauges and interfacial bonded FBG sensors increases with increasing the applied load, particularly at the mid-beam bottom-edge region (S_2). However, at the low loading range, the strain measured from the strain gauge and FBG sensor provide a linear load-strain relationship and give a good agreement with each other. After the load readings to 23 kN, the divergence of the strain measured by the strain gauge and FBG sensor increase rapidly.

It was found experimentally that high strain (5300με) occurred when the load was applied to 27 kN. The signal from the sensor S_2 disappeared when further increasing the load. It is suspected that the optical fibre was broken. The signal received from the sensor S_3 was therefore lost subsequently.

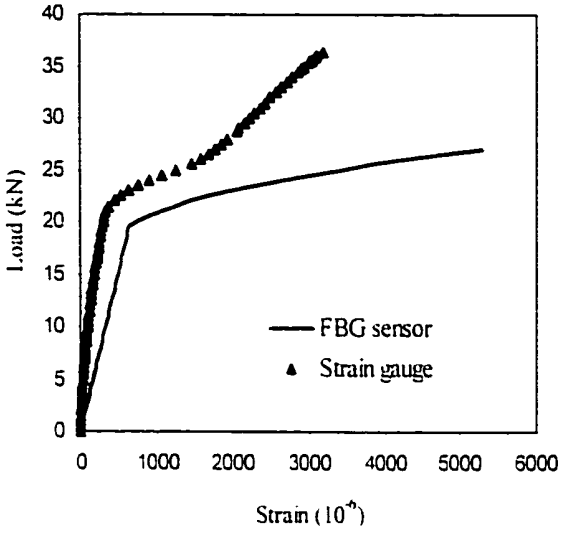
40
35
30
25
20
15
10
5
0
Load (kN)
0
1000
2000
3000
4000
5000
6000
Strain (10^{-6})
FBG sensor
Strain gauge

(a)

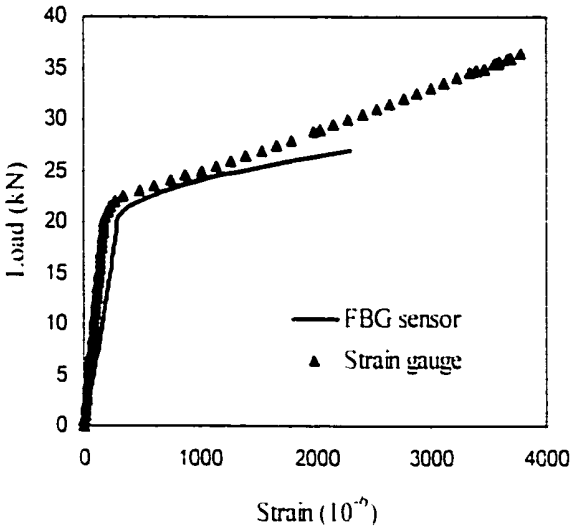
40
35
30
25
20
15
10
5
0
Load (kN)
0
1000
2000
3000
4000
Strain (10^{-6})
FBG sensor
Strain gauge

(b)

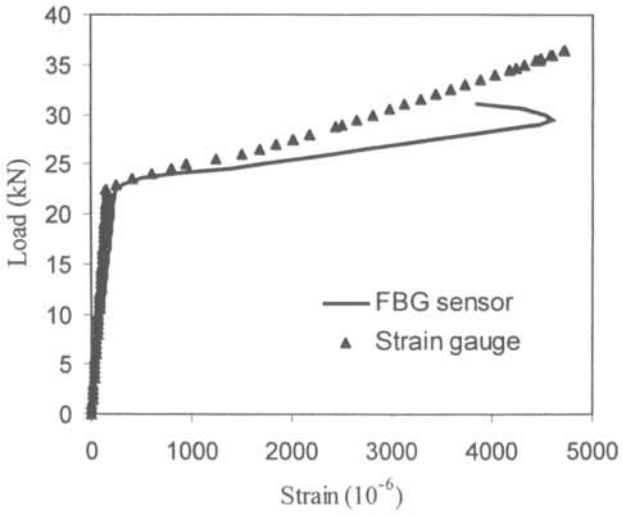

(c)

Figure 6.45 Strains measured from the FBG sensors and strain gauges for (a) S_1, (b) S_2 and (c) S_3.

At the notch-tip region, the FBG sensor gave the strain response up to 31.5 kN. It was observed that debond at the interface between the concrete and composite plate occurred and extended rapidly toward the opposite direction of the applied load. Shear cracking in the concrete and peel-off in composite were found when the applied load reached 36.5 kN. In Fig. 6.46, a photograph of the test specimen after testing is shown. It was clearly found that peel-off in the composite plate occurred at plate end region.

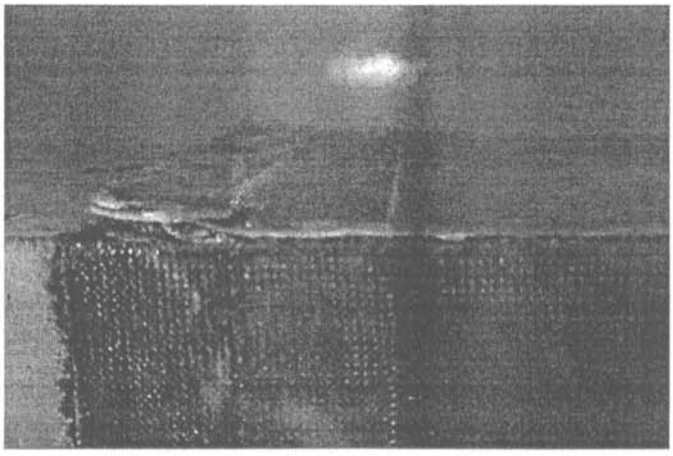

Figure 6.46 The peel-off failure at plate end region.

The result measured in the experiment show that the difference of the strain measured by the strain gauge and FBG sensor is relatively low when the applied load is small. The divergence increases when continuously applying the load to its ultimate condition. It was also shown that debond between the concrete and composite could not be detected directly by the externally bonded strain gauge. However, the FBG sensor gave the high strain value when debond occurred.

6.4 Summary

In this Chapter, the investigation on embedded FBG sensor for composite strengthened concrete structures have been conducted through theoretical analysis and experimental studies. The single and multiplexing sensors using FMCW technique were also used to measure strains either inside the concrete or at the interface between the concrete surface and externally bonded composite laminate. Throughout the whole study, several conclusions can be drawn.

1. A theoretical model is introduced to determine the mechanical behaviour of the fibre sensor embedding system with different mechanical properties and geometrical factors of surrounding matrix, fibre core, adhesive layer and protective coating materials.
2. The use of thick adhesive layer and low modulus of coating material with a short embedding length of sensor is not encouraged for fibre sensor embedding system because the maximum shear stress and stress transferring length increase with increasing thickness of adhesive layer and decreasing modulus of coating material.
3. Sufficient embedding length of the embedded sensor is essential to avoid mismeasurement using FBG strain sensor. A minimum embedding length can be evaluated by using Eq.(6.40).
4. The coating shear stress decreases with increasing the ambient temperature when the optical fibre is embedded to a material, which has a relative low value of CTE. (Carbon and Kevlar fibre composites) compared with the fibre-core. However, for a matrix material with high value of CTE., the coating shear stress increases with increasing the temperature of the system.

5. Embedded FBG sensors can revealed the true strain of measurement in real time compared with externally bonded strain gauge, particularly for a structure with surface coverage reinforcement.
6. Multiplexed FBG strain sensor enable to measure strains in different locations at the same time with only using one single optical fibre. In high strain condition, the properties change at the adhesive layer cannot be detected directly from the surface adhered strain- measuring devices while the FBG sensors can provide important signal to the operator.
7. The order and arrangement of the sensors is very important for multiplexed strain measuring system since the sensor may loss signal if any one of sensors, which are located in the direction from light source is broken.

CHAPTER 7

ENVIRONMENTAL EFFECTS ON COMPOSITE STRENGTHENED RC BEAMS

7.1 Introduction

Fibre reinforced plastic (FRP) composites are known to have excellent fatigue resistance, corrosion resistance and can be tailored to give optimal combinations of stiffness, strength, and thermal expansion by proper design and application. Due to these inherent properties of the FRP composites, they have been gradually accepted for concrete rehabilitation and repair works in recent years. However, the environmental attacks on the concrete structures, particularly when the structures are used in offshore or other high chemical emission areas are severe [Gibson, 1993]. Although the use of the FRP materials can overcome the problems arising from corrosion of metal and long term maintenance, several studies have addressed that E-glass epoxy composites suffer from moisture absorption which result in a reduction of strength of the structures [Toutanji (1999), Castaing and Lemoine (1995) and Bradley et al. (1997)]. In general, the mechanical properties of the matrix are reduced by moisture absorption, typically 1-3% of the weight of the matrix [Bradley, 1997]. It is because the cross-linked networks in resin bonding system are sensitive to a manifested chemical stress relaxation. Therefore, the failure of the structure is eventuated [Gutman, 1995]. For the fibre reinforced composites, absorbed moisture can not only plasticise the matrix as in the pure matrix system but also affect the bonding properties at fibre-matrix interface [Berry, 1977].

Investigations on the mechanical properties of glass fibre composite strengthened concrete structure in different chemical environments are very limited in previous research publica-

tions. In current study, the mechanical performances of steel reinforced (RC) concrete beams with and without being strengthened by externally bonded glass fibre composite laminates after submerging into different chemical solutions under room temperature for six months are experimentally investigated through standard three point bending test. The objective of the study is to evaluate the effects on the concrete and glass fibre composite strengthened concrete structures under long-term attacks by aggressive environments.

7.2 Specimens Fabrication and Experiment Set Up

Total 30 laboratory-sized rectangular RC beams were manufactured for investigation. To control the consistency in quality of all RC beams, 30 non-reusable wooden moulds were made for manufacturing concrete specimens at the same day with same concrete constituents. A steel bar with a diameter of 6 mm with surface grindering (increase surface roughness) was embedded into the concrete beam. The mixture ratio of the concrete was 1:1.5:3. Only 10 mm aggregates were used as coast aggregates. A schematic diagram of the RC beam used in the present study is shown in Fig. 7.1. The dimension of the beam is 525 mm x 55 mm x 84 mm and a steel bar with a diameter of 6 mm is located 20 mm above the tension surface of the beam.

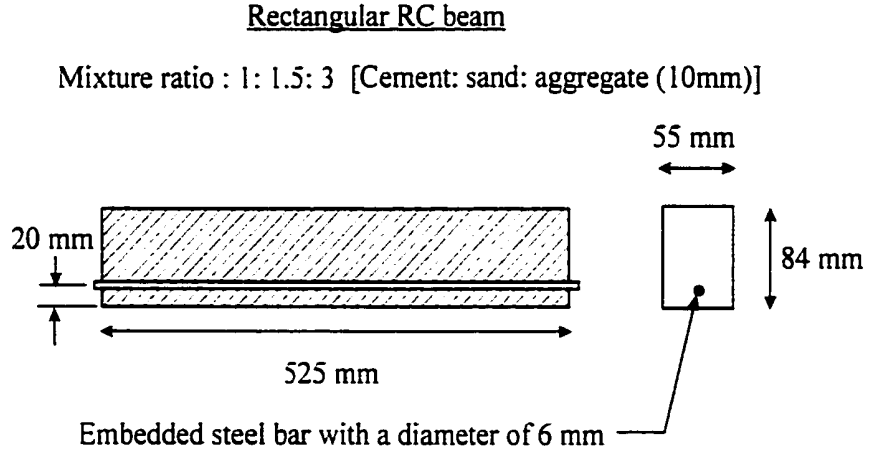

Figure 7.1 Schematic diagram of the RC beam used in present study.

All moulded concrete beams were demoulded after 24 hours of curing and stored inside the curing tank for another 28 days for curing. Both ends of protruded steel bar are protected by low-melting point rubber element in order to avoid corrosion during curing and chemical attack in later processes. The wooden moulds used for the present study and the rectangular RC beam with end protective rubber element are shown in Figs. 7.2 and 7.3, respectively.

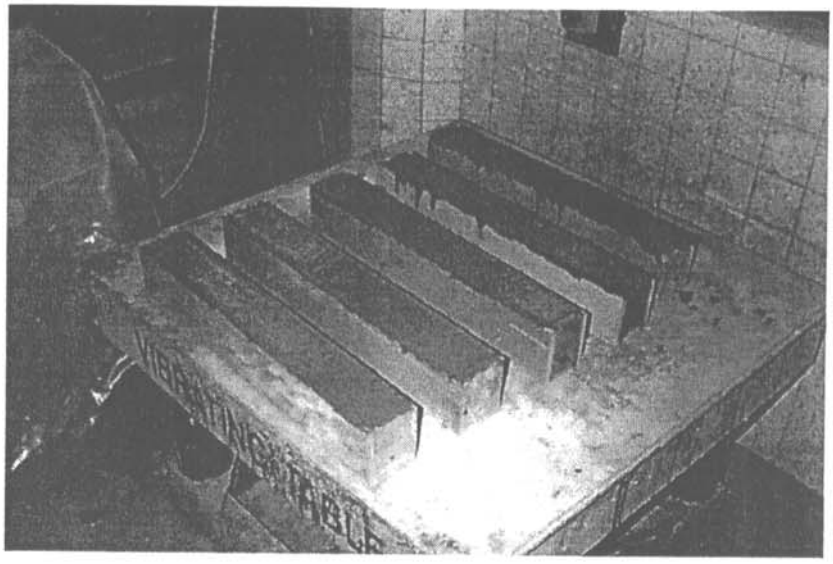

Figure 7.2 Wooden moulds used for making RC beams.

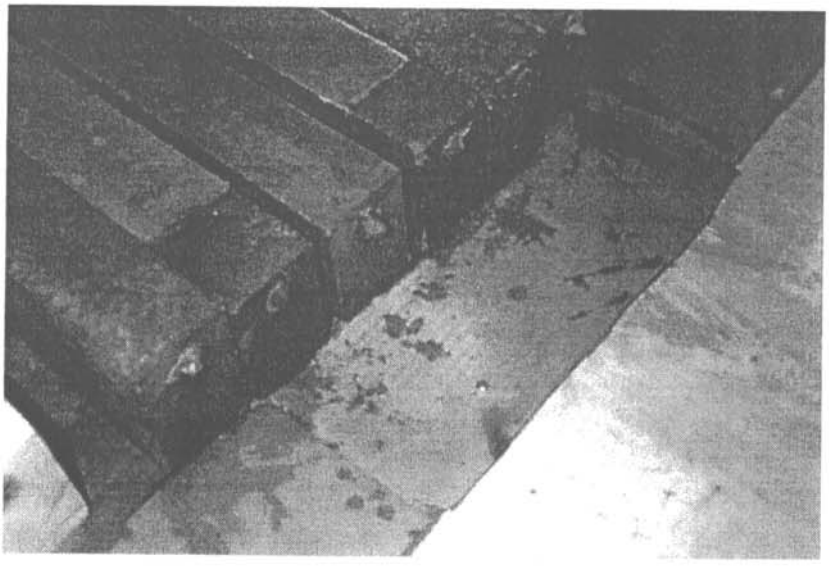

Figure 7.3 Both ends of the embedded steel bar are protected by rubber element.

The RC beams with and without being strengthened by three layers of glass fibre composite laminates were then submerged into different chemical solutions (see table 7.1) in order to investigate their durability by performing standard mechanical tested. The composite laminates were laid up directly on the concrete surfaces. The bonding length of the glass fibre composite laminates is 400 mm (covering the whole width of the beam). Six identical specimens were submerged into each type of chemical solution for six months. Three of the specimens were strengthened by externally bonded glass fibre composite while another three were in un-strengthened status.

Table 7.1 Specimen types for current study.

Specimen code	Surrounding Environments
PRC	Ambient condition (25°C)
RCH_2O	Fresh water
RCPH4	PH 4 buffer solution
RCPH10	PH 10 buffer solution
RCNaCl	Saline solution

The submerged specimens were then kept at room temperature for six mouths after 1 month of standard curing process. In Fig. 7.4, plastic containers made by Polyethylene (PE), which were used to store the strengthened and un-strengthened specimens are shown. The submerged beams were then removed from the tanks and cleaned by fresh water to remove the chemical solution remained on the concrete surface. The beams were then placed in room temperature (25°C) and humidity (60%) conditions for two days to dry up.

Many small crystals remained on the surface of the concrete beams, which have been submerged into the tanks filled with acidic, salty (NaCl) and fresh water solutions. It was suspected that part of the solution was diluted because of the formation of these crystal elements by chemical reaction. This particle is definitely undesirable and may cause the reduction of strength of the structure. However, for the specimens, which have been submerged into the alkali solution, there were no small crystal elements observed. In Fig. 7.5, a photograph for the specimens after submerging into saline solution is shown.

Figure 7.4 Plastic containers used for storing RC beams for three point bending test. Acidic solution PH 4 (left), alkali solution PH 10 (middle) and sea water NaCl (right).

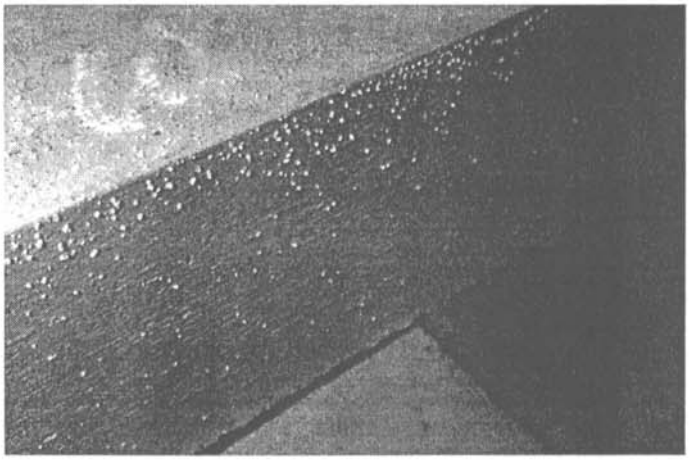

Figure 7.5 Many small crystal particulars were formed on the concrete beam after submerging into saline solution.

Since concrete is mixed by Portland cement material which is being highly alkaline. It does not resist the attack of strong acids or compounds which may convert to acids [Neville, 1997]. Romben (1978) found that concrete would be seriously attacked by the solution at a PH 5.5. In general, PH level of acid rain is between 4.0 and 4.5. However, the concrete can also be attacked by saline solution and fresh water containing free CO_2. The existence of these materials in solution may result in sulfate attack to hydrated cement paste [Mehta, 1993].

All glass fibre composite strengthened and un-strengthened RC beams were subjected to three point bending test. The MTS 810 tension and compression testing machine with a pre-designed fixture was used in the test. The loading rate was set as 0.2 mm/min. The experiment set up for strengthened RC beam and testing specimens are shown in Fig. 7.6 and 7.7, respectively.

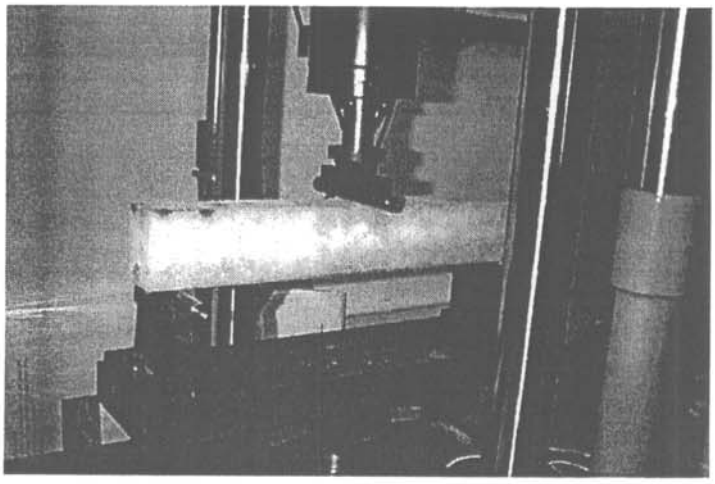

Figure 7.6 Experiment set up for three point bending test for composite strengthened RC beams.

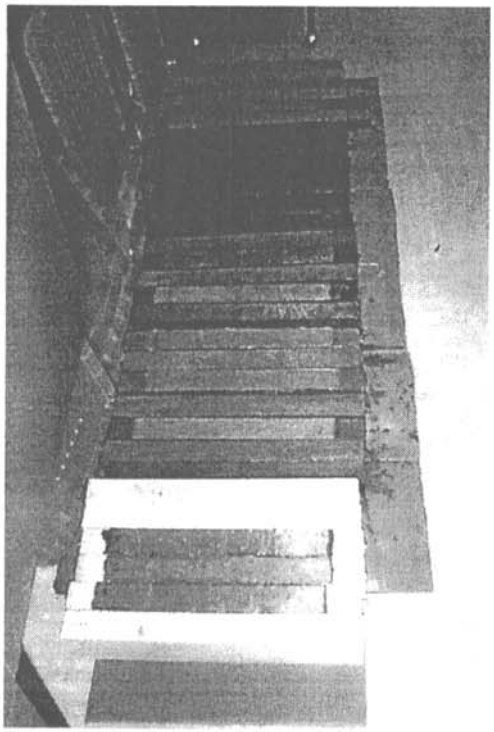

Figure 7.7 All submerged RC concrete specimens prepared for testing.

7.3 Results and Discussions

The experimental results for all strengthened and un-strengthened RC beams subjected to three point bending test are shown in Fig. 7.8 to 7.12 and the result summary is listed in Tables 7.2 and 7.3. Fig. 7.13 shows the difference of all un-strengthened RC beams subjected to three point bending load. The explanation of the plot in schematic form is shown in Fig. 7.14.

According to the result shown in the table, it is obviously indicated that the use of glass fibre composite laminate for RC beam strengthening in different environmental conditions can increase the maximum flexural load capacity of the beams, which are degraded after being submerged in fresh water, saline solution, acidic and alkalic solutions. The maximum flexural load denotes the load when a crack appeared at the tension surface of the beam. The result clearly indicates that the decrease in flexural strength of the concrete in acids is severe. The percentage reduction of the applied load carrying capacity is 24.8% compared to the controlled beams, which were remained in room temperature (25°C) and humidity (55%) conditions for six months. However, the results from other specimens show a slight reduction in ultimate flexural load capacity.

Table 7.2a Experimental results (flexural load at crack formation) for the RC beams without being strengthened by glass fibre composite.

Submerged solution	PH Level	Sample 1 (N)	Sample 2 (N)	Sample 3 (N)	Mean Value (N)	S.D. (N)
Nil (RT)	----	3937	4010	3675	3874	176.1
Fresh water	7.0	3451	3624	3500	3525	63.17
Salty water	7.9	3848	4058	3557	3821	251.6
Alkaline	10.0	3573	3656	4230	3789	381.6
Acidic	4.0	2748	3068	2927	2914	160.4

Table 7.2b Experimental results (flexural load at crack formation) for the RC beams after being strengthened by glass fibre composite.

Submerged solution	PH Level	Sample 1 (N)	Sample 2 (N)	Sample 3 (N)	Mean Value (N)	S.D. (N)
Nil (RT)	----	4926	5013	5123	5020	98.73
Fresh water	7.0	4462	5165	4495	4707	396.6
Salty water	7.9	4500	4686	4754	4646	131.4
Alkaline	10.0	4906	4786	4558	4750	176.7
Acidic	4.0	4644	4448	4937	4676	246.1

Table 7.3a Percentage increase in flexural load capacity of the beams after being submerged into different solutions compared with those of the beams (PRC) in controlled room temperature condition.

Submerged solution	PH Level	% increase of un-strengthened RC beams compared with PRC	% increase of strengthened RC beams compared with PRC*
Nil (RT)	----	0.0	29.6
Fresh water	7.0	- 9.0	21.5
Salty water	7.9	- 1.4	19.9
Alkaline	10.0	- 2.2	22.6
Acidic	4.0	- 24.8	20.7

* PRC beam strengthened by glass fibre composite.

Table 7.3b Percentage increase in flexural load capacity of the beams with and without being strengthened by glass fibre composite after submerged into different solutions.

Submerged solution	PH Level	Un-strengthened condition	Strengthened beam	Percentage increase in flexural load
Nil (RT)	----	3874	5020	29.56
Fresh water	7.0	3525	4707	33.54
Salty water	7.9	3821	4646	21.61
Alkaline	10.0	3789	4750	25.35
Acidic	4.0	2914	4676	60.46

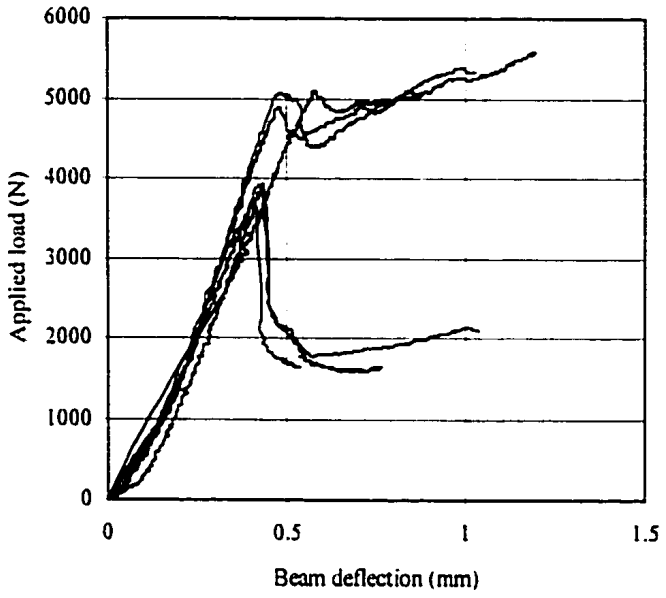

Figure 7.8 Plot of flexural load versus mid-beam deflection of PRC beams subjected to three point bending test. The beams with (top lines) and without (bottom lines) strengthening by glass fibre composite laminates.

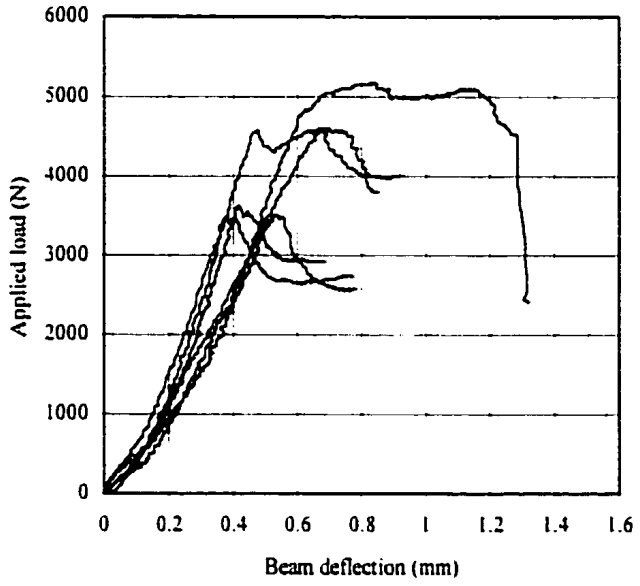

Figure 7.9 Plot of flexural load versus mid-beam deflection of RCH_2O beams subjected to three point bending test. The beams with (top lines) and without (bottom lines) strengthening by glass fibre composite laminates.

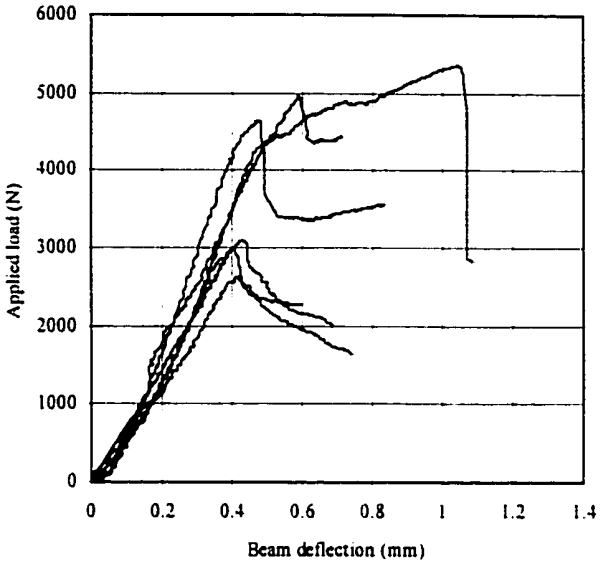

Figure 7.10 Plot of flexural load versus mid-beam deflection of RCPH4 beams subjected to three point bending test. The beams with (top lines) and without (bottom lines) strengthening by glass fibre composite laminates.

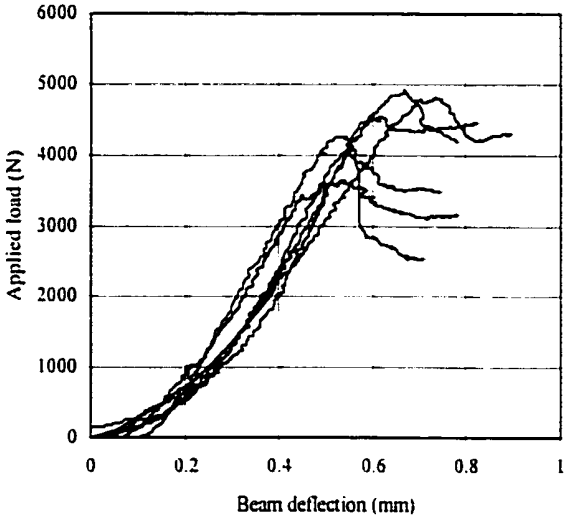

Figure 7.11 Plot of flexural load versus mid-beam deflection of RCPH10 beams subjected to three point bending test. The beams with (top lines) and without (bottom lines) strengthening by glass fibre composite laminates.

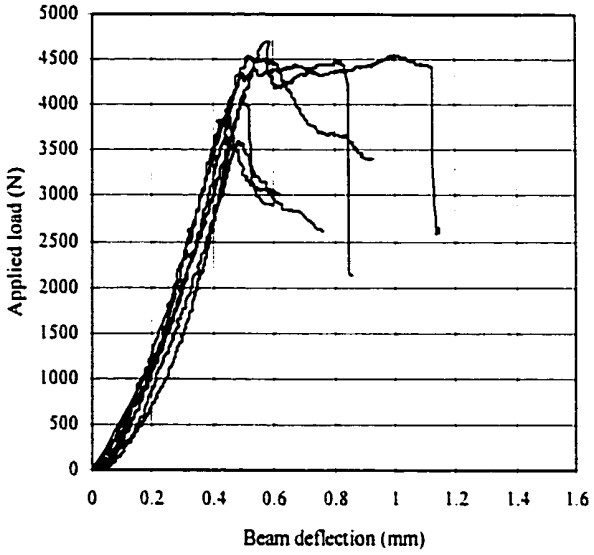

Figure 7.12 Plot of flexural load versus mid-beam deflection of RCNaCl beams subjected to three point bending test. The beams with (top lines) and without (bottom lines) strengthening by glass fibre composite laminates.

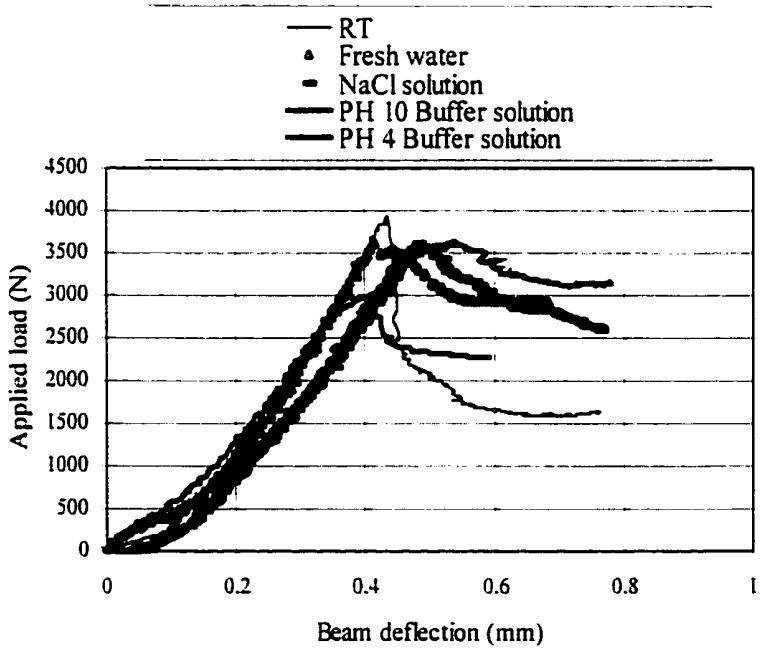

Figure 7.13 Plot of applied load versus mid-beam deflection for all un-strengthened RC beams subjected to three point bending load.

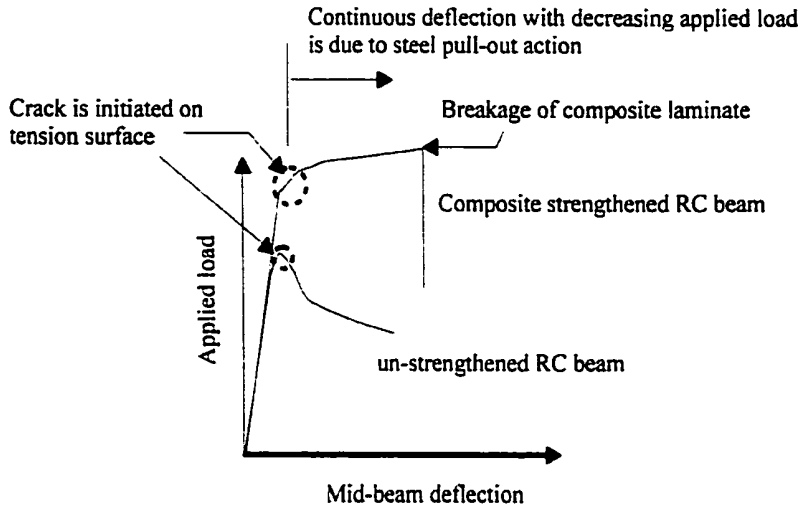

Figure 7.14 Detailed explanation of composite-strengthened RC beam subjected to three point bending load.

From the diagrams, it is clearly shown that the flexural load capacity for all composites strengthened RC beams are increased substantially compared with those of the beams without strengthening at the same ambient environments for six months. The load-deflection curves for all RC beams are linearly increased followed by suddenly drop due to crack formation on tension surface. Deflection is continuously increased with decreasing the applied load, which is caused by the pull-out of embedded steel bar. However, this phenomenon is different for the RC beams strengthened by glass fibre composite on the tension surface.

Initially, the deflection of the strengthened RC beams is increased with increasing the applied load until crack appeares in the concrete. In this stage, the glass fibre composite is still in perfect condition without any crack or debond observed. Cracks or damage in the composite is occurred when further applying the deflection to the beams. The failure patterns of the strengthened RC beams (RCNaCl) is shown in Fig. 7.15. Cracks in the glass fibre composite laminates are found of two testing beams, which are shown in right hand side of the diagram. Debonding occurs on the remained testing beams, which are still under steel pull-out process. The failure modes are well merged to the experimental data shown in Fig. 7.12.

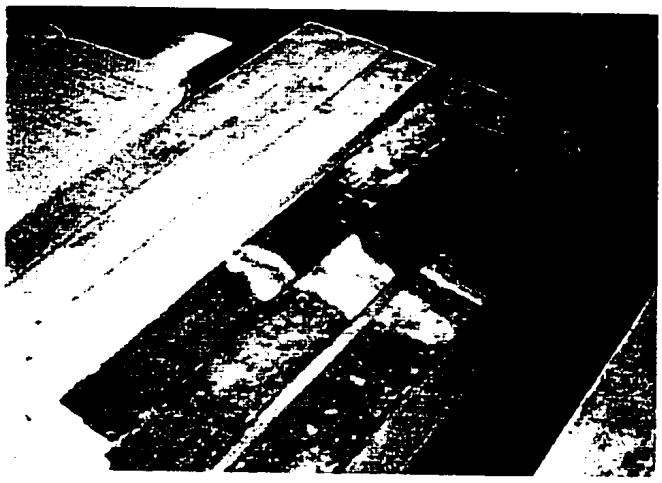

Figure 7.15 Failure patterns of the testing beams RCNaCl strengthened by glass fibre composite laminates.

The experimental results shows that the concrete is susceptible to acidic environment. The reduction of flexural strength is 24.8% after being submerged into the solution with PH level of 4. For the other beams, which were submerged into the fresh water, saline solution and alkaline solution, the reduction of flexural strengths is within 10%. However, it is excited that the flexural strength of all degraded RC beams are increased to the points just slightly below the strength value of the strengthened beam (strengthened PRC beam) without degrading by ambient environment (refer to the Table 7.3a). This implies that the flexural strength of the strengthened RC beam is dominated by the strength of the FRP materials. The degradation of the concrete due to the chemical attack does not influence its flexural strength significantly after strengthening by externally bonded glass fibre composite materials. However, these comments can only be applied to the type of resin-fibre system used in present study.

Throughout the whole experiment, it is concluded that the flexural strength of the RC beams strengthened by glass fibre composite laminates is increased compared with the RC beam without strengthening in high moisture, alkaline and acidic environments. The flexural strength of the RC beam is reduced significantly in acidic environment.

The ultimate flexural strengths measured at a point where a crack was initiated on the beams, which have been submerged into the different chemical substances, are less than that

of the beams stored in the controlled environment. These phenomena may be due to the chemical effects of the submerging solutions on both the concrete and glass fibre composite with. The effects on the concrete have been demonstrated in Fig. 7.13. Bradley et al. (1997) addressed that the presence of moisture inside the composite would lessen the adhesion between fibre and matrix such as glass and epoxy [Kaw, 1997]. However, the percentage increases of ultimate flexural strength for all the testing beams after being strengthened are more than 20%. All tested RC beams are shown in Fig. 7.16.

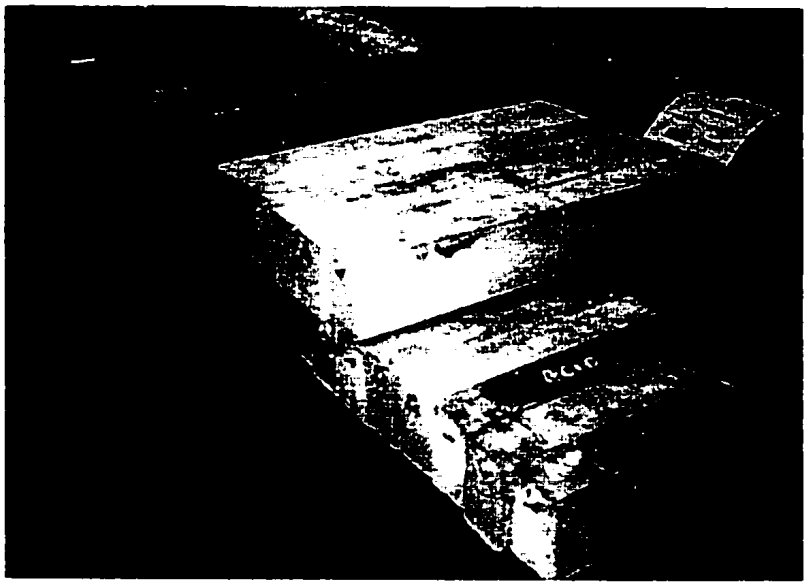

Figure 7.16 All rectangular RC beams after testing.

It has been reported that E-glass is highly susceptible to an environment with high alkalinity. The hydroxide ions (OH^-) in an alkaline environment attack the primary component of glass (silica or SiO_2) and cause a break down in the Si-O-Si single bond forming the glass molecular structure. The results in fiber corrosion and loss of strength. For the concrete strengthening, E-glass fibers are protected by an alkaline-resistance epoxy matrix. All edges of composite reinforcements are sealed-off by the matrix and no fibers are exposed to the air. Besides, the surface of the cured (dry) concrete is experienced in neutral pH level (~ pH 7). The use of E-glass/epoxy composites for concrete strengthening should not be degraded by alkaline attack.

CHAPTER 8

CONCLUDING REMARKS AND SUGGESTIONS FOR FUTURE STUDY

8.1 Conclusion

A comprehensive study on concrete rehabilitating and strain monitoring techniques by using fibre reinforced plastic (FRP) materials and fibre-optic Bragg grating (FBG) sensors has been conducted through many experimental works, theoretical and numerical analyses. Laboratory-sized concrete cylinders and rectangular concrete beams were used for present study. Glass fibre composite was used to strengthen concrete cylinders and beams by wrapping around the circumference of the cylinder and bonding on the beam surfaces, respectively. The mechanical responses of the structures subjected to various types of loading conditions were investigated through standard laboratory tests.

Some un-measurable mechanical parameters such an adhesive shear and peel-off stresses in composite strengthened concrete structures were investigated and interpreted by using linear elastic theories. The results from the finite element method (FEM) explain several failure phenomena and fracture problems of the structures. All predicted theoretical equations were verified by the experimental validated FEM solutions. Based on the current research achievements, several conclusions can be drawn in the following paragraphs.

Glass fibre composite wrapping is an effective solution to strengthen and restore the strength of concrete cylinders, which are designed to endure compressive load with and without crack formation. The ultimate load capacity of the concrete cylinder increases with

increasing the number of composite wrapping layers and area. The strength of the composite-wrapped concrete cylinder increases with an increase of the stiffness as well by using composite wrapping method. The composite wrap provides a strong bond between concrete and composite laminate without slipping and debonding at failure condition. The load carrying capacity of the composite-wrapped structure is governed by the mechanical properties of both the concrete and composite materials.

The axial deflection of the composite wrapped cylinder decreases as the modulus, thickness and wrapping size of the composite materials are increased, and these bring higher wrapping efficiency, η_w. However, negative hoop stress and higher adhesive shear stress in the wrapping sheet may be resulted in by using thick wrapping material with high modulus. The optimised bonding length of the wrapping sheet can be evaluated by using the method shown in Fig. 4.21. The adhesive shear stress and axial stress of wrapping sheet can be determined by Eqs.4.14 and 4.15.

Experimental results show that the flexural strengths of rectangular concrete beams strengthened by glass fibre composite laminates in either bonding on the tension or shear surfaces are increased compared to those of plain beam. Tension face strengthening method gives substantial increase in flexural strength of the beam with notch formation. Direct hand lay-up method gives higher flexural strength of the beam compared with pre-cured plate bonding technique. Filling the epoxy inside the notch can increase the flexural load capacity of the notched concrete beam. The epoxy can provide a strong bonding characteristic to both notch inner surfaces. Therefore, to repair or rehabilitate damaged concrete structure, using advanced composite materials as strengthening medium associated with resin injection method in crack or damage zone can maximise the strengthening characteristic of the structure.

The maximum adhesive shear and peel-off stresses of the composite-bonded beam increase with increasing the modulus and thickness of both strengthened plate and adhesive materials while the stress transferring length is decreased. Failure in an adhesive layer may occur by

using thick and high modulus composite plate for concrete strengthening. The adhesive shear and pee-off stresses for the composite with different ply orientations can be estimated by using the predicted theoretical equations shown in Eqs.(5.63) and (5.28). Recent publications addressed that an externally bonded plate and concrete are normally separated as a unit from underside of the main reinforcement in plate bonded RC beams [Raoof and Hassanen, Aug. 2000]. A high adhesive peel-off stress induced due to the fault use of plate materials may increases the risk of concrete spalling underneath the steel reinforcement of plate strengthened RC beam significantly.

Stress intensity factor, K_I of cracked concrete beam after being strengthened by externally bonded plate on the beam tension surface is initially increased with increasing the crack-depth ratio, a/h under same loading conditions. The K_I is then decreased from a critical a/h value, which is dependent on the mechanical properties of both the concrete and externally bonded plate to a negative value. The use of high modulus and thick materials as the plate to strengthen cracked concrete beam would reduce the value of K_I while the tension force in the plate is increased. The K_I and the closing force in the plate can be evaluated by Eqs.(5.74) and (5.79). However, the proposed method is valid only when the strengthening system is satisfied to Eq.(5.81).

The flexural strengths of steel reinforced concrete (RC) beams are increased by bonding glass fibre composite laminates on its tension surface after submerging the beams into fresh water, seawater, alkaline and acidic solutions for six months of room temperature condition.

A 24.8% drop in flexural strength of the plain RC beams after being submerged into acidic solution. The plain RC beams are less susceptible to the fresh water, seawater and alkaline solution. The experimental results show that the composite strengthened RC beams, which were stored in ambient environment gives a little high flexural strength compared to those of all chemical attacked RC beams after strengthening. However, the overall performances give more than 20% gain in flexural strengths compared to the beams without being strengthened by glass fibre composites when stored in same chemical environments.

Fibre-optic Bragg grating (FBG) sensor is able to measure strain locally for the composite strengthened concrete structures by embedding the sensor either inside the concrete structure or at the interface between the concrete surface and externally bonded composite laminates. The use of embedded FBG sensor enable to detect debonds and surface crack on the concrete, and meaure true strain in real time where the externally bonded strain measuring devices cannot measure accurately, particularly for a structure with a thick surface coverage element.

Multiplexed FBG sensors enable to measure strains in different points of the structure by using only single optical fibre. However, the signal from the sensor is lost when any one of the sensors, which are located in the direction of the light source is damaged.

Sufficient embedding length of the embedded sensor is significant to avoid mis-measurement, in which the grating is located at stress transferring region. The minimum fibre embedding length can be determined by Eq.(6.40). The use of thick adhesive layer and low modulus of fibre coating materials with a short embedding length is not encouraged for fibre embedding system because the stress transferring length increases with increasing thickness of adhesive layer and decreasing modulus of the coating material.

8.2 Suggestions for Future Study

In the past three years, a comprehensive study in concrete rehabilitating and structural strain monitoring techniques by using glass fibre composite materials and Fibre optic Bragg grating sensor has been addressed in this thesis. Due to the time limitation for completion of the current research project, some of the problems arising from the size effects of concrete structures, utilisation of different material as strengthening medium and in-depth study on three faces strengthening technique for rectangular concrete structures have not been addressed in this thesis.

Extensive studies in finding out the optimised design for different composite-strengthening systems are essential to determine minimum use of strengthening material with maximum structural load bearing capacity, particularly in large scale concrete structure. The dynamics responses for the composite-strengthened structure in sustaining seismic and fatigue loading are essential for real-life applications.

In the future, investigation on composite strengthened steel reinforced concrete (RC) structure is important in real life structural applications. Study on steel pullout mechanism for RC structure after being strengthened by different externally bonded materials is also important.

In-depth investigation on the use of optical fibre sensors as local or field strains measuring devices still need more efforts to study its applicability and durability in harsh environments, such as chemical aggressive environments with different ambient temperature conditions. The sensor arraying system to avoid mis-signalling due to the damage of one FBG sensor along the optical fibre is also essential in further study.

REFERENCES

ACI 363R-92. State-of-the-art report on high strength concrete. ACI manual of Concrete Practice Part I: Materials and General Properties of Concrete. Vol.55 (1994).

Aliabadi, M. H. and Rooke, D. P. Numerical fracture mechanics. Computational mechanics publications, London, 1991.

Ansari, F. and Wang, J., Rate sensitivity of high birefringent fiber optic sensors under large dynamic loads. IEEE J. Lightwave Eng., Vol. 13 (1995) 1992-1997.

Ansari, F and Yuan, L., Mechanics of bond and interface shear transfer in optical fibre sensors, *J. of Eng. Mech.*, No.4, Vol. 124 (1998) 385-394.

Arduini. M. and Nanni. A. Behaviour of precracked RC beams strengthened with carbon FRP sheets. J. Comp. for Construct., Vol. 1 (1997) 63-69.

Ballinger, C. Infrastructure repair and retrofit strengthening with external FRP systems. Composites fabrication., Vol. 10 (1997) 18-22.

Baluch M. H. Fracture mechanics application to reinforce concrete members in flexure. In application of Fracture Mechanics to Reinforced Concrete, Elsevier Applied Science, London, (1992) 413-436.

Bascom, W. D. & Jensen, R. M., Stress transfer in single fiber/resin tensile tests. J. Adhes., Vol. 19 (1986) 219-239.

Berry, J. p. and Standford, J. L. Reinforced thermoplastics II, Plastic Rubber Conference, Manchester, England, (1997) 34-78.

Bizindavyi, L. and Neale, K. W. Transfer lengths and bond strengths for composite bonded to concrete. J. Comp. for Construct., No. 4, Vol. 3 (1999) 153-160.

Bradley, W. L., Wood, C. A., Pratt, B. A. and Chatawanich, C. S. The effect of moisture on the interfacial strength of graphite-epoxy and E-glass epoxy composites. Proceed. ICCM-11, Gold coast, Australia, (1997) 483-492.

Brook, M. K. M. and Dewar, J. D. Concrete material and Practice. Edward Arnold. 6th Ed., (1991).

Budansky, B., Drucker, D. C., Kino, G. S. & Rice, R. J., The pressure sensitivity of a clad optical fiber. Appl. Opt., Vol. 18 (1979) 4085-4088.

Butler, C. D. & Hocker, G. B., Fiber optic strain gauge. Appl. Opt., Vol. 17 (1978) 2867.

Buyukozturk, O. and Hearing, B. Failure behaviour of pre-cracked concrete beams retrofitted with FRP. J. Comp. for Constr., No. 3, Vol. 2 (1998) 138-144.

Carpinteri, A., Chiaia, B. and Ferro, G. A new explanation for size effects on the flexural strength of concrete. Mag. of Concrete. Research, No. 178, Vol. 49 (1997) 45-53.

Carpinteri, A. Mechanical damage and crack growth in concrete. Martinus Nijhoff Dordrecht (1986).

Castaing, ph and Lemoine, L. Effects of water absorption and osmotic degradation on long term behaviour of glass fibre reinforced ployester. Polymer Comp., No. 5, Vol. 16 (1995) 349-356.

Chaallal, O., Nollet, M. J. and Perraton, D. Shear strengthening of RC beams by externally bonded side CRFP strip. J. Comp. for Constr., No. 2, Vol.,2 (1998) 111-114.

Christropher, P.R. Analysis of concrete cylinder with a composite hoop wrap. Infrastructure: New materials and methods of repair proceeding of the materials engineering conference 804. ASCE New York 1994; 8-21.

Claus, R. O., Gunther, M. F., Wang, A. B., Murphy, K. A. & Sun, D., Extrinsic Fabry-Perot sensor for structural evaluation. In Applications of Fiber Optic Sensors in Engineering Mechanics, ASCE-EMD Spec. Pub., ed F. Ansari. ASCE, New York, (1993) 60-70.

Cole, J. H., Johnson, R. L. & Bhuta, P. B., Fiber optic detection of sound. J. Acoust. Soc. Am., Vol. 62 (1977) 1136-1138.

Connor, J. S. O., New York state gives FRP's a try. Structure Magazine, summer (1999).

Czarnek, R. Guo, Y. F., Bennett, K. D. and Claus, R. O. Interferemetric measurements of strain concentrations induced by optical fiber embedded in a fiber reinforced composite. Proc. SPIE – Int. Soc. Opt. Engg., (1989) 43-54.

Davis. M. A., Bellemore. D. G., Putnam. M. A. and Kersey. A. D., High strain monitoring in composites-wrapped concrete cylindrical using embedded fibre Bragg grating arrays. Proc. SPIE., Vol. 2721 (1998) 149-154.

Dellow, N. Advanced Composites Bulletin, Sept., (1999) 5-9.

Delta Structure Technology, Inc. News. Building columns, 1998.

Dewynters-Marty, V., Ferdinand, P. Bourasseau, S., Dupont, M. and Balageas, D. Embedded fibre Bragg grating sensors for industrial composite cure monitoring. J. of Intel. Mater. Sys. And Struct., Vol. 9 (1998) 785-787.

Du. W., Tao. X. M., Tam. H. Y. and Choy. C. L., Fundamentals and applications of optical fibre Bragg grating sensors to textile structural composites. J. Comp. and Struct., Vol. 42 (1998) 217-229.

Duck, G. and LeBlanc, M., Arbitrary strain transfer from a host to an embedded fibre-optic sensor. J. Smart Mater. Struct., Vol. 9 (2000) 492-497..

Ehsani, M. R., Saadatmanesh, H. and Velazquez-Dimas, J. I. Behaviour of retrofitted URM walls under simulated earthquake loading. J. of Comp. for Construct., No. 3, Vol. 3 (1999) 134-142.

Engel, R. S. Carbon fibre reinforcement grids for concrete. Advanced Composite Bulletin, Nov., (1999) 4.

Fitzgibbon, M. E., Heat generation and control. Concrete , No. 12, Vol. 10 (1976) 33-35.

Foote, P. D. Fibre Bragg grating strain sensor for aerospace smart structures. Proc. SPIE., Vol. 2361 (1994) 162-166.

Fuhr, P. L., Spammer, J. and Zhu, Y. A novel signal demodulation technique for chirped Bragg grating strain sensor. J. Smart. Mater. Struct., Vol.9 (2000) 85-94.

Garden. H. N., Hollaway. L. C. and Thorne. A. M., The strengthening and deformation behaviour of reinforced concrete beams upgraded using prestressed composite. J. Mat. and Struct., Vol. 31 (1998) 247-258.

Gibson, A. G. Composite structures in offshore application. Comp. Mater. Inn Marine Struct. Chapter 3, 1993. R. A. Shenoi, Ed. Cambridge Ocean Technology Series.

Gilstrap, J. M., Burk, C. R., Dowden, D. M. and Dolan, C. W. Development of FRP reinforcement guidelines for pre-stressed concrete structures. J. Comp. for Construct., No. 1, Vol. 4 (1997) 131-139.

Grace, N. F., Sayed, G. A., Soliman, A. K. and Saleh, K. R. Strengthening reinforced concrete beams using fibre reinforced polymer laminate. ACT Strcut. J., No. 5 Vol. 96 (1999) 865-874.

Groves-Kirkby, C. J. Optical fibre strain sensing for structural health and load monitoring. The GEC J, of Tech., No. 1, Vol. 15 (1998) 16-26.

Gutman, E. M. Environmental effects on stress relaxation in polyester fibreglass composite. Polymer Comp., Vol. 16 (1995) 518-521.

Harmon, T. G., and Slattery, K. T. Advanced composite confinement of concrete, Proc., 1st Int. Conf. on Advanced Compos. Mat. in Bridge and Struct. Sherbrook, Canada, (1992) 299-306.

Holton, W. C. Multiplexing sensors test new bridge material. Laser Focus World., No.7, Vol.4 (1998) 26-29.

Huang, S., Ohn, M. M., LeBlanc, M. and Measures, R. M., Continuous arbitrary strain profile measurements with fibre Bragg grating, *J. Smart Mater. Struct.*, Vol. 7 (1998) 248-256.

Hyer, M. W. Stress analysis of fibre-reinforced composite material. McGraw Hill. U.S.A. (1998).

Kalamkarov, A. L. Processing and evaluation of pultruded smart composites with embedded fibre optic sensors. Proc. of 7th International conference on Composites Engineering, (2000) B35-38.

Kaliakin. V. N., Chajes. M. and Januszka. T. F., Analysis of concrete beams reinforced with externally bonded woven composite fabrics. J. Comp., Vol. 27B (1996) 235-244.

Karbhari, V. M. and Gao, Y. Q. Composite jacketed concrete under uniaxial compression – vertification of simple design equations. J. Mat. in Civ. Engg., No. 4, Vol. 9 (1997) 185-193.

Kashyap, R., Armitage, J. R., Campbell, R. J., Williams, D. L., Maxwell, G. D. and Ainslie, B. J., Light sensitive optical fibres and planar waveguides. BT Technol. J., Vol. 11 (1993) 150-158.

Kattsuyami, T., Matsumura, H. & Sugamume, T., Low-loss single-mode polarization fibers. Electronics Lett., Vol. 17 (1981) 473.

Kaw, A. K. Mechanics of composite materials. CRC Press. U.S.A, 1997.

Kersey, A. D. & Morey, W. W., Multiplexed Bragg grating fiber-laser strain sensor system with mode-locked interrogation. Electronic Lett., Vol. 29 (1993a) 112.

Kersey, A. D., Bekoff, T. A. & Morey, W. W., Multiplexed fibre Bragg grating strain sensor system with a fiber Fabry-Perot wavelength filter. Opt. Lett., Vol. 18 (1993b) 1370-1372.

Kersey, A. D., Davis, M. A., Berkoff, T. A., Bellemore, D. G., Koo, D. G. and Jones, K. P. Progress towards the development of practical fibre Bragg grating instrumentation systems. Proc. SPIE., Vol. 2839 (1996) 40-63.

Kumar, M.and Monteriro, P. J. M. Concrete – Structure, Properties and Materials. Prentice Hall, Inc. 1993. 2nd Ed. U.S.A.

Larralde, J. Compressive strength of small concrete specimens confined with fibreglass laminates. J. Cem. Con. And Aggreg., No. 1, Vol. 19. (1997) 17-21.

Lee, S. W. R., Li, Z., Tang, J. M., Lee, S. and Tong, P. Development of composite grid tubes for the reinforcement of concrete column. Proceeding, ICCM 12 (1999).

Lo, Y. L. and Xiao, F. Y. Measurement of corrosion and temperature using a singl-pitch Bragg grating fibre sensor. J. of Intel. Mater. Sys. And Struct., Vol. 9 (1998) 800-807.

Luke, S. Mouchel hands out repairs on a plate, Construct. News, 25, Oct (1997).

Luke, S. Using advanced composites to strengthen existing and new structures. Open seminar held in HKIE (1999).

Mallick, P. K., Composite Engineering Handbook. Marcel Dekker, Inc., USA, 1997.

Malek, A. M., Saadatmanesh, H and Ehsani, M. R. Prediction of failure load of RC beams strengthened with FRP plate due to stress concentration at the plate end. ACI Structural Journal, No. 1, Vol. 95 (1998) 142-152.

Maaskant, R., Alavie, T., Measures, R. M., Tadros, G. Rizkalla, S. H. and Guha-thakurta, A. Fibre-optic Bragg grating sensor for bridge monitoring. J. Cement and Concrete Comp., Vol. 19 (1997) 21-33.

Mayo, R. Bridge tests reveal strengths of composite reinforcements. Mag. Civil Engg. ASCE, Vol. 17 (1999).

Measures, R. M. Smart structures: A revolution in civil engineering, keynote address. ACMBA-1 Conf. Sherbrook, Quebec, Canada (1992).

Measures, R. M., Alavie, A. T., Maaskant, R., Ohn, M., Karr, S. and Huang, S. Bragg grating structural sensing system for bridge monitoring. Proc. SPIE., Vol. 2294 (1994) 53-60.

Mehta, P. K. Sulfate attacks on concrete – a critical review. Mat. Sci. of Concrete III. Ed. J. Skalny, American Ceramic Society, (1993) 105-30.

Meier, U. and Deuring, M. The application of the fibre composites in bridge repair. Strasse und Verkehr., No. 9, Vol. 77 (1991) 775-777.

Meier, U. Strengthening of structures using carbon fibre/epoxy composites. Contr. And Build. Mat., No. 6, Vol. 9 (1995) 341-351.

Michael, L. D., Stephen, W. J. and Ralph, P. T. Fibre Bragg gratings fabricated using a wavelength tinable laser source and a phase mask based interferometer. J. Meas. Sci. Tech., No. 4, Vol. 7 (1996) 445-448.

Mirmiran, A. and Shahawey, M. A new concrete-filled hollow FRP composite column. J Comp. Pt. B 27B (1996) 263-268.

Mirmiran, A., Shahawy, M., Samaan, M., Echary, H. E., Mastrapa, J. C. and Pico, O. Effect of column parameters on FRP-confined concrete. J. of Comp. for Construt., No. 4. Vol. 2 (1998) 175-185.

Miya, T., Terunuma, Y., hosaka, T. and Miyashita. Ultimate low-loss single mode fibre at 1.55μm, Electr. Lett., Vol. 15 (1979) 106-108.

Mo. Y. L., Tsai. S. P. and Lee. I. S., Seismic performance behaviour of beam-column connections in pre-stressed concrete bridges. J. Mat. and Struct., Vol. 31 (1998) 411-417.

Morey, W. W., Meltz, G., Glenn, W. H. Fibre optic Bragg grating sensors. Proc. SPIE., Vol. 1169 (1989) 98-107.

Morey, W. W., Ball, G. A. and Singh, H. Application of fibre grating sensors. Proc. SPIE., Vol. 2839 (1996) 2-7.

Neville, A. M. Properties of Concrete. 4th Ed. Addison Wesley Longman Ltd. England. 1997.

Niu, C. Y. M. Airframe structural design - practical design information and data on aircraft structures, Technical book company, California, U.S.A. (1993).

Personick, S. D. Fibre Optics Technology and Applications. Plenum Press, N.Y. (1985)
Peter, E. Strengthening and protecting concrete. Advanced Composites Bulletin. Sept., Vol. 8 (1999).

Peter, E., Strengthening and Protecting Concrete., Advanced Composite Bulletin, Sept. (1999) 8.

Powers, J. P. An Introduction to Fiber Optic Systems. 2nd. Time Mirror Higher Education Group, Inc Company. U.S.A. (1997).

Rao, Y. J. Recent progress in applications of in-fibre Bragg grating sensors. J. Optics and Lasers in Engg., Vol. 31 (1999) 297-324.

Raoof, M. and Hassanen, M. Peeling failure of reinforced concrete beams with fibre-reinforced plastic or steel plates glued to their soffits. Proc. Institution of Civ. Engg. Struct. And Build. No.140, Vol. 3 (2000) 291-305.

Raphael, J. M. Tensile strength of concrete. Concrete International., No. 2, Vol. 81, (1984) 158-165.

Ritchie, P. A., Thomas, D. A., Lu. L. W/ and Connelly, G. M. External reinforcement of concrete beams using fibre reinforced plastics. ACI Struct. J., No. 4, Vol. 88 (1998) 490-500.

RMIT. Design and manufacture of advanced fibre composite structures – A practical course in the application of advanced composite technology. Pressed by Royal Melbourne Institute of Technology University (1996).

Romben, L. Aspects of testing methods for acid attack on concrete. CBI Research, 1:78 (1978) 61-72.

Rooke, D. P. Simple methods of determining stress intensity factors. Key Eng. Fgract., Vol. 14 (1981) 397-426.

Rubin, I.I. Handbook of plastic materials and technology. John Wiley & Sons, Inc. U.S.A. 1990.

Rutherford, P. S. and Westerman, E. A. Aircraft structural integrity and smart structural health monitoring. Proc. Active Mat. and Adaptive, Vol. 16 (1992) 267-270.

Sakai, H., Otaguro, H., Hisabe, N., Mitsui, Y. and Murakami, K. The experimental study on the effect of reinforcing the rectangular beam shearing due to carbon fibre sheet. Textile comp. in Build. Constr., (1996) 145-151.

Sameer, H. and Ahmad, S. H. Concrete crack repair by stitches. J. Mater. And Struct., Vol. 30 (1997) 418-423.

Saouma, V. E., Anderson, D. Z., Ostrander, K., Lee, B. and Slowik, V. Application of fibre Bragg grating in local and remote infrastructure health monitoring. J. Mat. and Struct., Vol. 31 (1998) 259-266.

Seible, F., Priestley, M. J. N., Hegemier, G. A. and Innamorato, D. Seismic retrofit of RC columns with continuous carbon fibre jackets. J. Comp. for Construct., No. 2, Vol. 1 (1997) 52-62.

Shahawy, M. A., Beitelman, T., Arockiasamy, M. and Sowirajan, R. Experimental investigation on structural repair and strengthening of damaged prestressed concrete slabs utilising externally bonded carbon laminates. J. Comp., Pt. B, Vol. 27B (1996) 217-224.

Sih, G. C. Handbook of stress intensity factors. Institute of Fracture and Solid Mechanics, Pennsylvania (1973).

Spoelstra, M. R. and Monti, G. FRP confined concrete model. J. Comp. for Construct., No. 3, Vol. 3 (1999) 143-150.

Steiner, W. Strengthening of structures with CFRP strips. Proc. 2nd Int. Conf. On Advanced Mat. in Bridges and Strcut., The Canadian Soc. For Civ. Engg., Montreal, Canada, (1996) 407-417.

Tada, H., Paris, P. C. and Irwin, G. R., The stress analysis of crack handbook. Paris Productions Incorporated (1985).

Taljsten, B. Strengthening of existing concrete structures by epoxy bonded plates of steel or fibre reinforced plastic. Con. Repair. Reh. And Protect. (1996).

Tateda, M. & Horiguchi, T., Advances in optical time domain reflectometry. IEEE J. Lightwave Technol., Vol. 7 (1989) 1217-1223.

Toutanji, H. A. Durability characteristics of concrete columns wrapped with advanced composite materials. J. of Comp. Struct., Vol. 44. (1999) 155-161.

Toutanji, H. A. Evaluation of the tensile strength of cement-based advanced composite wrapped specimens. J. Comp. Sci. and Tech., Vol. 59 (1999) 2261-2268.

Toutanji, H. and Balaguru, P. Durability characteristics of concrete columns wrapped with FRP tow sheets. J. Mat. in Civ. Engg., No. 1, Vol. 10 (1998) 52-57.

Townsend, R. D. and Taylor, N. H. Fibre optic monitoring of temperature and strain along insulated pipe work at high temperature. Proc. oF Euromaintenance (1996).

Triantafillou, T. C., Shear strengthening of reinforced concrete beams using epoxy-bonded FRP composites, *J. ACI Structural*, No.2, Vol. 95 (1998) 107-115.

UDD. E., Fibre optic smart structures. John wiley & sons, Inc (1995).

Uomoto. T. Utilisation of FRP reinforcements for concrete structures. Proc. Asian-australasian conference on composites materials, Vol. 1 (1998) 105.

Yuan, L., and Ansari, F., White light interferometric fiber-optic strain distribution sensing system, Sensors and Actuators: A, Vol. 63 (1997) 177-181.

Yuan, L. and Zhou, L. M., Sensitivity coefficient evaluation of an embedded fiber optic strain sensor, Sensors and Actuators: A, No. 2, Vol. 68 (1998a) 98-104.

Yuan, L., and Ansari, F., Embedding white light interferometer fiber optic strain sensor for concrete beam crack-tip opening monitoring. Measurement Science and Technology, Vol. 9 (1998b) 261-266.

Yuan, L., and Zhou, L. M., Temperature compensated fiber optic strain sensor using differential white-light interferometric technique. Measurement Science and Technology, Vol. 9 (1998c) 1174-1179.

Yuan, L. and Zhou, L. M., 1×N star coupler as distributed fiber optic strain sensor using in white light interferometer, Appl. Opt., Vol. 37 (1998d) 4168-4172.

Zhang, Q., Brown, D. A., Reinhart, ., Morse, T. F., Wang, J. Q. and Xiao, G. Tuning Bragg wavelength by writing gratings on prestrained fibres. IEEE Photon Technol. Letter, Vol.6 (1994) 839-841.

Zhang, S., A study on reinforcing concrete columns using fibre reinforced composite wraps. The PhD thesis, University of Sydney (1998).

PUBLICATIONS AND AWARDS ARISING FROM THE PRESENT STUDY

Refereed Book Chapter and International Journal papers

1. **K. T. Lau**, L. B. Yuan, L. M. Zhou and C. H. Woo., "Strain monitoring in FRP laminates and concrete beam using FBG sensors", Journal of Composite Structures., **51** (2001) 9-20.

2. **K.T. Lau**, L.M. Zhou, J. S. Wu and C. H. Woo, "Strengthening and strain monitoring concrete structures using fibreglass composites and FBG sensor", Journal of Materials Science Research International, No.3. **5** (1999) 216-221.

3. **K.T. Lau**, L. M. Zhou and J. S. Wu, "Investigation on strengthening and strain sensing techniques for concrete structures using FRP composites and FBG sensors", Journal of Materials and Structures, No. 235. **34** (2001).

4. **K. T. Lau**, L. M. Zhou and L. Ye, "Strain evaluation on strengthened concrete beam by using FBG sensor", Non-destructive Characterisation of Materials, Chapter, Edited by R. E. Green, American Institute of Physics (AIP) (ISBN 1-5639-911-4), New York, 303-308, 1999.

5. **K. T. Lau**., L. M. Zhou and L. Ye, "Investigation on upgrading and health monitoring the civil concrete structures using FRP and FBG sensor", Advanced Composites Letters, No.6, **8** (1999) 323-332.

6. Peter K. C. Chan, W. Jin, **K. T. Lau** and L. M. Zhou, "Multi-point strain measurement of composite-bonded concrete materials with a FMCW multiplexed FBG sensor array", Sensors and Actuators A, **87** (2000) 15-25.

7. **K. T. Lau** and L. M. Zhou, "The mechanical behaviour of composite-wrapped concrete column subjected to uni-axial compression load", Journal of Composite Structures, (2000) in press.

8. **K. T. Lau**, S. Q. Shi and L. M. Zhou., "Stress intensity factor for the concrete beam strengthening by composite plate", Fracture Mechanics and Advanced Engineering Materials, Chapter, Edited by L. Ye and Y. W. Mai, The University of Sydney press (ISBN 1-86487-283-7), Australia, 84-91, 1999.

9. **K. T. Lau**, S. Q. Shi and L. M. Zhou., "Estimation of stress intensity factor (K_I) for the plate bonded concrete beams by using superposition method", submitted to the Magazine of Concrete Research, **53**(2001) 31-41.

10. **K. T. Lau** and L. M. Zhou, "Mechanical performance of composite-strengthened concrete structures", Journal of Composites, Part B: Engineering, **32** (2000) 21-31.

11. **K. T. Lau**, C. C. Chan., L. M. Zhou and W. Jin. "Strain monitoring in composite-strengthened concrete structures using optical fibre sensors", Journal of Composites, Part B: Engineering, **32** (2001) 33-45.

12. **K. T. Lau**, L. M. Zhou and Y. Le, "Rehabilitating and real-time strain monitoring on concrete structures using advanced composites and optical fibre sensor", J. Society of Manufacturing Engineering, CM01-112 (2001). ***(invited paper)***

13. C. C. Chan, Y. J. Gao, **K. T. Lau**, H. L. Ho, L. M. Zhou, and W. Jin, "Reduction of unwanted interferometric signals in a TDM FBG sensor array using a laser source", Optical, and Laser Technology., (2000) in press.

14. **K. T. Lau**, L. B. Yuan and L. M. Zhou, "Thermal effects on embedded grating sensor for FRP structure", accepted for publication in Smart Materials and Structures., (2000).

15. **K. T. Lau**, L. B. Yuan, L. M. Zhou and C. H. Woo., "Applications of composites, optical fibre sensors and smart composites for concrete rehabilitation: an overview", accepted for publication in Applied Composite Letters

16. L. B. Yuan, W. Jin, L. M. Zhou and **K. T. Lau**. "The temperature characteristic of fibre-optic pre-embedded concrete bar sensor", submitted to the Sensors and Actuators A. (2000).

17. L. B. Yuan, L. M. Zhou, W. Jin and **K. T. Lau**. "The measurement of cement-based composite materials thermal expansion coefficient by using fibre optic white light interferometer", submitted to Composite Structures. (2000).

Refereed Conference Papers

18. Peter K. C. Chan, W. Jin, **K. T. Lau** and L. M. Zhou., "Strain monitoring of composite-bonded concrete specimen measurements by use of FMCW multiplexed fibre Bragg grating sensor array"., *Proc. of ICSC* 2000, Wuhan, China, June 19-21.

19. C. K. Chan, **K. T. Lau**, L. M. Zhou and W. Jin, "Utilisation of fibre-optic bragg grating sensor in cylindrical concrete column confined with glass fibre reinforced plastic laminate under uni-axial compression load", *Proc. International Society for Optical Engineering*, Boston, Massachusetts, **3538** (1998) 64-72.

20. **K. T. Lau**, L. M. Zhou and C. H. Woo, "Monitoring technique of strengthening civil concrete materials by using advanced composite materials with the aid of fibre-optic

bragg grating sensor". *Proc. Asian-Australasian Conference on Composite Materials, Osaka, Japan,* **2** (1998) 6271-6274.

21. **K. T. Lau**, L. M. Zhou, L. Ye and M. Diao. "Strengthening and strain sensing techniques in rectangular concrete beam using fibreglass composites and fibre bragg grating sensors", *Proc. International Conference on Composite Materials, Paris,* (1999).

22. L. B. Yuan., L. M. Zhou., Y. Liang and **K. T. Lau.**, "Fibre optic ultrasonic sensors for concrete nondestructive detecting"., *Proc. of The International Conference on Trends in Optical Nondestructive Testing*, May 3-6 2000, Switzerland.

23. **K. T. Lau** and L. M. Zhou., "Using Fibre-optic Bragg grating sensor for strain measurement in composite-strengthened concrete structure"., *Proc. of ICCE/7*, July 2-8, 2000, Denver Colorado.

24. L. B. Yuan, L. M. Zhou, W. Jin, **K. T. Lau**, "Effect of thermally induced strain on optical fibre sensor embedded in cement-based composites", NDT of Materials and Composites, Proc. of SPIE . 4336 (2001).

25. **K. T. Lau**, L. M. Zhou and L. B. Yuan, "Smart composite for repair of concrete structure", accepted for presentation in International Conference on FRP Composites in Civil Engineering., December (2001), Hong Kong.

AWARDS AND HONOURS

1. M. C. Chui, **K. T. Lau** and L. M. Zhou, "Mechanical Characterisation of Concrete Structure With and Without Strengthening by Using Fibreglass Composites", **The Best Paper Award** (1st Prize) on Materials 1998 in the Best Paper Competition of The Hong Kong Institution of Engineers.

2. The **Sir Edward Youde Memorial Fellowship Award** 1999/2000 based on the research achievement from current research project.

3. A paper entitled "A study on strengthening and strain sensing techniques in rectangular concrete beam using glass fibre composite and FBG sensor" has been selected by the Board of Advisors of the Society of Manufacturing Engineers (SME) in USA as **Benchmark** for the composites manufacturing and tooling industry

4. **Scientific reviewer** for Journal of Composites, Part B: Engineering.

5. **Chairperson** in the Seventh Annual International Conference on Composites Engineering (ICCE/7), Denver, Colorado (2000).

6. **Who's Who** in Science and Engineering (2001-2002)

7. **Who's Who** in the World (2001-2002)

APPENDIX

(Copies of the publications)

ELSEVIER

Composites: Part B 32 (2001) 21–31

composites
Part B: engineering

www.elsevier.com/locate/compositesb

Mechanical performance of composite-strengthened concrete structures

Kin-tak Lau, Li-min Zhou*

Department of Mechanical Engineering, The Hong Kong Polytechnic University, Hunghom, Kowloon, Hong Kong, People's Republic of China

Received 9 August 2000; accepted 7 September 2000

Abstract

The interest of using fibre reinforced plastic (FRP) materials in rehabilitating damaged concrete structures respectively has been increased rapidly in recent years. In this paper, the structural behaviours of the glass–fibre composite strengthened concrete structures subjected to uniaxial compression and three point bending tests are discussed through experimental studies. Two types of concrete structure are used in present study, they are concrete cylinder and rectangular concrete beam. Discussion on the environmental effects of composite strengthened reinforced concrete (RC) structures is also addressed. Experimental results show that the use of glass–fibre composite wrap can increase the load carrying capacity of the plain concrete cylinders with and without notch formation. The flexural load capacity of the concrete beam increases to more than 50% by bonding 3 layers of glass–fibre composite laminate on the beam tension surface. Direct hand lay up method gives better strengthening characteristic in term of the ultimate flexural load compared with pre-cured plate bonding technique. The flexural strengths of composite strengthened RC beams submerged into different chemicals solution for six months are increased compared with the RC beams without strengthening. The strength of the concrete structure is seriously attacked by strong acids.

Keywords: Glass–fibre reinforced plastic

1. Introduction

In recent years, the demands of upgrading and rehabilitating existing concrete structures have been growing rapidly. The continuing deterioration of the world's civil concrete structures due to ageing and corrosion of steel reinforcements highlights the urgent need for the effective rehabilitation techniques in terms of low costs and fast processing time with minimising the time for traffic interruption. In some developing countries, the needs on replacing and strengthening the concrete structures are also increased due to the considerable increase in traffic volume, which is beyond the original design limit [1–2].

Fibre reinforced plastic (FRP) has been recognised as a one of the most innovative materials in the applications ranging from the aerospace industry to prevalent sport goods and facilities for more than 30 years. It has been demonstrated that the FRP could be used successfully to replace conventional materials for most primary structural elements in modern aircraft with safe and durability [3]. Unfortunately, the adoption of the FRP in civil construction side is still limited up-to-date. The serious concerns regarding the use of the FRP as reinforcements or substitutes for concrete structures are lack of experimental history, international design code and recognised specifications, and economics related to fabrication [4].

The use of the FRP in the applications of concrete rehabilitation has been recognised as an innovative technology. When the FRP plate with high tensile strength properties bonds on the concrete surface, it can strengthen the structure with minimum changes of weight and dimension. The FRP offers substantial improvements in solving many practical problems that conventional material cannot be settled to provide a satisfactory service life of the structure. Unlike the conventional steel materials, the FRP have better corrosion resistant property [5–6]. The beneficial characteristics of using the FRP in concrete construction include its high strength-to-weight ratio, low labour intensive, easy to perform, less traffic interruption during repair, cost reductions in both transportation and in situ maintenance in long term strategy. Recently, researches in the application of using the FRP plate for strengthening deteriorated, deficient, and some damaged concrete structures have been gained rapidly in Europe, Asia and North America [7–11]. Therefore, applying this material in infrastructure application is becoming more and more important to extend the service life of the civil construction facilities into the twenty-first century.

* Corresponding author. Tel.: +852-2766-6663; fax: +852-2365-4703.
E-mail address: mmlmzhou@polyu.edu.hk (L.-m. Zhou)

1359-8368/01/$ - see front matter
PII: S1359-8368(00)00043-3

Table 1
Result from the sieve analysis test of fine and coarse aggregates

ASTM sieve size (mm)	Weight retained (g)	Weight passing (g)	Percentage passing	Standard criteria (%)
19.0	77.9	2876.2	97.36	≥ 80
9.50	1024.6	1851.6	62.68	≥ 60
4.75	672.7	1178.9	39.91	≥ 10
2.36	286.5	892.4	30.21	≥ 15
0.6	436	457.4	15.48	≥ 5
0.3	156.3	301.1	10.19	≥ 2
0.15	119.4	181.7	6.15	≥ 0
Remainder	181.7	0	0	
Total loss in	2954.1			
Process	3.4			

Table 2
Mechanical properties of concrete, adhesive and glass–fibre composite materials

Mechanical properties	Concrete	Adhesive (epoxy)	Glass–fibre composite
Diameter (mm)	100	-	-
Modulus of elasticity (GPa)	27.8	3.3	13.33
Tensile strength (Mpa)	4	90	180
Compressive strength (MPa)	49.99	110	50
Max. service temperature (°C)	200	200	200
Coefficient of thermal expansion (10^{-6})	16	60	4.8

2. Experimental procedure

The experimental procedure consisted of the examination of the quality of concrete constituent, specimen fabrications and mechanical properties tests. Two different types of concrete geometreis were used in present study, they were concrete cylinder and rectangular concrete beam with and without notch formation. All the concrete cylinders and beams were subjected to uni-axial compression and three-point bending tests after strengthening by glass–fibre composite laminates, respectively. In the initiation, the quality of the concrete constituents was justified through the sieve analysis test according to ASTM C 136 in order to determine the particle size distribution, and the result is listed in Table. 1. According to the results showed in the table, it is found that the percentages of the particles passing through different size of sieves are satisfied to the standard requirement.

2.1. Detail of test specimen

The concrete consists of Portland cement, fine (sand) and coarse aggregates and water. In some situations, admixture is used to control the rate of chemical reaction inside the concrete. In the present study, mixture ratios of 1:1.5:3 in concrete and 0.5 in water to cement were used. All concrete specimens were cast in standard steel mould and cured for 28 days, at 25°C with 100% humidity condition for completion of the hydration process. The dimensions of the concrete cylinder and rectangular beams are 100 mm in diameter and 200 in height, and 154 mm in square and 508 mm in length, respectively. Notches were made for some specimens in order to pretend damaged structures for repair.

2.2. Concrete-wrapped concrete cylinders

A total of 27 concrete cylinders were made. Two types of specimens were used, they are plain and notched concrete

Table 3
Details of all testing concrete cylinders (CWC, composite wrapped concrete; NC, notched concrete; CWNC, composite wrapped notched concrete)

Specimen code	Cylinder type	Wrapping layer (s)	Bonding length (mm)	Bonding pattern
PC	Plain	-	-	Nil
CWC200-1		1	200	Nil
CWC200-2		2	200	Fully covered the whole circumference of the cylinder
CWC200-3		3	200	
CWC150-3	Plain	3	150	Partly covered the circumference of the cylinder
CWC150-5		5	150	
CWC150-10		10	150	
NC100	Notched	-	-	-
CWNC100-15		15	100	The first three layers: $L = 100$ mm, $\theta = 360°$
			75	The second four layers: $L = 75$ mm, $\theta = 280°$
			50	The third four layers: $L = 50$ mm, $\theta = 200°$
			25	Third four layers: $L = 25$ mm, $\theta = 106°$

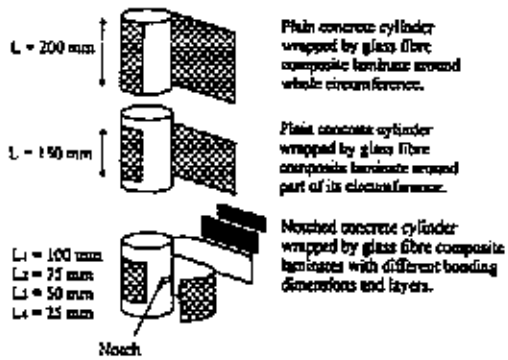

Fig. 1. Schematic diagrams of the plain and notched concrete cylinders wrapped by glass–fibre composite.

cylinders. For the notched concrete cylinder, a notch was cut in notch to diameter ratio of 0.2 at the mid-height of the cylinder and in the direction perpendicular to the beam axial axis. Balanced type (0°/90°) glass–fibre composite laminates were used to lay-up directly on the circumference of the concrete surface to activate the constraint action when the concrete is subjected to compression load. Sand blasting and vacuuming were required on all bonding surfaces in order to remove unbonded particles and dusts. The composite lay-up process was performed after 28 days of curing of the concrete. All wrapped concrete cylinders were then subjected to uni-axial compression test. Surface mounted strain gauges were used to measure strain in both the longitudinal (loading) and lateral (hoop) directions. Three identical testing specimens were used for each individual test, i.e. specimens were made at the same day and controlled environment. The mechanical properties of the glass–fibre composites and concrete used in the present study are listed in Table 2. The configurations of the composite wrapped concrete cylinders are summarised in Table 3. Fig. 1 illustrates schematic diagrams of the plain and notched concrete cylinders wrapped by glass–fibre composite laminates on its circumferences. The CONTROLS 50-C4330 compression-testing machine was used to conduct the test. A loading rate of 200 kPa/min was set and all data were recorded up to maximum load value.

2.3. Composite-bonded concrete beams

A total of 54 rectangular concrete beams were made for the three point bending test. Three standard size steel moulds were used to manufacture the concrete beams. The following five different types of beam configuration were tested in the study:

(1) plain rectangular concrete beam;
(2) notched concrete beam;
(3) plain concrete beam strengthened by glass–fibre composite;
(4) notched concrete beam with pre-filled epoxy resin inside the notch;
(5) specimen same as in (4) strengthened by glass–fibre composite.

All the concrete beams were then subjected to the three point bending test in order to investigate their mechanical

Table 4
Descriptions of all testing beams for three point bending test

Code	Type of concrete specimen	Bonding method	No. of laminate layer	Bonding length (mm)	
PC	Plain	None	–	–	–
PC3L3		Tension surface (pre-cured plate bonding)	3	3	76
PC3L6			3	6	152
PC3L10			3	10	254
PC6L3			6	3	76
PC6L6			6	6	152
PC6L10			6	10	254
PC10L3			10	3	76
PC10L6			10	6	152
PC10L10			10	10	254
PC3L10H	Plain	Hand lay-up	3	10	254
NC	Notched	–	–	–	–
NCF		Notch filled by Epoxy resin	–	–	–
NCF1LT16*		Tension surface	1	16	406
NCF2LT16*		Tension surface	2	16	406
NCF1LS16-W*		Shear surfaces	1	16	406
NCF2LS16-W*		Shear surfaces	2	16	406
NCF6L36V*		Three faces	6	Various	

* All glass–fibre composites were laid-up directly on the concrete surfaces and notches were filled by epoxy resin.

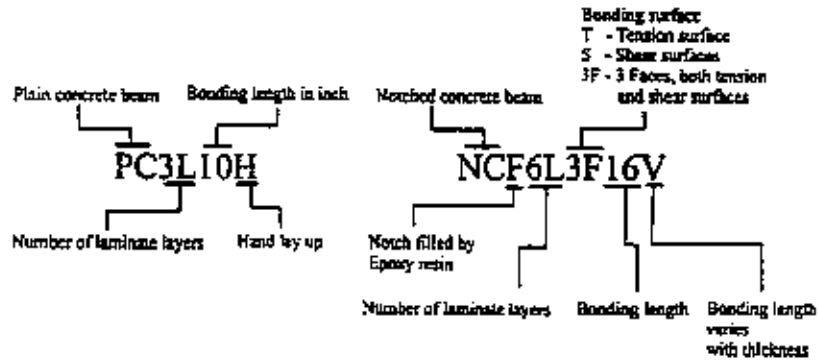

Fig. 2. Abbreviation of all testing cylinders.

responses after strengthening. The mixed concrete beams were demoulded after 24 h from the steel moulds and placed inside a temperature controlled water bath for an extra 28 days for curing. Notch was made in some concrete beams on its tension (bottom) surface by using high speed cutting disc with a notch-to-depth ratio of 0.2 in order to pretend damaged concrete structure for repair. The width of the notch was 2 mm apart from both inner surfaces. Total three identical concrete beams were used for each individual test. The configurations of all testing specimens are summarised in Table 4 and the abbreviations of the specimen code are illustrated in Fig. 2. The Sintech MTS tensile and compression testing machine with pre-designed supporting fixture was used for three point bending test. A loading rate was set as 0.5 mm/min to the centre of the beam. The experiment set-up and schematic illustration for all testing beams are shown in Figs. 3 and 4.

Two types of composite bonding method were used to strengthen the concrete beams, they are: (1) pre-cured plate bonding; and (2) direct hand lay-up techniques as indicated in Table 4. For the first method, the pre-cured glass–fibre composite plates were bonded on the concrete surfaces by using epoxy resin. Pressure was applied on the surface of the bonded composite plate in order to produce

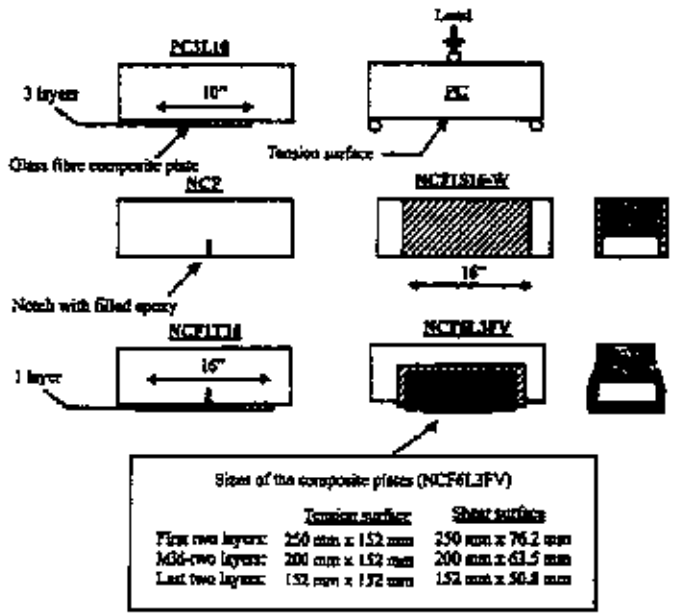

Fig. 3. Schematic illustrations for all rectangular beams strengthened by glass–fibre composites.

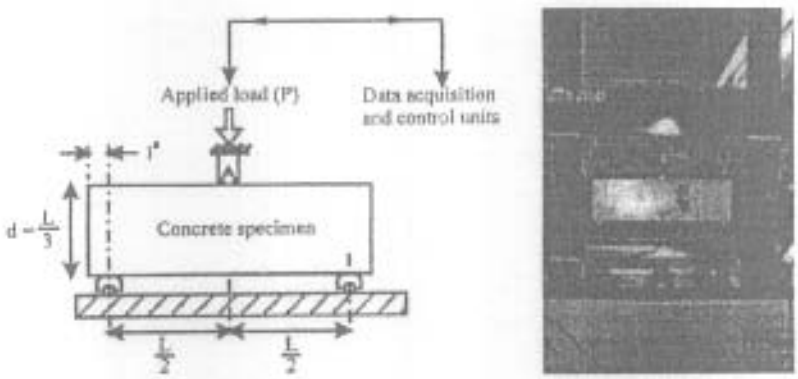

Fig. 4. Experiment set up for three point bending test.

a thin and uniform adhesive layer. For the notched concrete beams, notch was pre-filled by epoxy resin and remained in place for 48 h before laying-up the composite laminates.

2.4. Environmental effects from chemical attacks

Since the FRP materials have been recognised as an innovative material for concrete rehabilitation without suffering from corrosion like steel. However, the survivability of the glass–fibre composite strengthened structures in different chemical environments must be investigated before bringing this technology in real-life applications. Gibson [12] found that the environment attack on the concrete structures constructed near offshore and chemical emission areas is severe. For the E-glass–epoxy composites alone, they are suffered to moisture absorption and resulted in a reduction of strength of the structure [13–14].

In the present study, the mechanical performance of steel reinforced (RC) concrete beams with and without strengthening by glass–fibre composite laminates on its tension surface after submerging into different chemical solutions for six months were investigated. The mixture ratio of concrete was 1:1.5:3 and the maximum aggregate size of 10 mm was used in making the RC beams. A steel bar with a diameter of 6 mm was embedded into the concrete beam. Half of the RC beams were strengthened by three layers of glass–fibre composite laminates on tension surface by using direct hand lay-up method in order to compare their mechanical response with the beams without strengthening under the same chemical environments. The bonding length of the glass–fibre composite laminates was 400 mm and covered the whole width of the beam. The values of the load versus deflection of the beam were recorded automatically through the testing machine.

A total of 24 RC beams were distributed evenly into four Polyethylene (PE) tanks, which contained fresh water, saline water, alkaline (pH 10) and acidic (pH 4) solutions. Another six RC beams were stored in laboratory in controlled environment, i.e. the magnitudes of temperature and percentage of moisture in air were 25°C and 60%. Half of the beams in each tank were strengthened by glass–fibre composites while another half were remained in plain status. All the RC beams were stored for six months before performing the three point bending test. A schematic diagram and photography of the RC beam used in the present study is shown in Figs. 5 and 6. The abbreviations for all the RC beams are listed in Table 5.

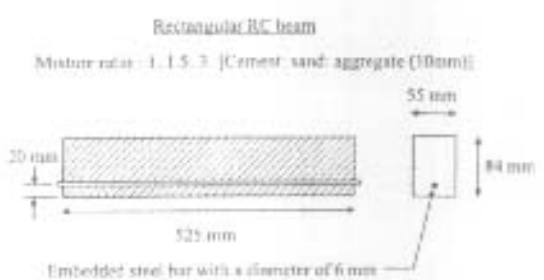

Fig. 5. Geometry of the RC beam used in the present study.

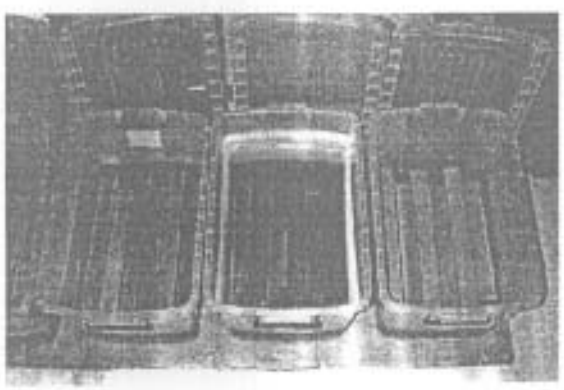

Fig. 6. The RC beams submerged into different PE tanks with containing different chemical solutions.

Table 5
Specimen types of current study

Specimen code	Surrounding Environments
PRC	Ambient condition (25°)
RCH$_2$O	Fresh water
RCPH4	pH 4 buffer solution
RCPH10	pH 10 buffer solution
RCNaCl	Saline solution

3. Result interpretations

3.1. Concrete-wrapped concrete cylinders

The experimental results for the plain and notched concrete cylinders with and without wrapping by glass–fibre composite sheets are listed in Table 6. The results indicate that the ultimate compressive load of the composite wrapped concrete cylinders increases with increasing the number of wrapping layers and size. In Figs. 7 and 8, combined curves for the cylinders with two different wrapping lengths are shown. From the figures, they obviously show that the strength of the composite wrapped concrete cylinders increases with the increase of the stiffness as well compared with the plain concrete cylinder. The load strain relationship in hoop direction was found similarly and remained approximately unchanged in load up to 75% of its ultimate load value. However, the divergence of the results was found when further increasing the compression load, it was suspected that micro-cracks and debonds between cement and aggregates were initiated.

The results also show that the cylinder with a larger wrapping length gives higher ultimate compressive strength than that the cylinder with a shorter one. The ultimate compressive strength of the cylinder with 10 layers of composite wrap and bonding length of 150 mm is just similar to the cylinder with three layers of composite wrap and bonding length of 200 mm.

In Fig. 9, failed cylinders with ine layer of glass–fibre composite wrap after performing the compression test are shown. Several visible white shallows, which might be due to the formation of cracks on the concrete surface, were observed in the experiment. Split-off failures were resulted for all testing cylinders, crack in the wrapping sheet was initiated at the middle region of the cylinder with a thin composite wrap. However, crack was started at both ends of the wrapping sheet for the cylinder with a thick composite wrap. Lau et al. [15] found that high hoop stress in wrapping material is resulted when using high modulus and thick wrapping material for concrete confinement. The failure modes for the cylinders with 10 layers of composite wrap are shown in Fig. 10, no debond and slip at the interface of bond were found. The concrete was still bonded well on the wrapping composite material. The ultimate loads of the notched concrete cylinders with and without wrapping by glass–fibre composite laminates are 331 and 431 kN, respectively, as indicated in Table 6. The results show that the ultimate compression load of the notched concrete cylinder after wrapping by glass–fibre composite increases to 31 and 11% compared to its original notched and plain status, respectively.

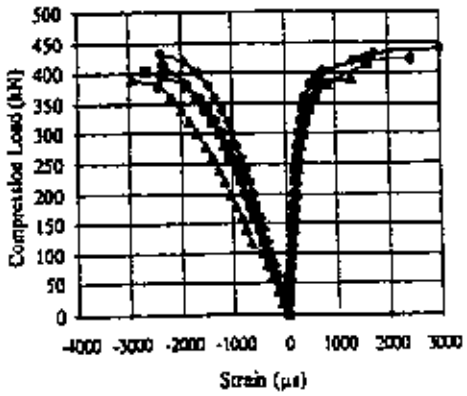

Fig. 7. Load-deflection curve of composite-wrapped concrete cylinders with a bonding length of 150 mm.

Table 6
The average ultimate compressive load of all testing cylinder

Specimen type	Wrapping length (200 mm) Mean (kN)	SD (kN)
Plain concrete cylinder		
PC	391.1	7.64
Composite wrapped concrete cylinder		
CWC200-1	415	5
CWC200-2	433.33	11.5
CWC200-3	446.66	2.88
CWC150-3	410.8	14.17
CWC150-5	416	16.5
CWC150-10	437.2	4.32
Notched concrete cylinder		
NC	333.3	15.27
Composite wrapped NC cylinder		
NC 100-15	431.67	7.63

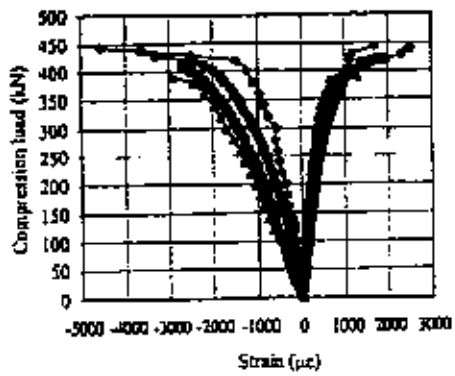

Fig. 8. Load-deflection curve of composite-wrapped concrete cylinders with a bonding length of 200 mm.

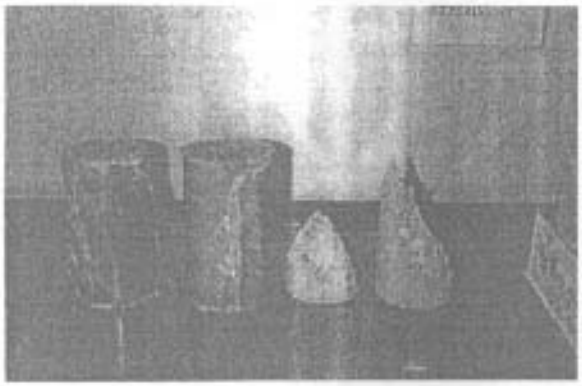

Fig. 9. Failure modes of the concrete cylinder CWC200-1.

3.2. Composite-bonded concrete beams

All the experimental results are listed in Table 7, it shows that the ultimate flexural strengths of all composite-bonded concrete beams are increased compared to the beam in plain status. A reduction of the flexural strength of the notched concrete (NC) beam is 22% compared with the beam without notch formation. A epoxy filled notched concrete (NCF) beam gives 29% and 0.6% increase of the ultimate flexural strength compared to NC and PC beams, respectively. Since the concrete is a low tensile strength material ($\sigma_t \approx 4$ MPa), the epoxy inside the notch could sustain the tensile strength much higher than that the concrete material. It therefore prolongs the maximum allowable beam deflection as indicated in Fig. 11. Unlike the notched-concrete beam, crack was initiated beside the notch region when the notch was filled by epoxy resin. In Fig. 12, it is clearly observed that the crack was started at an adjacent region of the notch mouth.

For the beams bonded with a long composite plate, several cracks were found on the concrete tension surface and beneath the composite plate when the maximum flexural load reached its ultimate value. Figs. 13 and 14 show the failure patterns of the tested specimens PC3L6 and PC10L6. It is obviously shown that debonds in matrix and mirco-cracks on the concrete surface appeared. Eventually, rupture in the concrete due to the crack initiation on the concrete surface was resulted when further increasing the mid-beam deflection.

The experimental results also reveals that shear faces bonding method becomes less significance compared with the beam strengthening in tension surface in terms of ultimate flexural load capacity. Direct hand lay-up method also provide better strengthening characteristic than that the precured plate bonding method. During the bonding process, it was found that the composite laminate could lay-up well

Table 7
The ultimate flexural load of the composite-bonded rectangular beams

Specimen code	Maximum flexural load	
	Mean value (kN)	SD (kN)
Plain concrete beams		
PC	21.57	0.42
PC3L3	29.4	0.38
PC3L6	33.45	0.49
PC3L10	33.46	0.77
PC6L3	34.21	1.11
PC6L6	25.64	1.05
PC6L10	37.10	0.94
PC10L3	33.55	1.06
PC10L6	35.66	1.40
PC10L10	38.2	1.16
PC3L10H	35.16	2.01
Notched concrete beams		
NC	16.77	0.78
NCF	21.71	0.56
NCF1T16	32.90	0.96
NCF2T16	35.89	0.57
NCF1S16-W	21.91	0.53
NCF2S16-W	23.18	1.46
NCF6L3FV	39.01	0.15

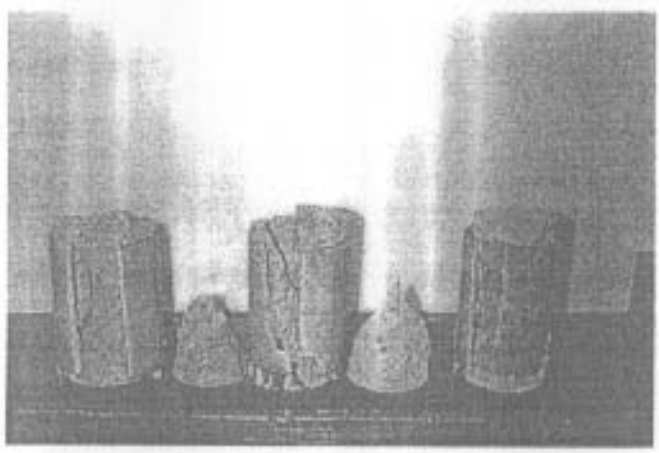

Fig. 10. Failure modes of the concrete cylinder CWC150-10.

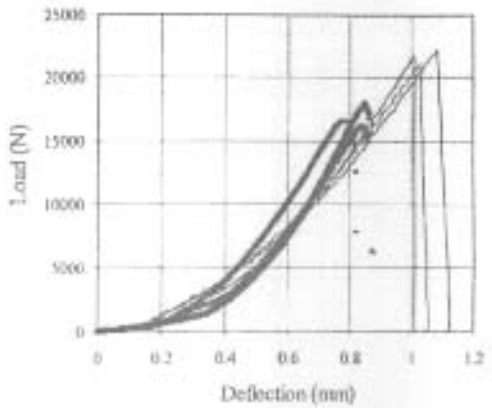

Fig. 11. Load–deflection curve of the composite-bonded beams NC and NCF.

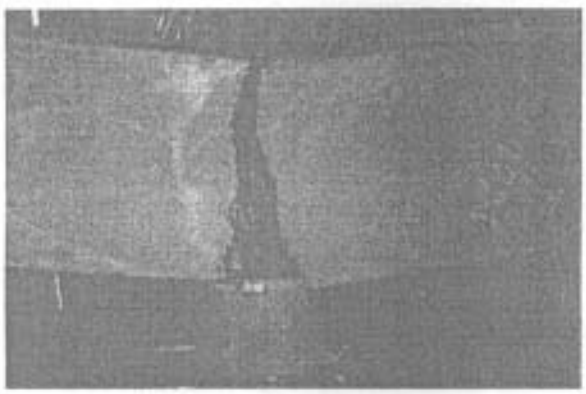

Fig. 12. Failure pattern of the beam NCP, crack is initiated beside the notch-mouth.

along the contour of the concrete surface by using direct hand lay-up method. The bonding properties of the pre-cured plate bonding method are highly restricted by the stiffness of the composite plate, voids content on and contour of the concrete surfaces. We found that partial of air was trapped at the interface between concrete surface and externally bonded pre-cured composite patch after consolidation.

The failure pattern of NCF6L3FV as showed in Fig. 15 shows that the use of thick composite plate would induce high adhesive peel-off and shear stresses of the plate bonded concrete structure. Taljsten [16] has developed a theoretical model to explain the effects on plate thickness for beam strengthening. He pointed out that both the plate modulus and thickness would influence the magnitudes of the maximum shear and peel-off stresses in an adhesive layer, and the high stress zones are closed to the plate end region.

One major concern in composite plate bonded concrete structure is the allowable shear stress in the concrete material. The failure pattern of PC10L3 specimen (Fig. 16) reveals that the use of thick composite plate may not benefit to the whole strengthening system. The ultimate load capacity of the strengthened structure is dominated by the allowable tensile and shear stresses in concrete material rather than the tensile strengthening capacity of the externally bonded composite materials.

3.3. Environmental effects from chemical attacks

The experimental results are summarised in Table 8. It is obviously showed that the use of glass–fibre composite laminate for strengthening the RC beams in different chemical environments can increase the maximum flexural load capacity of the beams, which are degraded under the submersion of water, saline, alkaline and acidic solutions. The maximum flexural load denotes a load where a crack is appeared on the tension surface of the RC beam. The result clearly demonstrates that the concrete is susceptible to acidic environment. The reduction of the flexural strength of the RC beam to 24.8% after submerged into the solution with a pH level of 4 for six months. However, for the other beams, where were placed in high humidity, saline water and alkaline solution conditions found that the reductions of

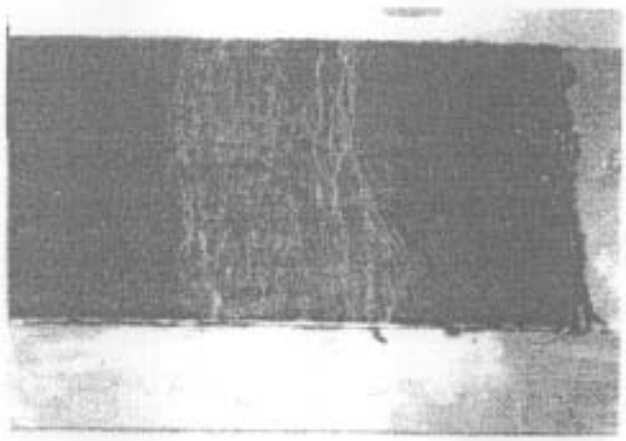

Fig. 13. Failure pattern of the beam PC3L6, many small crack in matrix system and on the concrete surface are shown.

Fig. 14. Failure pattern of the beam PC10L6, several cracks are propagated from the bottom of the beam (white marks).

the flexural strength are within 10%. Many chemical reacted particles were appeared on the concrete surface when the beams were placed in saline solution. In Figs. 17 and 18, the plots of the RC beams with and without strengthening by glass–fibre composites in ambient and acidic environments are shown. The first drop of the curve is due to crack initiation of the concrete surface. Further increase of the applied load with an increase of mid-beam deflection is due to the embedded steel bar pull-out action inside the concrete. The photography of the failure RC beam is shown in Fig. 19.

However, it is excited that the flexural strength of all degraded RC beams after strengthening by externally bonded glass–fibre composite patch are increased compared to the RC beams with the same environmental condition. The degradation of the concrete due to chemical attacks does not influence significantly to its flexural strength after strengthening by glass–fibre composites. The overall flexural strengthens of composite strengthened RC beams after submerged into chemical solutions are slight lower than that the strengthened RC beam in controlled ambient environment. This reduction of strength may due to the moisture absorption in composite matrix system and degradation of concrete in chemical substance.

4. Conclusions

In the present study, the mechanical behaviours of the composite strengthened concrete structures were investigated through standard laboratory tests. Two types of concrete geometry were used, they were concrete cylinder and rectangular concrete beam. The small-scale rectangular RC beams were also used to investigate the durability of the composite strengthened RC beams in different chemical environments. Throughout the results from all experiment works, several conclusions can be drawn as follows:

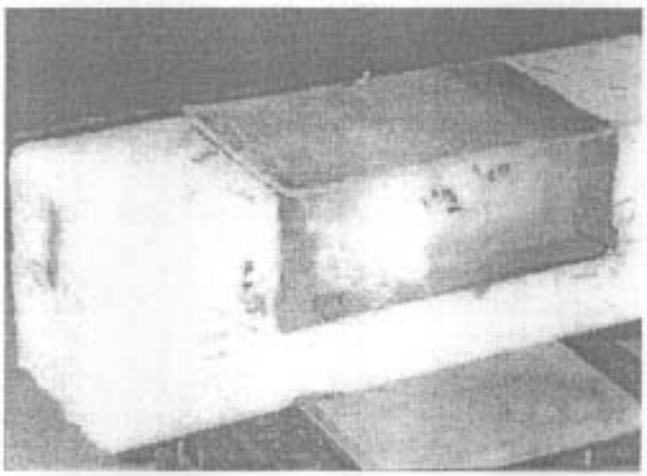

Fig. 15. Peel-off failure at the plate end region for the beam NCF6L3FV.

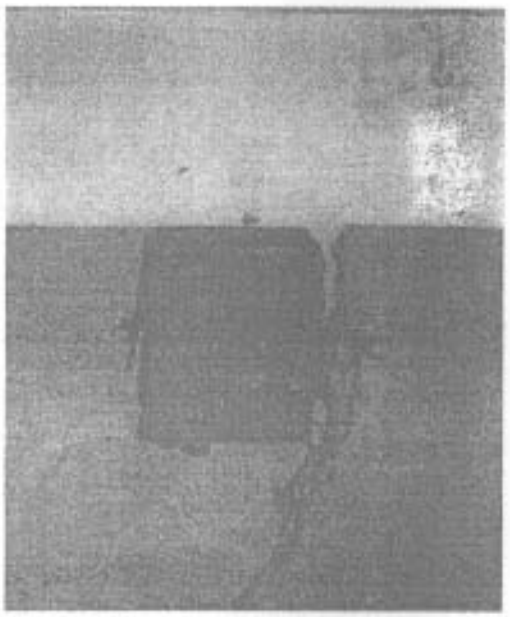

Fig. 16. Shear crack in concrete for the beams PC10L3. No visible failure occurred in the externally bonded composite plate.

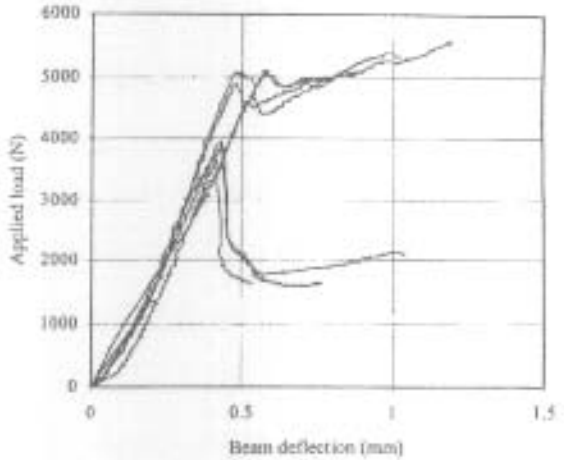

Fig. 17. Load deflection curve for the RC beam PRC with and without strengthening by glass–fibre composite.

1. The ultimate compression load capacity as well as stiffness of concrete cylinder increases with the use of composite wrap technology. The percentage of the load capacity increases with increasing the number of wrapping layer and size.
2. The compressive strength of the concrete cylinder with the use of a long bonding length and thin composite wrap is similar to that of the cylinder with a short bonding length and thick composite wrap.
3. The flexural strengths of the rectangular concrete beams with and without notch formation are increased with the use of externally bonded glass–fibre composite. The shear side strengthening method is less significant in term of the flexural load capacity of the beam compared with tension surface strengthening method.

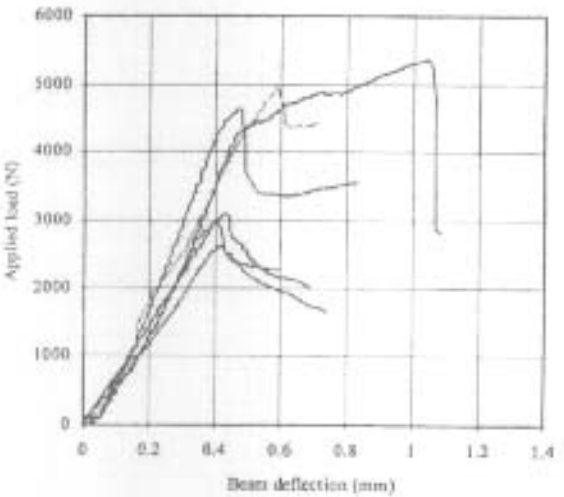

Fig. 18. Load deflection curve for the RC beam RCPH4 with and without strengthening by glass–fibre composite.

Table 8
Experimental results of all RC beams strengthened by glass–fibre composites after submerging into different chemical solutions for six months

Ultimate flexural load (kN)					
Chemical environment	pH level	Plain status		RC beam strengthened by three layers of glass–fibre composites	
		Mean value	SD	Means value	SD
Nil (room condition)		2874	176	5020	98.7
Fresh water	7.0	3525	63.2	4707	396
Saline water	7.9	3821	251	4646	131
Alkaline	10.0	3789	381	4750	176
Acidic	4.0	2914	160	4676	246

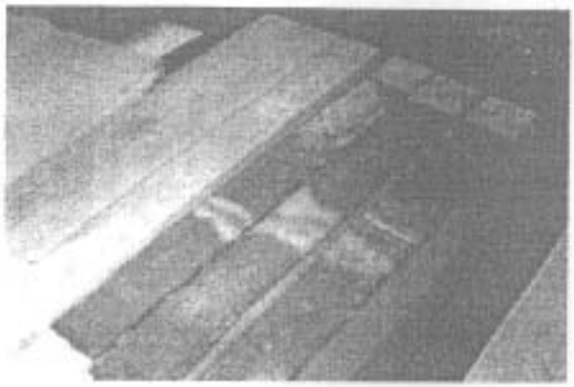

Fig. 19. Failure patterns of the RC beam RCNaCl strengthened by glass–fibre composite.

4. Hand lay-up technique gives better strengthening characteristic compared to precured plate bonding method.
5. The epoxy provides a strong bond between notch surfaces of the notched concrete beam. The flexural strength of the notched beam can be restored to the its original status by filling up the epoxy resin inside the notch.
6. The strength of the concrete is highly influenced by the acidic environment. However, the use of glass–fibre composite for concrete strengthening can improve the flexural strength properties of the degraded RC structures in harsh environment.

Acknowledgements

This research project was funded by The Hong Kong Polytechnic Research Grant GV528 and the Research Grant Council of Hong Kong (PolyU 5121/98E).

References

[1] Karbhari VM, Zhou L. Issues related to composite plating and environmental exposure effects on composite-concrete interface in external strengthening. J Composites Struct 1998;40:293–304.

[2] Shahawy MA, Beitelman T, Arockiasamy MA, Sowrirajan R. Experimental investigation on structural repair and strengthening of damaged prestressed concrete slab utilizing externally bonded carbon laminates. J Composites 1996;27B:217–24.

[3] Niu CY. Airframe structural design-practical design information and data on aircraft structures. California, USA: Technical Book Company, 1993.

[4] Gilstrap JM, Bruk CR, Dowden DM, Dolan CW. Development of FRP reinforcement guidelines for pre-stressed concrete structures. J Composites Construction 1997;1(4):131–9.

[5] Hiromichi S, Hirofumi O, Nobuhiro O, Yoshiyuki Kyushi M. The experimental study on the effect of reinforcing the rectangular beam shearing due to carbon fibre sheet. Proceedings of the Textile Composite in Building Construction, 1996. p. 145–51.

[6] Zollo RF. Fibre reinforced concrete: an overview after 30 years of development. J Cement Concrete Composites 1997;19:107–22.

[7] Seible F, Nigel Priestley MJ, Hegemier GA. Seismic retrofit of RC columns with continuous carbon fibre jackets. J Composites Construction 1997;2(1):52–62.

[8] Buyukozturk O, Hearing B. Failure behaviour of precracked beams retrofitted with FRP. J Composites Construction 1998;3(2):138–44.

[9] Rochette P, Labossiere P. Axial testing of rectangular column models confined with composite. J Composites Construction 2000;4(3):129–39.

[10] Lau KT, Zhou LM, Woo CH. Strengthening and strain monitoring concrete structures using fibre glass–composites and FBG sensor. J Mater Sci Res Int 1999;3(5):216–21.

[11] Dutta PK. Fatigue testing of composite bridge decks under extreme temperatures. Proceedings of the Seventh International Conference on Composites Engineering, 2000. p. 755–6.

[12] Gibson AG. Composite structures in offshore application. In: Shenoi RA, editor. Comp. Mater. Inn. Marine Struct., chap 3, Cambridge Ocean Technology Series, 1993.

[13] Toutanji HA. Evaluation of the tensile strength of cement-based advanced composite wrapped specimens. J Comp Sci Technol 1999;59:2261–8.

[14] Bradley WL, Wood CA, Pratt BA, Chaiwanich CS. The effect of moisture on the interfacial strength of graphite-epoxy and E-glass-epoxy composites. Proceedinfs of the ICCM-11, Gold Coast, Australia, 1997. p. 483–92.

[15] Lau KT, Zhou LM. The mechanical behaviour of composite-wrapped concrete column subjected to uni-axial compression load. J Composites Struct 2000 (in press).

[16] Taljsten B. Strengthening of beam by plate bonding. J Mater Civil Engng 1997;4(9):206–12.

ELSEVIER

Composites: Part B 32 (2001) 33–45

composites
Part B: engineering

www.elsevier.com/locate/compositesb

Strain monitoring in composite-strengthened concrete structures using optical fibre sensors

Kin-tak Lau[a], Chi-chiu Chan[b], Li-min Zhou[a,*], Wei Jin[b]

[a]*Department of Mechanical Engineering, The Hong Kong Polytechnic University, Hunghom, Kowloon, Hong Kong, People's Republic of China*
[b]*Department of Electrical Engineering, The Hong Kong Polytechnic University, Hunghom, Kowloon, Hong Kong, People's Republic of China*

Received 9 August 2000; accepted 7 September 2000

Abstract

In this paper, the mechanical behaviour of the composite-strengthened concrete structures is addressed. Optical fibre sensor presents a great deal of potential in monitoring the structural health condition of civil infrastructure elements after strengthening by externally bonded composite materials. The use of embedded optical fibre sensor for strain and temperature monitoring enables to reveal the status of the composite-strengthened structure in real-time remotely. In this paper, an experimental investigation on the composite-strengthened concrete structures with the embedment of fibre-optic Bragg grating (FBG) sensors is presented. Single- and multiplexed-point strain measuring techniques were used to measure strains of the structures. Frequency modulated continuous wave (FMCW) method was used to measure strains in different points of the structure with using only one single optical fibre. All strains measured from the sensors were compared to conventional surface mounted strain gauges. Experimental results show that the use of the embedded FBG sensor can measure strain accurately and provide information to the operator that the structure is subjected to debond or micro-crack failure. Multiplexed FBG strain sensors enable to measure strain in different locations by occupying only one tiny optical fibre. Reduction of strength in composite laminate is resulted if the embedded optical fibre is aligned perpendicular to the load-bearing direction of the structure. © 2001 Elsevier Science Ltd. All rights reserved.

Keywords: Optical fibre

1. Introduction

Optical fibres have been developed for long-distance data transmission in the telecommunications industry. However, in their earliest application, optical fibre was conceived as a medium for transmission of light in medical endoscopy. The use of optical fibres for applications in the telecommunications industry actually started in the mid 1960s, and ever since has gone through tremendous growth and advancement. The development of optical fibre sensors started in 1977 even though some isolated demonstrations proceeded this date [1–3]. The increased use of advanced composites in aeronautics instigated the need for new damage detection techniques, which can monitor the integrity of structural components during service period. Therefore, the optical fibre sensors have been extensively employed as real-time damage detection tools in advanced aircraft and space vehicles [4].

Recently, a strong demand on developing high performance structures, which are able to monitor the physical and mechanical properties such as temperature and strain during service condition is appreciated as a "Smart structural health monitoring system" [5]. Fibre-optic Bragg grating (FBG) sensor has been recognised as a new non-destructive evaluation (NDE) technique to suit this purpose for all structural applications [6,7]. The speciality of using FBG sensor for strain sensing application is that it is able to measure strain locally with high resolution and accuracy. As the physical size of an optical fibre is extremely small compared with other strain measuring components, it enables to be embedded into structures for determining the strain distribution without influencing the mechanical properties of the host materials [8,9].

Dewynter-Marty [10] embedded the FBG sensor into glass fibre composite laminate to monitor thermal and residual strain properties during curing process in autoclave. Lo et al. [11] developed a single pitch FBG sensor for corrosion detection for structure served in harsh environment. Kalamkarov pointed out that the FBG sensor could be used without suffering creep problem in long term application [12]. Moreover, he also found that the embedded sensor could be sustained load in high alkaline environment with no effect on the behaviour of measurement.

* Corresponding author. Tel.: +852-2766-6663; fax: +852-236-54703.
E-mail address: mmlmzhou@polyu.edu.hk (L.-m. Zhou).

1359-8368/01/$ - see front matter
PII: S1359-8368(00)00044-5

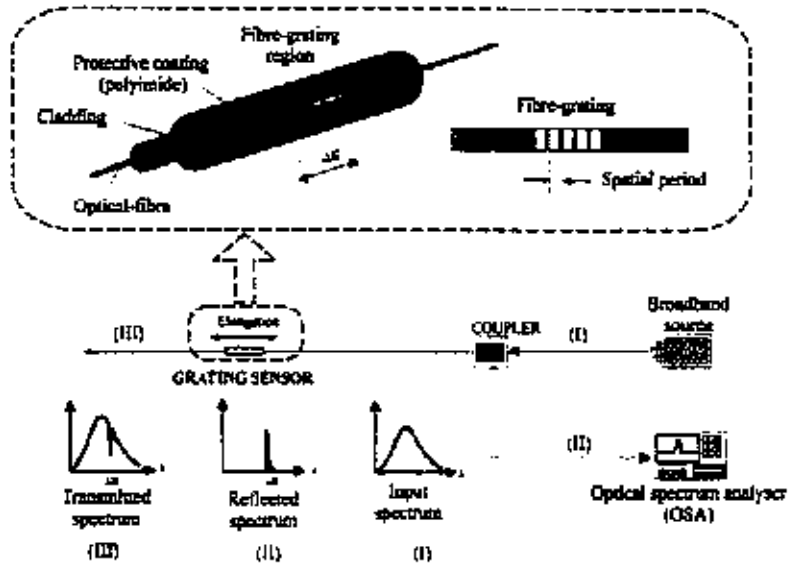

Fig. 1. FBG strain measuring system.

In this paper, experimental studies on strain measurements using embedded FBG sensors in composite, concrete and composite-strengthened concrete structures are presented. The mechanical properties of the composite laminates with the embedment of optical fibre are firstly discussed through short beam shear and flexural strength tests. The embedding technique of the sensor into concrete structure is also addressed. The FBG sensors were also embedded into the composite-strengthened concrete structure and located at the interface between concrete surface and externally bonded composites for strain measurement. Externally mounted strain gauges were used to compare results measured from the sensors.

2. Principle of FBG sensors

2.1. Strain measurement

FBG technology has been discovered by Hill et al. in 1978 [7]. It was found that the reflective grating could be photorefractively formed in the core of germanium droped silicate fibre. In general, the FBG system is comprised of broadband source (light emission device), coupler, optical spectrum analyser (OSA) and optical fibre with prewritten grating sensors. For the structural strain monitoring purpose, load is directly transferred from host material to fibre core of the grating region by the action of shear [13]. This causes the length of the grating region to be changed and the resultant refractive index of the core section to vary accordingly. The mechanical properties of the structure are simply determined by measuring the reflected wavelength change from the system. In Fig. 1, a schematic illustration of the FBG system for strain measurement is shown. Grating is written by exposing the fibre to a pair of strong Ultra-violet (UV) interference signal. This creates the grating in the core of the optical fibre, which acts essentially as a wavelength selective mirror. This method to write the grating in the optical fibre for strain and temperature measurements is called Phas mask technique (Fig. 2).

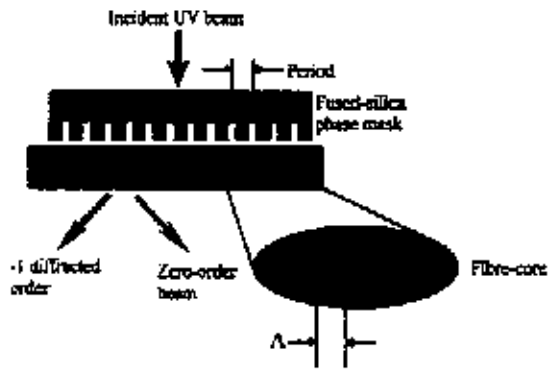

Fig. 2. Phase mask technique.

When the light is illuminated from the broadband source via the coupler, part of light is reflected back to the coupler and the reflected-wavelength is detected by the OSA as indicated in Fig. 1. The strain variation in the grating region is simply determined by the reflected wavelength shift from the sensor. According to Bragg's law, the reflective wavelength can be defined as

$$\lambda_B = 2n_{eff}\Lambda \tag{1}$$

where n_{eff} is the core refractive index and Λ is the spatial period of the index modulation. Any changes of the strain in the grating region result in changing of spatial period and core refractive index. The measurement of the mechanical

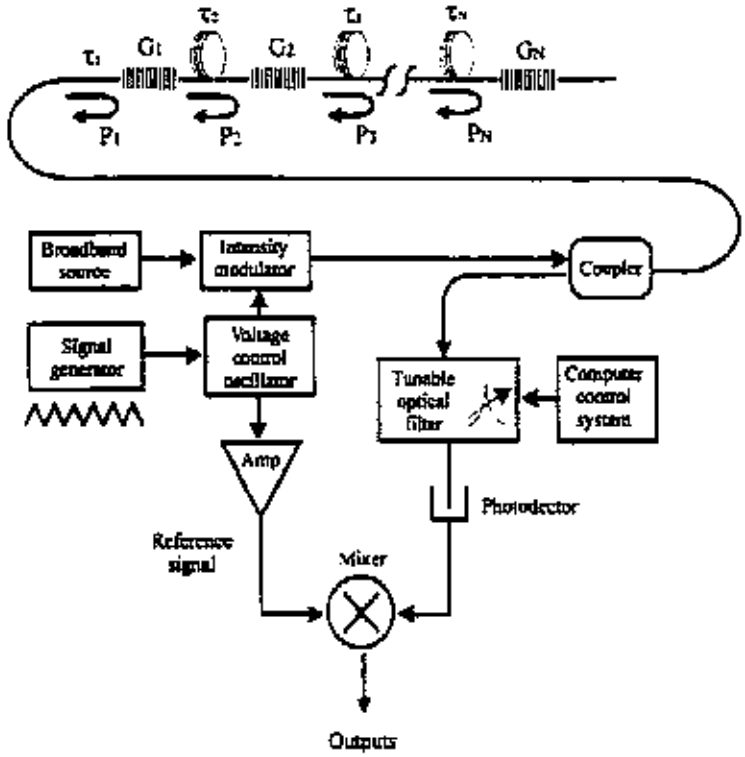

Fig. 3. Multiplexed FBG sensor arraying system by using frequency modulated continuous wave (FMCW) technique.

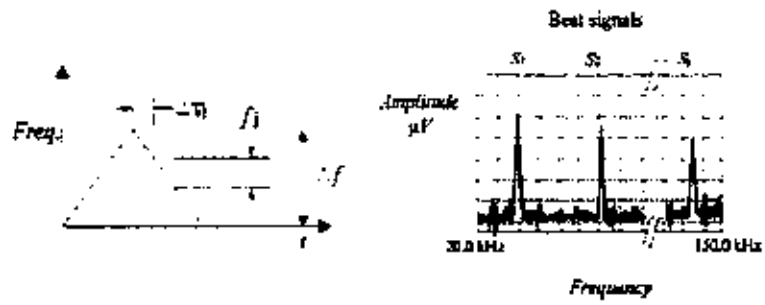

Fig. 4. The principle of the FMCW technique.

strain ($\epsilon = DL/L$) is determined by the variation of the Bragg wavelength ($\Delta\lambda_B$) shift. It has been approved that the sensors give a linear strain relationship to the reflected wavelength shift from the sensor within the elastic deformation limit of the fibre [7]. The change of the Bragg wavelength can be expressed as

$$\frac{\Delta\lambda}{\lambda_B} = \left(1 - \frac{n^2}{2}\rho_{12}\right)\epsilon_1 - \frac{n^2}{2}(\rho_{11}\epsilon_2 + \rho_{12}\epsilon_3) + \xi_0\Delta T \quad (2)$$

where ϵ_1 is the axial strain along the lengthwise direction of the fibre. ϵ_2 and ϵ_3 are the principle strains in the cross-sectional plane of the fibre core. ξ_0 is the coefficient of both the thermo-optic component and the thermal expansivity of the optical fibre, and has the nominal value of 6×10^{-6}/°C. ρ_{11} and ρ_{12} are the photoelastic coefficients. In normal, the

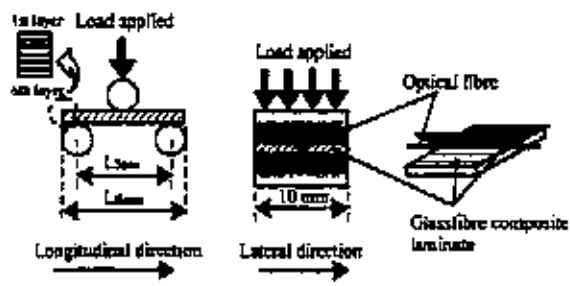

	Short beam shear test	Flexural strength test
L_{span}	10 mm	100 mm
L_{Beam}	12 mm	120 mm

Fig. 5. Details of the composite beams for short beam shear and flexural strengths tests.

Table 1
Experimental results of the short beam shear and flexural strength tests for the optical fibre embedded glass fibre composite beam

Optical fibre	Short beam shear test (MPa)				Flexural strength test (MPa)			
	Lateral		Longitudinal		Lateral		Longitudinal	
	Mean	SD	Mean	SD	Mean	SD	Mean	SD
Sensor located at								
1st and 2nd layer	17.73	0.54	18.72	0.27	189.1	4.54	203.8	2.18
3rd and 4th layer	17.94	0.26	18.66	0.36	188.6	3.56	200.3	3.94
5th and 6th layer	18.91	0.43	18.52	0.12	190.9	3.79	198.7	2.96
No Sensor specimen	18.82	0.15	18.8	0.142	202.1	2.13	203.1	2.36

strain transfer to the fibre in transverse directions is very small and can be neglected in practical applications [14]. Therefore, the full equation for the Bragg wavelength shift by considering the effects from thermal expansion and mechanical strain of the fibre at the grating region is expressed as

$$\Delta\lambda_B = K_\varepsilon \varepsilon_l + \lambda_B \xi_0 \Delta T \tag{13}$$

where K_ε is called "Theoretical gauge constant" [15], which can be determined experimentally. The second term in Eq. (3) represents the wavelength shift due to the temperature change in the system, which is normally used in inspecting the manufacturing process of composite materials [16]. For the silica fibre, the wavelength–strain sensitivity of 1.55 μm FBGs has been measured as 1.15 pm $\mu\varepsilon^{-1}$ [17].

2.2. Multiplexing technique

One of the major advantages of using the FBG sensor in real life applications is the ability in measuring strains in different locations along structure with occupying only one single optical fibre [14,18]. This technique is normally called "Multiplexing" or "Quasi-distributed" measurement. Frequency modulated continuous wave (FMCW) technique presents it excellent ability to measure the strain variation along a single optical fibre with more than one grating sensor [19]. The FMCW offers a number of advantages compared with the current multiplexing techniques such as wavelength division (WDM) and optical time-domain reflectometry (OTDR). Typically, the maximum number of sensors that can be multiplexed by using WDM technique is about 10–12. Besides, the OTDR technique requires injecting a short pulse of optical power to the optical network and waiting for separating pulse from each sensor. It therefore requires a relatively high power in the pulse system to maintain the same average optical power at the receiving end. By using FMCW technique, it enables to produce up to 20 grating sensors along the single optical fibre if the reflectivities of the grating are correctly chosen. However, the power required is comparatively less than that by using OTDR for the same number of sensors used. Fig. 3 illustrates the multiplexed FBG sensors arraying system by using FMCW demodulating technique.

The light signal launched from the broadband source is modulated as a triangular chirped frequency carrier to the FBG sensors. The delayed frequency signal from each individual FBG sensor is returned to the tunable optical filter (TOF) and the photodetector. The detector output is

Fig. 6. Cross-sectional view of composite laminates with an embedment of optical fibre

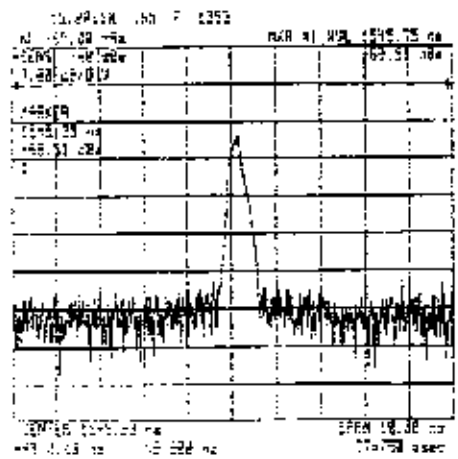

Fig. 7. Reflected wavelength spectrum from single grating sensor.

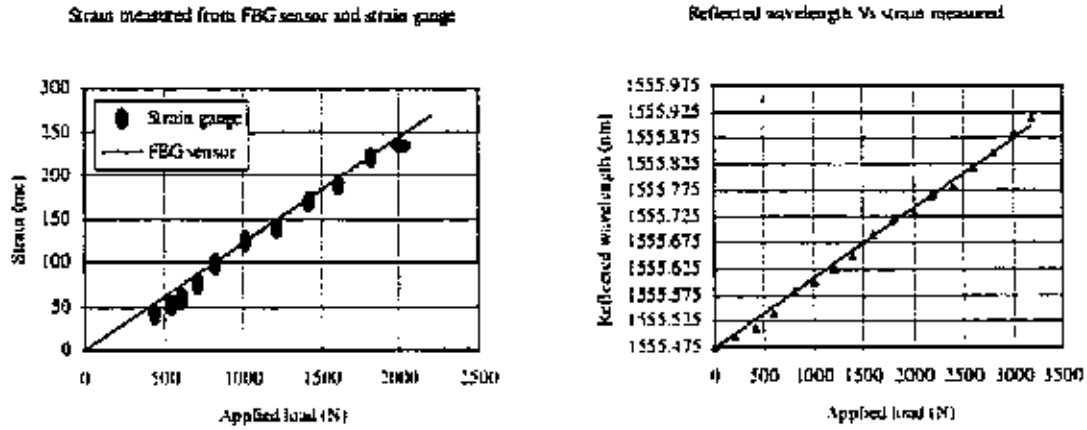

Fig. 8. Results from the sensor calibration tests.

electrically mixed with a reference chirp signal from the voltage-controlled oscillator (VCO), which produces a beat frequency associated with each sensor element. The magnitudes of the beat signals are proportional to the convolution of the individual grating reflection and the transmission spectrums of the tunable filter.

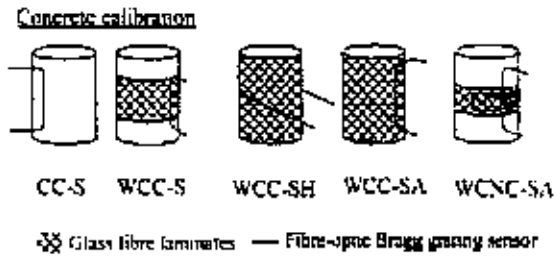

Fig. 9. Types of concrete cylinder for uni-axial compression test.

The beat signals can be viewed by using an electrical spectrum analyser (ESA). The amplitude (voltage) measured in the ESA can be converted to the corresponding strain (ε) of the grating. The principle of operation of the FMCW technique is illustrated in Fig. 4. The beat frequency for sensor can be expressed as

$$f_j = \Delta f \frac{\Delta T_j}{T} \tag{4}$$

where f_j, Δf, ΔT_j and T denote the beat frequency, the chirp frequency excursion, the optical delay from the source to detector for the jth sensor and the chirp period, respectively. Two major factors limit the spatial separation between two neighbouring FBG sensors. The first factor is that the separation should be long enough to avoid the coherence noise that occurs. The second one is that the separation between gratings must be large enough to separate the beat

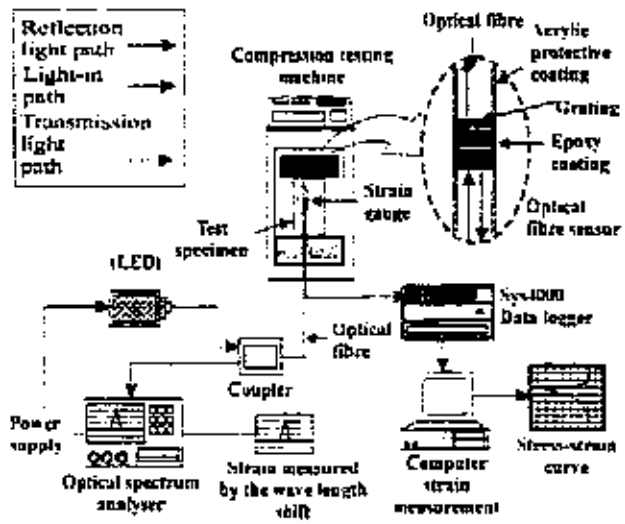

Fig. 10. Strain measuring system for the optimum separation in uni-axial compression test.

Table 2
Descriptions of all testing cylinders

Specimen code	Sample type	Bonding length	Direction of optical fibre
CC-S	Plain concrete cylinder	–	Axial
WCC-S	Composite-wrapped cylinder	100 mm	Axial
WCC-SH	Composite-wrapped cylinder	200 mm	Hoop
WCC-SA	Composite-wrapped cylinder	200 mm	Axial
WCNC-SA	Composite-wrapped notched cylinder	Various	Axial

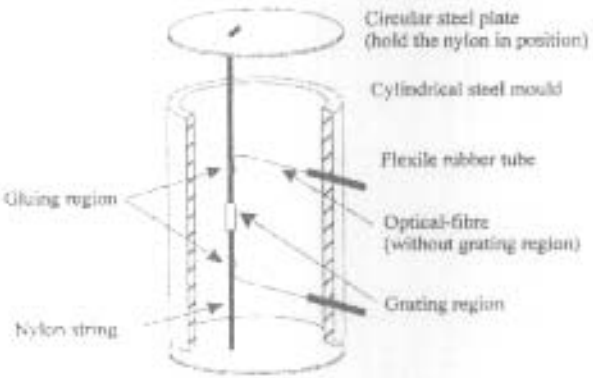

Fig. 11. Optical fibre installation technique.

signals with their frequency different between sensors and larger than the resolution of the spectral analysis techniques.

3. Strain measurement by using FBG sensors

3.1. Single grating sensor

3.1.1. Mechanical properties of glass fibre composite with the embedment of optical fibre

In the present study, the FBG sensors were used to measure strain for composite and composite-strengthened concrete structures. Since the diameter of the optical fibre (≈ 250 μm) is relatively small compared to the concrete structure, we can assume that the mechanical properties of the structure would not be influenced by this tiny embedded optical fibre. However, for the composite structure, which is generally fabricated in a very thin cross-sectional form, the influence in mechanical strength of the structure after embedding the optical fibre becomes significant.

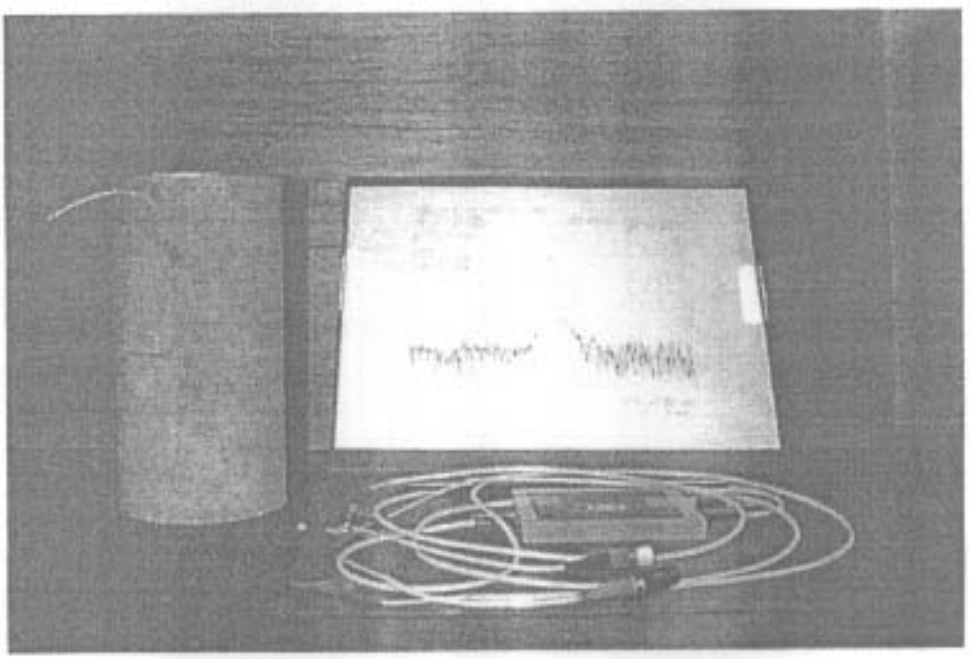

Fig. 12. Notched concrete cylinder with an embedment of FBG sensor (left) and connection to coupler (right).

Table 3
Descriptions of all strengthened beams with the embedment of FBG sensors

Code	Strengthening surface(s)	Number of layer(s)	Size of GFRP plate
SB-S1	Tension	1	250 mm × 152 mm
SB-S2	Tension	1	250 mm × 152 mm
	Shear	1	250 mm × 76.2 mm
SB-S3	Tension	6	250 mm × 152 mm (1st two layers) 200 mm × 152 mm (2nd two layers) 152 mm × 152 mm (last two layers)
	Shear	6	250 mm × 76.2 mm (1st two layers) 200 mm × 63.5 mm (2nd two layers) 152 mm × 50.8 mm (last two layers)

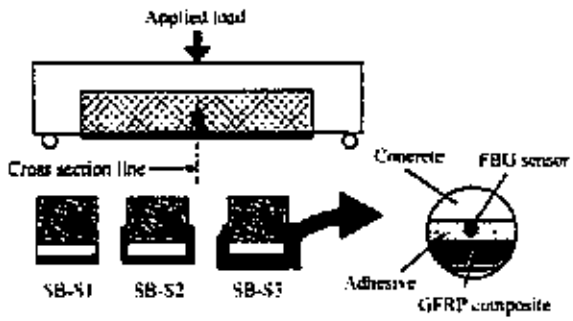

Fig. 13. Rectangular beams for three point bending test.

The short-beam shear and flexural strength tests were firstly performed to investigate the interlaminar shear and flexural strength properties of composite beams with the embedment of optical fibre. The tests followed the procedures from the ASTM D 2344 and ASTM D790. A total of 160 pieces of testing specimen were made and ten specimens for each individual test were used to ensure the reliability of the testing result. The optical fibres were aligned in both the beam longitudinal and lateral directions, and embedded in different laminate layers for the tests. In Fig. 5, a schematic diagram of the experiment illustration is shown. The results from the experiment are listed in Table 1. According to the testing results, it obviously shows that there are no significant effects to the composite structure when the optical fibre is embedded longitudinally in terms of its short beam shear and flexural strengths. The reduction of the flexural strength to 12% is resulted when the optical fibre is embedded laterally at the interface between the 1st and the 2nd layers of the glass fibre composite laminate. This may be due to the compressive buckling at the top layer of the composite laminate which occurred when the beam was subjected to bending load, resulting in a slight reduction in the short beam shear strength for the composite with the embedment of optical fibre in the lateral direction. Fig. 6 shows a cross-sectional view of the composite plate with the embedment of the optical fibre.

3.1.2 Calibration

A calibration test was performed to determine the gauge constant value as indicated in Eq. (3) for the FBG strain measuring system. Since all experiments were conducted

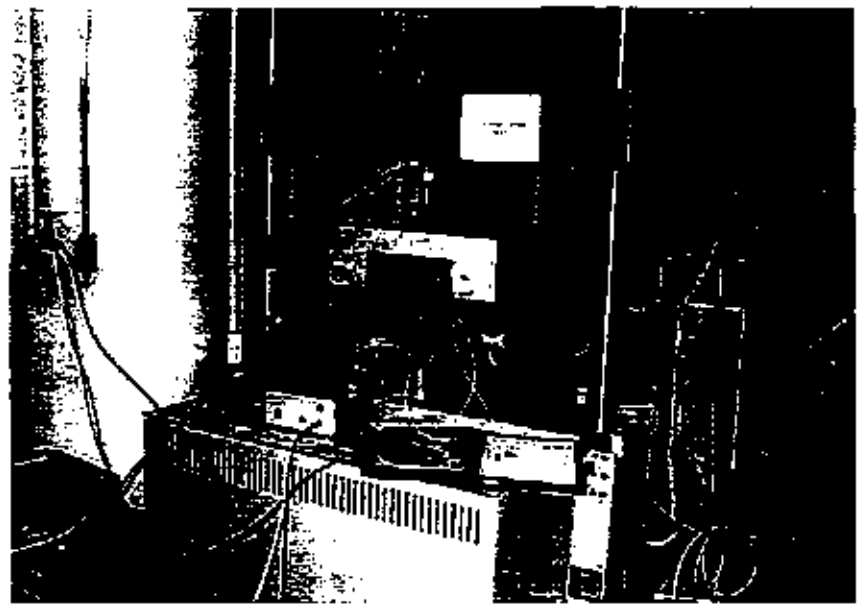

Fig. 14. Experimental set up for strain measurement in composite-bonded concrete beam.

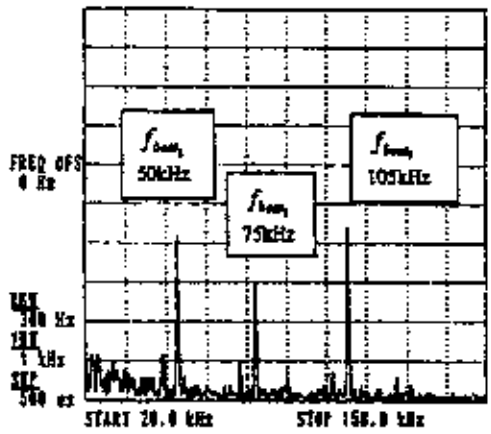

Fig. 15. Reflected wavelength spectrum for multiplexed FBG sensors.

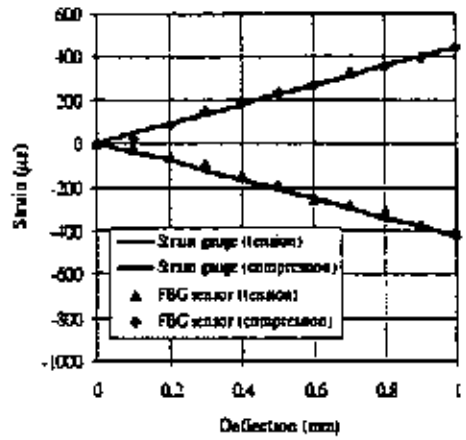

Fig. 16. Strains measured from multiplexed FBG sensors and strain gauges under four point bending test.

in temperature controlled environment, the thermal effect could be neglected in the study. A standard dog bone shape steel plate was used for a tensile strength test. An optical fibre with a grating was adhered on one side of the steel plate while strain gauge was bonded on another side to compare measuring parameters. The grating and total embedding lengths of the FBG sensor were 12 and 235 mm, respectively. The selected Bragg wavelength used was 1555 nm and the loss was less than 0.2 dB/km [20]. The spectrum captured from the OSA and experimental results during the test are plotted in Figs. 7 and 8. From the figure, the value of K^{-1} was calculated by fitting a curve as 947.55 nm^{-1}. This implies that each 947.55 nm^{-1} shift of the reflective wavelength corresponds to 1×10^{-6} strain change. Eq. (3) can be written as the reverting form

$$\epsilon_f = 947.55\lambda_B - 1473917.45. \quad (5)$$

3.1.3. Composite-wrapped concrete cylinders

The FBG sensors were installed in various forms in concrete cylinders with and without wrapping by glass fibre composite laminates. These include: (1) embedded into plain concrete cylinder (intrinsically); (2) bonded at the interface between concrete surface and glass fibre composite laminates in the directions parallel and perpendicular to the axial axis of the composite-wrapped concrete cylinder; (3) embedded into composite-wrapped notched concrete cylinder and located in front of the notch-tip. The schematic diagram of the testing specimens and experiment set up are illustrated in Figs. 9 and 10. The FBG sensors were adhered on the concrete surface by using epoxy adhesive and remained in place for 24 h. The glass fibre composite laminates were then laid-up directly on the concrete surface. Surface mounted strain gauges were used to measure surface strains of the wrapped concrete cylinder and compare the results from the internal strain measured by

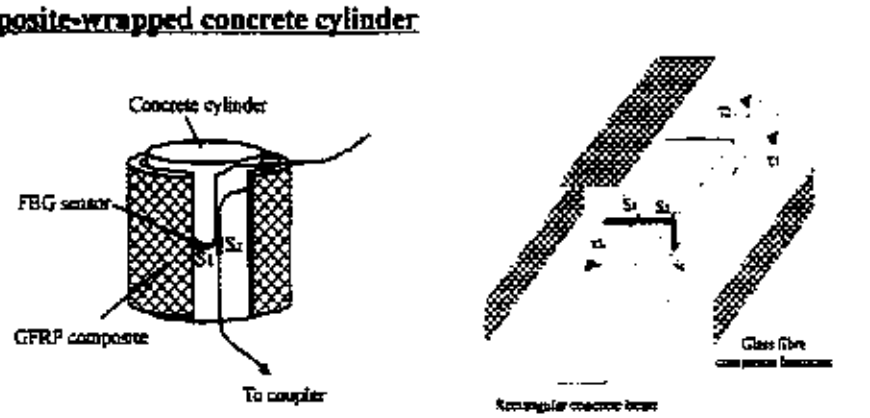

Fig. 17. Composite strengthened concrete cylinder and beam with the installation of multiplexed FBG sensors.

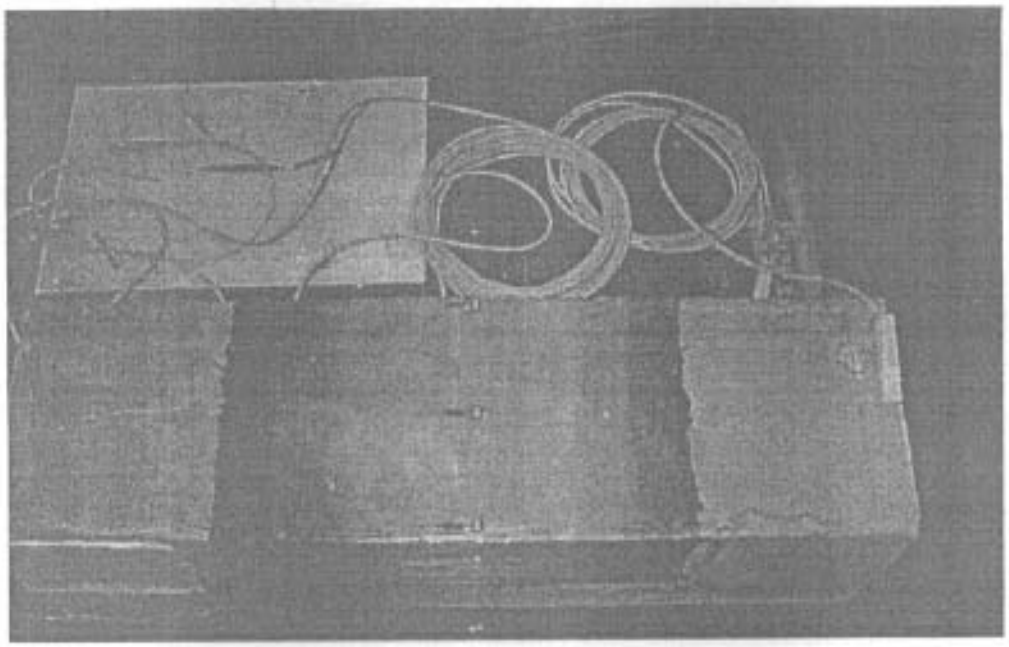

Fig. 18. Photography of the composite-bonded concrete beam for strain measurement

the embedded FBG sensor. The descriptions of all the testing cylinders are listed in Table 2.

To avoid damage of the fibre sensor during handling and moulding processes, a special supporting fixture for aligning and reinforcing the sensor is introduced. Thin and tough nylon string was used to align and guide the optical fibre in line parallel to the load direction. Both ends of the sensor were stuck on the string by using epoxy adhesive. High flexible rubber tubes were used to protect the fibre at both entrance and exit locations of the concrete cylinder to minimise the risk of fibre breakage due to the formation of sharp turning or other unexpected damage during moulding and de-moulding processes. An illustration of the optical fibre installation technique and a photograph of the notched concrete cylinder with the optical fibre before laying-up the composites are shown in Figs. 11 and 12.

3.1.4. Composite-bonded concrete beams

Three laboratory size concrete beams with a notch formation on tension surface were used in the present study. Glass fibre composites were laid up directly on the beams by using hand lay-up method. FBG sensors were bonded either on the tension or tension and shear surfaces of the concrete beam before laying up the composites. Detailed information and schematic illustration of the testing specimens are listed in Table 3 and Fig. 13. All the beams after strengthening by composite laminates were then subjected to three point bending test. The strain measured from the embedded sensors and the externally bonded strain gauges were recorded simultaneously. The experiment set-up for the strain measurement of the composite-strengthened beam is shown in Fig. 14. The FBG strain measuring system is same as illustration, which is shown in Fig. 10 for the wrapped concrete cylinder.

3.2. Multiplexed grating sensors

The FMCW technique was used to demodulate the frequency response from multiplexed grating sensors. Three grating sensors were written into one single optical fibre to measure strains in different points of the structure. The separation of each sensor was 1 m, which was for long sufficient enough to avoid the occurrence of coherent noise,

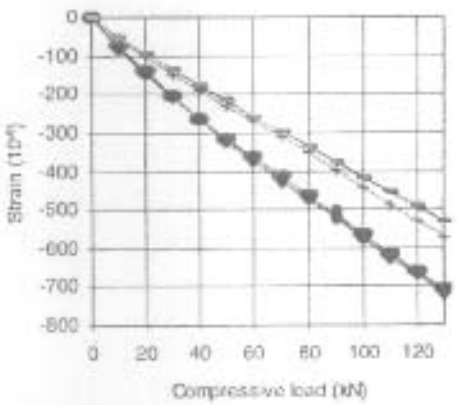

Fig. 19. Experimental result for the cylinder WCC-5 (top) and CC-5 (bottom). Dot and solid lines represent results measured from strain gauges and FBG sensors, respectively.

which interferes the incoming responses from the sensors inside the fibre core. The FBG sensors were embedded into 20 layers of balanced type glass fibre composite beam with a fibre volume fraction of 42%. The dimension of the beam was 235 mm (length) × 26.6 mm (width) and 3.8 mm (thickness). Two grating sensors were embedded at the interfaces between the 1st and the 2nd layer, and the 19th and the 20th layer of glass fibre composite laminates. A four point bending test was investigated to observe the responses measured from the sensors. One grating was used as a reference during measurement. Surface mounted strain gauges were attached on the top and bottom surfaces of the composite to compare results from the embedded sensors. A high radio frequency (RF) spectrum analyser of 30 Hz resolution and the rate of frequency excursion is approximate 4×10^{11} Hz^2 was used in the study. The selected wavelength and corresponding beat frequency in the experiment for the sensors S_1, S_2 and S_3 were 1536.3, 1554.24 and 1554.24 nm, and 50, 75 and 105 kHz, respectively. The beat frequencies measured in the experiment and the result of the measurement are shown in Figs. 15 and 16. The strain measured from multiplexed sensors give a very good match with the surface mounted strain gauges. This implies that the multiplexed sensors can be used with confidence.

The multiplexed sensors were used to measure strains for composite wrapped and bonded concrete structures when they were subjected to uni-axial compression and three-point bending tests, respectively.

The concrete cylinder was wrapped by five layers of glass fibre composite laminates. A single optical fibre with three grating sensors was pre-adhered on the concrete surface. Two sensors, S_1 and S_2 were adhered on the mid-height of the cylinder in both longitudinal and hoop directions to measure strains. Glass fibre composite laminates were then laid up directly on the concrete surface. Externally bonded strain gauges were used to measure strains on the composite surface and at the same locations that the sensors were embedded.

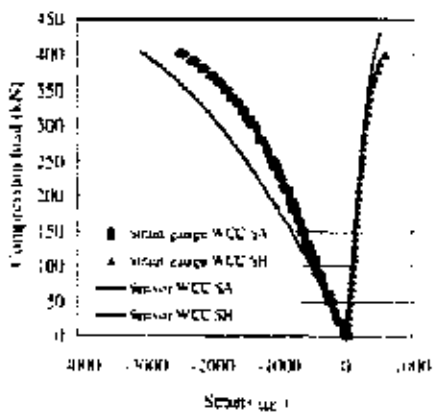

Fig. 20. Experimental results for cylinders WCC-SA and WCC-SH.

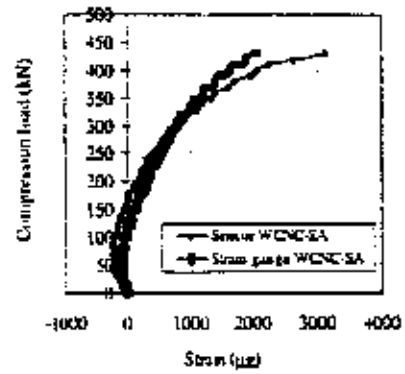

Fig. 21. Experimental results for notched concrete cylinder WCBC-SA.

For the notched rectangular concrete beam, three grating sensors were bonded on the concrete surface and at the bottom edge and centre regions, and at the notch-tip of the notched concrete beam. The sensor S_1 was located at 1 mm in front of the notch-tip, which is suspected to be highest stress area for the notched-beam without strengthening by external reinforcement. S_2 was located at the mid-beam bottom edge while S_3 was at the bottom centre and in front of the notch mouth regions. Sensors S_2 and S_3 were arrayed serially in single optical fibre and in parallel with the sensor S_1. The schematic diagrams of the composite wrapped concrete cylinder and bonded concrete beam with the embedment of multiplexed FBG sensors are shown in Figs. 17 and 18.

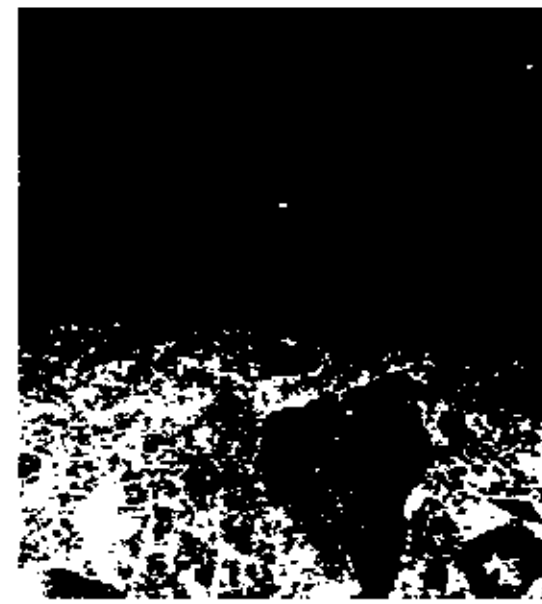

Fig. 22. Cross-sectional view of the composite-wrapped concrete cylinder with the embedment of the FBG sensor.

4. Results and discussions

Initial calibrations for the plain concrete cylinders with and without wrapping by the glass fibre composite laminates were performed. The grating sensors were located at the mid-height of the cylinder with a depth of 20 mm measured from the circumference of the cylinder surface. The specimens of CC-S and WCC-S were compressed to 1/3 of the ultimate load of the plain concrete cylinder for three repeated cycles. Surface mounted strain gauges were used to compare the results from the sensor. The experimental results are shown in Fig. 19. The results show that the internal compression strains measured from the embedded sensor well agreed with the surface mounted strain gauges at low loading range.

The experimental results for the strain measurement by using single grating sensor for the composite-wrapped concrete cylinders WCC-SH, WCC-SA and WCNC-SA are shown in Figs. 20 and 21. For the plain concrete cylinders, the compressive strains measured from the experiment give consistent reading between the FBG sensor and strain gauge when the compression load was applied to 70% of its ultimate load value. The readings are diverged when the applied load continuously increases. It is speculated that the wrapped concrete cylinder develops considerably more cracks than that for the un-wrapped concrete specimen, particularly on the concrete surface, which is located inside the wrapping region. However, the difference on the strain readings from the FBG sensor and strain gauge is large for the composite-wrapped notched-concrete cylinder at peak load condition. It was revealed that high stress was still concentrated at the notch-tip, where a sensor was embedded on the composite wrapped concrete cylinder. The properties change in this high stress concentration zone cannot be directly measured through external strain measuring device.

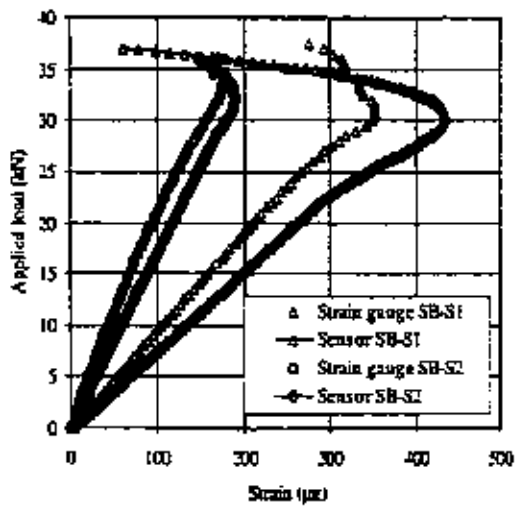

Fig. 23. Experimental results for beams SB-S1 and SB-S2.

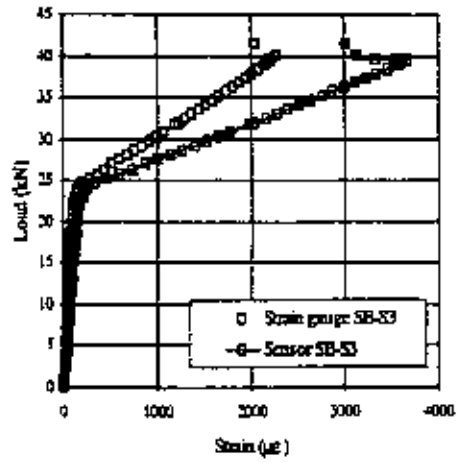

Fig. 24. Experimental result for a beam SB-S3.

In Fig. 22, a cross-sectional view of the composite wrapped concrete cylinder with the embedment of the FBG sensor is shown.

The experimental results of the strains measured from the FBG sensors and strain gauges of the specimens SB-S1, SB-S2 and SB-S3 are plotted in Figs. 23 and 24. According to the figures, it is obviously found that the strain on the concrete surface is always higher than that of the surface strain of the composite material. The FBG sensor can monitor the strain condition of the concrete and detect failure earlier than the strain gauge, which is mounted on the surface of the outer reinforcement. The result of the beam SB-S1 shows the repaid change of strains when the load is applied beyond 23 kN. During the experiment, several visible cracks and debonds were observed at adjacent areas near notch-mouth when the load reached 30 kN. Due to the formation of cracks, where besides the location of the sensor and strain gauge, the strain relaxation occurred when further increasing the applied load. However, this phenomenon may not influence the strain on the outer surface of the composite laminate. Therefore, the strain measured from the FBG sensor is much more sensitive to the surface crack of

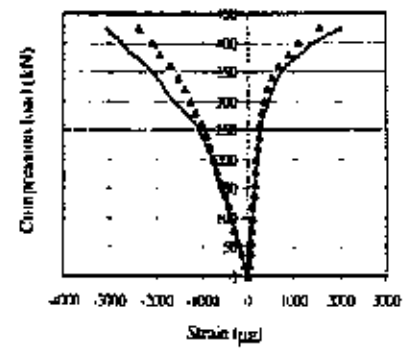

Fig. 25. Experimental results for a cylinder with embedment of multiplexed FBG sensors.

concrete and physical condition change such as debond of an adhesive layer.

For the testing specimen with the embedment of the multiplexed FBG sensors, the results are shown in Figs. 25–27. The experimental result for the composite-wrapped concrete cylinder shows that the difference of the strain measurement from the FBG sensors and strain gauges increases with increasing the applied compression load beyond 250 kN. This phenomenon implies that the axial deformation in concrete is larger than the outer surface of wrapping laminates. The differences of the strain measurement might be due to the existence of cracks on the concrete surface and high shear deformation in composite laminate (see Fig. 28). However, the divergence of the result measured in the hoop direction is relatively small when compared to the result in the axial direction since there is no shear deformation that existed in the lateral direction of the wrapping laminates.

In Figs. 26 and 27, they show that the difference of the strain measured by the externally bonded strain gauges and embedded FBG sensors increase with increasing the applied load, particularly for the sensor S_2. However, at the low loading range, the strain measured from the strain gauge and FBG sensors provide a linear load–strain relationship and give good agreement with each other in general. After the load readings to 23 kN, the divergence of the strain measurements is resulted. It was found in the experiment that high strain (5300 $\mu\varepsilon$) occurred when the load was applied to 27 kN. The signal from the sensor S_2 disappeared when further increasing the applied load. It is suspected that the optical fibre was broken. The signal received from the following sensor, S_3 was therefore lost subsequently.

At the notch-tip region, the FBG sensor gave the strain response up to 31.5 kN. It was observed that the debond at the interface between the concrete and the composite laminates occurred and extended rapidly towards the opposite direction of the applied load. Shear cracking and peel-off failure were found when the applied load reached 36.5 kN. However, the surface mounted strain gauge gave a strain, which was much smaller that than the real strain measured on the concrete surface by embedded FBG sensor.

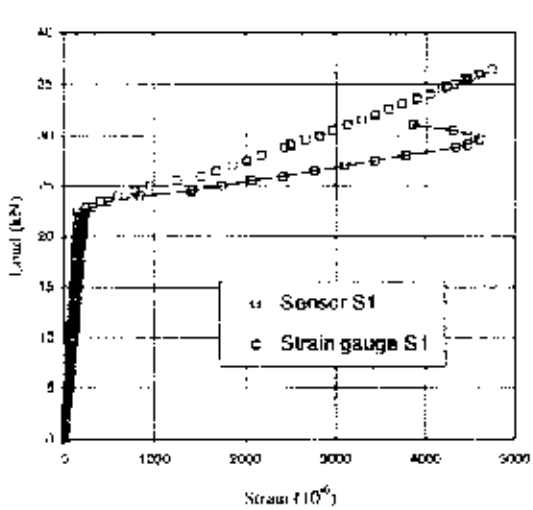

Fig. 26. Experimental result (S_1) for a beam with embedment of multiplexed FBG sensors.

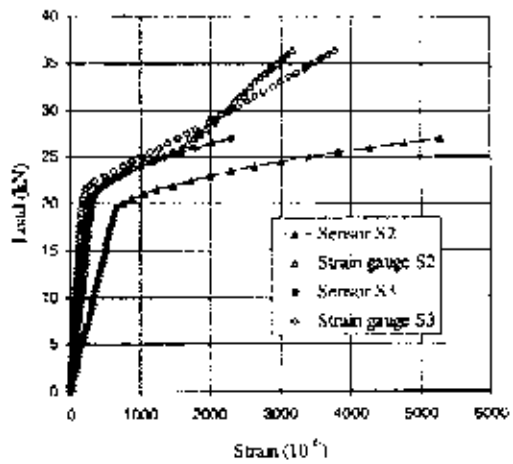

Fig. 27. Experimental results (S_2 and S_3) for a beam with embedment of multiplexed FBG sensors.

5. Conclusions

Strain measurements in composite-bonded concrete structures by using fibre-optic Bragg grating (FBG) sensors were conducted experimentally. Single and multiplexed grating sensors were used in the present study. Frequency modulated continuous wave (FMCW) technique was used to demodulate the response signals from the optical fibre with more than one grating sensor. Throughout the whole study, several conclusions can be drawn:

1. Embedded FBG sensors revealed the true strain of measurement in real time compared with externally bonded strain gauge, particularly for a structure with surface coverage reinforcement.
2. Different embedding direction of optical fibre may influence the mechanical properties of the composite structure with the embedment of optical fibre sensor. Great reduction in flexural strength of the composite structure with

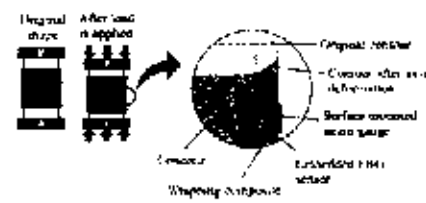

Fig. 28. Schematic illustration for composite wrapped cylinder subjected to uni-axial compression test.

the embedment of optical fibre, which orients perpendicularly to the load bearing direction.

3. Multiplexed FBG strain sensors enable to measure strains in different locations at the same time with only using one single optical fibre. In high strain condition, the properties change at the adhesive layer cannot be detected directly from the surface adhered strain-measuring devices while the FBG sensors can provide important signal to the operator.
4. The order and arrangement of the sensors is important for multiplexed strain measuring system since the sensor may loss signal if any one of the sensors, which are located in the direction from light source is broken.

Acknowledgements

This research project was funded by The Hong Kong Polytechnic Research Grant G-V528 and the Research Grant Council of Hong Kong (PolyU 5121/98E).

References

[1] Cole JH, Johnson RL, Bhuta PB. Fiber optic detection of sound. J Acoust Soc Am 1977;62:1136–8.
[2] Butter CD, Hocker GB. Fiber optic strain gauge. Appl Opt 1978;17:2867.
[3] Rutherford PS, Westerman EA. Aircraft structural integrity and smart structural health monitoring. Proc Active Mat Adapt 1992;16:267–70.
[4] Wood K, Brown T, Rogowski R, Jensen B. Fibre optic sensors for health monitoring of morphing airframe: Bragg grating strain and temperature sensor. J Smart Mater Struct 2000;9:163–9.
[5] Czarnek R, Guo YF, Bennett KD, Claus RO. Interferometric measurements of strain concentrations induced by optical fiber embedded in a fiber reinforced composite. Proc SPIE-Int Soc Opt Engng 1989:43–54.
[6] Huang S, Ohn MM, LeBlanc M, Measures RM. Continuous arbitrary strain profile measurements with fibre Bragg grating. J Smart Mater Struct 1998;7:248–56.
[7] Maaskant R, Alavie T, Measures RM, Tadros G, Rizkalla SH, Guha-thakurta A. Fibre-optic Bragg grating sensor for bridge monitoring. J Cement Concrete Compos 1997;19:21–33.
[8] Lau KT, Zhou LM, Ye L, Ding M. Investigation on upgrading and health monitoring the civil concrete structures using FRP and FBG sensor. Adv Compos Lett 1999;6(8):123–32.
[9] Lau KT, Zhou LM, Woo CH. J Mater Sci Res Int 1999;3(5):216–21.
[10] Dewynters-Marty V, Ferdinand P, Bourasseau S, Dupont M, Balageas D. Embedded fibre Bragg grating sensors for industrial composite cure monitoring. J Intell Mater Syst Struct 1998;9:785–7.
[11] Lo YL, Xiao FY. Measurement of corrosion and temperature using a single-pitch Bragg grating fibre sensor. J Intell Mater Syst Struct 1998;9:800–7.
[12] Kalamkarov AL. Processing and evaluation of pultruded smart composites with embedded fibre optic sensors. Proceedings of the Seventh International conference on Composites Engineering, University of New Orleans, USA. B35–38.
[13] Lau KT, Yuan L, Zhou LM. Strain monitoring in FRP laminates and concrete beam using FBG sensors. J Compos Struct 2000 (in press).
[14] Udd E. Fiber optic smart structures. New York: Wiley, 1995.
[15] Saouma VE, Anderson DZ, Ostrander K, Lee B, Slowik V. Application of fibre Bragg grating in local and remote infrastructure health monitoring. J Mat Struct 1998;31:259–66.
[16] Rutherford PS, Westerman EA. Aircraft structural integrity and smart structural health monitoring. Proc Active Mat Adapt 1992;16:267–70.
[17] Morey WW, Meltz G, Glenn WH. Fibre optic Bragg grating sensors. Proc SPIE 1989;1169:98–107.
[18] Lau KT, Zhou LM, Ye L. Strain evaluation on strengthened concrete beam by using FBG sensor. Non-destructive characterization of materials IX. Am Inst Phys, USA 1999:303–8.
[19] Chan KC, Fu W, Lau KT, Zhou LM. Multi-point strain measurement of composite-bonded concrete materials with a FMCW multiplexed FBG sensor array. J Sensor Actuator 2000;87:19–25.
[20] Miya T, Terunuma Y, Hosaka T, Miyashita. Ultimate low-loss single mode fibre at 1.55 μm. Electron Lett 1979;15:106–8.

ELSEVIER

Composite Structures 51 (2001) 9–20

COMPOSITE STRUCTURES

www.elsevier.com/locate/compstruct

Strain monitoring in FRP laminates and concrete beams using FBG sensors

Kin-tak Lau [a], Libo Yuan [a], Li-min Zhou [a,*], Jingshen Wu [b], Chung-ho Woo [a]

[a] Department of Mechanical Engineering, The Hong Kong Polytechnic University, Kowloon, Hong Kong
[b] Department of Mechanical Engineering, The Hong Kong University of Science and Technology, Hong Kong

Abstract

The fibre-optic Bragg grating (FBG) sensor is broadly accepted as a structural health monitoring device for fibre reinforced plastic (FRP) materials by either embedding into or bonding onto the structures. The accuracy of the strain measured by using the FBG sensor is highly dependent on the bonding characteristics among the bare optical fibre, protective coating, adhesive layer and host material. In general, the signal extracted from the embedded FBG sensor should reflect the straining condition of the host structure. However, due to the existence of an adhesive layer and protective coating, part of the energy would convert into shear deformation. Therefore, the mechanical properties of these materials would affect the resultant strain measured by embedding a FBG sensor into the structure. This paper presents a theoretical model to evaluate the differential strains between the bare fibre and host material with different adhesive thickness and modulus of the protective coating of the embedded FBG sensor. The results are then compared with numerical analysis by using the finite element method (FEM). Experimental work was conducted for both glass fibre composites and FRP strengthened concrete beams with embedded FBG sensors. Externally bonded strain gauges were used to compare the results obtained from the FBG sensors. The theoretical predictions reveal that the axial strain measured at the fibre-core region is lower than the true strain of the host material with increasing thickness of adhesive layer. A thick adhesive layer and low modulus of coating material would enlarge the shear stress concentration area at the bonded end region. An experimental investigation also shows that the FBG sensor can be confidently used with sufficient bond length.

Keywords: Fibre-optic Bragg grating; Strain sensing; Fibre reinforced composites; Concrete structure

1. Introduction

The fibre-optic Bragg grating (FBG) sensor has been extensively adapted as a new non-destructive evaluation (NDE) technique in monitoring strain and temperature profiles of structures under service conditions [1]. The speciality of using FBG sensor for strain sensing application is that it is able to measure strains locally with high resolution and accuracy. As the physical size of an optical fibre is extremely small compared with other strain measuring components, it enables it to be embedded into the structures for determining the strain distributions without influencing the mechanical properties of the host materials [2]. Recent research reports showed that optical fibre sensors could be effectively used for damage detection and cure monitoring of advanced composite materials (ACM) [3]. Du et al. [4] demonstrated that the FBG sensor was capable of measuring the strain at the inter-laminate layers of textile structural composite (TSC) beams. Hong et al. [5] also found that the strains could be remotely "real-time" measured by using the FBG sensing technique for graphite–epoxy (Gr/Ep) composite plate when subjected to a tensile loading. Recent researchers have started to pay an attention to the utilisation of FBG sensor in civil concrete structures. Saouma et al. [6] and Holton [7] adhered FBG sensors on to a reinforced steel bar of cast-in-place concrete structures in order to monitor the strain response in situ.

In recent years, many research efforts have concentrated on using ACM for concrete rehabilitation and retrofits [8–12]. A high strength fibre reinforced plastic (FRP) laminate has been adhered to the concrete surface in order to improve the stiffness and tensile strength of damaged structures. The attraction of using FRP in the construction industry is their high strength, low weight, and resistance to corrosion and high fatigue life.

* Corresponding author. Tel.: +852-2766-6663; fax: +852-2365-4703.
E-mail address: mmlmzhou@polyu.edu.hk (L.-M. Zhou).

0263-8223/01/$ - see front matter
PII: S0263-8223(00)00094-5

However, further inspection of the mechanical properties of the strengthened structures may not be possible since the damaged surface is covered by an externally bonded reinforced-laminate. Therefore, a pre-adhered strain-measuring device on the damaged surface before installing the FRP laminate is essential. The FBG is one of the most mature technologies for the purpose of monitoring surface strain in order to guarantee structural safety, particularly at areas of high stress concentration.

The precision of measurement using the FBG strain sensors is highly dependent on the bonding characteristics of the fibre core, protective coating, adhesive layer and host material. The principle of FBG technology is to gauge the light reflective signal from the grating (the region where the sensor is located) region when it is subjected to strain. Ideally, the embedded sensor should provide a straining signal that is equivalent to the strain of the host structure. However, the existence of an adhesive layer and protective coating absorbs part of energy when the structure is under applied load. Therefore, the strains experienced by host material are not wholly transferred to the bare fibre and some may be lost through interface shear transfer within the protective coating and adhesive layer.

Ansari et al. [13] and Duck et al. [14] proposed theoretical models to investigate the mechanical load transfer from the bare fibre to the host material. They assumed that the fibre (with coating) perfectly contacted with the host material. The effects generated by the thickness of an adhesive layer were neglected.

In this paper, a theoretical model for the mechanical load transfer from the host material to the bare fibre is addressed by considering the adhesive material thickness. The results are then compared with numerical analysis using the finite element method (FEM). Mechanical property tests were performed for both a glass fibre composite plate and a strengthened concrete beam with embedded FBG sensors. The strains measured from the FBG sensors were compared with that from externally bonded strain gauges.

2. Principle of FBG sensor

The basic principle of the FBG sensor is to measure the changes in reflective signal from the grating when it is subjected to elongation or thermal deformation. Any changes of the physical properties at the grating region would influence the reflective index (n_B) and the spatial pitch Λ at the core section of the sensor. A schematic illustration of the FBG strain measuring system is shown in Fig. 1. Light is emitted from a broadband source (LED) to the grating via a 3-dB fiber optic cou-

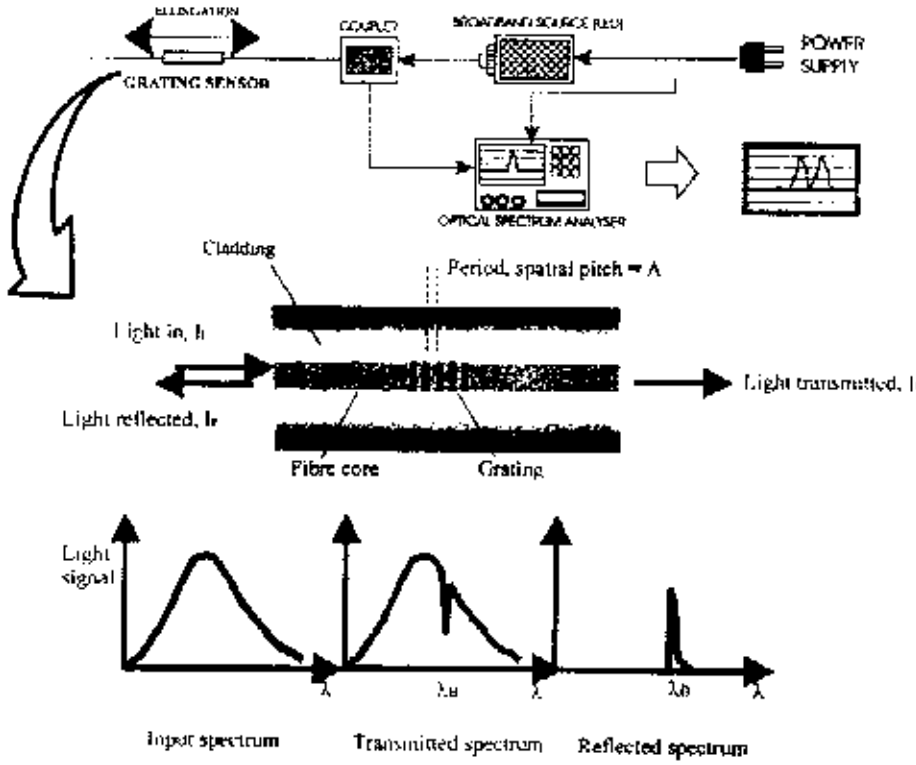

Fig. 1. The FBG strain measuring system.

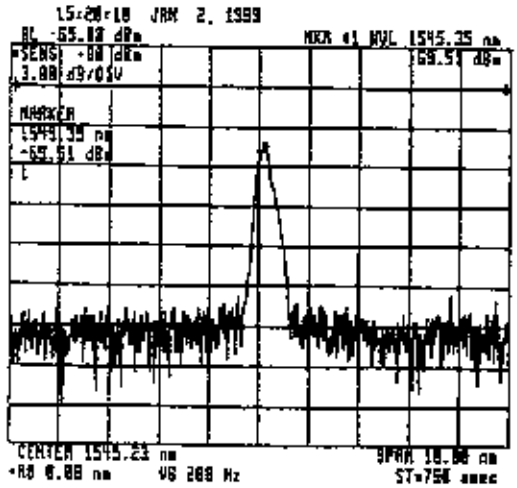

Fig. 2. Reflected spectra extracted from the OSA.

pler. The coupler acts as a Y-type channel to guide the emissive light to the FBG sensor and at the same time, guide the reflective signals back to the optical spectrum analyser (OSA). The sensor is basically formed by three different materials, viz. the bare fibre, cladding and protective coating. The fibre core is surrounded by dielectric materials called "cladding", which are generally made from silica glass. The reflective index at the cladding ($n \simeq 1.45$) is slightly lower than the fibre core ($n \simeq 1.46$) in order to satisfy Snell's law to produce the total internal reflection in the core section. However, the mechanical properties of the fibre core and cladding material are the same. The outer shell called "protective coating" is used to provide the fibre with mechanical strength and protect the fibre from damage and moisture absorption. The Bragg wavelength (λ_B) that is reflected at the sensor is given by

$$\lambda_B = 2n_B\Lambda. \tag{1}$$

where Λ is the spatial pitch (the distance between each written grating), which changes with modulating strain at the grating region. Fig. 2 shows the reflected spectrum of the fibre-Bragg grating recorded by an OSA during the experiment.

The relationship between the reflective Bragg wavelength shift ($\Delta\lambda_B$) corresponding to the changes of strain and temperature at the grating region (ε_g) can be expressed as

$$\Delta\lambda_B = K_\varepsilon\Delta\varepsilon_g + \beta\Delta T \tag{2}$$

in which

$$\beta = \beta_{core} + K_\varepsilon(\alpha_{fibre} - \alpha_{core}), \tag{3}$$

where K_ε is called the theoretical gauge constant. α and β represent the thermal expansion and thermo-optic coefficients, respectively. Any changes in the external parameters of the surrounding material would alter the grating characteristics and result in a shift of the reflected Bragg wavelength. K_ε can be expressed as a function of the strain constants of the optic fibre (p_{11} and p_{12}) and Poisson's ratio (ν)

$$K_\varepsilon = \lambda_B\left(1 - \frac{n_B^2}{2}(p_{12} - \nu(p_{11} - p_{12}))\right). \tag{4}$$

It has been proved experimentally that the value of K_ε for a silica fibre responds linearly if the fibre is loaded within its elastic limit [15].

The successful implementation of the FBG sensor is highly dependent on the bonding characteristics between the sensor and host material. In practice, the strain measured at the grating region (ε_g) is not identical to the strain of the host material (ε_h), i.e.,

$$\varepsilon_g = \eta\varepsilon_h, \tag{5}$$

where η is the rectification coefficient which is a function of the material properties and geometric factors of the adhesive, protective coating, bare fibre and host materials. Ideally, the coefficient η becomes unity if there are no protective coating and adhesive layer between the bare fibre and the host material. The strain measured from the optical fibre is identical to the strain of the host material if a perfect bond is assumed [16]. However, embedding the bare optical fibre into the structure is impractical since the bare fibre is extremely brittle. It requires protection by an extrinsic material. Indeed, for surface strain measurement, using an adhesive to hold the sensor in place is inescapable. The coating and adhesive layer would absorb part of energy to cause shear deformations when load is applied to the structure. Therefore, the resultant strain at the grating region may not truly represent the strain of the host material.

3. Theoretical approach

For the practical problem mentioned above, the bonding characterisation at the interfaces between the host material and adhesive layer, adhesive layer and protective coating, and protective coating and bare fibre (the actual segment from that the strain is measured) would influence the true strain measured from the FBG sensor. The adhesive layer and the protective coating would absorb part of energy and shear deformation results [13]. Also, the total embedding length ($2L_f$) of the fibre would affect the accuracy of measurement using the FBG sensors because shear stress concentrations exists at the fibre ends. Fig. 3 shows a four-cylinder model for analysis of the stress transfer. A cross-section microscopy photograph of a test specimen is given in Fig. 4. The longitudinal axis z represents the direction of the applied load. Transverse direction r represents the

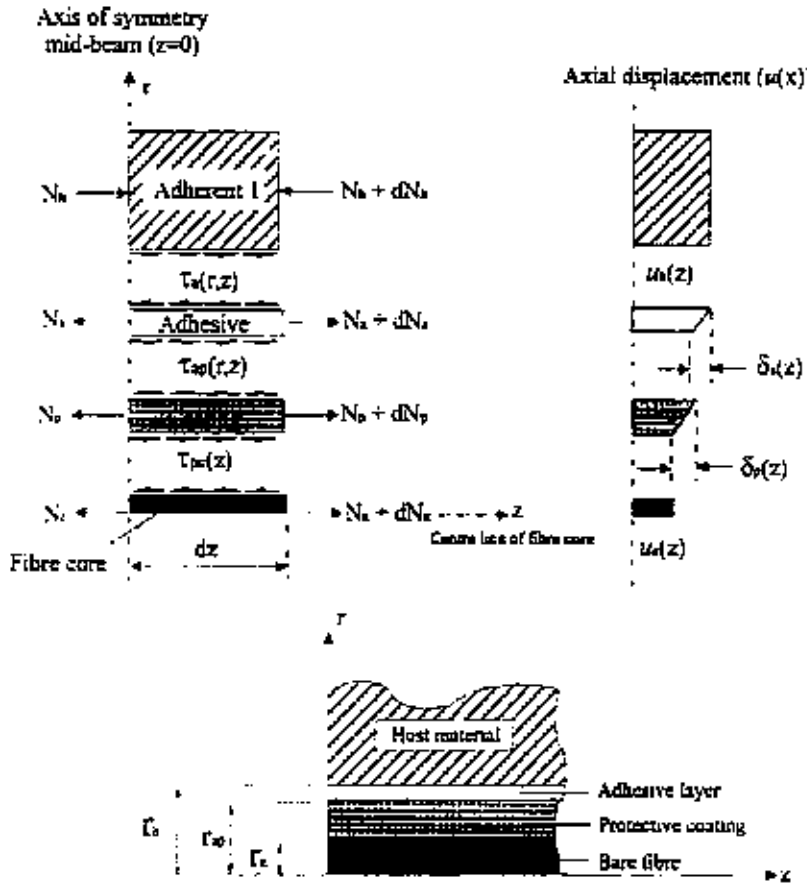

Fig. 3. Four cylindrical model for the present study

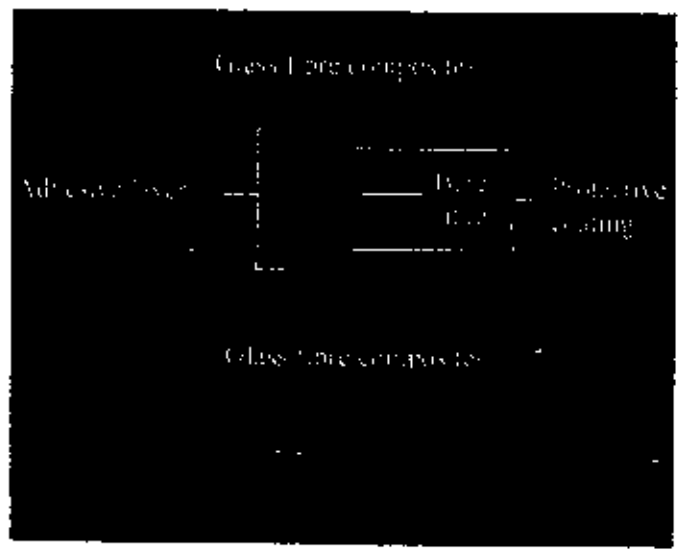

Fig. 4. Cross-section view (macroscopic scale) for the composite structure with the embedded FBG sensor

distance measured from the centre ($r = 0$) of the fibre core. In Fig. 3, the subscripts c, p, a and h denote the bare fibre, protective coating, adhesive layer and host material, respectively. Tensile and shear moduli are given by E and G, respectively. $\tau_a(r,z)$ and $\tau_{ap}(r,z)$ denote the shear stresses along the axial direction at the

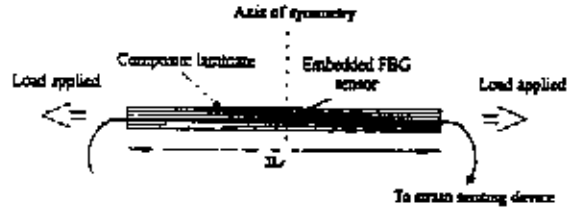

Fig. 5. A typical composite structure with the embedded FBG sensor.

interfaces between the host material and adhesive layer and between the adhesive layer and protective coating, respectively. The symbols r_h, r_{ap}, and r_c represent the inner radius of the host material, the outer radii of the protective coating and bare fibre, respectively measured from the centre of the fibre core. Axial loads are applied to the host material, adhesive layer, protective coating and the bare fibre along model by N_h, N_a, N_p and N_c, respectively. Because of the symmetry about both r- and z-axes, only a quarter section of the embedding fibre system is considered for the strain analysis. A typical composite laminate with an embedded FBG sensor is shown in Fig. 5. The following basic assumptions are made to simplify the case of current study:

1. Mechanical behaviour of the bare fibre, protective coating, adhesive layer and host material are linear, elastic and isotropic.
2. All interfaces are perfectly bonded. Therefore, the displacement conditions are described by

$$u(z) = \begin{cases} u_h(r,z) = u_a(r,z) & \text{for } r = r_h, \\ u_a(r,z) = u_p(r,z) & \text{for } r = r_{ap}, \\ u_p(r,z) = u_c(r,z) & \text{for } r = r_c. \end{cases} \tag{6}$$

The relative displacements (δ) of the adhesive material and the protective coating due to shear deformation are given by

$$\delta_a(z) = u_h(r_h,z) - u_a(r_{ap},z), \tag{7}$$

$$\delta_p(z) = u_p(r_{ap},z) - u_p(r_c,z). \tag{8}$$

At the mid-beam region ($z = 0$), the strains for all elements are mathematically identical, i.e.,

$$\varepsilon_h(0,r) = \varepsilon_a(0,r) = \varepsilon_{ap}(0,r) = \varepsilon_c(0,r). \tag{9}$$

3. No thermal load is applied in the system. The strain evaluated at the core region only responds the strain induced by the load applied axially.

By considering the force equilibrium for an element of the protective coating in the loading direction shown in Fig. 3, the shear stress in the protecting coating can be approximately obtained by [12]

$$\tau(z,r) = \frac{r_{ap}}{r}\tau_{ap}(z,r), \quad r_c \leqslant r \leqslant r_{ap}. \tag{10}$$

Similarly, the shear stress in the adhesive material is expressed by

$$\tau(z,r) = \frac{r_{ap}}{r}\tau_{ap}(z,r), \quad r_{ap} \leqslant r \leqslant r_h. \tag{11}$$

The axial displacement of the host material can be obtained by considering the condition of compatibility for all elements shown in Fig. 3

$$u_h(z) = \delta_a(z) + \delta_p(z) + u_c(z), \tag{12}$$

in which the relative displacement of the adhesive layer is determined by

$$\delta_a(z) = \frac{1}{G_a}\int_{r_{ap}}^{r_h} \tau(z,r)\,dr \tag{13}$$

and the relative displacement of the protective coating is given by

$$\delta_p(z) = \frac{1}{G_p}\int_{r_c}^{r_{ap}} \tau(z,r)\,dr. \tag{14}$$

For the host material and the bare fibre, the axial displacements are given by

$$u_h(z) = \int_0^z \frac{\sigma_h(z)}{E_h}\,dz \tag{15}$$

and

$$u_c(z) = \int_0^z \frac{\sigma_c(z)}{E_c}\,dz. \tag{16}$$

The tensile force of the fibre core can be expressed as

$$\begin{aligned} N_c(z) &= \pi r_c^2\sigma_c - 2\pi r_c\int_0^z \tau_{pc}(z,r_c)dz \\ &= \pi r_c^2\sigma_c - 2\pi r_{ap}\int_0^z \tau_{ap}(z,r_{ap})\,dz. \end{aligned} \tag{17}$$

where σ_c is the axial stress of the bare fibre at mid-beam section ($z = 0$). Substituting Eqs. (13)–(16) into Eq. (12) yields the following integral equation:

$$\begin{aligned} \int_0^z \frac{\sigma_h}{E_h}dz = {} & \frac{r_{ap}}{G_a}\tau_{ap}(z,r_{ap})\ln\left(\frac{r_h}{r_{ap}}\right) \\ & + \frac{r_{ap}}{G_p}\tau_{ap}(z,r_{ap})\ln\left(\frac{r_{ap}}{r_c}\right) - \frac{1}{E_c\pi r_c^2} \\ & \times \int_0^z \left[\sigma_c\pi r_c^2 - 2\pi r_{ap}\int_0^z \tau_{ap}(\xi,r_{ap})d\xi\right]dz. \end{aligned} \tag{18}$$

By differentiating Eq. (18) and combining the compatibility condition (9), the equation is simplified as

$$\begin{aligned} & \frac{-2r_{ap}}{E_c r_c^2}\int_0^z \tau_{ap}(z,r_{ap})dz + \left[\frac{r_{ap}}{G_a}\ln\left(\frac{r_h}{r_{ap}}\right)\right. \\ & \left. - \frac{r_{ap}}{G_p}\ln\left(\frac{r_{ap}}{r_c}\right)\right]\frac{\partial\tau_{ap}(z,r_{ap})}{\partial z} = 0. \end{aligned} \tag{19}$$

Further, differentiating Eq. (19) gives

$$\frac{\partial^2\tau_{ap}(z,r_{ap})}{\partial z^2} - \lambda^2\tau_{ap}(z,r_{ap}) = 0. \tag{20}$$

where

$$\lambda = \sqrt{\frac{2\pi_{ap}}{E_c\pi_c^2[(r_{ap}/G_a)\ln(r_b/r_{ap}) + (r_{ap}/G_p)\ln(r_{ap}/r_c)]}}. \tag{21}$$

The solution to Eq. (20) is given by

$$\tau_{ap}(z, r_{ap}) = C_1\cosh(\lambda z) + C_2\sinh(\lambda z). \tag{22}$$

Two unknowns C_1 and C_2 are determined using two boundary conditions. The first boundary condition is evaluated at $z = 0$. The axial load (N_c) at the bare fibre is determined by the compatibility condition (Eq. (9)). The strain of the fibre core at the mid-beam region is equal to the strain of the host material. The second boundary condition is evaluated at the point, where the axial load of the fibre core is zero, i.e.,

$$N_c(0) = \sigma_b\pi r_c^2\frac{E_c}{E_b} \quad \text{and} \quad N_c(L_f) = 0, \tag{23}$$

in which L_f is the distance measured from the mid-beam ($z = 0$) to the point of zero axial load of the fibre. Using above boundary conditions, the constants C_1 and C_2 are obtained by

$$C_1 = \frac{\sigma_c r_c\lambda}{2\sinh(\lambda L_f)} \quad \text{and} \quad C_2 = 0. \tag{24}$$

Combining Eqs. (24) and (22) yields the final form of shear stress distribution at the interface between the adhesive layer and protective coating

$$\tau_{ap}(z, r_{ap}) = \frac{\sigma_c r_c\lambda}{2\sinh(\lambda L_f)}\cosh(\lambda z). \tag{25}$$

Further, the axial stress of the bare fibre, $\sigma_c(z)$, can be determined by substituting Eq. (25) into Eq. (17)

$$\sigma_c(z) = \frac{1}{\pi r_c^2}\left(\sigma_c\pi r_c^2 - 2\pi r_c\left(\frac{C_1}{\lambda}\sinh(\lambda z)\right)\right). \tag{26}$$

Considering the compatibility condition (Eq. (9)), the axial strain, $\epsilon_c(z)$, in the fibre core region is given by

$$\epsilon_c(z) = \epsilon_0\left(1 - \frac{\sinh(\lambda z)}{\sinh(\lambda L_f)}\right), \tag{27}$$

where ϵ_0 is the axial strain of the host material at $z = 0$. From Eq. (27), it is clearly shown that the strain distribution along the axial direction is dominated by the constant variable λ. This parameter is a function of the material properties and geometric factors of the adhesive layer, protective coating and bare optical fibre. Any changes of these properties and factor would influence the stress distribution at bonded ends due to the existence of a hyperbolic function ($\sinh(\lambda z)$). Eq. (27) also shows that the maximum strain of the fibre is equal to the maximum strain of the host material at $z = 0$.

The axial strains of the bare optical fibre along the bonded length are plotted in Fig. 6 for the different bonded length (L_f), tensile moduli of the protective coating (E_p) and thickness of the adhesive layer ($t_a = r_b - r_{ap}$). In Fig. 6, it is apparently demonstrated that a steady strain measurement can be achieved at the fibre core region only when a long bonded length is

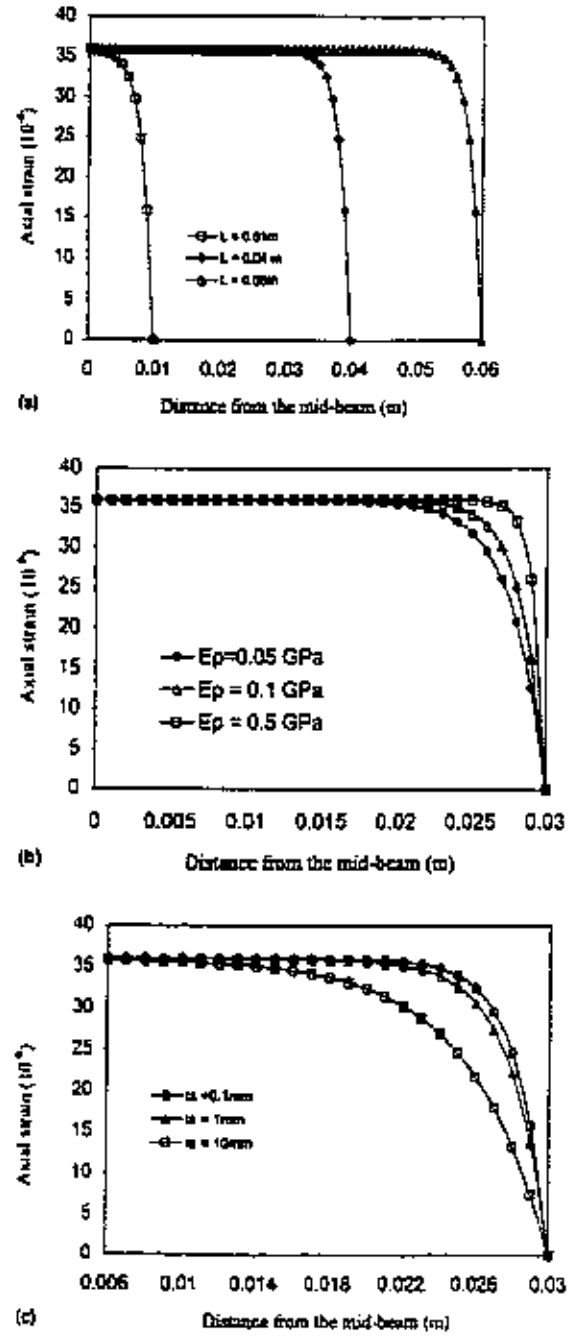

Fig. 6. Axial strain of the bare fibre against the distance measured from the axis of symmetry ($z = 0$) with different: (a) embedding length; (b) modulus of the protective coating; (c) adhesive thickness.

used. In order to determine a reasonable embedded optical fibre length, an approximate method (error $\leqslant 1\%$) is used to estimate the minimum fibre bonded length

$$L_f = \frac{1}{\lambda}\sinh^{-1}\left(\frac{1}{0.01}\sinh(\lambda L_g)\right), \tag{28}$$

where L_g represents the FBG sensor length.

In Fig. 6(b) and (c), the axial strain of the bare fibre for different moduli of protective coating material and thickness of adhesive layer are plotted. The results indicate that if a high modulus material is used as a fibre protective coating and a thin adhesive layer is used as a bond interface layer, it requires a shorter load transfer distance to transfer the load from the host material to the fibre core region. Conversely, a longer distance is required to transfer all loads to the fibre core using a low modulus material and thick adhesive layer. A large part of the energy is converted into shear deformations at the coating and adhesive materials. The axial shear stresses ($\tau_{ap}(z, r_{ap})$) are shown in Fig. 7 for different adhesive thickness. The shear stress concentration at the bonded end region rapidly vanishes with increasing distance toward the mid-beam ($z = 0$) region. The high shear stress region reduces with decreasing thickness of the adhesive layer. However, the maximum shear stress $\tau_{ap}(z, r_{ap})$ increases with increasing adhesive thickness. Increasing the thickness of the adhesive layer prolongs the shear stress concentration region at the bonded end region.

In Eq. (28), it is obviously indicated that the maximum strain of the fibre core (ε_c) at $z = 0$ is same as the strain measured at the host material (ε_0) due to the basic assumption ($N_z = N_p = 0$). However, it may not be true when a thicker adhesive layer is used. During the adhesion process, a thin adhesive layer cannot in general be precisely controlled. The thickness of an adhesive layer is normally beyond the desired limit. A thick adhesive layer, in turn may take up part of the axial load from the host material. The strain measured from the fibre core region is slightly less than the strain of the host material. Therefore, Eq. (28) should be rewritten in the following form:

$$\varepsilon_c = A_1\varepsilon_0\left(1 - \frac{\sinh(\lambda z)}{\sinh(\lambda L_f)}\right), \tag{29}$$

where A_1 is the function of the material and geometric constants of the adhesive layer, protective coating, bare fibre and host material. It is assumed that, a part of the axial load is taken up by an adhesive layer (N_p). By considering force equilibrium at mid-beam region ($z = 0$) and substituting the compatibility condition (9), the maximum strain of the bare optical fibre at the mid-beam region is obtained by

$$\varepsilon_c = \varepsilon_0 \times \frac{1}{\left\{E_h/E_c + E_a/E_c\left((r_a^2 - r_{ap}^2)/(r_{ho}^2 - r_a^2)\right) + (r_c^2/(r_{ho}^2 - r_a^2))\right\}}, \tag{30}$$

where r_{ho} is the outside radius of the host material.

The solution from the proposed theoretical model is verified by a FEM using the commercial package Msc/Nastran. Six node (Trias6) elements were used to generate meshes. Since the model is bi-symmetric about its r- and z-axes, only a quarter segment is considered. The boundary conditions are $v|_{r=0} = 0$ and $u|_{z=0} = 0$, where u and v are the displacements along r- and z-directions, respectively. Details of the mechanical and geometrical properties are listed in Table 1. The results evaluated from Eqs. (25), (28) and (30) are plotted in Fig. 8. It is shown that the theoretical solutions are in good agreement with the FEM results. In Fig. 8(c), it is demonstrated that the axial strain at the fibre core region

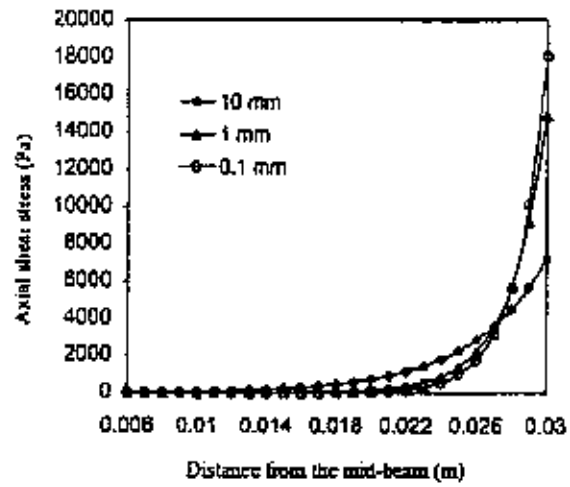

Fig. 7. Shear stress against the distance measured from the axis of symmetry ($z = 0$) with different adhesive thickness.

Table 1
Mechanical and geometrical properties

Description	Symbols	Values
Diameter of bare fibre (μm)	r_c	125
Outer diameter of protective coating (μm)	r_{ap}	250
Young's modulus (GPa)		
Fibre core	E_c	72
Protective coating	E_p	0.1
Adhesive material	E_a	3.3
Concrete	E_h	27.8
Shear modulus (GPa)		
Adhesive material	G_a	1.2
Protective coating	G_p	0.037
Thickness of an adhesive layer (mm)	t_a	0.1

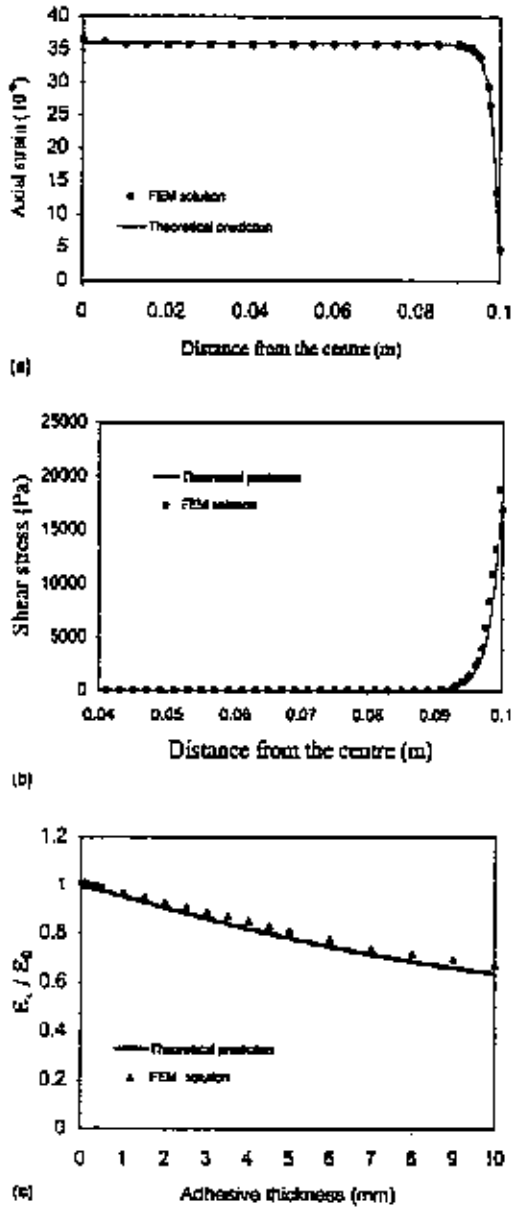

Fig. 8. The comparison of the results between the analytical and FEM solutions for: (a) the axial strain of the bare fibre; (b) shear stress of the protective coating against the distance measured from the axis of symmetry ($z = 0$); (c) the relative strain ($\varepsilon_c/\varepsilon_0$) against the adhesive thickness.

decreases with increasing thickness of adhesive layer. Eq. (30) is able to predict the difference of strain between the fibre core and the host material for a specified thickness of adhesive layer.

4. Experimental results

4.1. FBG sensor calibration

Calibration is generally performed through a tensile test by adhering the sensor to a test coupon. The calibration factor pertains to the slope of the linear relationship between the FBG reflect wavelength shift and the strain measured by a conventional foil strain gauge. Near the strain gauge, an FBG sensor has been adhered to the centre of the test coupon with epoxy. The grating length of FBG sensor was 12 mm and the total embedding length was 235 mm. According to the theoretical results, the coefficient λ was calculated to be 600 m^{-1}, and the required minimum embedding length evaluated from Eq. (28) was 19.67 mm. Therefore, the sensor should provide the strain reading within the steady measuring region as the strain reading would not influence by the bonded end shear stress concentration. The shifts of fibre Bragg grating reflective wavelength peak and the corresponding strain were recorded by an OSA and strain indicator, respectively during the experiment. In present study, the coefficient K_s has been calibrated as 947.55 nm^{-1} and the result is plotted in Fig. 9.

4.2. Glass fibre composite laminate deflection experiments

FBG sensors were embedded into the 20 layers of balanced type glass-fibre composite laminates. The sensors were located at the interfaces between first and second layer and between 19th and 20th layer. A four-point bending test was performed to investigate the strain response measured from the sensors. External bonded strain gauges were used to compare the results from the FBG sensors. The testing setup and test couple

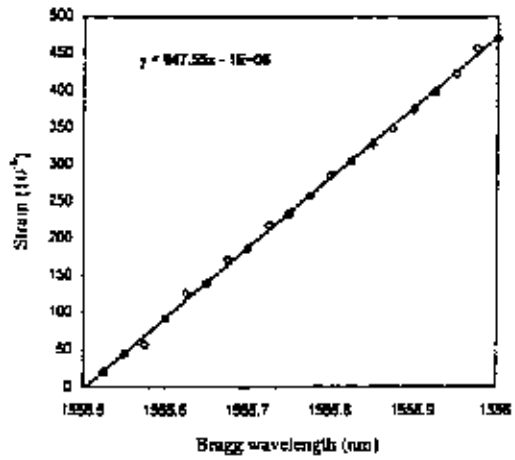

Fig. 9. Plot of measured strain against the Bragg wavelength for the sensor used in the present study.

are shown in Figs. 10 and 11, respectively. A high fibre volume fraction ($v_f = 47\%$) was used to reduce the adhesive thickness between the sensor and its surrounding material.

The experimental results for the strain measured from both FBG sensors and two external strain gauges versus mid-beam deflection are plotted in Fig. 12. The positive portion represents the tensile strain measured on the bottom surface while the negative portion is compressive strain measured on the top surface of the specimen. The strains measured by the FBG sensor are in good agreement with that from the surface bonded strain gauges.

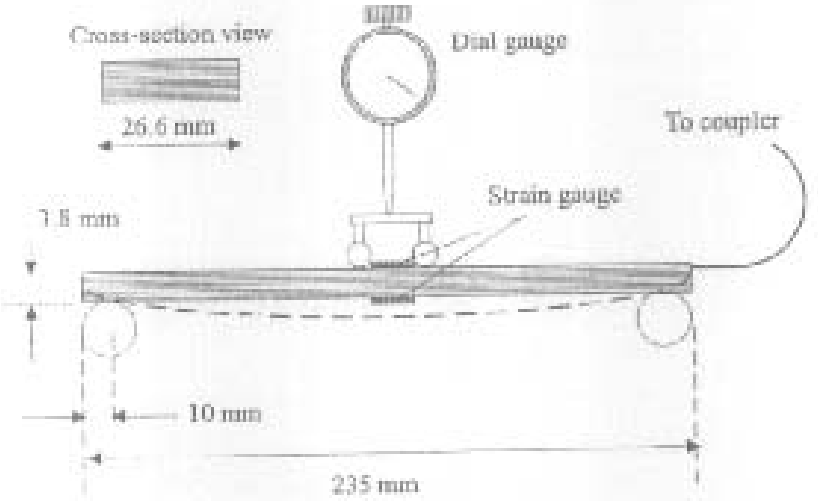

20 layers of glass fibre laminate (V_f = 42%)
FBG sensors are located at the interface between
- 1st and 2nd layers
- 19th and 20th layers

Fig. 10. Experimental setup for the four-point bending test.

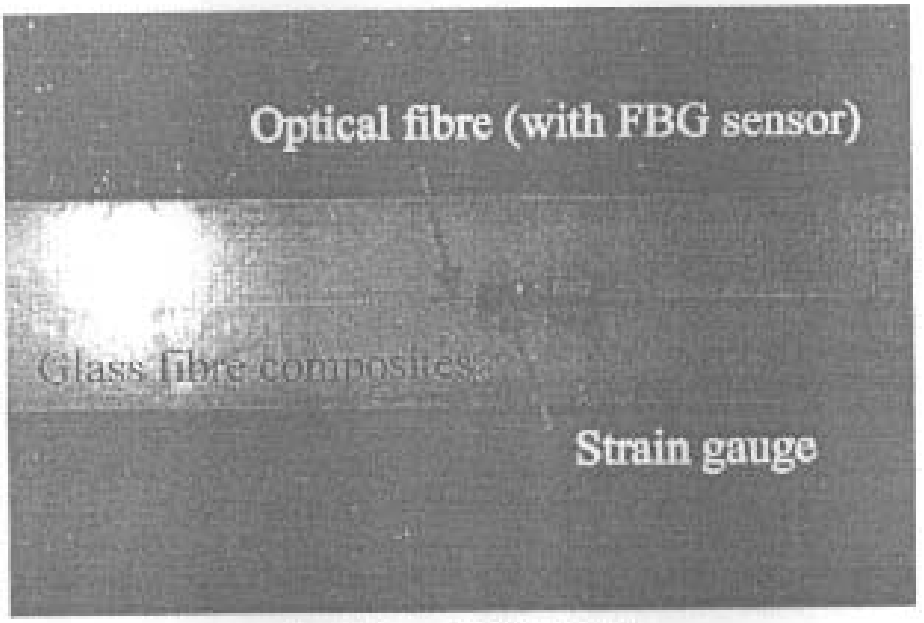

Fig. 11. Photograph of the testing couple.

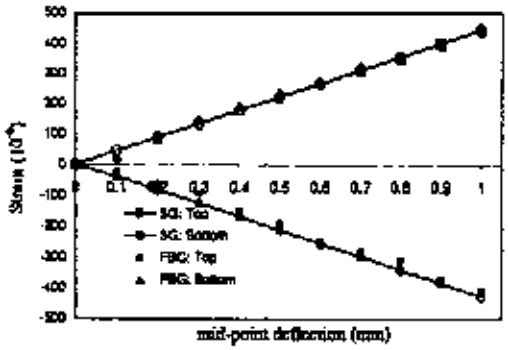

Fig. 12. Comparison of the strains measured by FBG sensors and external bonded strain gauges.

4.3. Test on strengthened notched-concrete beam with the embedded FBG sensor

The FBG sensors were embedded at the interface between a notched-concrete beam surface and an externally bonded glass fibre composite. The maximum compressive and flexural strengths of the concrete used in present experiment were 49.99 and 4.16 MPa, respectively. The concrete was mixed using an aggregate, sand, cement and water in pre-determined proportions. The rectangular beams were formed by a 152.4 × 152.4 × 500 mm^3 steel mould. The curing period was 28 days for completing the full hydration process in order to achieve the maximum concrete strength. The notch was then made to a notch/depth ratio of 0.2. The maximum flexural loads applied to the plain and notched concrete beams were 22.5 and 17 kN, respectively.

The glass fibre composite was laid-up on the tensile and shear surfaces of the beam as shown in Fig. 13 in order to increase the tensile strength of the structure. The FBG sensors were attached to the notch-tip and bottom of the beam at the mid-beam region before laying-up the composite. The total embedding length was 400 mm, which is larger than the minimum length required from Eq. (28). Strain gauges were attached to the surface of the composite to compare the results from the embedded FBG sensors. Pressure was applied on all bonding surfaces after laying the glass fibre composite in order to reduce the thickness of adhesive layer.

The experimental results are plotted in Fig. 14. It is shown that differences between the strain measured from the FBG sensor and the externally bonded strain gauges increase with increasing the applied load. For the beam

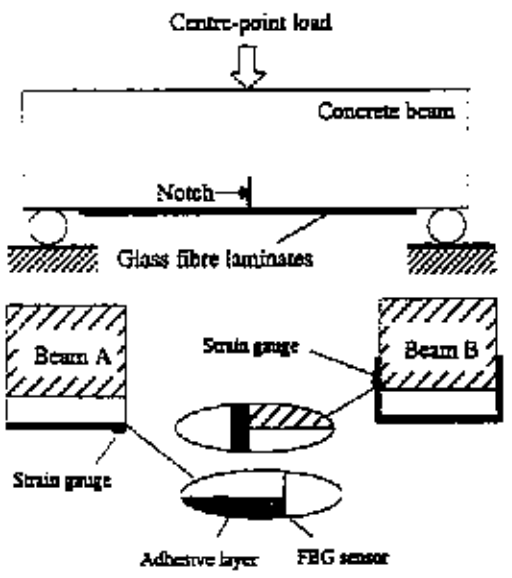

Fig. 13. Schematic illustration of the composite bonded cracked-concrete structure with the embedded FBG sensor.

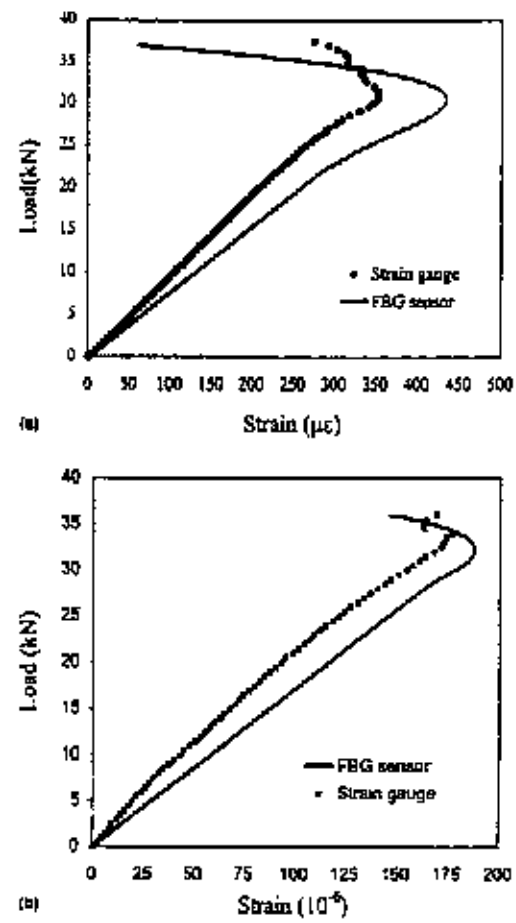

Fig. 14. The experiment results for: (a) beam A; (b) beam B.

Fig. 15. The failure mode of the beam A after testing.

"A", the strain measured by the FBG sensor is higher than the strain measured by foil strain gauge at the bottom edge region. Small cracks and debond were observed visibly at the notch-mouth region when the load was applied to 30 kN. As the crack was forming, strain relaxation occurred at the region where the sensor was embedded. Therefore, the regression of strain is indicated in the graph for further increasing the load beyond 30 kN. This phenomenon cannot be precisely indicated by the externally bonded strain gauges.

For the beam "B", the FRP composites were bonded on both sides and bottom surface. The FBG sensor was attached at the notch-tip of the beam side as shown in Fig. 13. The strain measured by FBG sensor is also higher than the strain given by externally bonded strain gauge.

The failure profile of the beam "A" is shown in Fig. 15. It is apparently shown that the debonding and cracks exist at the bottom surface. It is suspected that the micro-cracks existed on the concrete surface and this could not be revealed by the externally bonded strain gauges.

5. Conclusion

In the present study, a theoretical model to interpret the effects induced by adhesive thickness and protective-coating material for embedded FBG sensors is presented. It is found from the theoretical analysis that short bonding lengths influence the final strain measurement at the fibre-optic grating region. According to the theoretical predictions and experimental results, several conclusions are summarised as follows:

1. The use of thick adhesive layer and low modulus of coating material with a short embedding length of sensor is not encouraged for embedded FBG strain sensing systems because the maximum shear stress $\tau_{ap}(z=r_{ap})$ and shear stress concentration region increase with increasing thickness of adhesive layer and decreasing modulus of coating material.
2. Sufficient embedding length of the sensor is essential to avoid mis-measurement using FBG strain sensors. A minimum embedding length can be evaluated by using Eq. (28).
3. Embedded FBG sensors can reveal the true strain in a structure in real time compared with externally bonded strain-sensing devices, particularly for a structure, which is covered by an externally bonded plate.

Acknowledgements

This research project was funded by The Hong Kong Polytechnic Research Grant G-V528 and the Research Grant Council of Hong Kong (PolyU 5121/98E).

References

[1] Huang S, Ohn MM, LeBlanc M, Measures RM. Continuous arbitrary strain profile measurements with fibre Bragg grating. J Smart Mater Struct 1998;7:248–56.

[2] Maaskant R, Alavie T, Measures RM, Tadros G, Rizkalla SH, Guha-Thakurta A. Fibre-optic Bragg grating sensors for bridge monitoring. J Cement Concrete Compos 1997;19:21–33.
[3] Liu K, Davis A, Ohn MM, Park B, Measures RM. Embedded optical fibre sensors for damage detection and cure monitoring. Proc AMAS 1992;395–98.
[4] Du W, Tao XM, Tam HY, Choy CL. Fundamentals and applications of optical fibre Bragg grating sensors to textile structural composites. J Compos Struct 1998;42:217–29.
[5] Hong CS, Ryu CY, Park DI. Strain measurements of composite laminates using fibre Bragg grating sensor. Proc ACCM-1 1998;1:625I–4.
[6] Sirocmn VE, Anderson DZ, Ostrander K, Lee B, Slowik V. Application of the fibre Bragg grating in local and remote infrastructure health monitoring. J Mater Struct 1998;31:259–66.
[7] Multiplexed sensors test new bridge materials. Laser focus world. PennWell, USA, No. 7, 1998;34:24–8.
[8] Spadea G, Bencardino, Swamy RN. Structural behaviour of composite RC beams with externally bonded CFRP. J Compos Construct 1998;2(2):132–7.
[9] Lau KT, Zhou LM, Woo CH, Chan KC, Jin W. Strengthening and monitoring concrete structures using glass fibre composites and FBG sensor. J Mater Sci Res Inter 1999;5(3):216–21.
[10] Lau KT, Zhou LM, Ye L. Investigation on upgrading and health monitoring the civil concrete structures using FRP and FBG sensor. Adv Compos Lett 1999;8(6):323–32.
[11] Bayrukeryurk O, Hearing B. Failure behaviour of pre-cracked concrete beams retrofitted with FRP. J Compos Construct 1998;3(2):138–44.
[12] Triantafillou TC. Shear strengthening of reinforced concrete beams using epoxy-bonded FRP composites. J ACI Struct 1998;95(2):107–15.
[13] Ansari F, Yuan L. Mechanics of bond and interface shear transfer in optical fibre sensors. J Eng Mech 1998;124(4):385–94.
[14] Dunk G, Renaud G, Measures M. The mechanical load transfer into a distributed optical fibre sensor due to a linear strain gradient: embedded and surface bonded cases. J Smart Mater Struct 1999;8:175–81.
[15] Rao YJ. In fibre Bragg grating sensors. J Meas Sci Technol 1997;8:355–75.
[16] Kim KS, Kollar L, Springer GS. A model of embedded fibre optic Fabry–Perot temperature and strain sensors. J Compos Mater 1993;27:1618–62.

Magazine of Concrete Research, 2001, 53, No. 01, February, 31–41

Estimation of stress intensity factor (K_I) for an FRP bonded concrete beam using the superposition method

K.-T. Lau*, S.-Q. Shi* and L.-M. Zhou*

The Hong Kong Polytechnic University

The deterioration of civil concrete infrastructures has increased dramatically in recent years. The majority of recent studies have focused on the use of fibre-reinforced plastic (FRP) materials to strengthen or reinforce decayed concrete structures by bonding the FRP plate externally onto the damage surface. These studies have concentrated on the shear and peel-off effects of the adhesive material rather than the failure mechanisms of the concrete itself. However, the stress intensity factor, K_I, at the crack-tip of the strengthened cracked concrete structures, cannot be overlooked. Numerical and experimental investigations have prove that K_I of the strengthened structure is highly influenced by the modulus and geometry of the reinforced plate. Therefore, the failure of the strengthened specimen may be due to a high K_I value in the concrete material. In this paper, a theoretical model is proposed to estimate the value of K_I with different reinforced plate properties for a strengthened concrete beam using a simple superposition method. The results from the proposed method compare well with the numerical solutions obtained from the finite-element method. Both results show that the stress intensity value, of the beam decreases as the modulus and thickness of the reinforced plate increase, while the closing force of the beam, induced by the reinforced plate, increases.

Notation

a	crack length for the centre-crack model ($2a = a_c$)
a_c	crack length for the strengthened beam
b	plate width for the centre-crack model ($b = h - a$)
d	distance measured from the support to the plate end
E_c	Young's modulus of the concrete beam
E_p	Young's modulus of the reinforcement
F_P	tension force in the reinforcement at mid-beam region ($x = 1$)
F_t	tensile force from the embedded reinforced steel bar (Carpinteri model)[14]
$f_P(\alpha)$	shape function for the beam subjected to the pair of edge forces
$f_M(\alpha)$	shape function for the beam subjected to the centre-point loading
h	depth of the beam
K_F	stress intensity factor in the concrete material due to the closing force, F_t
K_M	stress intensity factor in the concrete material due to centre-point loading, P
K_{IA}	stress intensity factor in the strengthened concrete beam
L	distance between two supporting points
l	half distance between two supporting points
P	centre-point load
t_p	thickness of the reinforcement
X_n	distance measured from the bottom of the beam to its neutral axis
β	modulus ratio (E_c/E_p)
σ_p	maximum tensile stress in the reinforcement
σ_n	maximum tensile stress in the concrete
ω	width of the beam

* Department of Mechanical Engineering, The Hong Kong Polytechnic University, Hung Hom, Kowloon, Hong Kong.

(MCR 522) Paper received 6 October 1999; last revised 26 July 2000; accepted 20 September 2000

Introduction

Fibre-reinforced plastic (FRP) has been recognized as a new advanced material in civil concrete rehabilitation because of its high strength and stiffness-to-weight ratio, resistance to corrosion and substantial fatigue durability compared with conventional materials. There is an urgent need to apply FRP material in real-life applications such as restoring the strength of archaic structures instead of replacing them. Since concrete is a low tensile strength material (it is approximately one-tenth of its ultimate compressive strength), it requires an extra reinforcing structural member to overcome this intrinsic problem.

Several studies have concluded that reinforced concrete (RC) beams could be upgraded by externally bonding FRP plate onto plain or cracked concrete surfaces.[1–7] These studies showed that the flexural strength and fatigue life of the plate-bonded beam were increased compared to its unstrengthened status. Buyukozturk and Hearing[8] found that the deflection of the concrete beam after strengthening by the post-tensioned FRP sheet was also reduced. The recent work done by Arduini and Nanni[9] proved that using the FRP as a reinforced plate could increase the ultimate flexural load-carrying capacity of a rectangular concrete beam as well as its stiffness. Toumi *et al.*[10] and Xie and Gerstle[11] simulated the crack propagation of a beam subjected to three-point bending without strengthening by an external reinforcement. Unfortunately, these theoretical predictions cannot be applied to the beam after rehabilitation. Taljsten[12] and Triantafillou[13] introduced theoretical methods for solving the stress problems of a plain concrete beam with epoxy-bonded FRP composites. They focused on the evaluation of shear and peel-off stresses of an adhesive material at the plate-end region. It was found that the modulus, thickness and geometry of the reinforced plate influence the maximum adhesive shear and peel-off stresses induced at the plate-end region. Close to zero stresses were evaluated at the region furthest from the plate end.

However, if cracking exists at the mid-beam region of the structure, the tensile stress of the plate cannot be easily determined by theories pertaining to beams without cracking. Moreover, there is no current closed-form solution for solving the value of the stress intensity factor K_I and tensile stress in the reinforced plate for the cracked beam after strengthening. Therefore, establishing a simple method to determine the value of K_I for strengthened concrete structures is essential to provide a more efficient engineering approach. This paper, therefore, presents a superposition method for evaluating the value of K_I for the strengthened concrete beam and the maximum tensile stress in the reinforced plate.

Background

Although there have been numerous studies conducted into cracking of concrete beams with steel bar reinforcement, there has been limited research into the cracking of concrete beams strengthened by an externally bonded reinforcement. A model for solving the fracture problem of steel RC beams using the superposition method was first proposed by Carpinteri[14] (Fig. 1). The stress intensity factor, K_I, of the RC beam was determined by two independent factors

(*a*) the stress intensity factor, K_M, due to the load P applied at the middle of the cracked beam

(*b*) the stress intensity factor, K_F, due to the tensile force F_s (closing force) from the embedded reinforced steel bar.

However, F_s was estimated from the ultimate tensile or yield stresses of the steel bar, which implies that the failure of the structure is dominated by the steel bar rather than the concrete beam itself. Since F_s is an assumed value and not directly related to the external applied force P, this method may not be practicable for determining K_I and F_s as a function of P.

A recent improved model assumed that the strain is linear along the depth of the RC beam and proportional to the distance measured from the beam neutral axis as

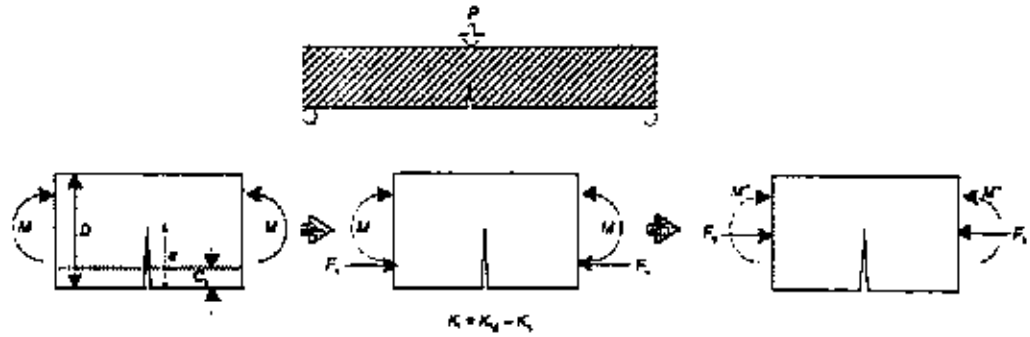

Fig. 1 The LEFM model established by Carpinteri for the RC beam[14]

shown in Fig. 2.[15] In this method, the critical crack length a_c and the tensile force F_s are initially assumed. F_s and M can then be computed by the iteration method until the results converge. This improved model provides a more realistic solution than the Carpinteri method. However, the numerical analysis verifies that the strain distribution along the depth of the cracked RC beam is not linear in form, especially at the crack section. Therefore, this improved model cannot be used to accurately predict the stresses of the strengthened cracked beam with external reinforced FRP plate.

In realistic engineering application, K_I is a factor that engineers should take into account when designing and maintaining concrete structures. The shear and peel-off stresses of the adhesive layer are not as critical because there are many anchoring mechanisms available for attaching the plate which are not prone to peeling. Consequently, the stresses in the concrete beam and reinforced plate/bar become the major factors in investigating the failure modes of the structures. From this discussion, the magnitude of F_s cannot be found directly by using the strain continuity method. Therefore, it is necessary to develop a simpler and more convenient method to predict the failure stress of the strengthened beam.

The method

This paper introduces a simple method for determining the stress intensity factor, K_{Ia}, of a rectangular cracked concrete beam strengthened by externally bonding a plate on to the tension surface. Fig. 3 shows a diagrammatic representation of a rectangular concrete beam with a crack of depth a_c at the mid-section. The depth of the crack is assumed uniform throughout the width, a, of the beam. The composite plate is fixed to the tension surface of the beam by an adhesive material with uniform thickness throughout the whole bonding length. The mechanical properties of both concrete and externally bonded plate are linear elastic. A perfect bond at the interface between the concrete and reinforced plate is assumed—that is, there is no crack formation along the bonded interface.

A superposition method is proposed to evaluate the value of K_I at the crack-tip of the beam when it is

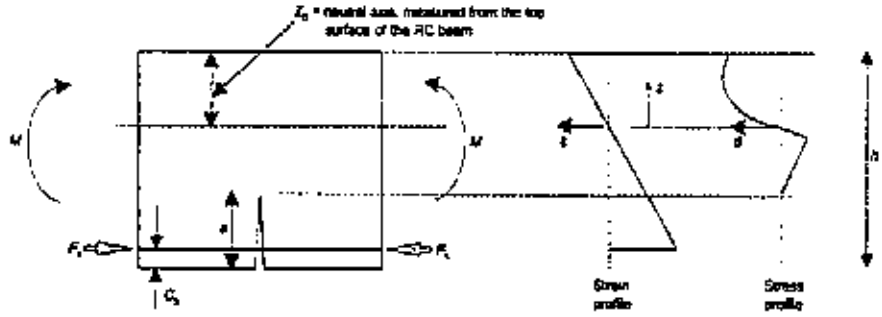

Fig. 2. Improved model by Ballarini, Azad and Ashimura;[15] strain (middle) and stress (right) distributions along the depth of the beam

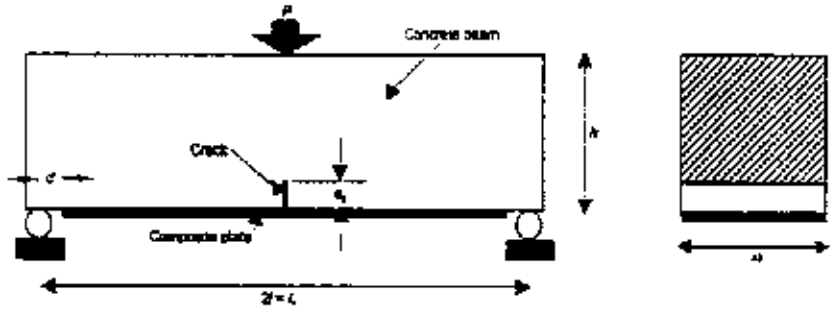

Fig. 3. Schematic model of a rectangular cracked concrete beam strengthened by a externally bonded plate

subjected to three-point bending. The method treats an edge-crack problem as a centre crack in order to determine the value of K_I, which cannot be directly solved by existing closed-form solutions. Figs 4 and 5 give a step-by-step illustration of the method used in the present study. It can be separated into three stages as follows.

(*a*) Determination of the stress function $\sigma_c(x)$ with respect to the material properties and geometric factors for both the concrete and reinforced plate of the strengthened cracked beam as indicated in Fig. 4. It is assumed that the stress function along the crack surface is the same as that determined for the whole system.

(*b*) Evaluation of K_{IA} by treating the existing edge-crack problem as a centre crack since both crack tips have zero displacement constraints in the beam longitudinal direction. The stress function on the crack surface is determined from stage (*a*). Only the crack tip which is furthest from the plate is of interest—that is, point 'A' in Fig. 5.

(*c*) Determination of plate normal force, F_P. The well-known superposition method for estimating the value of K_F by determining the actions of the tensile force in the plate and bending moment of the beam is illustrated in Fig. 5.

The major focus of the present study is to evaluate K_{IA} in a cracked concrete beam after strengthening by an externally bonded plate on the tension surface. The original edge-crack problem of the beam is considered as an inner-crack problem after strengthening since both ends of the crack have a zero-displacement characteristic—that is, the displacement at the crack tips in the beam longitudinal direction is equal to zero when $\theta = 0°$. The stress distribution along the crack surface can be estimated by the superimposition method given by Rooke *et al.*;[17] that is, the stress distribution along the crack surface is equal to the determined from the whole system without cracking within the region $-a \leq x \leq a$ under the same loading condition. Effects arising from the plate with different mechanical properties to the beam under the centre-point loading are overcome by the stress function estimated from the same strengthened beam without cracking. However, a tip (point 'A'), which is remote from the boundary of the bond, is assumed to have no significant influence by the stress induced due to the bi-material effect at the bonding region.

Stress function of a strengthened concrete beam without cracking

In the initial stage, the stress distribution along the centreline of the concrete structure without cracking but with the externally bonded reinforcement, is evaluated. Since the thickness of the reinforced plate is normally much smaller than the depth of the beam to be reinforced, the uniform axial strain of the plate is assumed through its thickness, ε_p. The stress profile along the depth of the beam is linear. The bottom surface is under tension while the top surface is in compression. Since the beam is symmetrical about its centre axis ($y = 0$), the shear deformation of an adhesive material is theoretically equal to zero at the centre

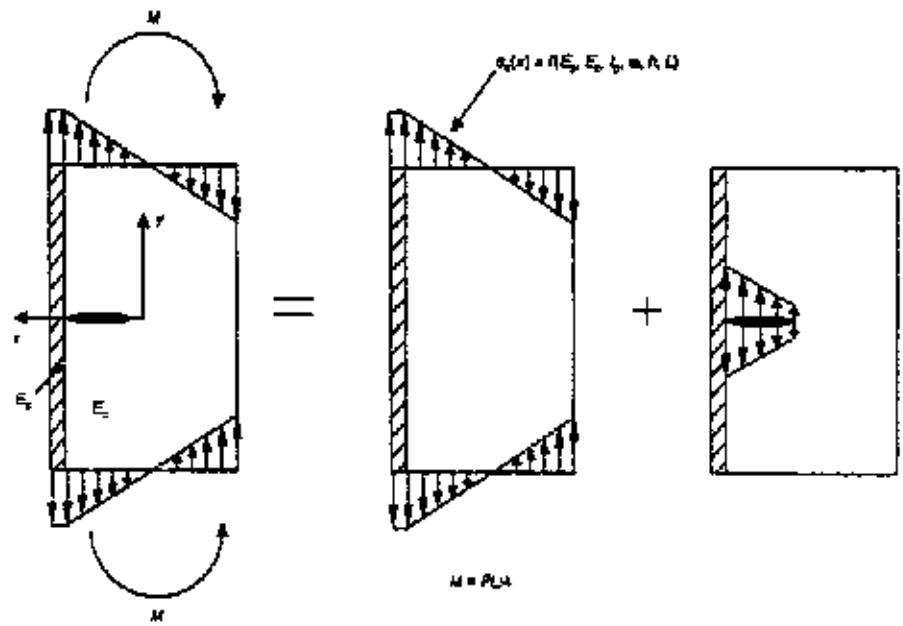

Fig. 4. Schematic diagram of the superposition method to interpret the stress distribution along the crack surface

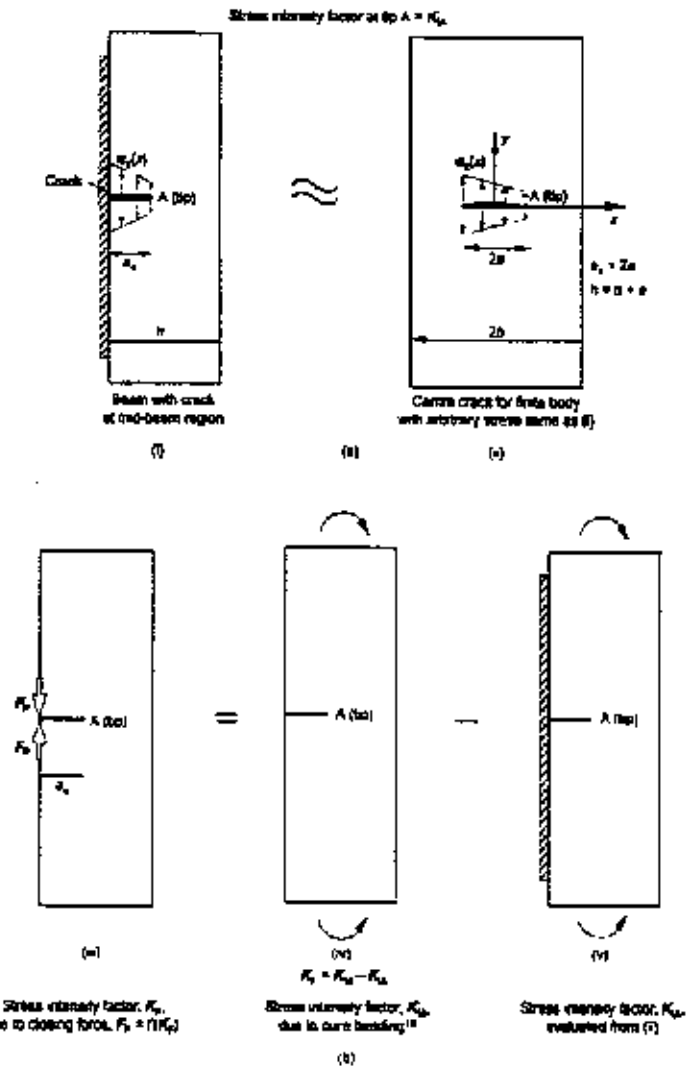

Fig. 5. Model to treat an edge-crack problem as an inner crack problem: (a) superposition method for evaluation of stress intensity factor at point A; and (b) for the beam with a pair of edge closing forces, F_p

region ($y = 0$). The strain of the reinforced plate, ε_p, at the mid-beam section should be same as the surface strain of the concrete, ε_0, at the bonding region, that is, at $(x, y) = (X_0, 0)$

$$\left.\frac{\sigma_0}{E_c}\right|_{y=0,x=X_0} = \left.\frac{\sigma_p}{E_p}\right|_{y=0,x=X_0} \tag{1}$$

where σ_0, σ_p, E_c and E_p denote the maximum tension stress of the concrete beam and reinforced plate, and the tensile moduli of the concrete and reinforced plate, respectively. Accordingly, the normal stress distribution along the lateral direction $(x, 0)$ at the mid-beam section can be expressed as

$$\sigma_c(x, 0) = \sigma_0 \frac{x}{X_0} = \sigma_p \frac{E_c}{E_p} \frac{x}{X_0} = \frac{F_p \beta x}{t_p \omega X_0 |_{y=0}} \tag{2}$$

where β is the Young's modulus ratio of the concrete and reinforced plate ($\beta = E_c/E_p$), and F_p is the closing force (in the beam longitudinal direction) induced by the reinforced plate at the mid-beam region. The

location of zero stress, $\sigma_c(x) = 0$, of the strengthened beam is called the neutral axis, X_0; it can be evaluated using the force balance equation, $\sum F_y = 0$, thus

$$F_p + \int_{-(h-X_0)}^{X_0} \sigma_c(x, 0)\omega\, dx = 0|_{y=0} \qquad (3)$$

Substituting equation (2) into equation (3) yields

$$X_0 = \frac{\beta h^2}{2(\beta h + t_p)} \qquad (4)$$

The maximum tensile stress σ_0 in the concrete material can be estimated by using the moment-equilibrium method, that is, $\sum M = 0$

$$F_p X_0 + \int_{-(h-X_0)}^{X_0} \sigma_c(x, 0)\omega x\, dx = \frac{PL}{4}\bigg|_{y=0} \qquad (5)$$

By substituting equation (2) into equation (5), σ_0 can be expressed as

$$\sigma_0 = \frac{PL\beta}{4t_p\omega\left[X_0 + \dfrac{\beta}{3t_pX_0}(X_0^3 + (h - X_0)^3\right]} \qquad (6)$$

Stress intensity factor, K_{IA}

Whereas the boundaries of both sides of the crack have tips with zero displacement, the problem can be considered essentially a centre-crack problem as mentioned previously and only a tip at the concrete region is of interest. Therefore, the effective crack length a for the centre-crack problem is equal to $a_e/2$ and the origin (0, 0) is shifted to the centre of the crack. The direction of the x-axis is also reversed. The crack tips are now located at the coordinated $x = \pm a$. For the strengthened cracked beam, the stress function of the beam along the crack surface can be treated as the same stress function obtained from equation (2) but only the region of crack is of interest. Then, the stress function along the crack surface is calculated by

$$\sigma_c(x) = \sigma_0\left(1 - \frac{x + a}{X_0}\right) \quad -a \leq x \leq a \qquad (7)$$

For the finite plate under a point loading condition as illustrated in Fig. 6 the stress intensity factor K can be given by [17]

$$\begin{bmatrix} K_I \\ K_{II} \\ K_{III} \end{bmatrix}_s = \frac{1}{\sqrt{2b}} \begin{bmatrix} P \\ Q \\ T \end{bmatrix} \begin{vmatrix} F\left(\frac{a}{b}, \frac{c}{a}\right) & & \\ & F\left(\frac{a}{b}, \frac{c}{a}\right) & \\ & & F_{III}\left(\frac{a}{b}, \frac{c}{a}\right) \end{vmatrix}_s \qquad (8)$$

in which

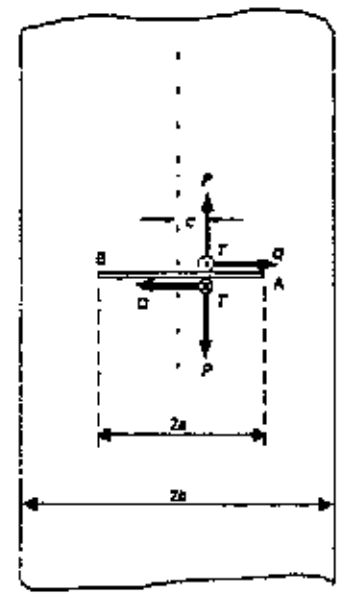

Fig. 6. Schematic diagram of the finite plate geometry with a concentrated point load

$$\left[F\left(\frac{a}{b}, \frac{c}{a}\right)\right]_s = \sqrt{1 - \left(\frac{\pi}{\sqrt{\pi^2 - 4}} - 1\right)\left(\frac{c}{a}\right)^2} \times \left[1 - \cos\left(\frac{\pi a}{2b}\right)\right]\left[F_{III}\left(\frac{a}{b}, \frac{c}{a}\right)\right]_s \qquad (9)$$

$$\left[F_{III}\left(\frac{a}{b}, \frac{c}{a}\right)\right]_s = \sqrt{\tan\left(\frac{\pi a}{2b}\right)} \frac{1 - \left|\dfrac{\sin\left(\frac{\pi c}{2b}\right)}{\sin\left(\frac{\pi a}{2b}\right)}\right|}{\sqrt{1 - \left|\dfrac{\cos\left(\frac{\pi c}{2b}\right)}{\cos\left(\frac{\pi a}{2b}\right)}\right|^2}} \qquad (10)$$

The foregoing solution can be extensively applied to the finite body with the applied arbitrary load distribution along the crack surface by integrating the stress and geometry functions within the region of $-a \leq x \leq +a$. The stress intensity factor K_{IA} of the beam thus becomes

$$K_{IA} = \frac{1}{\sqrt{2b}} \int_{-a}^{a} \sigma_c(x)\left[F\left(\frac{a}{b}, \frac{x}{a}\right)\right] dx \qquad (11)$$

where $F(a/b, x/a)$ is given by equation (9).

Closing force F_p of the reinforced plate

The final step is to estimate the closing force F_p of the reinforced plate at the crack-mouth region. Consider the model mentioned previously in Fig. 5, from which it is obtained that

$$K_{IA} = K_M - K_F \tag{12}$$

where K_M is the stress intensity factor for the rectangular beam with the edge-crack at the mid-beam region when it is subjected to three-point bending load. It can be evaluated by using the well-known closed-form solution given by

$$K_M = \frac{3PL}{2bw^2}\sqrt{\omega} f_m(\alpha) \tag{13}$$

where $f_m(\alpha)$ is the shape function for the beam with notch formation under three-point bending and α is the notch-to-depth ratio a/h. K_F is given by [18]

$$K_F = \frac{2F_p}{w\sqrt{\pi a_c}} f_F(\alpha) \tag{14}$$

where

$$f_F(\alpha) = \frac{0{\cdot}46 + 3{\cdot}06\alpha + 0{\cdot}84(1-\alpha)^5 + 0{\cdot}66\alpha^2(1-\alpha)^2}{(1-\alpha)^{3/2}} \tag{15}$$

From equations (11–14), the closing force F_p induced by the centre-point load P can be calculated by

$$F_p = \frac{w\sqrt{\pi a_c}}{2 f_F(\alpha)}(K_M - K_{IA}) \tag{16}$$

Result verification

The result obtained from the proposed method was verified by comparing it with the numerical analysis solution using the finite-element method (FEM). An MSC/NASTRAN FEM package was used for investigating the stress concentration at the crack-tip and the tensile stress in the reinforced plate. The area close to the crack-tip and at the mid-beam section of the reinforced plate were meshed into very fine element size (QUAD4 element with 0·0003125 m each side) in order to obtain more accurate results. A schematic illustration of the model is given in Fig. 7. Since the strengthened beam is symmetrical to its central axis, only half of the beam was modelled. The load P is applied vertically on the top and aligned at the centre of the beam to simulate the real three-point bending test. Boundary constraints were applied at the nodes along the centreline of the beam so that only vertical movement was permitted. Vertical movement was not permitted at the bottom supporting point (S). Linear elastic properties were assumed for both concrete and reinforced plate. The thickness and modulus of the reinforced plate, ranging from 1 to 2·5 mm and 50 to 200 GPa respectively, were used to compare the results obtained from the proposed method. All details of the simulated model are shown in Table 1.

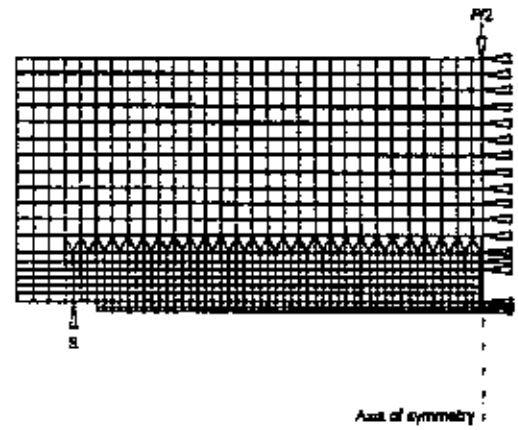

Fig. 7. FEM model for estimating the parameters K_I and F_p

The FEM model has been validated by comparing it with the experimental data for the concrete specimen bonded to a glass fibre composite plate. The plate normal strain was measured directly during the test by an externally bonded strain gauge. The results are plotted in Fig. 8. It is shown that the strains measured from the experiment agree well with the FEM solution. Therefore, it is concluded that the FEM result can be used as real experimental data for predicting the stress distribution of the strengthened beam with different bonding plate materials.

The stress intensity factor of K_I was estimated from the displacements of two nodes closest to the crack-tip. Assuming that the beam was subjected to a load at the plane strain condition, the following empirical equation was used [19]

$$\begin{pmatrix} u \\ v \end{pmatrix} = \frac{K_I}{\mu\left(\frac{1}{1-\upsilon}\right)}\sqrt{\frac{r}{2\pi}} \times \begin{bmatrix} \cos\left(\frac{\theta}{2}\right)\left[\left(\frac{1-2\upsilon}{1-\upsilon}\right) + \left(\frac{1}{1-\upsilon}\right)\sin^2\left(\frac{\theta}{2}\right)\right] \\ \sin\left(\frac{\theta}{2}\right)\left[2 - \left(\frac{1}{1-\upsilon}\right)\cos^2\left(\frac{\theta}{2}\right)\right] \end{bmatrix} \tag{17}$$

The results obtained from the FEM and proposed method are plotted in Figs. 9 and 10. Accordingly, it is

Table 1. The details of the beam model for analytical and numerical analyses

Sample	P: kN	E_c: GPa	E_p: GPa	t_p: mm	h: m	L: m	d: m	α
1	0–20	27·8	50–200	1·0–2·5	0·15	0·2175	0·0125	0·2

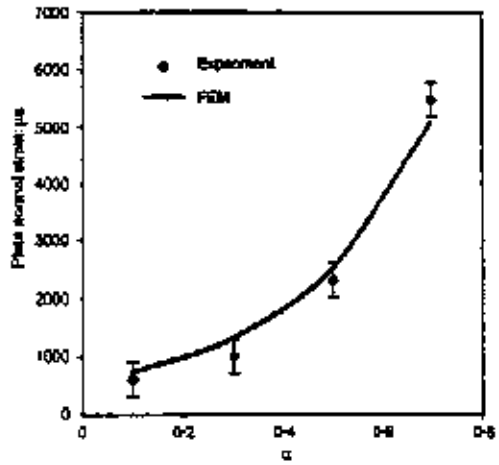

Fig. 8. The comparison of plate normal strain measured from the experiment and the FEM solution

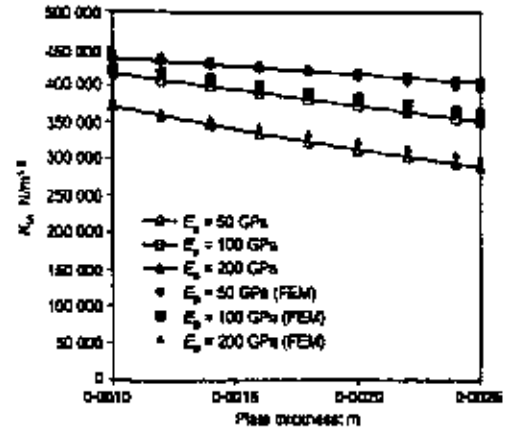

Fig. 10. The stress intensity factor (K_{IA}) of the strengthened beam plotted against different plate thicknesses used for the strengthened beam model

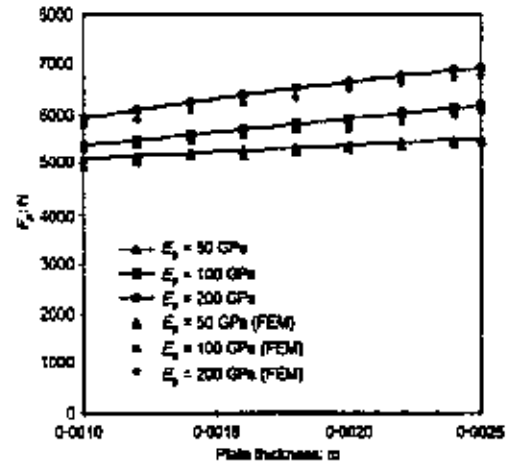

Fig. 9. The normal force (F_p) of the reinforced plate plotted against different plate thicknesses used for the strengthened beam model

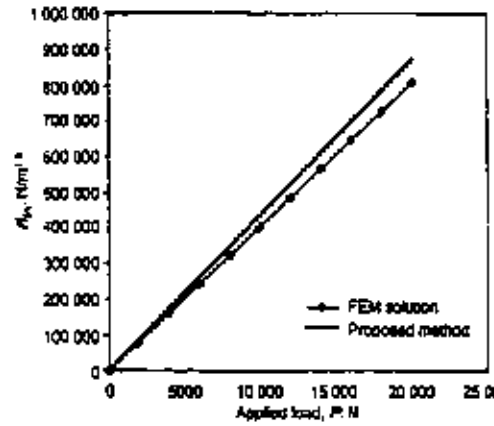

Fig. 11. Load–plate normal force (F_p) curves for the thin and thick reinforced plates

found that the values of K_{IA} and F_p obtained from the proposed solution compare well with FEM for the model with $\alpha = 0{\cdot}2$. The relative error is less than 4%. The tensile force of the reinforced plate increases with increasing thickness. The corresponding stress intensity factor, K_{IA}, decreases when the thickness of the plate is increased. This implies that using the thick reinforced material would reduce the chance of failure by cracking in the concrete material. A high modulus material used as the reinforced plate would reduce the value of K_I, while the maximum normal stress at the plate is increased. Figures 11 and 12 show the effect of the applied load, P, to the values of K_{IA} and F_p. Both show good agreement with the FEM results.

The present proposed method provides a simple but accurate tool for estimating the values of K_{IA} and F_p for the strengthend beam with $\beta = 7{\cdot}2$ when the a/h ratio is less than 0·45. The effects are clearly demonstrated in Fig. 13. The results show that the errors are within 6% compared with the FEM solution. According to the results shown in Fig. 13, it is also demonstrated that the maximum K_{IA} is reached at $\alpha \approx 0{\cdot}2$. Beyond this limit, K_{IA} decreases with increasing crack length. The failure mechanism of the structure is dominated by the mechanical properties and geometric factors of the external bonded reinforcement.

The stress intensity factor, K_I, of the strengthened

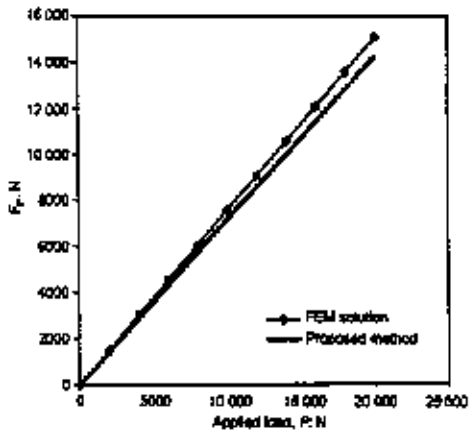

Fig. 12. Load–stress intensity factor ($K_{I,A}$) curves for the thin and thick reinforced plates

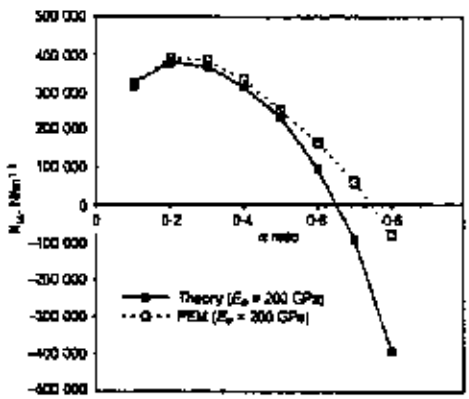

Fig. 13. Plot of $K_{I,A}$ against α for E_p = 200 GPa

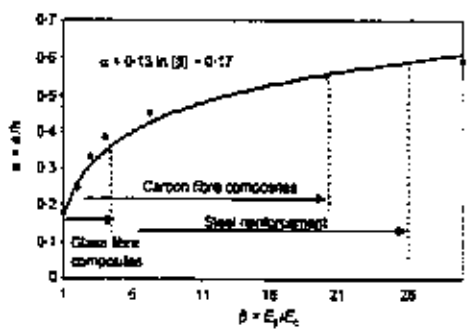

Fig. 14. Plots of stress intensity factor ($K_{I,A}$) against notch–depth (a) ratios of different modular ratios (β) between the reinforced plate and concrete beam

Table 2. Details of the beam model for evaluating K_I with different α ratios

Curve	Modulus of plate, E_p: GPa		Modulus of concrete, E_c: GPa		β
1	Glass fibre composites	30	Medium strength	30	1
2	Graphite composites	120	Medium strength	30	4
3	Steel plate	200	Medium strength	30	7·2
4	Steel plate	200	Low strength	10	20
5	High-strength material	300	Low strength	10	30

beam against the notch–depth ratio α for different modulus ratios of β is plotted in Fig. 14. The details of the beam model are listed in Table 2. Figure 14 clearly shows that the difference between the theoretical prediction and the numerical analysis increases with increasing the ratio of β and increasing the ratio of α. This may be due to the following factors.

(a) In general, the tensile modulus of the reinforced plate is larger than that of the beam to be strengthened, that is, $\beta \geq 1$. For the reinforced plate with high tensile modulus, it is strong enough to constrain to crack-mouth (crack-tip at the interface of the bond between the concrete and plate) opening and maintain the assumption of inner crack characteristics. However, a low tensile modulus plate cannot give the same characteristics and therefore a high K_I value results from the FEM solution.

(b) For further increasing the ratio of α, the difference between the analytical and FEM results at the decreasing branch is increased because the neutral axis (X_0) determined by the structure without cracking is normally shorter than that from the cracked structure. Therefore, the internal compressive stress at the crack-tip appears earlier from the theoretical solution than that from the FEM results.

The validity of the present proposed method is plotted in Fig. 14. All data points are extracted from the calculated results for different ratios of E_p/E_c on condition that the error margin between the theoretical prediction and the FEM result at each data point is ≈6%. The smooth curve is plotted after fitting all data points. Figure 15 demonstrates that the current proposed method is able to accurately evaluate K_I for values of α up to 0·5 when the ratio of E_p/E_c is larger than 13. However, for a reinforcement with low tensile modulus, such as balanced-type glass fibre composites ($E_p \leq 20$ GPa), the proposed method is also available for values of α up to 0·2. The limitation of the current analytical method for evaluating K_I and F_p is shown as follows

$$\alpha \leq 0{\cdot}13 \ln\left(\frac{E_p}{E_c}\right) - 0{\cdot}17 \qquad (18)$$

Equation (18) shows that the accuracy of the current analytical method increases with increasing the plate

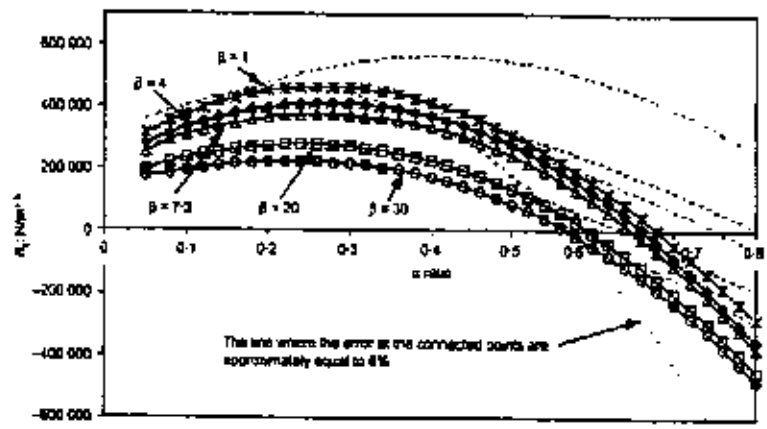

Fig. 15. Validity of the present proposed method

modulus. Therefore, for a large β ratio, the proposed equation is not valid for estimating the value of K_I in a strengthened concrete beam. However, the proposed method provides good predictions of K_I and F_p for small cracked structures in an engineering application. A deeply cracked beam would normally not be used for a realistic study of concrete structures.

Conclusions

The conclusions of this paper can be summarized as follows.

(*a*) This paper proposes a superposition method that is simple and effective for evaluating the stress intensity factor K_I and maximum tensile stress σ_0 in a concrete beam and externally bonded reinforcement respectively, when the conditions of equation (18) are satisfied.

(*b*) The use of high modulus and thick materials as the reinforced plate for the strengthened cracked beam reduces the value of K_I. However, the value of σ_0 increases as the modulus and thickness of the plate increase.

(*c*) The failure mode of the strengthened beam is highly dependent on the modulus ratio of the concrete and reinforced materials, thickness of the reinforced plate and the crack-length of the structure.

Acknowledgements

This project was supported by a grant from the Research Grant Council of Hong Kong (grant number PolyU5160/99E).

References

1. SAADATMANESH H. and EHSANI M. R. Fibre composite plates can strengthen beam. *Journal of the American Concrete Institute*, 1990, 12, No. 3, 65–71.
2. RITCHIE P. A., THOMAS D. A., LU L. W. and CONNELLY G. M. External reinforced concrete beam using fiberglass reinforced plastic. *ACI Structural Journal*, 1991, 88, No. 4, 490–500.
3. ETEBAR K. Integrity of repaired concrete under repeated loading condition. *Proceedings of Concrete Repair, Rehabilitation and Protection*, Scotland, UK, 1996, pp. 27–28.
4. QUALLAL O., NOLLET M. J. and PERRATON D. Shear strengthening of RC beams by externally bonded side CFRP strips. *Journal of Composites for Construction*, 1998, 2, No. 2, 111–114.
5. GARDEN H. N., HOLLAWAY L. C. and THORNE A. M. The strengthening and deformation behaviour of reinforced concrete beams upgraded using prestressed composite plates. *Journal of Materials and Structures*, 1998, 31, 247–258.
6. LAU K. T., ZHOU L. M., YE L. and DIAO M. Strengthening and strain sensing techniques in rectangular concrete beam using glass fibre composites and fibre bragg grating sensors. *Proceedings of the ICCM*, 1999, 12, 917.
7. LAU K. T., ZHOU L. M. and YE L. Investigation on upgrading and health monitoring of the civil concrete structures using FRP and FBG sensor. *Advanced Composites Letters*, 1999, 8, No. 6, 333–337.
8. BUYUKOZTURK O. and HEARING B. Failure behaviour of precracked concrete beams retrofitted with FRP. *Journal of Composites for Construction*, 1998, 2, No. 3, 138–144.
9. ARDUINI M. and NANNI A. Behaviour of precracked RC beams strengthened with carbon FRP sheets. *Journal of Composites for Construction*, 1997, 1, No. 2, 63–69.
10. TOUMI A., BASCOUL A. and TURATSINZE A. Crack propagation in concrete subjected to flexural cyclic loading. *Journal of Materials and Structures*, 1998, 31, 451–458.
11. XU M. and GERSTLE W. H. Energy-based cohesive crack propagation modeling. *Journal of Engineering Mechanics*, 1995, 121, No. 12, 1349–1358.
12. TAKEDEN B. Strengthening of beams by plate bonding. *Journal of Materials in Civil Engineering*, 1997, 9, No. 4, 206–212.
13. TRIANTAFILLOU T. C. Shear strengthening of reinforced concrete beams using epoxy-bonded FRP composites. *ACI Structural Journal*, 1998, 95, No. 2, 107–115.

14. CARPINTERI A. *Mechanical Damage and Crack Growth in Concrete*. Martinus Nijhoff, Doedrecht, 1986.
15. BALUCH M. H., AZAD A. K. and ASHMAWI W. Fracture mechanics application to reinforced concrete members in flexure. In *Application of Fracture Mechanics to Reinforced Concrete*. Elsevier Applied Science, London, 1992, pp. 413–436.
16. ROOKE D. P., BARATTA F. I. and CARTWRIGHT D. J. Simple methods of determining stress intensity factors. *Key to Engineering Fractures*, 1981, 14, 397–426.
17. SIH G. C. *Handbook of Stress Intensity Factors*. Institute of Fracture and Solid Mechanics, Pennsylvania, 1973.
18. TADA H., PARIS P. C. and IRWIN G. R. *The Stress Analysis of Crack Handbook*. Paris Productions Incorporated, Paris, 1985.
19. ALIABADI M. H. and ROOKE D. P. *Numerical Fracture Mechanics*. Computational Mechanics Publications, London, 1991.

Discussion contributions on this paper should reach the editor by 9 July 2001

ELSEVIER SCIENCE LTD., Jobs 4.1.01
JOURNAL COST ARTICLE No. 1496
PAGES 1-10 DISPATCH: 1 November 2000
COST 1496 A
PROD. TYPE: FROM DISK

ELSEVIER

Composite Structures 000 (2000) 000–000

COMPOSITE STRUCTURES

www.elsevier.com/locate/compstruct

The mechanical behaviour of composite-wrapped concrete cylinders subjected to uniaxial compression load

Kin-tak Lau *, Li-min Zhou

Department of Mechanical Engineering, The Hong Kong Polytechnic University, Kowloon, Hong Kong

Abstract

Recent earthquake damages have repeatedly demonstrated the vulnerabilities of older reinforced concrete columns to seismic deterioration. The use of steel and fibre-reinforced plastic (FRP) materials wraps on aged and damaged concrete structures has been recognised as an effective method to restore the load carrying capacity and extend the service life of the structures. Steel, glass and carbon fibre composites have been increasingly used to reinforce the concrete column by putting the wraps around its circumference in order to maintain its structural integrity by constraining the lateral dilation of the column when it is subjected to axial compression load. This paper presents the behaviour of the wrapped concrete cylinder with different wrapping materials and bonding dimensions using finite element (FEM) and analytical methods. The experimental results show that the deflection of the wrapped concrete cylinder in the load direction decreases with increasing the length, thickness and modulus of the wrapping sheet. However, using a longer wrapping sheet with high modulus may not benefit the structure since it creates negative hoop stress in the wrapping sheet. An analytical equation is provided to estimate the shear stress distribution of an adhesive material for different wrapping geometries. The results of the equation compare well with FEM solutions. © 2000 Elsevier Science Ltd. All rights reserved.

Keywords: Concrete; Fibre-reinforced plastic; Concrete wrapping and finite element method

1. Introduction

Deterioration in civil concrete structures is a principal challenge facing the infrastructure and bridge industries worldwide [1]. Recent earthquake damages have repeatedly demonstrated the vulnerabilities of older reinforced concrete columns to seismic deterioration [2]. Most recent research focused on the use of other high tensile strength materials to improve the overall mechanical performance of concrete structures [3–6]. Steel, glass and carbon fibre composites are frequently used to reinforce the concrete column. For the cylindrical concrete column, these materials may constrain expansion in the hoop direction by putting the wraps around its circumference in order to increase the compression load carrying capacity of the structure [7].

Steel jacketing is conventionally used for seismic retrofit and in some cases to increase load capacity of the concrete structure. It is easy to install and has been well accepted in practice for more than half a decade. In recent years, advanced composite materials, particularly glass and carbon fibre composites, have been widely used to replace steel for concrete rehabilitation. Its advantages in civil engineering applications include high strength to weight ratio and corrosion resistance. It is also easy to manufacture and transport. The use of these advanced composite materials brings saving in the overall application cost and improved durability. From the structural point of view, Seible [2] pointed out that using carbon fibre composite as wrapping jacket is just as effective as conventional steel jacketing. Glass fibre composite is more attractive in most engineering applications because of its competitive material cost. However, its tensile modulus is lower than that of the carbon fibre composites and steel. Research on the use of this material to strengthen concrete structures has grown recently. The mechanical properties of all the typical materials used for the wrapped concrete structure are listed in Table 1. Detailed explanation on the failure mechanism and the mechanical responses of the wrapped concrete structure is however limited.

Lau, Karbhari and Zhang [8–10] found that the stress–strain response of the wrapped concrete cylinder under uniaxial compression load shows a bi-linear characteristic, i.e. the initial response is almost linear up to a point, which is called 'kink point'. At this point, the wrapping sheet starts to activate the confining action.

* Corresponding author. Tel.: +852-2766-6655; fax: +852-2365-4703.
E-mail address: 97900130@polyu.edu.hk (K.-t. Lau).

0263-8223/00/$ - see front matter
PII: S0263-8223(00)00167-7

Table 1
Mechanical properties of all typical materials used for wrapped concrete structure

Property	E-glass[a]		Kevlar-49[a]	Graphite[a] (T-300)	Steel[a]	Concrete[a]
	Type A[c]	Type B[d]				
Fibre volume fraction	46	32	60–65	63	-	-
Resin types	Epoxy	Epoxy	Epoxy	Epoxy	-	-
Specify gravity	1.80	1.80	1.38	1.61	7.68	2.4
Tensile strength, 1° (GPa)	1.1	0.18	1.31	1.725	1.24	0.004
Tensile modulus, 0° (GPa)	39	11	83	159	200	-
Compression strength, 0° (MPa)	600	0.08	286	1366	1197	49.99
	32	10.5	77	138	-	27.8
Compression modulus, 0° (GPa)	0.25	0.13	0.34	0.38	0.3	0.15–0.22
	5.4	-	~2.3 - 4.0	0.045	-	-
Longitudinal Poisson's ratio	16	-		20.2	-	-
Longitudinal coefficient of thermal expansion (10^{-6}/°C)			35			
Transverse coefficient of thermal expansion (10^{-6}/°C)						

[a] Data extracted from [1].
[b] Results obtained by the experimental investigation.
[c] Uni-directional E-glass fibre composite.
[d] Balanced type E-glass fibre composite.

The concrete began to fail beyond this point, and the curve continues almost in liner manner with a reduction of slope. After the kink point, substantial visible cracks in the concrete and debonds at the interface between composite and concrete appear [11]. Fig. 1 shows the typical stress–strain response of the glass-fibre composite wrapped concrete cylinder subjected to uniaxial compression load [6].

This paper discusses wrapped concrete structures of different wrapping materials, thicknesses and bonding lengths, using finite element and analytical methods. The concrete, which has a kink point, is assumed in current study. Deflection of the wrapped concrete cylinder in the load direction decreases as the bonding length, thickness and modulus of the wrapping sheet increases. At the same time, the kink load and the adhesive shear stress increase substantially. The hoop stress measured in the wrapping sheet for the wrapped structure must be emphasised since negative value is measured if the thickness, bonding length and modulus of the wrapping sheet are increased. This phenomenon may dis-stress the wrapped concrete structure because of the existence of high tensile stress in the concrete material. An analytical equation is established to estimate the shear stress distribution of an adhesive material for different wrapping systems. The results compare well with FEM solution.

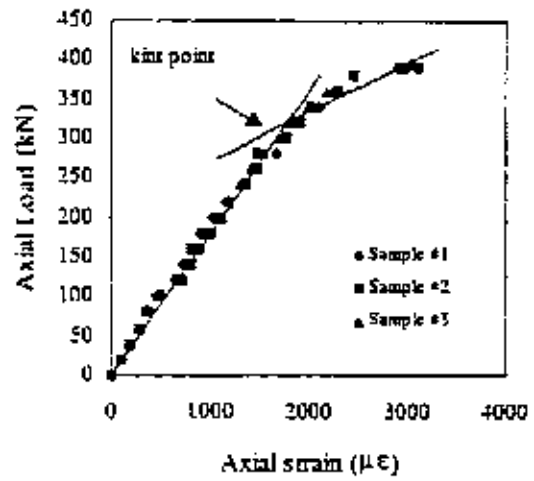

Fig. 1. Stress–strain response for E-glass fibre composites wrapped concrete cylinder subjected to uni-axial compression load.

2. Characterisation of wrapped concrete system

The load-deformation response of the typical civil concrete structure is shown in Fig. 2. The stress–strain behaves in a linear fashion up to yield stress and rapidly reaches its ultimate stress (called the compressive strength). Following this is a descending branch, which is normally called the softening region. The axial strain of the concrete cylinder continues to increase as the compressive stress decreases. At a stress level of approximately 70% of the peak-strength, lateral deformation raises rapidly and many extensive vertical cracks appear, the value of Poisson's ratio at peak being equal to 0.5 [12]. Fig. 3 shows the deformation of the plain concrete cylinder subjected to uni-axial compression load with different platen materials. It demonstrates that the radial expansion of the column is highly dependent on the modulus and Poisson's ratio of the wrapping material. Therefore, in designing the wrapping system, attention should be paid to the real practical situation, particularly at the load bearing joint and connection of the wrapped concrete structure in order to achieve the

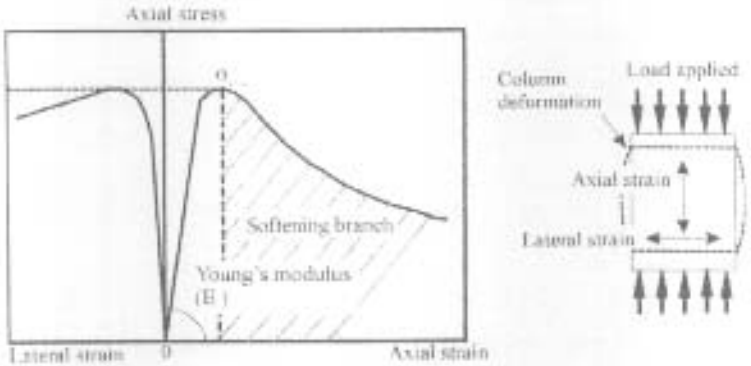

Fig. 2. Stress and strain curve for plain concrete cylinder subjected to uni-axial compression load.

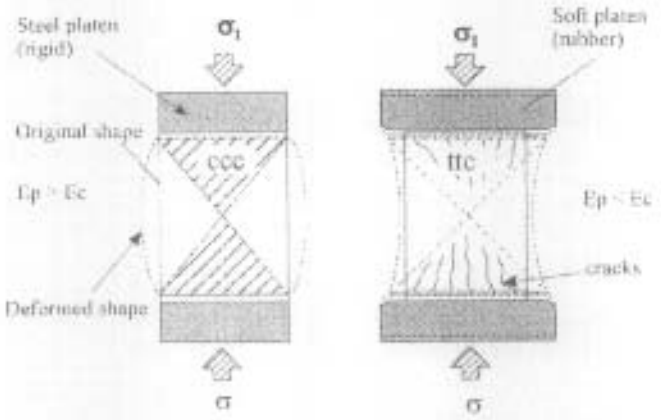

Fig. 3. Effects of deformation on concrete cylinder under compression with different platen properties: (a) hard platen and (b) soft platen.

maximum strengthening capacity of the structure. Steel and composite wrapped systems are used to constrain the expansion of the concrete structure in order to maintain its structural integrity by minimising crack formation.

Zhang [10] found experimentally that splitting failure in the hoop direction of the wrapped concrete cylinder starts at both ends of the wrapping sheet and propagates toward the middle of the column. The failure mode of the composites wrapped concrete cylinder is shown in Fig. 4. The failure mechanism of the wrapped column after testing is schematically illustrated in Fig. 5. The column was wrapped by thick E-glass woven composites and tested under steel platen, i.e. the top and bottom-centre regions inside the concrete were subjected to tri-axial compression stress so that no deformation would occur in either radial or hoop direction. According to the test result shown above, it is worth to investigate in depth the mechanical behaviours of this wrapped concrete system, particularly at the bond-end regions.

In the current study, FEM has been used to investigate the mechanical responses of the concrete cylinder wrapped by different wrapping materials, bonding

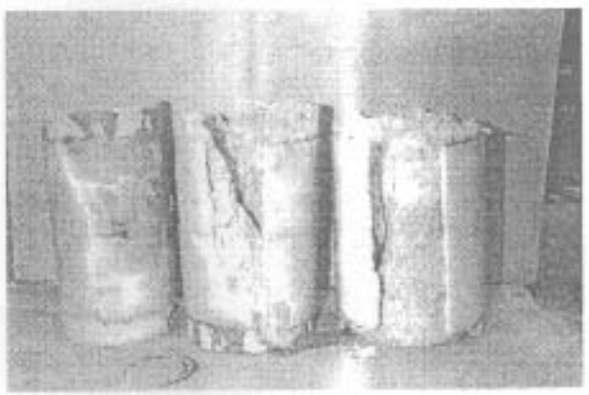

Fig. 4. Failure modes of the E-glass/epoxy laminate wrapped concrete cylinder after compression test.

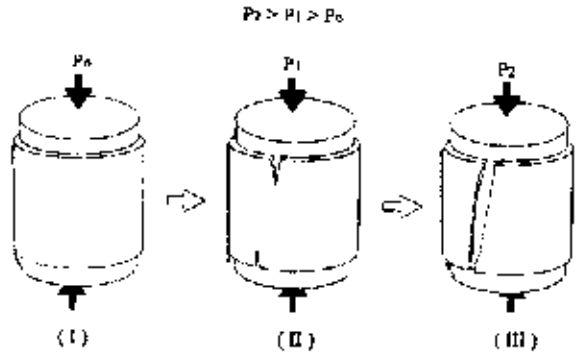

(I) Load is applied the surface of the wrapped concrete column
(II) Cracks are initially started at both ends of the reinforced plate.
(III) Cracks are propagated toward the middle of the wrapped column.

Fig. 5. Failure mechanism of wrapped concrete cylinder subjected to compression load.

lengths and thicknesses. A theoretical equation has been established to determine the shear stress distribution along the bonding line of an adhesive material. The results are then compared with the FEM solutions.

3. Fem model

The wrapped concrete cylinder is modelled as an axis-symmetrical cylinder. The size of the plain concrete cylinder is 100 mm in diameter (D) and 200 mm in height (h_0). A global co-ordinate system is used: x, y and z-axes represent the radial, hoop and axial directions, respectively, of the wrapped column. MSC/Nastran FEM Package was used to model the geometry. The element used to mesh the column was Parabolic Tria6 (Fig. 6). Three nodes are distributed along the three edges of each parabolic triangular element. The mesh consists of 50 and 200 elements in the radial and axial directions, respectively. Steel platen is modelled at the top of the wrapped concrete cylinder. Uniform pressure is applied on the top of the platen in order to simulate the real testing condition and to prevent stress concentration at the top surface of the concrete cylinder. The top surface of the wrapped concrete cylinder is constrained in the radial and hoop directions while the bottom surface is fixed. The centre line of the column is allowed to move vertically.

Different bonding lengths, wrapping materials and sheet thicknesses have been modelled individually to observe the mechanical responses under the same loading condition. The kink load is determined by applying the load to its critical axial deformation value δ^* of the plain concrete cylinder, i.e. a point where the deflection of plain concrete cylinder at yield condition.

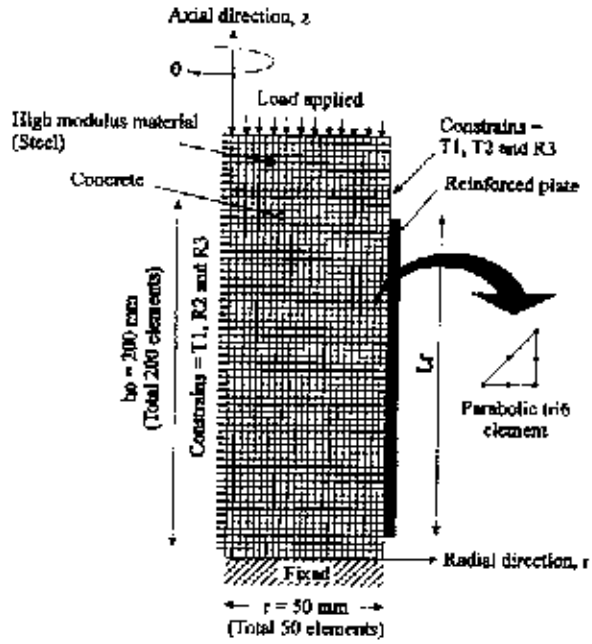

Fig. 6. Finite element model for wrapped concrete cylinder.

3.1. Axial deformation (δ)

The axial deformations of the wrapped concrete cylinder are plotted in Fig. 7. The figure shows that increasing the bonding length of the wrapping sheet greatly reduce the axial deformation of the wrapped concrete cylinder, especially when a high modulus wrapping sheet is used. A thick wrapping sheet also provides a better holding force to the concrete cylinder compared to thin wrapping sheet. In turn, the low modulus material does not influence the structure significantly regardless of the bonding length or the thickness of the material.

3.2. Kink load and wrapping efficiency

The plots of the kink load versus modulus of the wrapping material are shown in Fig. 8. The kink load increases significantly as the bonding length increases. For the $E_p = 200$ GPa with a bonding length of 200 mm, the value of the kink load measures almost twice as the same model with a bonding length of 50 mm under the same loading condition. However, for the $E_p = 11$ GPa, the kink load also increases with the bonding length but the increase is less significant. The wrapping efficiency η_w presented in percentage can be expressed as [10]

$$\eta_w = \frac{k_0 - k_\delta^*}{k_\delta^*} \times 100\%, \tag{1}$$

where k_δ^* and k_0 denote the kink load for the plain and wrapped concrete cylinders at δ^* condition, respectively.

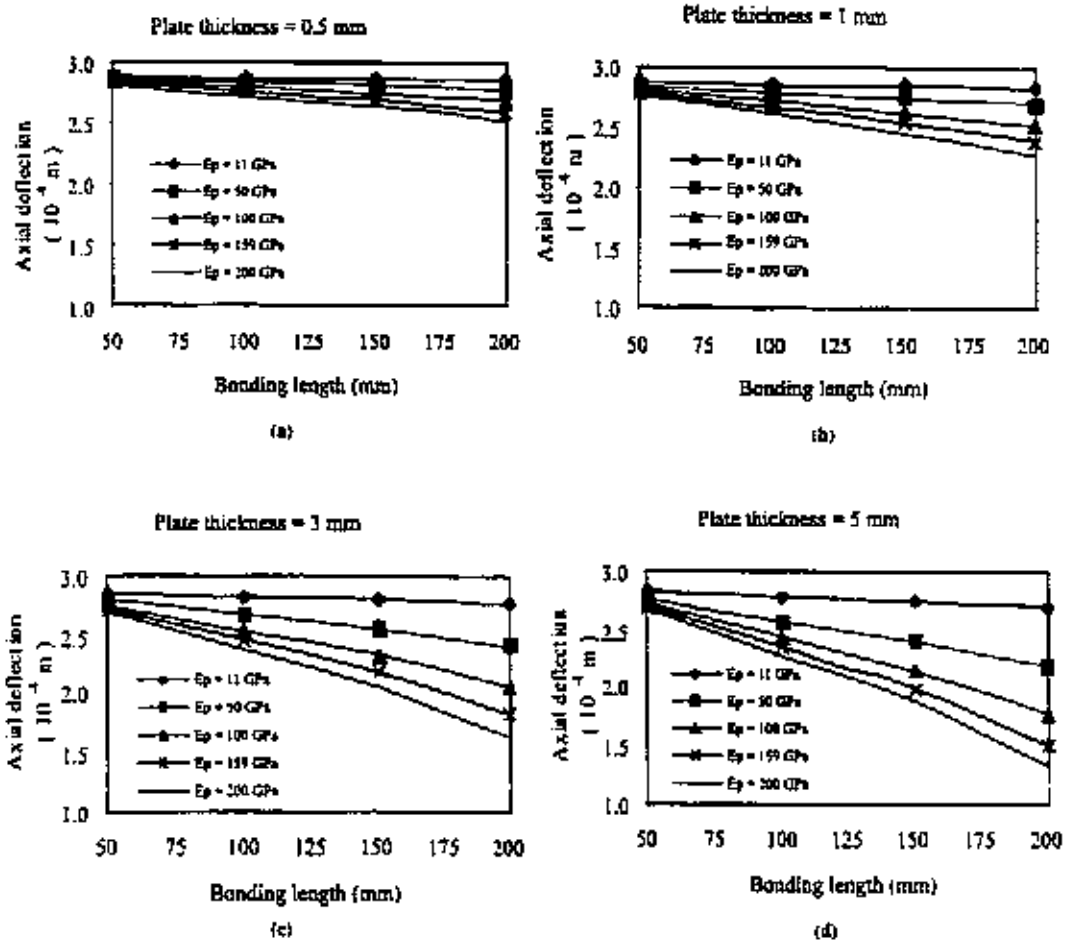

Fig. 7. Axial deflection versus bonding length of the wrapping sheet for (a) $t_p = 0.5$ mm, (b) $t_p = 1$ mm, (c) $t_p = 3$ mm and (d) $t_p = 5$ mm.

3.3. Hoop stress of the wrapping sheet

The phenomena of splitting failure at both ends in the wrapping sheet can be explained by the result obtained from the FEM. Negative hoop stress is observed for the models with long bonding length and high wrapping material modulus. However, this does not happen with short bonding length and low wrapping material modulus (and low Poisson's ratio) material. Maximum hoop stress is measured at both ends of the bond in the wrapping sheet. Fig. 9 shows the plots of the hoop stress along the bonding length from $z = 0$ with different wrapping sheet modulus. High hoop stress is found at the end of the wrapping sheet ($z/L_f = 0$) and gradually decreases towards the middle of the column ($z/L_f = 0.5$). For the wrapping sheet with $E_p = 11$ GPa and $\nu = 0.13$, the hoop stress is positive for bonding lengths from $L_f = 50$ to 150 mm. However, for the plots of $L_f = 100$ and 150 mm, negative hoop stress is measured closed to the middle of the column for the wrapping sheets with modulus $E_p \geq 50$ GPa. This implies that the wrapping sheet may not provide the constraint action in the hoop direction throughout the whole wrapping system. Part of the concrete cylinder, particularly closed to the middle of the column, sustains the tensile stress rather than constraint force from the wrapping sheet. However, the lateral strain measured experimentally of the wrapped concrete specimen shows a positive value due to the Poisson's effect

$$\varepsilon_\theta^p(z) = \frac{1}{E_p}\left[\sigma_\theta^p - \nu^p(\sigma_z^p - \sigma_r^p)\right]. \tag{2}$$

The axial compressive stress of the wrapping sheet reaches maximality at the middle of the column. The Poisson's expansion in the hoop direction due to the large compressive stress in the wrapping sheet becomes the main contribution to the hoop strain (ε_θ^p) of the whole wrapping system. Thereupon, the hoop stresses in concrete and wrapping material are dependent on the difference of Poisson's ratio and axial compressive stress in both materials. For the wrapping sheet with high modulus and Poisson's ratio, a large part of the axial

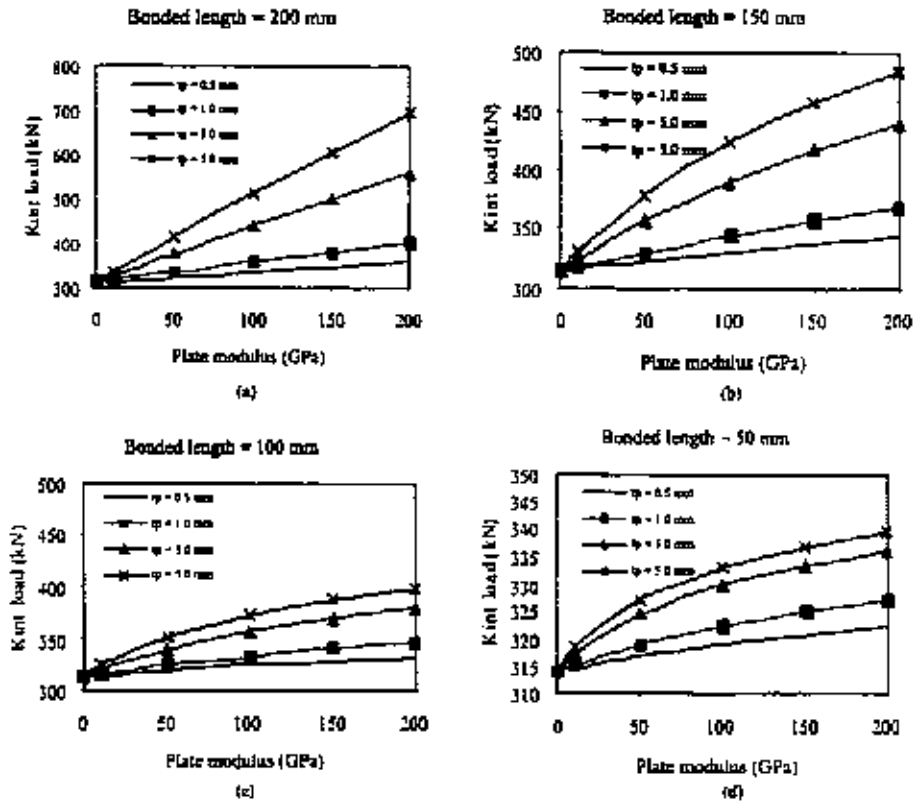

Fig. 8. Kink load versus modulus of the wrapping sheet for (a) L_f = 200 mm, (b) L_f = 150 mm, (c) L_f = 100 mm and (d) L_f = 50 mm.

load is taken by the wrapping sheet, and therefore, the Poisson's expansion in the wrapping sheet becomes greater than that in the concrete. Eventually, the negative hoop stress occurs due to the existence of these differential Poisson's and modulus effects. The schematic diagram of this Poisson's effects at the middle of the wrapped column is shown in Fig. 10.

The maximum hoop stress in the wrapping sheet and the distance of zero hoop stress from the bond end increase as the modulus of the wrapping sheet and the bonding length decreases, respectively. This infers that the effect of negative hoop stress can be minimised by reducing the bonding length to some critical limit. Fig. 9 shows that the maximum hoop stress of L_f = 150 mm with a modulus of wrapping sheet of 200 GPa is almost twice as measured for the same wrapping system with the modulus of 100 GPa.

The optimisation of this phenomenon can be achieved by plotting the diagram, which indicates the location of zero hoop stress z_0 versus different bonding length (see Fig. 11). The diagram indicates that no negative hoop stress occurs when the bonding length L_f is less than $0.35h_0$, where h_0 is the height of the column.

4. Theoretical approach (adhesive shear stress)

Current literature in the field tends to pay little attention to the effect of adhesive shear stress in the wrapped concrete system. However, the adhesive material plays a very important role in the wrapping system. It must function to fully transfer stress from the concrete cylinder to the wrapping sheet without failure. Otherwise, the effective bonding length of the wrapping sheet is reduced. However, in some particular case, a bond is not required for seismic retrofit [2].

Fig. 12 shows a theoretical model for determining the adhesive shear stress in the axial direction. The subscripts po and co denote the condition of the concrete and the wrapping sheet at the middle of the wrapped concrete cylinder, respectively. σ and L_f represent the axial stress and total wrapped length, respectively. To simplify the procedure of analysis, several assumptions are used, which include: (1) the stresses in the adhesive layer do not change with the thickness; (2) all materials behave elastically and iso-tropically under loading condition; (3) no slipping occurs at the interfaces between all bonded layers and (4) the axial strains in different

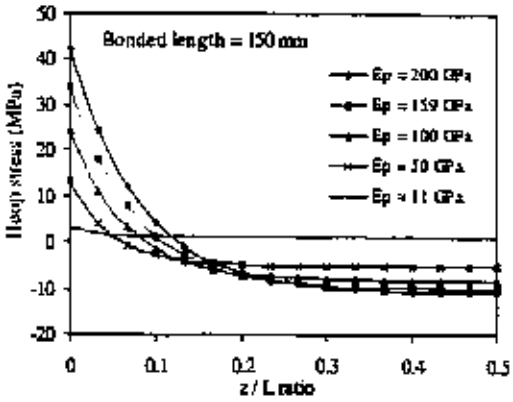

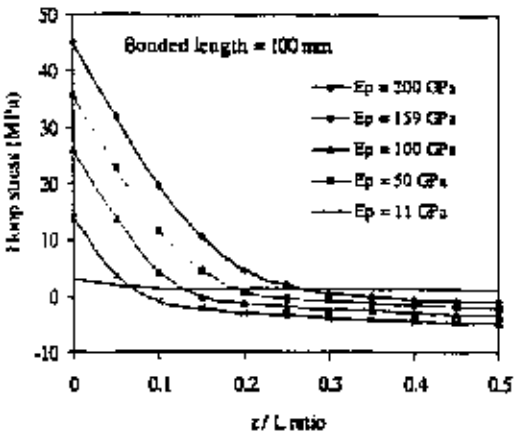

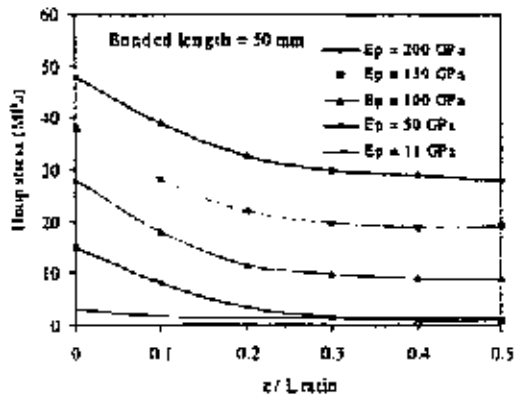

Fig. 9. Hoop stress distributions along the bonded line for tp = 1 mm with (a) L_1 = 150 mm, (b) L_2 = 100 mm and (c) L_3 = 50 mm.

materials distribute uniformly through the depth of each section.

The adhesive shear stress $\tau_a(z)$ is expressed as the product of shear modulus G_a and shear strain $\gamma_a(z)$ of the adhesive material in any particular position, z along the bonding line.

$$\tau_a(z) = G_a\gamma_a(z) \tag{3}$$

and $\gamma_a(z)$ can be expressed as

$$\gamma_a(z) = \frac{\omega_p(z) - \omega_c(z)}{t_a}, \tag{4}$$

where $\omega_p(z)$ and $\omega_c(z)$ denote the axial displacements of the wrapping sheet and the concrete, respectively. Substituting Eq. (4) into Eq. (3), the following expression is obtained after differentiating Eq. (3) and considering the strain compatibility:

$$\frac{d\tau_a(z)}{dz} = \frac{G_a}{t_a}\left(\frac{d\omega_p(z)}{dz} - \frac{d\omega_c(z)}{dz}\right) = \frac{G_a}{t_a}\left[\varepsilon_p(z) - \varepsilon_c(z)\right], \tag{5}$$

where $\varepsilon_p(z)$ and $\varepsilon_c(z)$ denote the axial strains of the wrapping sheet and concrete. The axial loads in the concrete and wrapping sheet are given by

$$\frac{dP_p(z)}{dz} = \tau_a(z)b_p, \tag{6}$$

$$\frac{dP_c(z)}{dz} = \tau_a(z)b_c, \tag{7}$$

where $b_p(z) = 2\pi r_1$ and $b_c(z) = 2\pi r_2$. Differentiating Eq. (5) again after substituting Eqs. (6) and (7) yields

$$\frac{d^2\tau_a(z)}{dz^2} = \frac{G_a}{t_a}\left(\frac{2r_1}{E_p(r_2^2 - r_1^2)} - \frac{2}{E_c r_2}\right)\tau_a(z) \tag{8}$$

The solution to Eq. (8) is given by

$$\tau_a(z) = C_1\cosh(\beta z) - C_2\sinh(\beta z), \tag{9}$$

where

$$\beta = \sqrt{\frac{2G_a}{t_a}\left(\frac{r_1}{E_p(r_2^2 - r_1^2)} - \frac{1}{E_c r_2}\right)}. \tag{10}$$

Two boundary conditions are needed to determine the constants C_1 and C_2.

$$P_p(0) = 0 \text{ and } \begin{matrix} P_p(L_1) = P_l \\ \tau_a(L_1) = 0 \end{matrix} \tag{11}$$

in which P_l is the maximum axial load of the wrapping sheet and can be evaluated by applying the strain compatibility condition at the middle of the wrapped concrete cylinder, i.e. $\varepsilon_c(L_1) = \varepsilon_p(L_1)$:

$$P_l = \frac{PA_p}{(E_c/E_p)A_c + A_p}, \tag{12}$$

where P, A_p and A_c denote the applied load on the concrete surface, cross-section area of the wrapping sheet and concrete cylinder, respectively. The constants C_1 and C_2 are obtained as

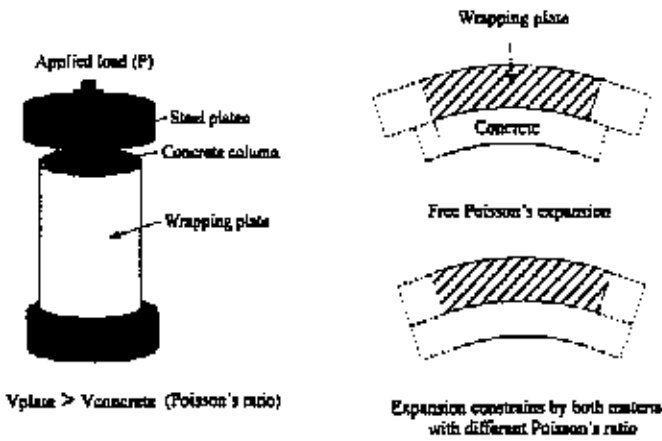

Fig. 10. Poisson's effects of the wrapped concrete cylinder.

$$C_1 = \frac{P_0\beta}{b_p(1 - e^{-\beta L_f})} \quad \text{and} \quad C_2 = C_1. \tag{13}$$

The axial stress in the wrapping sheet at $z = L_f$ and shear stress distribution in the adhesive layer along the bonding line give

$$\sigma_{pz} = \frac{P}{\alpha\eta + 1}, \tag{14}$$

$$\tau_a(z) = \frac{P_0\beta}{b_p(1 - e^{-\beta L_f})} e^{-\beta z}, \tag{15}$$

where α and η represent the modulus (E_c/E_p) and area (d_c/d_p) ratios of the concrete to wrapping sheet, respectively. In Eq. (15), it is obviously shown that the maximum shear stress of the adhesive material is reached when $z = 0$. It is then possible to write (15) as

$$\tau_{a\max} = \frac{P_0\beta}{b_p(1 - e^{-\beta L_f})}. \tag{16}$$

The results from Eqs. (14) and (16) and FEM are plotted in Figs 13 and 14. The theoretical results give good agreement with the FEM solutions. The axial stress in the wrapping sheet increases as the thickness and modulus of the wrapping sheet increase. This implies that a part of the axial load is shared by the wrapping sheet and therefore, the dilation of the concrete cylinder can be minimised. This phenomenon is true only when the wrap is covered along whole cylinder. It therefore a part of the load is directly applied to the end of wrapping sheet. In turn, for a shorter bond length of the wrap, this phenomenon is voided up to a point where the axial stress does not increase continuously with increasing the thickness and modulus. It is due to the failure of the concrete in unwrapped area.

However, for the low modulus of wrapping sheet, the effect caused by the wrapping thickness becomes less significant. The maximum adhesive shear stress $\tau_{a\max}$ increases with the modulus of the wrapping sheet, and decreases with the adhesive thickness. In general, modulus and strength are the dominating factors that are used to select the material for confining the concrete structure. However, adhesive shear stress increases with the use of thick, high modulus wrapping sheet. Once the failure of the adhesive material occurs, the effective bonded length of the wrapping sheet is reduced subsequently. Eventually, the increases of the hoop stress in the wrapping sheet and axial deformation of the wrapped concrete cylinder and the decrease of the wrapping efficiency in the wrapped concrete system are resulted.

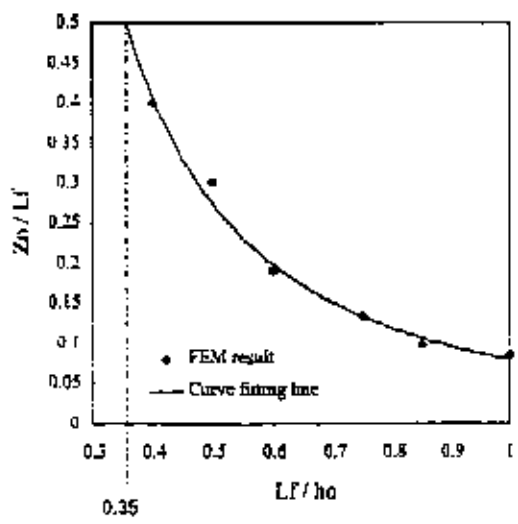

Fig. 12. Plot of the location of zero hoop stress z_o obtained from FEM (E_p = 200 GPa, t_{wp} = 3 mm and P = 40 MPa).

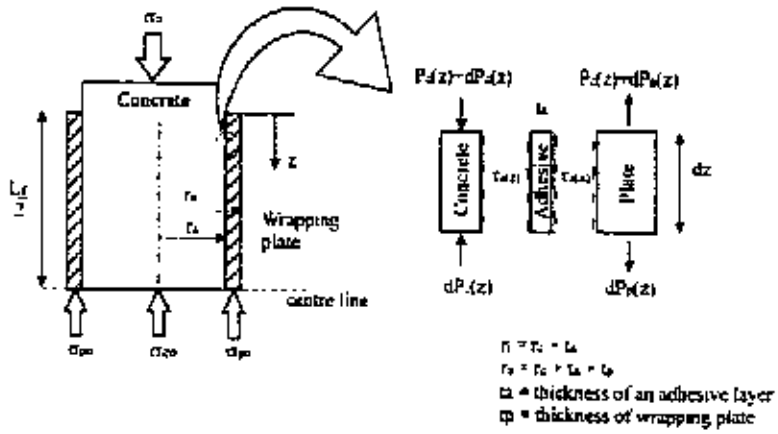

Fig. 12. Theoretical model for evaluating the shear stress distribution of the adhesive material along the bonded line

5. Conclusion

The significance in this paper is to explain the failure mechanism, which is not discussed previously in either numerical or theoretical ways, for the wrapped concrete system. Several conclusions can be drawn from the observations made in FEM analysis and through theoretical prediction:

1. The load carrying capacity of the wrapped concrete structure is governed by the mechanical properties, such as modulus and Poisson's ratio, of the wrapping sheet.
2. The deflection of the wrapped concrete cylinder in the load direction decreases as the modulus of the wrapping sheet, bonding length and thickness increase, bringing higher wrapping efficiency (η_w).
3. However, the effect of negative hoop stress may result from the use of thick and high modulus of wrapping sheet, and with long bonding length for the wrapped concrete system. The maximum hoop stress is located at both ends of the wrapping sheet. Splitting failure is observed in most existing experimental reports.
4. The optimised bond length of the wrap can be evaluated using the method shown in Fig. 11. However, too short a bonding length may increase the maximum hoop stress in the wrapping sheet.

6. Uncited reference

[13]

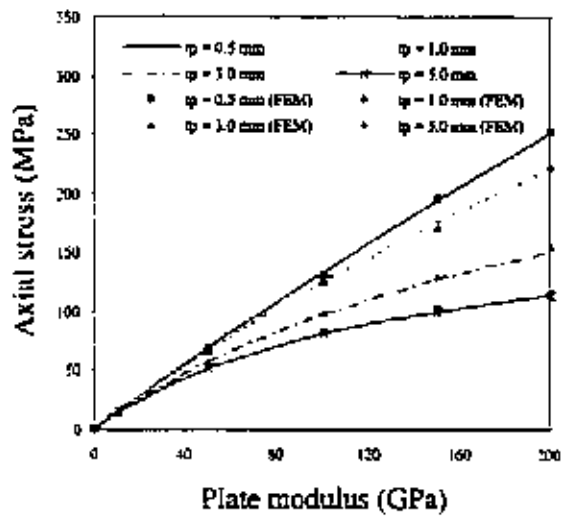

Fig. 13. The axial compressive stress in the wrapping sheet with different thickness and modulus of the wrapping sheet.

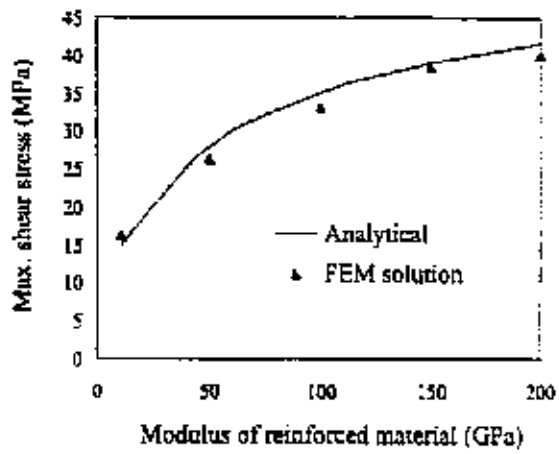

Fig. 14. Plot of the maximum shear stress of an adhesive material with different wrapping sheet properties.

Acknowledgements

This project was supported by a grant from the Research Grant Council of Hong Kong (PolyU5160/99E).

References

[1] Buyukozturk O, Hering B. Failure behaviour of pre-cracked concrete beams retrofitted with FRP. J Compos Construct 1998;2(2):138–44.

[2] Seible F, Priestly N, Hegemier GA, Innamorato D. Seismic retrofit of RC columns with continuous carbon fibre jackets. J Compos Construct 1997;2(1):52–62.

[3] Tsutanji H. Evaluation of the tensile strength of cement-based advanced composite wrapped specimens. J Compos Sci Technol59 1999:2261–8.

[4] Spoelstra MR, Monti G. FRP-confined concrete model. J Compos Construct 1999;3(3):143–50.

[5] Mirmiran A, Shahawy M. A new concrete-filled hollow FRP composite column. J Compos Part B27B 1996:263–8.

[6] Lau KT, Zhou LM, Woo CH, Chan KC, Jin W. Strengthening and monitoring concrete structures using glass fibre composites and FBG sensor. J Mater Science Res Int 1998;3(5):216–21.

[7] Toutanji H, Balaguru. Durability characteristic of concrete columns wrapped with FRP tow sheets. J Mater Civil Eng 1998;3(10):52–7.

[8] Lau KT, Zhou LM, Li Y. Investigation on upgrading and health monitoring the civil concrete structures using FRP and FBG sensor. Adv Compos Lett 1999;8(6):323–32.

[9] Karbhari VM, Guo YQ. Composite jacketed concrete under uniaxial compression-verification of simple design equation. J Mater Eng 1997;4(9):185–93.

[10] Ye L, Zhang S, Mai YW. Strengthening efficiency of E-glass fibre composite jacket of different architectures for concrete columns. J Appl Compos Mater5 1998:109–22.

[11] Christopher PR. Analysis of concrete cylinder with a composite hoop wrap infrastructure: new materials and methods of repair proceeding of the materials engineering conference 804. New York: ASCE; 1994. p. 8–21.

[12] Neville AM. Properties of concrete. 4th ed., New York: Longman; 1995.

[13] Herakovich CL. Mechanics of fibrous composites. New York: Wiley; 1998.

ELSEVIER

Sensors and Actuators 87 (2000) 19–25

SENSORS ACTUATORS A PHYSICAL

www.elsevier.nl/locate/sna

Multi-point strain measurement of composite-bonded concrete materials with a RF-band FMCW multiplexed FBG sensor array

Peter K.C. Chan [a,*], W. Jin [a], K.T. Lau [b], L.M. Zhou [b], M.S. Demokan [a]

[a] *Department of Electrical Engineering, The Hong Kong Polytechnic University, Hung Hom, Kowloon, Hong Kong, People's Republic of China*
[b] *Department of Mechanical Engineering, The Hong Kong Polytechnic University, Hung Hom, Kowloon, Hong Kong, People's Republic of China*

Accepted 8 May 2000

Abstract

We report the use of fiber Bragg grating (FBG) sensors for strain measurement in a rectangular composite-bonded concrete beam. Three FBGs are multiplexed by using a frequency modulated continuous wave (FMCW) technique in the RF-band and embedded at three different locations at the interface between the composite reinforcement and surfaces of the concrete beam specimen. Strain measurements were conducted with the concrete beam specimen subjected to a three-point bending test. The strains measured from the FBG sensors are compared with that from the external bonded strain gauges. © 2000 Elsevier Science B.V. All rights reserved.

Keywords: Fiber Bragg grating sensors; Frequency division multiplexing; Glass fiber composites; Strain measurement

1. Introduction

The use of fiber reinforced plastic (FRP) materials in concrete rehabilitation has been recognised as an innovative technology in recent years [1–3]. High strength glass fibers can be embedded into the soft matrix to form a composite with high tensile property. Bonding FRP on the tension surface of the concrete can increase the overall tensile strength of the concrete structure.

However, the mechanical properties of the host structure cannot be measured easily by use of the conventional non-destructive inspection (NDI) methods such as strain gauge and X-ray radiography due to the existence of the external bonded patches. Fig. 1 shows the mechanism of the strain transfer on the surface bonded reinforcement. The axial strain on the concrete surface (point A) after strengthening is normally greater than that measured on the surface of the reinforcement (point B) due to the bending effect caused by the shear of an adhesive material. This means that the surface mounted strain measuring method cannot be effectively used to measure the mechanical properties (e.g., internal strain) of the strengthened structures, in particular if the thick reinforcement is used. Besides, the environmental attacks on the surface of reinforcement may also influence the measurement accuracy of the external measuring devices.

Fiber Bragg grating (FBG) sensor has been identified as a very important technology for structure health monitoring [4–6]. FBG sensors offer a number of advantages over conventional electrical strain-sensing techniques. These include the resistant to corrosion and fatigue, small in size and light in weight. The FBG sensors can be embedded inside concrete, glassfiber composites and/or at the interface of a composite reinforced concrete without degradation or significant compromise of the strength of the host materials.

To reduce the cost per sensing point and to increase the competitiveness of FBG sensors against conventional electrical sensors, FBG sensors are often wavelength division multiplexed (WDM) and/or Time division multiplexed (TDM) [6,7]. In WDM systems, FBGs of different Bragg wavelengths have to be used and the sensor number that can be multiplexed is determined by the ratio of the source spectral width over the spacing between the Bragg wavelengths of the FBGs [6]. For strain measurement in concrete structure, maximum strain can be 5000 με or larger, thus the sensor number that can be multiplexed by use of WDM is limited to a few. FBGs of the same Bragg wavelength may be used in a TDM system, however, the signal-to-noise ratio from individual sensor at the photode-

* Corresponding author. Tel.: +852 2766 6190; fax: +852-2330-1544.
E-mail address: eekechan@ee.polyu.edu.hk (P.K.C. Chan).

PII: S0924-4247(00)00462-3

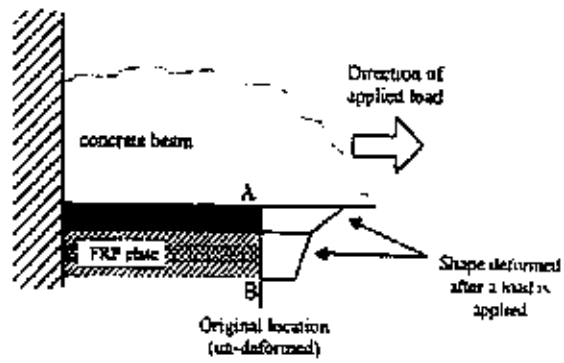

Fig. 1. Stress transfer from the host material to external reinforced patch.

tector is usually low, if a number of sensors are going to be multiplexed [7]. Furthermore, TDM system requires high extinction ratio electronic switch in order to reduce the crosstalk between sensors.

In this paper, we report the use of a RF-band FMCW approach for multiplexing of FBG sensors. The FMCW technique compared with TDM provides a larger average power level at the photo-detector because of the relatively high duty cycle involved and does not have a very strict requirement on the extinction ratio on the optical intensity modulator. We also report the results of an experimental investigation on using the multiplexed FBG sensor array for the monitoring of the strain development at the composite/concrete interface for a rectangular notched concrete beam sample strengthened by bonding the glass fiber reinforced plastic (GFRP) composites on the tension and shear surfaces when the sample is subjected to a three point bending test.

2. RF-band FMCW multiplexed of FBG sensor array

2.1. Principle of operation

The principle of the RF-band FMCW technique for multiplexing FBG sensors may be explained by use of Fig. 2, where a three-sensor array in serial-parallel topology was used. Light from a broadband source is modulated in

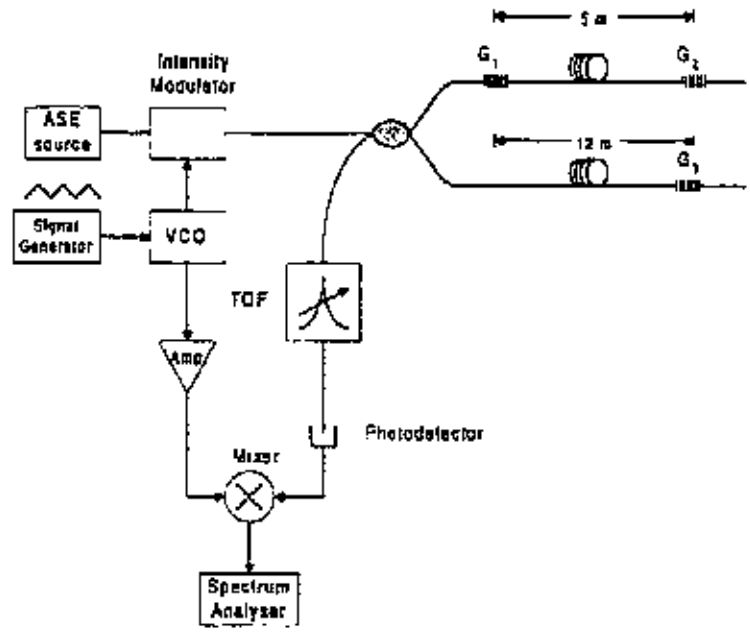

Fig. 2. Schematic diagram of a FMCW multiplexing FBG sensor array.

intensity with triangular swept RF-frequency carrier generated from a voltage-controlled oscillator (VCO) and launched into the FBG sensor array. The reflected signals from FBGs are guided back to a tunable optical filter (TOF) and then to a photodetector, and mixed with a reference signal from the VCO subsequently. The system output will consist of a number of beat notes with the beat frequencies determined by the time delay differences (τ_i, $i = 1, 2, \ldots, N$, corresponding to N sensors) between the reflected signals from individual FBG sensors and the reference signal. The magnitudes of the beat signals are proportional to the convolution of the individual grating reflection spectrum and the transmission spectrum of the TOF. By assigning different time-delay-difference to different sensors, the beat signals corresponding to different FBG sensors may be separated in frequency domain. The Bragg wavelength of a particular FBG can be interrogated by scanning the TOF and record the control voltage of the TOF that corresponding to the peak (or zero-crossing point if derivative response is detected) of the corresponding beat note signal.

Assuming that the triangular frequency sweeping is of a repetition rate of f_r and a frequency excursion of Δf. The beat frequency f_{beat_i} corresponding the ith sensor (or ith beat note) may be written as [8],

$$f_{beat_i} = 2 f_r \Delta f \tau_i \tag{1}$$

where τ_i is the time delay difference of the ith sensor relative to the reference signal.

In general, each beat note has a multiple line spectrum at intervals of f_r. The position of the peak in the envelope of the line spectrum gives the beat frequency. Because of the multiple line characteristics of the beat-note spectra, the crosstalk performance of the FMCW technique was in general regarded as "not good" when it is applied to multiplex a number of sensors. However, we found that for small time delay difference (compared with the period to frequency-sweeping modulation or $1/f_r$) between the signal and the reference wave, the beat note spectrum can be essentially a single line, if the following condition is satisfied [8],

$$f_{beat_i} = (2 f_r \Delta f)\tau_i = m f_r \tag{2}$$

where m is an integer.

This property of the FMCW was also reported in an early paper on multiplexing of vibrating fiber optic sensors [9]. This suggests that a low-crosstalk multiple FBG sensor array may be realized if the network is designed in a suitable way that different FBG signals coincide with different harmonics of the frequency-sweeping. We have demonstrated a sideline suppression ratio of -40 dB [10], implying a FBG network with sensor to sensor crosstalk of -40 dB may be realized. When combined with the WDM technique, the FMCW technique should be capable of potentially multiplexing a larger number of FBG sensors.

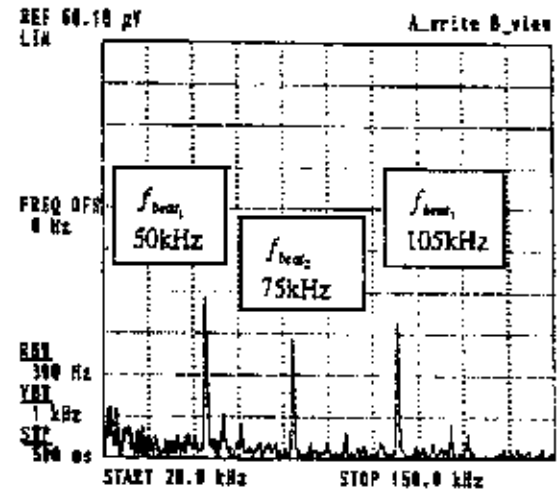

Fig. 3. Beat-note spectrum of the three sensor array

2.2. Optical measurement setup

A three-sensor system as shown in Fig. 2 has been constructed for the measurement of internal strain of a composite/concrete specimen (see Section 4 for details). The system used an Er-doped fiber ASE broadband source with peak wavelength of about 1558 nm. Light intensity modulation was achieved by use of a VCO driven integrated optic modulator by a triangular frequency-swept carrier from 58 to 99 MHz with 5 kHz repetition rate. The TOF used is a tunable filter (JDS TB2500) with linewidth 0.37 nm and a voltage-tuning coefficient of 2.95 nm/V. All FBGs were manufactured in our laboratory by using the phase mask technique. The Bragg wavelength of the FBG G_1, G_2 and G_3 are 1556.30, 1554.24 and 1554.24 nm, respectively. The reflectivity of the FBGs are approximately 100%. The Bragg wavelength of G_1 was chosen to be significantly larger than that of G_2 to ensure no crosstalk due to "spectral-shadowing" effect would occur during the experiment [11]. The spatial separations between G_1 and G_2 and between G_1 and G_3 are about 5 and 12 m, respectively. The electrical signal after photodetector is mixed with the reference directly from the VCO. The beat signals generated from the mixing were observed from an electrical spectrum analyzer. Fig. 3 shows a typical display of the spectrum analyzer. There are three major peaks in the spectrum displays at 50 kHz, 75 and 105 kHz, corresponding to sensor G_1, G_2 and G_3, respectively. No effort has been made to match the delay exactly to the harmonics of the repetition frequency.

3. Specimen preparation

A standard laboratory size rectangular concrete specimen for three-point bending test was prepared according to

Table 1
The mechanical properties of the concrete, adhesive and glass fiber composites

Mechanical properties	Material type		
	Concrete (cement/fine aggregate/coarse aggregate)	Adhesive (Epoxy) MY 750/HY 951	Glass fiber composites
Mixture ratio	1:1.5:3	5:1	N/A
Modulus of elasticity (GPa)	27.8	3.3	13.33
Compressive strength (MPa)	49.99	115 (yield)	90
Tensile strength (MPa)	N/A	90	280
Poisson's ratio	0.2 (average)	0.46	0.176
Shear modulus (MPa)	N/A	1.13	N/A

the ASTM C293-94. The specimen was 45 cm in length, 15 cm in width and 15 cm in height. The concrete was mixed at the ratio 1:1.5:3 to cement: fine aggregate: coarse aggregate and being cured for 28 days at room temperature before the tests were performed. Notch was made in the specimen with notch-to-width ratio of 0.2 and then filled with Epoxy based resin to avoid any environmental attacks on the notch-surfaces. To ensure a perfect bond between the concrete and composites, pre-treatment of the concrete surface was performed by sanding and vacuuming the surface of bond. Cleaning solvent (acetone) was then used to remove the degreasing agent and other chemical substances that were attached on the bonding surfaces. The mechanical properties of the concrete, adhesive and glass fiber composites used in the experiment are listed in Table 1. Three FBG sensors were then attached to the surface of the concrete specimen by epoxy resin at three strategic points near the notch (i.e., position 1, 2 and 3 see Fig. 4a).

In general, when a plain rectangular concrete beam without notch subjected to three-point loading, the high tensile stress is located at the bottom surface near the long horizontal edge region (position 1). The stress at the middle centre region would become lesser significant (position 2). However, if notch/crack exist, the stress would concentrate on the notch edge region, this phenomenon may cause the eventual failure of the structure due to the crack initiation at the notch region (position 3). Thus, the FBG sensors located at these positions may be used to the monitor mechanical behaviour of the specimen after strengthening by glass fiber composites.

Glass fiber mats with Epoxy based (Araldite MY 750) resin was used to form composites to strengthen the concrete beams by bonding on the tension and the two long vertical shears surfaces. Six-layer glass fiber mats were laid-up layer by layer directly on the surfaces of the concrete beam. Resin and hardener were mixed together by hand mixer until the homogeneous mix was achieved. The mixture was then smeared over the bonding surface of the concrete specimen evenly. The pre-cut glass fiber mat was then laid on the bonding surface. The process was repeated for layers of fiber mats. The sizes of the glass fiber mats are deliberately made different in order to minimise the stress concentration located at the end of the bonding laminate. The excess resin was squeezed out by using the press aluminium roller. Once the desirable numbers of glass fiber laminates were laid-up, the specimen was then rest for 24 h for curing at room temperature. The strain

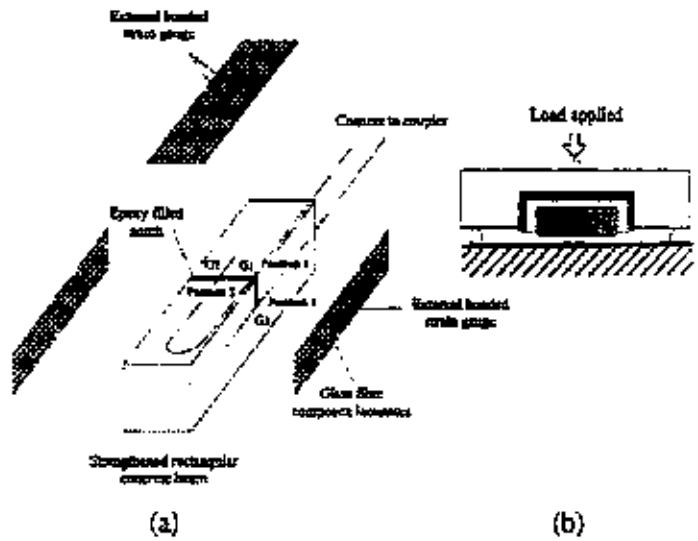

Fig. 4. Schematic diagram of the test specimen subjected to three point bending test.

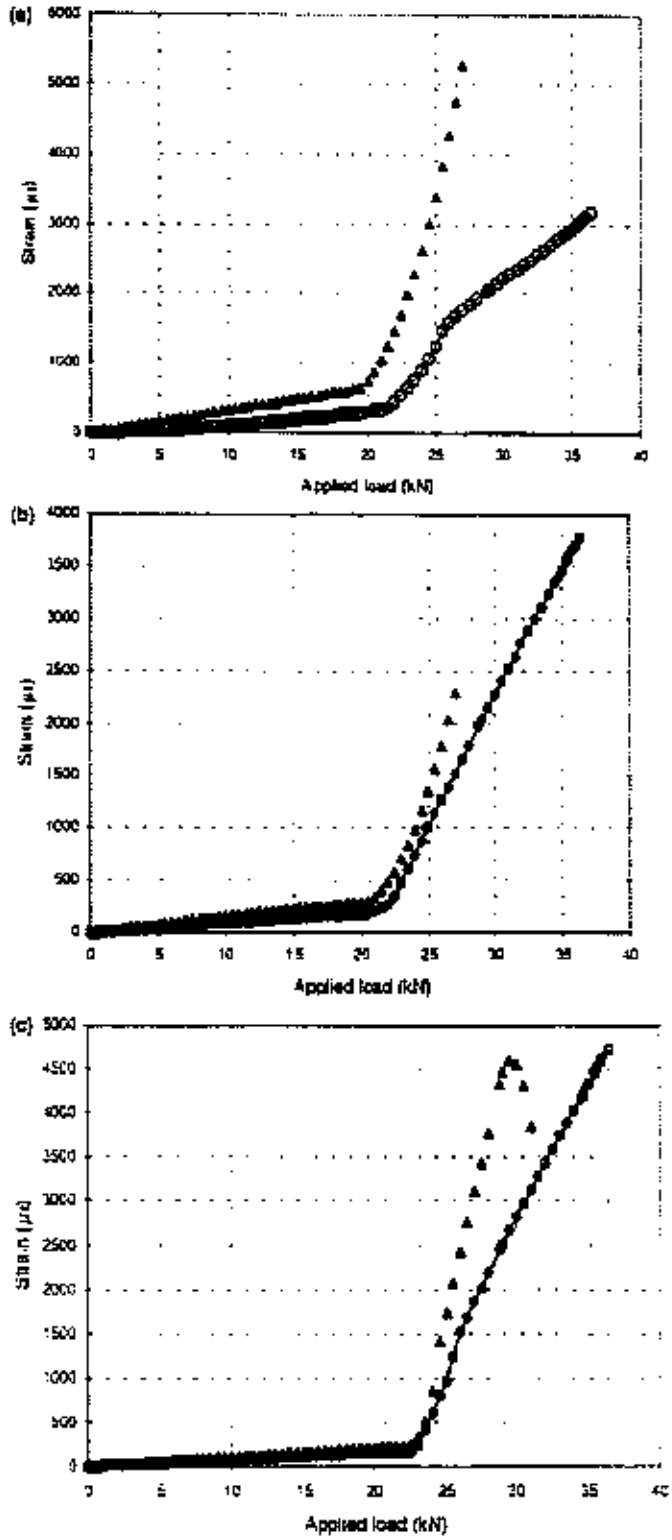

Fig. 3. Internal strain measured by FBG sensors and strain measured on the surfaces of composite by bonded strain gauges (a) strain measured at position 1, (b) strain measured at position 2, and (c) strain measured at position 3; ▲ strain from FBG sensor, ○ strain from bonded strain gauge.

gauges were then attached on the surfaces of reinforcements at the same positions where the FBG sensors embedded.

4. Measurement, result and discussion

The specimen prepared in Section 3 was subjected to a three-point bending test, where a load was applied to the specimen along a direction as shown in Fig. 4b. The strain condition at the concrete composite interface was monitored by use of the three FBG sensors where the TOF driven voltage that correspond to the maxima of the beat signals at 80, 75 and 105 kHz were used as the output of sensors G_1, G_2 and G_3. The strain-wavelength characteristics of the three FBG sensors are approximately the same with applied strain of 1 με corresponding to a shifted of the Bragg wavelength of 1.2 pm. The sensors also have a temperature dependence of about 10 pm/°C. However, the temperature effect can be neglected in this experiment because the temperature was a constant during the short measurement period. Previous investigations [12] show that FBG sensors are reliable alternative of electrical strain gauges when they are used for strain measurement in concrete structures, but FBG sensors can be embedded inside the materials that is difficult for electrical strain gauges. The surface strain condition of the reinforced specimen was measured by the surface mounted strain gauges. All strain and load values were recorded through a computer automatically.

Fig. 5a shows the results obtained from the embedded FBG sensor G_1 and the external-bonded electrical strain gauge at the bottom edge region (position 1) of the specimen. Linear load-strain characteristic was obtained for G_1 when the load was below 20 kN, which agrees with the result from the electrical strain gauge. When the applied load was further increased, debonding at the interface between the GFRP reinforcement and the concrete surface was observed. This debond might cause the strain increasing at the interface between the reinforcement and concrete surface. This effect can be revealed significantly by use of embedded FBG sensor rather than external-bonded strain gauge. When the applied was at about 25 kN, the growth rate of the strain obtained from strain gauge was slow down. It is suspected that the interlaminate shear deformation occurred in between the reinforcement layers of glass fiber composites. When the applied load was increased up to 27 kN, G_1 was broken and at the same time the strain information from G_2 was also missed, as they were serial-connected as shown in Fig. 2. Fig. 5b shows the strain characteristics of the specimen at the bottom centre region (position 2). Linear load-strain characteristic was obtained for G_2 when the load was below 20 kN, then debonding phenomenon occurred subsequently. In Fig. 5c, the strain measured from the FBG sensor G_3 and the strain gauge was very closed to each other when the applied load was below 23 kN. However, while the load was further increasing, the strain from G_3 increased rapidly, owing to debonding at the interface between the glass fiber composites and the concrete surface. When the load was approaching 30 kN, visible debonding appeared. A shadow region (Fig. 6) was actually observed on the surface where G_1 and G_2 were embedded and expanded when the applied load was increased. The strain obtained from G_1 decreased when the applied load was greater than 30 kN. It is suspected that the microcracking occurred at the concrete surface. The concrete surface was detached from the glass fiber composites, then the concrete surface compressed suddenly and the FBG sensor G3 was broken. By comparing Fig. 5a with c, the stress measured at the bottom surface is always higher than that measured at the notch-tip, which is the

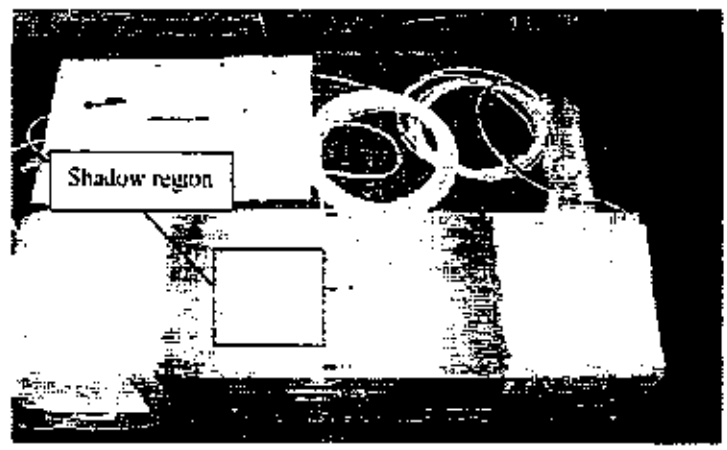

Fig. 6. The photographs of the test specimen

predicted high stress concentration region. The stress at the notch-tip region increased rapidly when the applied load exceeded 23 kN. Clearly showing that stress concentration exists when the applied load was beyond a critical value, which depends on both mechanical and geometrical properties of the reinforcement.

5. Conclusion

In conclusion, we have demonstrated the use of a FMCW multiplexed FBG sensor array for internal strain monitoring in a concrete structure specimen strengthened with glass fiber composites. The FBG sensors were used to measure the strains between the composite/concrete surfaces, and revealed that significant difference between the strain at the composite/concrete interface and that measured at the strengthen surfaces by use of external bonded electrical gauges. It proves the unique feature of FBG sensor for real internal strain monitoring. Although we demonstrated a three-sensor system in the present work, it is theoretically possible to multiplex a few tens of FBG sensors with the same nominal Bragg wavelength. This would allow a large number of points to be monitored by use of a single source/detector unit.

Acknowledgements

This work was supported by the Hong Kong Polytechnic University through No. V390 Research Grant.

References

[1] G. Spadea, F. Bencardino, R.N. Swamy, Structural behaviour of composite RC beams with externally bonded CFRP, J. Compos. Constr. 2 (1998) 132–137.

[2] K. Kabantsev, Applications of GFRP in Civil Engineering, Test. Compos. Build. Constr. (1996) 31–38.

[3] J. Larralde, Compressive strength of small concrete specimens confined with fiberglass laminates, J. Cem. Concr. Aggregates 19 (1997) 17–20.

[4] A.D. Kersey, Interrogation and multiplexing techniques for fiber grating strain sensors, Proc. SPIE 2071 (1993) 30–48.

[5] Y.J. Rao, In-fiber Bragg grating sensors, Meas. Sci. Technol. 8 (1997) 355–375.

[6] R.L. Idriss, M.B. Kodindouma, A.D. Kersey, M.A. Davis, Multiplexing Bragg grating optical fiber sensors for damage evaluation in highway bridges, Smart Mater. Struct. 7 (1998) 209–216.

[7] T.A. Berkoff, M.A. Davis, D.G. Bellemore, A.D. Kersey, Hybrid time and wavelength division multiplexing fiber Bragg grating sensor array, Proc. SPIE 2444 (1995) 288–294.

[8] P.K.C. Chan, W. Jin, I.M. Gong, M.S. Demokan, Multiplexing of fiber Bragg grating using a FMCW technique, Photon. Technol. Lett. 11 (11) (1999) 1470–1472, Nov.

[9] K.I. Mallalieu, R. Youngquist, D.E.N. Davies, FMCW of optical source envelope for passive multiplexing of frequency-based fibre-optic sensors, Electron. Lett. 22 (1986) 809–810.

[10] P.K.C. Chan, W. Jin, M.S. Demokan, Frequency domain technique for multiplexing of fiber Bragg grating sensors, SPIE Conference on Advanced Photonic Sensors and Applications ISPA '99, Dec., Singapore, 1999, pp. 488–496.

[11] A.D. Kersey, M.A. Davis, H.J. Patrick, M. LeBlanc, K.P. Koo, C.G. Askins, M.A. Putnam, E.J. Friebele, Fiber grating sensors, J. Lightwave Technol. 15 (8) (1997) 1442–1463, August.

[12] P.K.C. Chan, K.T. Lau, W. Jin, L.M. Lau, Utilization of fiber optic Bragg grating sensors in concrete columns confined with glass fiber reinforced plastic laminate under uni-axial, Proc. SPIE, Harsh Environment Sensors, November, Boston USA, 1998, pp. 62–72.